



**OPTIMISATION AND EFFICIENCY
IMPROVEMENT OF PELTON HYDRO TURBINE
USING COMPUTATIONAL FLUID DYNAMICS AND
EXPERIMENTAL TESTING**

AUDRIUS ŽIDONIS

PHD THESIS

**SUPERVISOR:
DR. GEORGE A. AGGIDIS**

Lancaster University
in collaboration with
Gilbert Gilkes & Gordon Ltd.

Department of Engineering, Faculty of Science and Technology, Lancaster University, Lancaster, UK

Declaration

The author declares that this thesis has not been previously submitted for award of a higher degree to this or any university, and that the contents, except where otherwise stated, are the author's own work.

Signed: *Audrius Židonis* 

Date: *30/04/2015*

Abstract

The aim of this PhD research was to develop a generic optimisation method for Pelton turbine runners and assess the key design parameters using Computational Fluid Dynamics (CFD). This optimisation was applied on a modern commercial Pelton turbine runner taken as a base design. The design together with the field knowledge and experience was provided by a turbine manufacturing company *Gilbert Gilkes and Gordon Ltd.* to establish the state of the art starting point.

The work described in this thesis can be divided into three main parts:

- 1) developing of numerical modelling technique by combining current commercial CFD models with engineering assumptions to produce results of acceptable accuracy within reasonable timescales and verifying this technique,
- 2) optimising the Pelton runner provided by *Gilkes* to produce better efficiency and simplify its design,
- 3) manufacturing of original and optimised design model runners and experimentally testing them.

The numerical techniques created during part 1) included many numerical and physical assumptions to simplify the problem. This was necessary because accurate modelling of impulse turbines (Pelton in this case) that include complex phenomena like free surface flow, multi fluid interaction, rotating frame of reference and unsteady time dependent flow is a challenge from a computational cost point of view. These simplifications included the usage of symmetry plane and modelling of only two consecutive buckets to reduce the size of the computational domain. Casing and any backsplash effects were not modelled at all expecting that a runner with higher hydraulic efficiency would reduce these effects since the remaining energy in the water that leaves the bucket would be reduced. For domain discretisation it was decided to use two types of mesh sizing. Fine mesh simulation was mesh independent but the required time to solve was still unfeasible for parametric optimisation. Therefore, this fine mesh sizing was used only at the key points to verify the design changes. Coarse mesh simulation was not mesh independent but reduced the timescale by the factor of 5; therefore, making it possible to acquire the results within a reasonable timescale. It was observed that the coarse meshes slightly underpredict the efficiency as compared to the fine mesh simulations. However, it was assumed that this underprediction is going to be constant when comparing small changes in geometry. Based on this assumption the coarse mesh simulations were chosen for design optimisation.

In part 2) some of the design parameters were expected to be interrelated and therefore were grouped together and analysed using Design of Experiments technique, some of the parameters were assumed to have low relation to other parameters and were analysed individually. In the end, CFD was predicting a 2.5 % increase of the original efficiency. Moreover, a reduction in the amount of buckets

to 15 (originally the runner contained 18 buckets) was investigated and provided some promising results. This reduction can be very beneficial from the manufacturing complexity and cost point of view.

In part 3) which was the final stage, three model runners were manufactured and experimentally tested in the Laboratory of Hydraulic Turbomachines at the National Technical University of Athens. It was decided to manufacture the original runner, the runner that contains 18 optimised buckets and the runner that contains 15 optimised buckets. The experimental results confirmed the increase in the efficiency and proved this optimisation technique to be valid.

Keywords

Renewable Energy, Hydropower, Impulse Turbines, Pelton Turbine, Numerical Modelling, Computational Fluid Dynamics, Optimisation, Experimental Testing

Acknowledgments

Firstly, I would like to thank my academic supervisor Dr. George Aggidis for his great support and encouragement. He has inspired me to proceed with the scientific carrier and pursue a PhD. The past few years have been an amazing and exciting chapter of my life.

I am very grateful for the sponsorship of my PhD provided by *Gilbert Gilkes and Gordon Ltd.* Moreover, for sharing the experience and industrial insights I am grateful to my industrial supervisors Jonathan Martin, Alan Robinson, Dr. Jo Scott and Anthony Watson. I am also very grateful to other *Gilkes* employees who were involved in this research. It was a real pleasure working with every each of you.

My thanks go to Shaun Benzon, Nilla Karlsen and Sean Petley, fellow PhD students from the Hydro and Pump section of the Lancaster University Renewable Energy Group (LUREG), for those entertaining conversations on CFD and beyond.

I was very lucky to know as a friend and be able to collaborate with Alexandros Panagiotopoulos from the National Technical University of Athens. Working with him and his supervisors Dr. John Anagnostopoulos and Professor Dimitris Papantonis has broadened my knowledge and was a wonderful experience.

Also, I would like to thank all the reviewers of my publications and my thesis examiners. Their constructive comments were very valuable and have helped me to significantly improve and refine my work.

Lastly and most importantly I am thankful to my family. Many thanks for your love, support, guidance and inspiration. Nothing would have happened without you.

Academic Achievements

1. Lancaster University Faculty of Science and Technology Dean's Award for PhD Excellence.
16 December 2014
2. Institution of Mechanical Engineers Best Project Award Certificate and Medal.
23 November 2011
3. *Pilkington* award for excellent performance at Part 1.
15 July 2008

List of Journal Publications

1. Aggidis, G. A. and Židonis, A. 2014. Hydro Turbine Prototype Testing and Generation of Performance Curves: Fully Automated Approach. *Renewable Energy*, 71, 433-441.
2. Židonis, A. and Aggidis, G. A. 2015. State of the Art in Numerical Modelling of Pelton Turbines. *Renewable & Sustainable Energy Reviews*, 45, 135-144.
3. Židonis, A., Benzon, D. S. and Aggidis, G. A. 2015. Development of Hydro Impulse Turbines and New Opportunities. *Renewable & Sustainable Energy Reviews*, 51, 1624-1635.
4. Židonis, A., Panagiotopoulos, A., Aggidis, G. A., Anagnostopoulos, J. S. and Papantonis, D. E. 2015. Parametric Optimisation of Two Pelton Turbine Runner Designs Using CFD. *Journal of Hydrodynamics Ser. B*. 27(3), 403-412.
5. Židonis, A. and Aggidis, G. A. 2016. Pelton Turbine: Identifying the Optimum Number of Buckets Using CFD. *Journal of Hydrodynamics Ser. B*, In-Press.
6. Benzon, D., Židonis, A., Panagiotopoulos, A., Aggidis, G. A., Anagnostopoulos, J. S. and Papantonis, D. E. 2015. Impulse Turbine Injector Design Improvement Using Computational Fluid Dynamics. *American Society of Mechanical Engineers, Journal of Fluids Engineering*, 137(4), 041106.
7. Benzon, D., Židonis, A., Panagiotopoulos, A., Aggidis, G. A., Anagnostopoulos, J. S. and Papantonis, D. E. 2015. Numerical investigation of the spear valve configuration on the performance of Pelton and Turgo turbine injectors and runners. *American Society of Mechanical Engineers, Journal of Fluids Engineering*, 137(11), 111201.
8. Panagiotopoulos, A., Židonis, A., Aggidis, G. A., Anagnostopoulos, J. S. and Papantonis, D. E. 2015. Flow Modeling in Pelton Turbines by an Accurate Eulerian and a Fast Lagrangian Evaluation Method. *International Journal of Rotating Machinery*, 2015, 679576.

List of Conference Publications

1. Židonis, A., Aggidis, G.A. 2014. *Application of CFD in Hydropower Development*. Lancaster University Science and Technology Christmas Conference. 16 December 2014.
2. Židonis, A., Aggidis, G.A. 2014. *Applied PhD Research*. National Student Academy 10 Year Anniversary Conference. Vilnius, Lithuania, 20 November 2014.
3. Židonis, A., Aggidis, G.A. 2014. *CFD Application in Development of Pelton Turbines*. Lancaster University Renewable Energy Group Seminar. 30 September 2014.
4. Židonis, A., Aggidis, G.A. 2014. *CFD Application in Development of Pelton Turbines*. Lancaster University Engineering Research Review Conference. 1-2 July 2014.
5. Židonis, A., Aggidis, G.A. 2014. *CFD Application in Development of Pelton Turbines*. Lancaster University Renewable Energy Group Seminar. 6 March 2014.
6. Židonis, A., Aggidis, G.A. 2013. *CFD Application in Development of Pelton Turbines*. Lancaster University Engineering Research Review Conference. 2-3 July 2013.
7. Židonis, A., Aggidis, G.A. 2012. *CFD Application in Development of Pelton Turbines*. Lancaster University Renewable Energy Group Seminar. 27 September 2012.
8. Židonis, A., Aggidis, G.A. 2012. *CFD Application in Development of Pelton Turbines*. Lancaster University Engineering Research Review Conference. 11-12 July 2012.
9. Židonis, A., Aggidis, G.A. 2011. *Computational Modelling Automation and Process Acceleration for Development of Hydro Turbine Performance Model Curves*. IMechE Fluid Machinery Group Board Meeting. 23 November 2011.

Contribution to Knowledge and Practice

Parametric Optimisation of Pelton Runner Design. Despite the abundance of publications suggesting that CFD has reached the stage to become a feasible tool for Pelton turbine design improvement, there was a lack of research showing successful, experimentally validated design optimisation of Pelton runner using CFD. Such experimentally validated optimisation was performed and is presented in this thesis.

Drastically Reduced Number of Buckets. Current Pelton runner design guidelines are either theoretical involving simplifications or assumptions that cause uncertainties or observational. They were found to be inconsistent and not based on any experimental testing or numerical modelling data. During the CFD optimisation study presented in this thesis, the number of buckets was reduced below the number suggested by any available design guidelines without reducing the efficiency. In addition to the efficiency increase achieved in this research, the reduction of buckets has simplified the complex design substantially resulting in reduced manufacturing cost and timescale.

Table of Contents

Declaration	ii
Abstract	iii
Keywords	iv
Acknowledgments	v
Academic Achievements	vi
List of Journal Publications	vi
List of Conference Publications	vii
Contribution to Knowledge and Practice	vii
List of Figures	xiii
List of Tables	xix
Nomenclature	xxi
Mathematical Notation	xxiii
Acronyms	xxiv
Chapter 1. Introduction	1
1.1. The Need for Renewable Energy Resources	1
1.2. Hydropower	2
1.3. Reaction and Impulse Turbines	2
1.4. Pelton Turbine	4
1.5. Computational Fluid Dynamics	4
1.6. Governing Equations	4
1.7. Aims and Goals	6
1.8. Structure of the Thesis	7
Chapter 2. Literature Review	8
2.1. Design of Pelton Turbines	8
2.1.1. History and Evolution of Pelton Turbines	8
2.1.2. Available Design Guidelines	11
2.2. Relevant CFD Codes	13

2.2.1. Eulerian and Lagrangian Methods.....	14
2.2.2. ANSYS CFX	15
2.2.3. ANSYS Fluent.....	16
2.2.4. OpenFOAM.....	17
2.2.5. Other Eulerian Solvers.....	17
2.2.6. Smoothed Particle Hydrodynamics	17
2.2.7. Fast Lagrangian Solver.....	18
2.2.8. Other Lagrangian Solvers.....	18
2.3. Application of CFD on Pelton Turbines.....	18
2.3.1. Injector and Jet Simulations.....	19
2.3.2. Stationary Bucket Simulations	19
2.3.3. Rotating Bucket Simulations	20
2.3.4. Summary of CFD Application on Pelton Turbines	23
2.3.5. State of the Art in Modelling of Pelton Turbines	23
Chapter 3. Computational Modelling	25
3.1. ANSYS CFX	25
3.2. Model Verification.....	26
3.2.1. Geometry Decomposition.....	26
3.2.2. Modelling Assumptions.....	31
3.3. Setup and Post-Processing.....	35
3.3.1. Computational Domain Geometry.....	35
3.3.2. Mesh	36
3.3.3. Physics Definition.....	37
3.3.4. Solver Definition	42
3.3.5. Post-Processing the Results	43
3.3.6. Simulation Sequence	45
3.4. Model Validation.....	49
3.4.1. Mesh Convergence Study.....	49
3.4.2. Fine and Coarse Mesh Simulations	52

3.5.	Summary of Computational Modelling	53
Chapter 4.	Design Optimisation.....	54
4.1.	Preparation.....	54
4.1.1.	Removing of the Bucket Reinforcing Ribs.....	55
4.1.2.	Geometry Parameterisation	55
4.1.3.	Splitter Simplification.....	57
4.2.	Design Parameters	57
4.3.	Design of Experiments Optimisation.....	62
4.3.1.	P1-P4: DOE Study 1 (L/B, H/B, β_e , β_i)	63
4.3.2.	P5-P7: DOE Study 2-1 (α , R_t , N_b)	68
4.3.3.	P5-P7: DOE Study 2-2 (α , R_t , N_b)	72
4.4.	Analytical Optimisation	79
4.4.1.	P3: Exit Angle β_e	79
4.4.2.	P10: Backside of the Splitter	80
4.4.3.	P11: Cutout Shape	83
4.4.4.	P11-P12: Splitter Tip and Cutout Shape.....	84
4.5.	Finalising	87
4.5.1.	Structural Analysis.....	88
4.5.2.	P5-P6: DOE Study 3 (α , R_t).....	93
4.5.3.	Final Design Approved for Manufacturing	96
4.6.	Summary of Design Optimisation (Fine Mesh Results)	96
Chapter 5.	Experimental Testing	97
5.1.	Overview.....	97
5.2.	Manufacturing.....	98
5.3.	Turbine Characteristic Equations.....	99
5.4.	Testing Procedure	100
5.5.	1 st Set of Tests.....	102
5.5.1.	Instruments and Calibration.....	102
5.5.2.	Estimation of the Uncertainty	111

5.5.3. Datum for Normalising the Results	112
5.5.4. Test Results.....	113
5.5.5. Estimation of the Mechanical Losses	117
5.5.6. Problems and Recommendations.....	120
5.6. 2 nd Set of Tests	122
5.6.1. Calibration	122
5.6.2. Estimation of the Uncertainty	123
5.6.3. Datum for Normalising the Results	124
5.6.4. Test Results.....	125
Chapter 6. Results and Discussion.....	130
6.1. Comparison of Numerical and Experimental Results.....	130
6.2. Comparison of Runner Designs.....	132
6.2.1. Effect of the bucket shape design modifications	133
6.2.2. Effect of the reduced number of buckets on the runner.....	135
6.3. Limitations of the CFD Model.....	140
Chapter 7. Conclusions and Recommendations.....	145
7.1. Summary.....	145
7.2. Contribution and Novelty of the Present Work	146
7.2.1. Parametric Optimisation of Pelton Runner Design.....	146
7.2.2. Drastically Reduced Number of Buckets.....	147
7.2.3. Economic Effect	147
7.3. Recommendations for Future Work	148
7.3.1. Coanda Effect	148
7.3.2. Optimum Number of Buckets.....	148
7.3.3. High Capacity Computing	148
7.3.4. Injector Design	149
7.3.5. Multi Jet Operation.....	149
7.3.6. Turbine Casing Design	149
7.3.7. Turgo Impulse Turbine Runner Development.....	150

References	151
Appendices	157
Appendix A Tables of Physical Properties	157
Appendix B CFX Command Language for the Run	160
Appendix C DOE – Response Surface Method	171

List of Figures

Fig. 1.1. Performance envelopes of various hydro turbines (Aggidis 2010, Aggidis, Luchinskaya et al. 2010). The indicative range of Pelton turbines and the indicative range of the Pelton runner used in this PhD as a case study are highlighted.	3
Fig. 2.1. Illustrations of the Pelton wheel from its patent (Pelton 1880).	8
Fig. 2.2. Sketch of a bucket that has a cutout. Published in 1937 (Fulton 1937).	9
Fig. 2.3. Sketch of a nozzle controlled by a spear valve. Published in 1911 (Prášil 1911).	9
Fig. 2.4. Sketch of a multi-jet vertical shaft Pelton. Published in 1937 (Fulton 1937).	9
Fig. 2.5. Typical layout of a modern Pelton turbine (Ecopolis 2010).	10
Fig. 2.6. Numerical diffusion on two meshes of different resolution.	16
Fig. 2.7. The exact VOF model volume fraction function for a smooth circular arc over a square grid (Scardovelli and Zaleski 1999).	17
Fig. 3.1. Project layout in ANSYS Workbench.	25
Fig. 3.2. Creation of the computational domain using functional decomposition.	26
Fig. 3.3. CFX-Pre: screen capture of the rotating and the stationary domains with the symmetry plain boundary highlighted in green.	27
Fig. 3.4. CFX-Pre: screen capture of the rotating and the stationary domains with the mirrored mesh. Original part of the domain (right hand side) coloured in grey and the mirrored part (left hand side) highlighted in green.	28
Fig. 3.5. Evacuating water sheets for different operating conditions (Jošt, Mežnar et al. 2010).	29
Fig. 3.6. Different torque measurement methods in simulations with three or two buckets. Reference surfaces contributing to the torque measurement are highlighted in green.	30
Fig. 3.7. Torque on one bucket acquired using different torque measurement methods.	31
Fig. 3.8. Domain geometries as imported from Solidworks: stationary (left), rotating (right).	35
Fig. 3.9. Mesh of the stationary domain.	36
Fig. 3.10. Mesh of the rotating domain.	37
Fig. 3.11. Rotating and stationary domains in CFX-Pre.	37
Fig. 3.12. Simulated results: a) inside and outside torque curves as acquired, b) inside torque curve summed with the synchronised outside torque curve to produce a curve of total torque on one bucket.	43
Fig. 3.13. Runner torque construction from a torque data acquired on a single bucket.	43
Fig. 3.14. User defined monitor point variables against the accumulated timestep number of the complete simulation.	46
Fig. 3.15. Timeframes of jet initialisation while the rotating domain is frozen.	47
Fig. 3.16. Timeframes of the jet entering the bucket until being completely switched off.	47

Fig. 3.17. Timeframes of water completely clearing the first bucket.....	48
Fig. 3.18. Mesh refinement study results. Grid spacing of each case is normalised by the grid spacing of the coarsest grid. Efficiency is normalised by the result acquired using the coarsest grid.	50
Fig. 3.19. Normalised torque curves of the grid refinement study.....	51
Fig. 3.20. Region of the normalised torque curves of the grid refinement study where the main difference was observed.	51
Fig. 4.1. Bucket geometry with definition of key features.....	54
Fig. 4.2. Original geometry with the reinforcing ribs (left), reinforcing ribs removed (right).....	55
Fig. 4.3. Inside (left) and outside (right) surfaces of one half of the bucket and their control curves. .	56
Fig. 4.4. Control curve of one bucket profile specifying the inlet (β_i) and exit (β_e) angles and the tangential length (l_t) at three key points of the spline.....	56
Fig. 4.5. Parameterised bucket geometry with the connecting surfaces highlighted in blue.....	56
Fig. 4.6. Bucket geometry before (left) and after (right) the splitter shape was simplified.	57
Fig. 4.7. Design Parameter P1 Bucket length to width ratio (L/B).	58
Fig. 4.8. Design Parameter P2 Bucket depth to width ratio (H/B).	58
Fig. 4.9. Design Parameter P3 Bucket exit angle (β_e).	58
Fig. 4.10. Design Parameter P4 Splitter inlet angle (β_i).	59
Fig. 4.11. Design Parameter P5 Inclination angle (α).	59
Fig. 4.12. Design Parameter P6 Radial distance (R_t).	59
Fig. 4.13. Design Parameter P7 Number of buckets (N_b).	60
Fig. 4.14. Design Parameter P8 Splitter level (H_s).	60
Fig. 4.15. Design Parameter P9 Splitter edge angle (β_s).	60
Fig. 4.16. Design Parameter P10 Backside of the splitter.	61
Fig. 4.17. Design Parameter P11 Splitter edge angle (β_s).	61
Fig. 4.18. Design Parameter P12 Splitter tip geometry.....	61
Fig. 4.19. Jet impacting bucket 1 (white) at the peak inside torque.....	64
Fig. 4.20. Range for the locations of the plane where the exit angle was measured.....	64
Fig. 4.21. Distribution of the exit angle (β_e).....	64
Fig. 4.22. Distribution of the losses caused by the exit angle (β_e).	64
Fig. 4.23. Distribution of the real exit angle (β_e) after the DOE Study 1.....	66
Fig. 4.24. Distribution of the losses caused by the exit angle (β_e) after the DOE Study 1.....	66
Fig. 4.25. Side view of the bucket geometry before (left) and after (right) the DOE Study 1.....	67
Fig. 4.26. Top view of the bucket geometry before (left) and after (right) the DOE Study 1.....	67
Fig. 4.27. Bucket geometry before (left) and after (right) the DOE Study 1.	67
Fig. 4.28. Water exiting the bucket sliding on the back of the following bucket.....	68
Fig. 4.29. Peak efficiency for different number of buckets N_b (DOE Study 2-1 Iteration 1).....	69
Fig. 4.30. Peak efficiency for different number of buckets N_b (DOE Study 2-1 Iterations 1 and 2).....	70

Fig. 4.31. Normalised efficiency contours for different N_b (DOE Study 2-1 Iteration 1).	71
Fig. 4.32. Comparison of the predicted peak efficiency and the simulated result for different number of buckets N_b . A: DOE Study 2-2 Iteration 1, B: DOE Study 2-2 Iteration 2.	73
Fig. 4.33. Peak efficiency for different number of buckets N_b (DOE Study 2-2 Iterations 1, 2 and 3).	74
Fig. 4.34. Normalised efficiency contours for different N_b (DOE Study 2-2 Iteration 3).	75
Fig. 4.35. Peak efficiency for different number of buckets N_b (DOE Study 2-2 Iterations 1, 2 and 3).	76
Fig. 4.36. Various views of flow behaviour inside two buckets of interest showing that no water particles were lost in the runner with 15 buckets.	77
Fig. 4.37. Various views of flow behaviour inside two buckets of interest showing that no water particles are lost in the runner with only 12 buckets.	78
Fig. 4.38. Normalised runner efficiency η vs. the relative exit angle β_e	79
Fig. 4.39. Normalised torque curves of a runner after the DOE Study 2 (modification c-16).	80
Fig. 4.40. Backside of the splitter modifications that have improved the efficiency.	81
Fig. 4.41. Backside of the splitter modifications that have reduced the efficiency.	81
Fig. 4.42. Bucket shape control curve (dashed line: before the modification, solid line: modified)	82
Fig. 4.43. Normalised torque curves of a runner after the backside of the splitter was modified and the thickness restored (modification d-5.1).	82
Fig. 4.44. Flow leaving through the cutout with high velocity	83
Fig. 4.45. Cutout shape modification.	83
Fig. 4.46. Cutout in the original bucket design (face of the cut highlighted in blue).	84
Fig. 4.47. Cutout in the modification e-0 (face of the cut highlighted in blue).	84
Fig. 4.48. Equivalent (Von-Misses) stress contours for the original (left) and e-0 (right) bucket design under runaway conditions.	85
Fig. 4.49. Stress concentration at the cutout caused by the inertial force F_c of the thick bucket wall. Modification e-0.	85
Fig. 4.50. Three initial FEA approved modifications of the cutout and the splitter tip.	86
Fig. 4.51. Two final FEA approved modifications of the cutout and the splitter tip. Modified regions highlighted in red.	87
Fig. 4.52. Thickness comparison of the original and modification e-10 designs at 3 different cross-section locations expressed as distance s from the symmetry plane.	88
Fig. 4.53. Thickness comparison of the original and modification e-11 designs at 3 different cross-section locations expressed as distance s from the symmetry plane.	89
Fig. 4.54. FEA results at various bucket angular positions under the nominal operating conditions. Left: peak stress at the cutout edge, right: peak stress at the splitter edge.	90
Fig. 4.55. Maximum thickness comparison of the original and modification e-10.1.	91
Fig. 4.56. Removed material from the bottom of e-10.1.	91

Fig. 4.57. FEA results at various bucket angular positions under the nominal operating conditions. Left: peak stress at the cutout edge, right: peak stress at the splitter edge.	92
Fig. 4.58. Normalised efficiency contours for $N_b = 15$	94
Fig. 4.59. Normalised efficiency contours for $N_b = 18$	95
Fig. 4.60. Summary of efficiency improvements during key development stages according to fine mesh CFD simulations.	96
Fig. 5.1. Segmented Pelton runner with 15 numerically optimised (Z120) buckets used for experimental testing.	98
Fig. 5.2. Z120 bucket CNC machined from aerospace grade aluminium alloy.	98
Fig. 5.3. Gilkes Pelton turbine testing facility at the Laboratory of Hydraulic Machines (NTUA).....	98
Fig. 5.4. Inside view of the Pelton turbine casing.	99
Fig. 5.5. Test plan and testing sequence.....	101
Fig. 5.6. Reference locations for pressure readings p_1 to p_5	103
Fig. 5.7. Types of pressure manifolds (IEC 60193:1999). 1) vent, 2) pressure measuring instrument, 3) manifold, 4) ring manifold, 5) drain and 6) gas-collecting chamber.....	103
Fig. 5.8. Dead weight tester connected to the pressure transducers (left) and the calibrated weights (right).....	104
Fig. 5.9. Calibration curve and the relative error of the pressure transducer p_1	104
Fig. 5.10. Inside of the volumetric tank used to calibrate the flow meter.	105
Fig. 5.11. Cross-sectional area of the volumetric tank vs. the elevation curve.	105
Fig. 5.12. Calibration curve and the relative error of the depth pressure sensor.....	106
Fig. 5.13. Electromagnetic flow meter.....	106
Fig. 5.14. Water elevation in the tank vs. time curve and its linear fit for $Q = 11.7 \text{ m}^3/\text{h}$	107
Fig. 5.15. Calibration curve and the relative error of the flow meter.....	107
Fig. 5.16. Arrangement using a torque meter with machine bearings and seals not in balance (IEC 60193:1999). 1) axial thrust bearing, 2) rotating part, 3) stationary part, 4) torque meter, 5) bearing of rotating part not in balance 6) mechanical seal of rotating part not in balance.....	108
Fig. 5.17. Torque meter.....	108
Fig. 5.18. Calibration of the torque meter.	109
Fig. 5.19. Calibration curve and the relative error of the torque meter.....	109
Fig. 5.20. Rotational speed sensor.....	110
Fig. 5.21. Checking the readings with a hand held tachometer.....	110
Fig. 5.22. Original runner in both jets operation: normalised efficiency vs. specific flow rate curves.	113
Fig. 5.23. Original runner in both jets operation: normalised efficiency hill chart.	113
Fig. 5.24. Original runner in single jet operation: normalised efficiency vs. specific flow rate curves.	114

Fig. 5.25. Original runner in single jet operation: normalised efficiency hill chart.	114
Fig. 5.26. Optimised runner with 18 buckets in both jets operation: normalised efficiency vs. specific flow rate curves.	115
Fig. 5.27. Optimised runner with 18 buckets in both jets operation: normalised efficiency hill chart.	115
Fig. 5.28. Optimised runner with 18 buckets in single jet operation: normalised efficiency vs. specific flow rate curves.	116
Fig. 5.29. Optimised runner with 18 buckets in single jet operation: normalised efficiency hill chart.	116
Fig. 5.30. Summary of best efficiency point results for each design tested.	117
Fig. 5.31. Friction torque vs. the rotational speed when $Q = 0 \text{ m}^3/\text{s}$	118
Fig. 5.32. Friction torque measurements with only a hub but no buckets.	118
Fig. 5.33. Bearing friction losses calculated using the measured torque at the BEP.	119
Fig. 5.34. Disc friction losses calculated using the measured torque at the BEP.	119
Fig. 5.35. Example of control points indicating problems in the testing.	121
Fig. 5.36. New torque meter.	122
Fig. 5.37. Optimised runner with 18 buckets in both jets operation: normalised efficiency vs. specific flow rate curves.	125
Fig. 5.38. Optimised runner with 18 buckets in both jets operation: normalised efficiency hill chart.	125
Fig. 5.39. Optimised runner with 18 buckets in single jet operation: normalised efficiency vs. specific flow rate curves.	126
Fig. 5.40. Optimised runner with 18 buckets in single jet operation: normalised efficiency hill chart.	126
Fig. 5.41. Optimised runner with 15 buckets in both jets operation: normalised efficiency vs. specific flow rate curves.	127
Fig. 5.42. Optimised runner with 15 buckets in both jets operation: normalised efficiency hill chart.	127
Fig. 5.43. Optimised runner with 15 buckets in single jet operation: normalised efficiency vs. specific flow rate curves.	128
Fig. 5.44. Optimised runner with 15 buckets in single jet operation: normalised efficiency hill chart.	128
Fig. 5.45. Summary of best efficiency point results for each design tested.	129
Fig. 6.1. Comparison of efficiency improvement predicted by CFD and measured experimentally at operating point used for optimisation.	131
Fig. 6.2. Overall efficiency improvement of each runner compared at their best efficiency point operating conditions – experimental results.	132
Fig. 6.3. Comparison of runner performance at the best efficient n_{11} using original and optimised bucket designs – both jets in operation.	133

Fig. 6.4. Comparison of runner performance at the best efficient n_{11} using original and optimised bucket designs - single jet operation.	134
Fig. 6.5. Comparison of the optimised runner performance at the best efficient n_{11} using 18 and 15 buckets – both jets in operation.....	136
Fig. 6.6. Comparison of the optimised runner performance at the best efficient n_{11} using 18 and 15 buckets – single jet operation.	136
Fig. 6.7. Torque curves on a single bucket in an optimised runner with different amount of buckets.	137
Fig. 6.8. Two inverted torque peaks generated by two jets (Wei, Yang et al. 2015).	137
Fig. 6.9. Two torque peaks taken from the single jet simulation and manually shifted by the angle between the jets (80°). Original runner.	138
Fig. 6.10. Two torque peaks taken from the single jet simulation and manually shifted by the angle between the jets (80°). Optimised runner with 18 buckets.....	138
Fig. 6.11. Two torque peaks taken from single jet simulation and manually shifted by the angle between the jets (80°). Optimised runner with 15 buckets.....	139
Fig. 6.12. Stationary and rotating domains of the simulation with 2 jets and 3 buckets of the Original runner. Surfaces contributing to the torque measurement are highlighted in green on the right hand side.	139
Fig. 6.13. CFD predicted efficiency improvement from 1 jet and 2 jet simulations.....	140
Fig. 6.14. Two torque peaks. Original runner.	141
Fig. 6.15. Two torque peaks. Optimised runner with 18 buckets.....	141
Fig. 6.16. Two torque peaks. Optimised runner with 15 buckets.....	141
Fig. 6.17. Water-air interface iso-surfaces at two different volume fractions during various moments of the two jet simulation.	142
Fig. 6.18. 1 st and 2 nd jet detaching in a different way.	143
Fig. 6.19. Simulation with wet surface initial conditions.....	143
Fig. 6.20. Comparison of results from simulations with different initial conditions.	144

List of Tables

Table 2.1. Selecting the number of buckets according to Nechleba (1957).....	12
Table 2.2. Resultant number of buckets for the Pelton runner used in this case as suggested by different authors.	13
Table 2.3. Comparison of CFD methods and software used for Pelton turbine modelling.....	24
Table 3.1. Efficiency calculated using different torque measurement methods. Efficiencies normalised to the result that was calculated using method 1.	31
Table 3.2. Buoyancy options as defined in CFX-Pre.	34
Table 3.3. List of named selections in the domain geometries.	38
Table 3.4. Constant material properties of air and water used in CFX.	39
Table 3.5. Boundary conditions in Stationary domain.	40
Table 3.6. Boundary conditions in Rotating domain.....	41
Table 3.7. Grid convergence results normalised to the coarsest grid (#3).	49
Table 3.8. Grid convergence criteria.	50
Table 3.9. Known relative numerical error band introduced by various assumptions.	53
Table 4.1. Design ranges for parameters L/B , H/B , β_e , β_i	63
Table 4.2. Test plan for parameters L/B , H/B , β_e , β_i	66
Table 4.3. Design ranges for parameters α , R_t and N_b	68
Table 4.4. Test plan for parameters α , R_t and N_b	69
Table 4.5. Suggestions on the amount of buckets found in the available literature.	72
Table 4.6. Design ranges for parameters α , R_t and N_b	72
Table 4.7. Test plan for parameters α , R_t and N_b	73
Table 4.8. Design modifications of the backside of the splitter geometry. Efficiency normalised to the latest modification c-16.	80
Table 4.9. FEA approved design modifications around the cutout.	86
Table 4.10. Operating conditions for FEA analysis.	89
Table 4.11. Design ranges for parameters α , R_t , whereand $N_b = 15$	94
Table 4.12. Test plan for parameters α and R_t , where $N_b = 15$	94
Table 4.13. Design ranges for parameters α , R_t , where $N_b = 18$	95
Table 4.14. Test plan for parameters α and R_t , where $N_b = 18$	95
Table 5.1. Systematic error of each instrument.....	111
Table 5.2. Calculating the random uncertainty.	112
Table 5.3. Systematic error of each instrument.....	122
Table 5.4. Calculating the random uncertainty.	123

Table 6.1. Comparison of CFD and experimental results at $n_{11} = 39.8$ rpm, $q_{11k} = 0.221$ m³/s normalised to the experimentally measured efficiency that was corrected for the estimated mechanical and injector losses. 131

Nomenclature

A	Area	[m ²]
a	Acceleration	[m/s ²]
B	Bucket maximum internal width	[m]
D	Diameter (related to the runner)	[m]
D_p	Pitch circle diameter	[m]
d	Jet or nozzle diameter	[m]
d_j	Jet diameter	[m]
d_o	Optimum jet diameter	[m]
E	Internal energy	[J]
E_k	Kinetic energy	[J]
E_p	Potential energy	[J]
F	Force	[N]
F_c	Centrifugal force	[N]
g	Acceleration due to gravity	[m/s ²]
H	Pressure head, elevation, height or vertical distance	[m]
H_s	Splitter level	[m]
h	Grid spacing	[m]
h_s	Specific static enthalpy	[m ² /s ²]
i, j	Index notation	[-]
k	Turbulence kinetic energy	[m ² /s ²]
L	Bucket length	[m]
l_t	Tangential length	[m]
m	Mass	[kg]
M	Torque	[N·m]
M_{Lm}	Friction torque	[N·m]
M_m	Runner torque	[N·m]
M_s	Shaft torque	[N·m]
\dot{m}	Mass flow rate	[kg/s]
n	Rotational speed	[rpm]
n_{11}	Turbine unit speed	[rpm]
N	Number of	[-]
N_B	Number of buckets	[-]
N_J	Number of jets	[-]

P	Power	[W]
P_{in}	Input power	[W]
P_{out}	Output power	[W]
p	Pressure	[Pa]
p_c	Order of convergence	[-]
Q	Flow rate	[m ³ /s]
Q'	Heat transfer	[J]
q	Heat flux	[W/m ²]
Q_{11}	Unit flow rate	[m ³ /s]
Q_{11k}	Unit flow rate specified to the bucket width and one jet	[m ³ /s]
R	Radius	[m]
R_p	Pitch circle radius	[m]
R_t	Radial distance	[m]
r	Refinement ratio	[-]
r^*	Required refinement ratio	[-]
S_e	Energy source	[kg/m ³ ·s ³]
S_m	Momentum source	[kg/m ² ·s ²]
s	Needle stroke (spear travel)	[m]
s_y	Standard deviation	[-]
T	Temperature	[K]
t	Time	[s]
t_T	Turbulence timescale	[s]
u, v, z	Velocity components	[m/s]
\bar{u}	Mean velocity	[m/s]
\vec{u}	Vector of velocity	[m/s]
V	Voltage	[V]
W	Work	[J]
W_B	Work produced on a bucket	[J]
W_{IN}	Work produced on the inside surface	[J]
W_{OUT}	Work produced on the outside surface	[J]
X_m	Measured (readout) value	[*]
X_{ref}	Reference value	[*]
x, y, z	Distances in coordinates 'X', 'Y', 'Z'	[m]
α	Bucket inclination angle	[°]
β_e	Bucket exit angle	[°]

β_i	Bucket inlet angle	[°]
β_s	Splitter edge angle	[°]
Δ	Absolute value of an error	[*]
δ	Percent error	[%]
ε	Turbulence dissipation rate	[m ² /s ³]
θ	Rotated angle	[°]
θ_H	Rotated angle from horizontal	[°]
φ	Latitude	[°]
η	Efficiency	[%]
η_0	Original efficiency	[%]
λ	Thermal conductivity	[K·m/W]
μ	Dynamic viscosity	[Pa·s]
ρ	Density	[kg/m ³]
ω	Rotational frequency	[rad/s]
ω	Specific turbulence dissipation rate	[s ⁻¹]
τ	Stress	Pa

Mathematical Notation

∇	Del operator
δ	Identity matrix or Kronecker Delta function
\otimes	Dyadic operator
$()^T$	Matrix transposition

Acronyms

BEP	Best Efficiency Point
CEL	CFX Expression Language
CFD	Computational Fluid Dynamics
CPU	Central Processing Unit
DES	Detached Eddy Simulation
DNS	Direct Numerical Simulation
DOE	Design of Experiments
DPM	Discrete Particle Model
EPFL	Ecole Polytechnique Fédérale de Lausanne
FEA	Finite Element Analysis
FLS	Fast Lagrangian Solver
GCI	Grid Convergence Index
LDA	Laser Doppler Anemometry
LES	Large Eddy Simulation
MPI	Message Passing Interface
MPS	Moving Particle Semi-implicit
NTNU	Norwegian University of Science and Technology
NTUA	National Technical University of Athens
NURBS	Non-Uniform Rational Basis Spline
RAM	Random Accessed Memory
RANS	Reynolds Averaged Navier-Stokes
RMS	Root Mean Square
RNG	Re-Normalisation Group
RSD	Response Surface Designs
SPH	Smooth Particle Hydrodynamics
SST	Shear Stress Transport
VF	Volume Fraction
VOF	Volume of Fluid

Chapter 1. Introduction

This chapter is an introduction to the work performed during the PhD research and describes the purpose of it. A quick discussion on the need of renewable energy sources and brief introduction to the general principles of hydro power as the branch of renewable energy technologies is provided here. Pelton turbine and its development using modern numerical methods known as Computational Fluid Dynamics (CFD) are also briefly overviewed. A more elaborate establishment of the state of the art in this area is provided in Chapter 2. *Literature Review*. UK's capacity in harvesting the small scale hydro-power was a key driver for this research. However technology developed during this research is not limited and can be used in any different location in the world. A structure of this thesis and a brief description of the following chapters are provided at the end of this chapter.

1.1. The Need for Renewable Energy Resources

Energy resources nowadays known as renewable resources were the very first ones to be harnessed by humankind. The first ships that were not powered by manpower were sailing-ships, the first automated mills were powered by wind or hydro power and the first heat source was firewood. It is only later when fossil-fuel and nuclear technologies were discovered and boosted the industry. The rapid development of the modern world happened because of the relatively high controllability and flexibility of fossil and nuclear power technologies at the time, leaving the renewable resources aside. However, the intensive use of conventional energy resources has gradually produced many problems such as pollution, contaminated waste management, depletion of resources and in many cases strong dependence on imported supplies. It was because of the reasons like these that the world started reconsidering the sustainable and renewable power resources as with modern technology more and more renewables are becoming competitive with conventional power (European Renewable Energy Council 2010) which is getting more expensive as the supply is getting shorter with time. Not to mention the world's concern about the impact made on our planet expressed by various international agreements like a binding target of all the EU members to produce 20% of final energy consumption from renewable power resources which was stated in Renewable Energy Sources (RES) Directive which entered into force in June 2009 (European Commission 2009) or Kyoto Protocol aiming to reduce greenhouse gasses worldwide which entered into force in 2005 (United Nations Framework Convention on Climate Change 2011). It is a clear message that renewable energy is the way to proceed.

1.2. Hydropower

There are plenty of different sustainable energy resources that could be used but usually there is no single resource that could provide enough energy on its own to completely satisfy the demand. That is why each and every resource is important and they all have to be used collectively. However, some countries are richer with one type of resources and some with another. For instance, in the United Kingdom, the amount of solar energy that could be taken from direct sunlight would not be such a big player as hydropower. The average UK's demand for electricity in 2013 was around 35 GW (National Grid 2014), whereas there are studies that show a capacity of 1.5 GW (more than 4% of the average demand) of untapped hydro power available in the UK (British Hydropower Association 2010).

Same as the wind is a transformed energy from the sun which heats the air and causes convection, hydro power is stimulated by radiant energy supplied by the sun. As the radiant energy heats the surface of the Earth most of which, 70% (Turner 1969), is covered by water (mostly the oceans) the evaporation is caused. This is how water molecules are lifted. When hot air and water mixture masses reach high altitudes and cool down, the condensation takes place, which results in water droplets emerging and then forming streams and rivers that go back to the oceans. The whole phenomenon is known as the hydrologic cycle (Pidwirny 2006). It could be seen from the potential energy formula (Eq. 1.1) that after water vapour condenses back into water droplets it has potential energy because of their altitude, H .

$$E_p = mgH \quad (1.1)$$

According to Mosonyi (1987) under normal run of river all that potential energy is dissipated in a form of heat loss when overcoming friction and creating eddies and swirls. Hence, Mosonyi states that 'the fundamental principle of water power development is to reduce the amount of energy dissipated as heat, without paralysing the flow of water'. These are the main reasons why hydropower is a very attractive field for further development. There is a huge variety of hydro turbines depending on specific requirements and on available river conditions. Based on the working principles they are separated into two distinct classes: reaction and impulse turbines and will be described in the following section.

1.3. Reaction and Impulse Turbines

In general reaction turbines produce power by combining the kinetic energy of the moving water and the potential energy available from the pressure difference. Popular examples of reaction turbines are Kaplan, Francis or Archimedes Screw. Usually reaction turbines are used for lower head and higher flow applications than impulse turbines. Typically reaction turbines are completely submerged in the

water. Fig. 1.1 presents performance envelopes of these turbines and gives graphical comparison to impulse turbines that are described in the following paragraph.

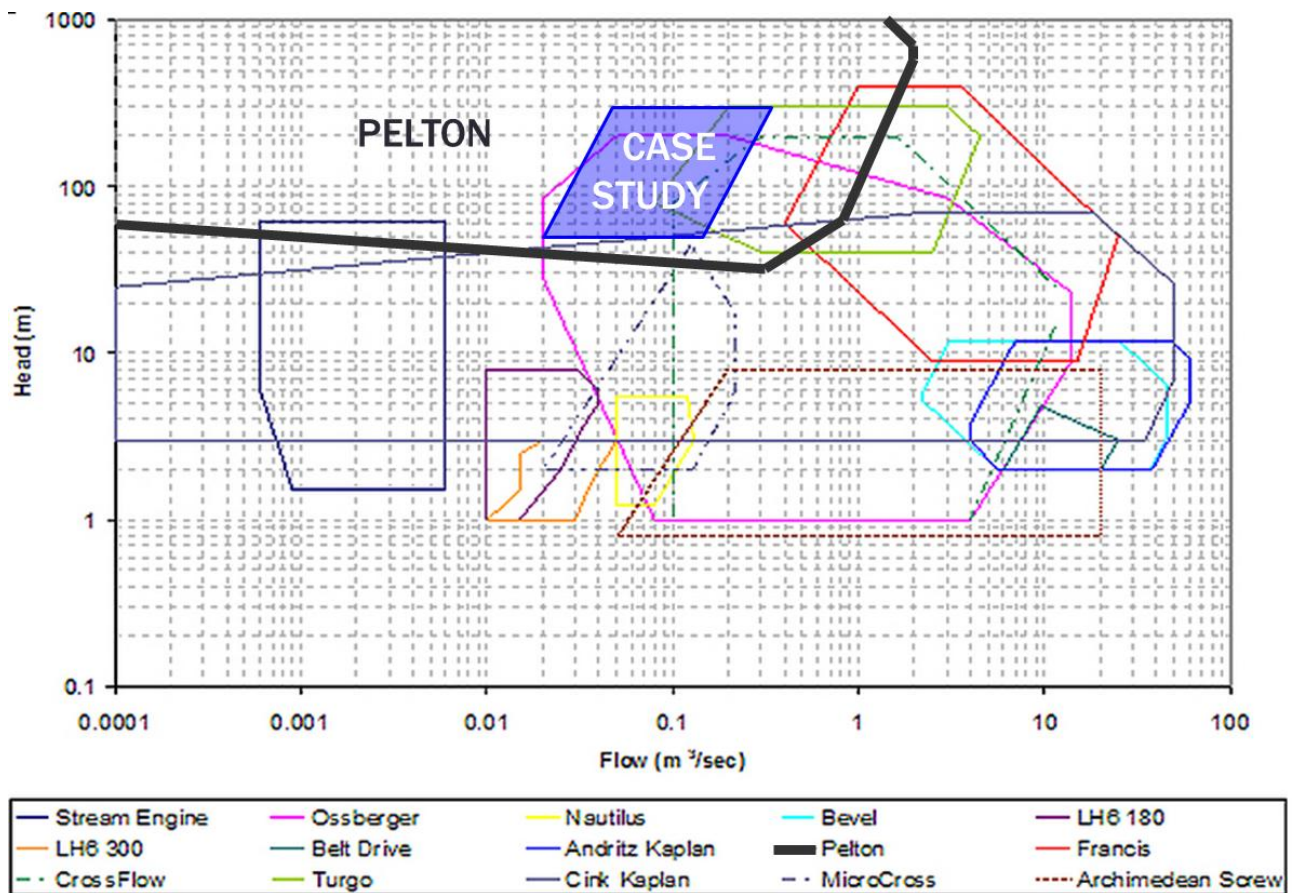


Fig. 1.1. Performance envelopes of various hydro turbines (Aggidis 2010, Aggidis, Luchinskaya et al. 2010). The indicative range of Pelton turbines and the indicative range of the Pelton runner used in this PhD as a case study are highlighted.

Impulse turbines generate power by converting potential energy available from the pressure difference, i.e. difference in water levels upstream and downstream. What happens inside of the turbine is the conversion of this potential energy of the pressure head into kinetic energy of the water stream. This kinetic energy of the water stream discharged into the atmospheric pressure is then utilised by the runner consisting of blades or buckets. In impulse turbines, there are two phases around the runner: water and air. Examples of impulse turbines are Pelton, Turgo or Cross-flow turbines. Typically impulse turbines are used for higher head and lower flow rate applications than reaction turbines as shown in Fig. 1.1. The range of Pelton turbines in general is highlighted using thicker black line. The area highlighted in blue shows an indicative range of operation for the Pelton runner used in this PhD.

1.4. Pelton Turbine

Pelton turbine (or Pelton wheel) is among the most efficient impulse turbines and has retained its existence in hydropower for well over a century since it was invented by Lester A. Pelton (1880). The turbine produces power by utilising water momentum impinging on buckets mounted on the periphery (Nechleba 1957, Mosonyi 1991). Despite its age, the design of Pelton turbine keeps improving (Patel, Patel et al. 2010) and this development is driven by a tough commercial competition between turbine manufacturers and availability of new tools for analysis and optimisation. The guidance for designing of Pelton turbine available in the public domain is based on existing know-how. This means that any design improvements were mainly conducted after extensive experimental testing by the trial-and-error approach. However, experimental testing is a very complex task itself (Aggidis and Židonis 2014). Not to mention the high costs and very long timescales of manufacturing that would be inevitable part of prototype testing. In recent years significant effort has been directed towards a better understating of the details of the complex unsteady flow in the runner with the aid of modern numerical modelling called Computational Fluid Dynamics.

1.5. Computational Fluid Dynamics

Computational Fluid Dynamics is a part of larger subject called fluid mechanics and is a very powerful tool for detailed flow analysis. CFD uses algorithms and numerical techniques to solve and investigate problems that include fluid flow. Computers are used to numerically solve the governing equations that cannot be solved analytically. CFD allows a simulation of fluid and solid substance interaction within a domain enclosed by boundary conditions. The main limitation when using CFD is the computational cost usually requiring a compromise between the accuracy and the timescale. Due to these limitations it was only recently that it became feasible to model the Pelton turbines that include a combination of complex problems such as multiphase, transient schemes and rotating frame of reference.

1.6. Governing Equations

CFD is based on governing equations of viscous flow that describe three fundamental principles of conservation:

- 1) Conservation of mass (continuity)

$$\frac{\partial \rho}{\partial t} + \nabla \cdot (\rho \vec{u}) = 0 \quad (1.2)$$

2) Conservation of momentum (Newton's 2nd law)

$$F = ma \quad (1.3)$$

expressed as the Navier-Stokes equation

$$\frac{\partial(\rho\vec{u})}{\partial t} + \nabla \cdot (\rho\vec{u} \otimes \vec{u}) = -\nabla p + \nabla \cdot \tau + S_m \quad (1.4)$$

where the stress tensor τ is related to the strain rate by

$$\tau = \mu(\nabla\vec{u} + (\nabla\vec{u})^T - \frac{2}{3}\delta\nabla\vec{u}) \quad (1.5)$$

3) Conservation of Energy (1st law of thermodynamics)

$$\frac{\partial(\rho h_{tot})}{\partial t} - \frac{\partial p}{\partial t} + \nabla \cdot (\rho\vec{u}h_{tot}) = \nabla \cdot (\lambda\nabla T) + \nabla \cdot (\vec{u} \cdot \tau) + \vec{u} \cdot S_m + S_e \quad (1.6)$$

where h_{tot} is the total enthalpy related to the static enthalpy by

$$h_{tot} = h_s + \frac{1}{2}\vec{u} \quad (1.7)$$

These Navier-Stokes equations were developed in the XIX century and are valid everywhere in the flow field of the flow continuum. They are presented here in their most general form. Usually many terms or even a whole equation can be neglected if various assumptions are made. Typical simplifications are based on assumptions that the flow is incompressible, isothermal, etc. Even though these equations were developed long time ago, no generalised analytical solution has been developed to solve them (Ladyzhenskaya 2003, Krause 2014). Solutions are available for only a limited number of simplified flow geometries (Munson, Young et al. 2005). Therefore CFD, a numerical technique that approximates the partial differential equations by replacing them with discretised algebraic linear equations, is used. These linear equations are then numerically solved at the discrete points in space and/or time.

1.7. Aims and Goals

The aim of this research was to develop a numerical modelling technique for Pelton turbines that would allow detailed analysis of the flow behaviour and performance of the turbine as well as become an optimisation tool for such turbines. The concentration was on the runner design. Runner optimisation was illustrated in the case study where a modern commercial runner design of Gilbert Gilkes and Gordon Ltd. was improved and experimentally tested. Identifying the importance of key Pelton bucket design parameters and their influence on performance was within the scope of this research.

The first stage was selecting available numerical models and introducing numerical and physical assumptions in order to create a reliable and relatively fast technique that could be applied for optimisation. These simplifications included the assumption of symmetry in the flow and periodic behaviour (modelling of only two consecutive half buckets) to drastically reduce the size of the computational domain and therefore the solving time. Casing and any backsplash effects were not modelled at all expecting that a more efficient runner design would reduce these unwanted effects because the remaining energy in the water that leaves the bucket would be reduced. Two types of mesh sizing to discretise the domain were used depending on the required accuracy.

The second stage was optimising the bucket geometry and positioning applying the modelling technique created in the first stage. Having the current computational resources and timescales in mind it was not possible to perform a parametric optimisation varying all the design parameters at the same time and retaining good accuracy. Therefore the parameters were grouped into separate sets based on their expected relation to each other.

The final stage was to experimentally test the optimised runners against the initial design to validate this modelling and optimisation technique.

1.8. Structure of the Thesis

This section provides an outline of the thesis and briefly describes the contents of the following chapters.

Chapter 2 - Literature Review: provides an overview of literature published and establishes the state of the art in the field of interest.

Chapter 3 - Computational Modelling: introduces the reader to the modelling methodology and provides justification for the assumptions used. Creation of the main numerical modelling technique that was used for design analysis and optimisation is presented. This chapter also contains the mesh refinement study and comparison of simplified physics or geometry against more computationally demanding simulations where possible.

Chapter 4 - Design Optimisation: describes the process of problem parameterisation and identification of key parameters. Different design optimisation stages employing the design of experiments technique or analytical development are described here in detail.

Chapter 5 - Experimental Testing: two numerically optimised runner designs were experimentally tested and compared with the initial design to support the numerical study. Experimental process and turbine performance hill charts of all the three runners (initial and two modifications) are provided in this chapter.

Chapter 6 - Results and Discussion: provides a comparison of expected (numerical) and actual (experimental) results and discusses the strengths and weaknesses of the numerical optimisation technique developed during this research.

Chapter 7 - Conclusions and Recommendations: presents the outcomes of the research, reflects on the goals set and success in meeting them. Moreover, this chapter provides a list of recommendations for future work.

Chapter 2. Literature Review

This chapter provides an overview of the published relevant literature to establish the state of the art in the field of interest. The history and evolution of Pelton turbines together with the design guidelines is reviewed and followed by the presentation of the relevant CFD codes used for modelling of incompressible, multiphase, free surface flows. Finally, available Pelton simulations are reviewed leading to a summary and comparison of the CFD codes used to model the Pelton turbine at the end of this chapter.

2.1. Design of Pelton Turbines

2.1.1. History and Evolution of Pelton Turbines

The Pelton turbine or Pelton Wheel was invented by Lester A. Pelton (1880) and followed by few modifications published in the late XIX century (Pelton Water Wheel Company 1898, Davidson 1900). Impulse turbines that were available before that time were extremely inefficient. The first Pelton turbine shown in Fig. 2.1 consisted of rectangular shape buckets that had a splitter in the middle to symmetrically divide the jet into two streams and deflect the flow back almost through 180°. However, first buckets of Pelton turbine had no cutout which is always present in modern Pelton designs and the injector design was very simplistic.

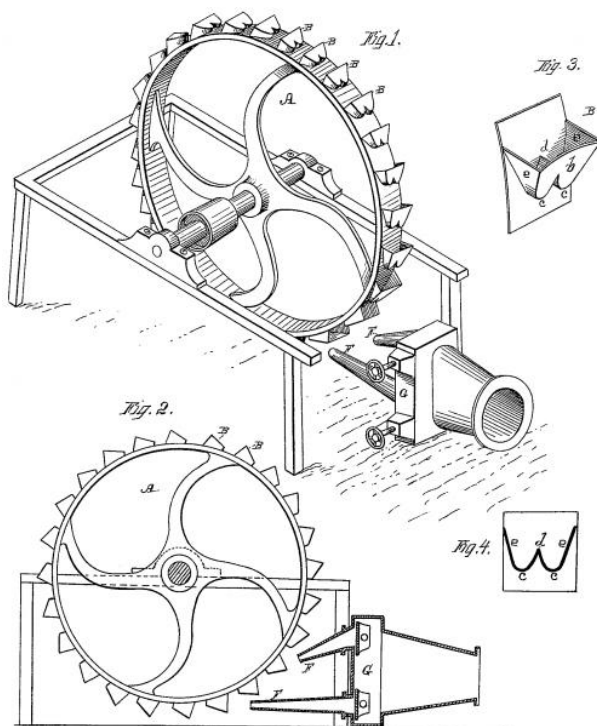


Fig. 2.1. Illustrations of the Pelton wheel from its patent (Pelton 1880).

In the first half of the XX century Pelton turbines have evolved into something more similar to what they look nowadays. There are publications available (Prášil 1911, Fulton 1937) showing a bucket shape that has a cutout (Fig. 2.2), injector design that includes spear valve (Fig. 2.3) and multi-jet arrangement of the turbine for vertical shaft operation (Fig. 2.4).

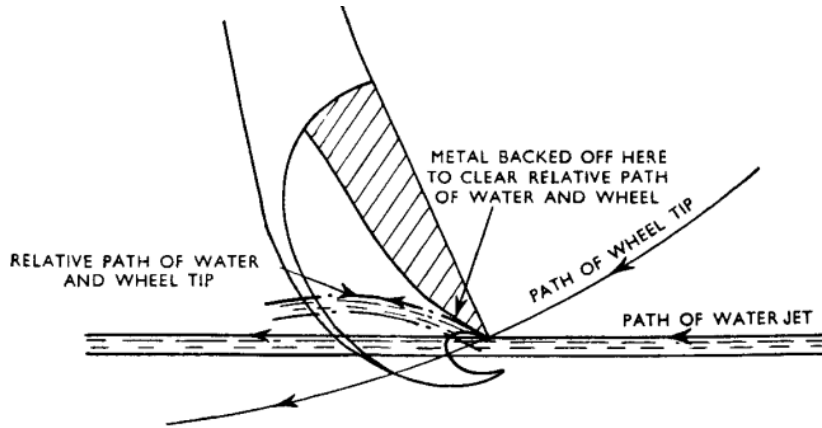


Fig. 2.2. Sketch of a bucket that has a cutout. Published in 1937 (Fulton 1937).

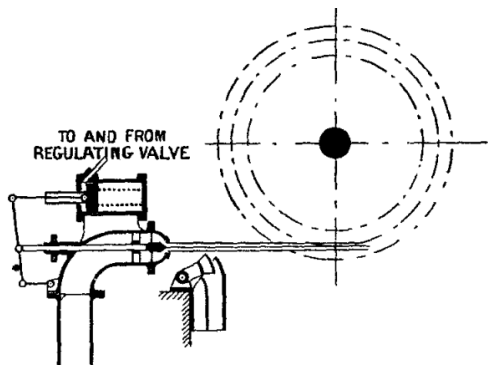


Fig. 2.3. Sketch of a nozzle controlled by a spear valve. Published in 1911 (Prášil 1911).

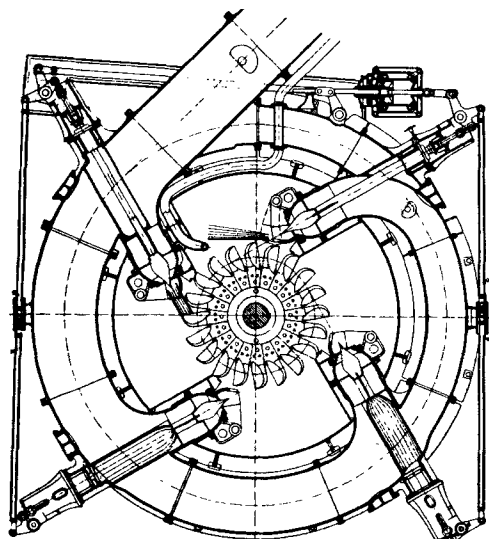


Fig. 2.4. Sketch of a multi-jet vertical shaft Pelton. Published in 1937 (Fulton 1937).

The Layout of a typical modern Pelton turbine is provided in Fig. 2.5. It can be seen that the bucket shape has evolved into much smoother round shape to reduce the flow losses inside of it. Moreover, the buckets have a cutout that ensures better transition as the jet goes from one bucket to another. In addition to that, the injector contains a nozzle and a spear valve to control the flow rate and maintain good quality of the jet.

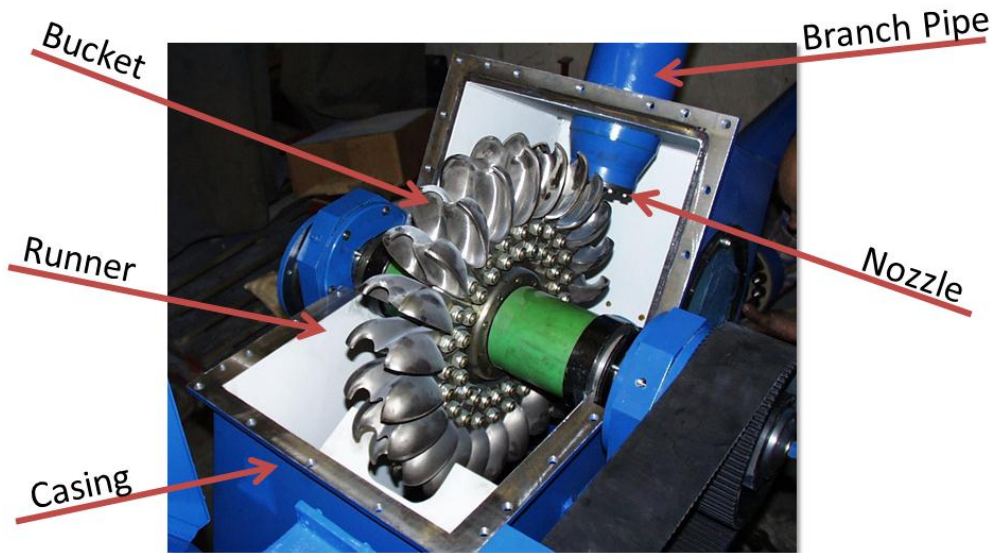


Fig. 2.5. Typical layout of a modern Pelton turbine (Ecopolis 2010).

Before CFD was applied on the impulse turbines, a graphical method (Brekke 1984, Hana 1999) was used to analyse and develop Pelton turbines. By the end of the XX century, first numerical results of Pelton jet simulation were published (Keck and Sick 2008) by Avellan, Dupont et al. (1998), Muggli, Zhang et al. (2000) and Sick, Keck et al. (2000). These were followed by more publications on numerical modelling of the jet by Parkinson, Garcin et al. (2002) or Staubli, Abgottspon et al. (2009).

Few years after presenting the first free jet simulations, publications on numerically modelled jet and bucket interaction appeared (Kvicinsky, Kueny et al. 2002, Parkinson, Vullioud et al. 2002, Parkinson, Neury et al. 2006). The jet and bucket interaction is the key part of any Pelton turbine as this is where the kinetic energy of the free jet is converted into momentum on the runner. Even though these results looked promising and suggested that CFD is finally getting to the level where it could be used for analysis and development of Pelton turbines, issues with accuracy or computational cost have caused the lack of publications regarding the design optimisation based on numerical results.

In 2012, a paper regarding this absence of publically available numerically based and experimentally validated Pelton optimisation results was published (Solemslie and Dahlhaug 2012). The intensions of the on-going PhD research at Norwegian University of Science and Technology expressed in that paper were to fill this gap in the public knowledge. However the outcome of this project is still unknown.

2.1.2. Available Design Guidelines

Vast amount of research was performed on the design of Pelton turbines throughout the years providing the hydro community with some guidelines or best practice recommendations. This section reviews the main design guidelines known up to date and the most know authors in the area.

Probably the best known book containing the design guidelines for Pelton turbines is *Hydraulic Turbines: Their Design and Equipment* by M. Nechleba (1957). However, looking at modern commercial turbines it is obvious that some of the designing trends have evolved since then. Nevertheless, theoretical calculations or equations for analysis of Pelton turbine performance provided in that book are still applicable. More recent textbooks that include design guidelines for Pelton turbines are *Water Power Development* by E. Mosonyi (1991), *MHPG Series: Harnessing Water Power on a Small Scale. Volume 9: Micro Pelton Turbines* by M. Eisenring (1991) or *The Micro-Hydro Pelton Turbine Manual* by J. Thake (2000). In addition to these textbooks, there are some publications that include design guidelines for Pelton turbines (Atthanayake 2009, Nasir 2013). However, usually it is not known what kind of research these guidelines are based on as most of the experimental data is not available to the public and is kept as commercial secret by the turbine manufacturers (Solemslie and Dahlhaug 2012). Nevertheless, some of the guidelines are based on theoretical calculations and assumptions and are usually in agreement with the commercial product designs of the leading turbine producers.

An important aspect of Pelton runner design is the number of buckets on the runner. Generally there is a tendency of fitting as many buckets on the runner as possible to ensure efficient transition of the jet from one bucket to another without wasting the energy of a water jet. However, there are energy losses associated with jet entering the bucket and providing some amount of counter-torque as the outer side of the bucket hits the surface of the jet (Eisenring 1991). Therefore a minimum amount of buckets ensuring that no water particles are lost during the transition from one bucket to another should be identified (Nechleba 1957, Eisenring 1991, Perrig 2007).

Theoretical suggestions on calculating the required amount of buckets exist. They are derived by looking at the relative paths of the water particles. Nechleba (1957) suggested acceptable number of buckets (N_B) based on a ratio: jet diameter (d_0) over runner diameter (D) as shown in Table 2.1. This suggestion gives quite wide ranges of buckets per different d_0/D ratios therefore is not very exact. Since then the industry has developed more exact guidance to calculate the amount of buckets including additional parameters like bucket width to assist engineers. These methods correlate with suggested ranges by Nechleba; however, they are not publically available.

Table 2.1. Selecting the number of buckets according to Nechleba (1957).

Select number of buckets	
d_o/D	N_B
1/6	17 to 21
1/8	18 to 22
1/10	19 to 24
1/15	22 to 27
1/20	24 to 30
1/25	26 to 33

Eisenring (1991) suggests Eq. (2.1) to calculate the optimum number of buckets by relating the length of the pitch circle to the optimum jet diameter.

$$N_B = \frac{\pi D_p}{2d_o} \quad (2.1)$$

Moreover, a statement is made that a minimum of at least 16 buckets should be installed. This statement does not agree with Nechleba (1957) who suggests 17 buckets to be the minimum as presented in Table 2.1.

Work published by Atthanayake (2009) suggests an empirical relationship given in Eq. (2.2) to select the number of buckets. However, no references are given to the work establishing and supporting this empirical relationship.

$$N_B = \frac{D_p}{d_j} + 15 \quad (2.2)$$

Nasir (2013) has also published a paper that covers the number of buckets in which it is suggested to use Eq. (2.3) to calculate the optimum number of buckets.

$$N_B = \frac{D_p}{2d} + 15 \quad (2.3)$$

The fact that it is not clearly stated if d is the nozzle diameter or the jet diameter gives some uncertainty to this equation as the jet diameter might be different to the nozzle opening diameter. This difference is even more pronounced at the best efficiency point when the flow rate is not at its maximum and where the turbine is usually optimised. It will be therefore assumed that the nozzle diameter is to be used in Eq. (2.3) since it is a constant value.

The suggestions of all the authors reviewed in this section are taken into account and the suggested number of buckets is calculated according to each suggestion using the parameters of the Pelton turbine used in the case of this PhD research. The dimensions of the prototype runner are in accordance with the minimum required values for model size and test parameters (IEC 60193:1999):

pitch circle diameter = 320 mm, jet diameter at the best efficiency point = 30.1 mm and the nozzle diameter = 46.9 mm. Table 2.2 provides the resultant number of buckets according to each suggestion.

Table 2.2. Resultant number of buckets for the Pelton runner used in this case as suggested by different authors.

Author	Suggested N_B
M. Nechleba (1957)	18 to 21
M. Eisenring (1991)	17
I. U. Atthanayake (2009)	26
B. A. Nasir (2013)	18

It is evident, that not only there is a strong disagreement between the suggested ways of identifying the optimum number of buckets in the available literature but none of them provide any experimental or numerical research data to support their suggestions. Moreover, they do not take into account the fact that performance of runners with different amount of buckets should be compared when the bucket is mounted at its optimum radial and angular position which could be different for each number of buckets because of different spacing. The main dimensions of bucket positioning will be described in detail in Chapter 4, section 4.2. The angular position describes at what angle is the bucket mounted on the runner and the splitter tip circle diameter describes the radial position of the bucket while keeping the pitch circle diameter fixed.

Finding the best angular and radial position per each number of buckets empirically is a costly process that involves long timescales. This might be an explanation why there is a lack of experimentally established guidance on selecting the optimum number of buckets. On the other hand, the theoretical guidelines that are inevitably based on assumptions are prone to have limitations. That is why the existing guidelines were quite inconsistent as presented in Table 2.2.

2.2. Relevant CFD Codes

Computational Fluid Dynamics (CFD) has been successfully used as a numerical modelling tool for developing of reaction turbines for more than 20 years now (Keck and Sick 2008). Due to the maturity of CFD application to develop reaction turbines and fundamental differences from impulse turbines in terms of operating principals and numerical point of view the modelling of reaction turbines will not be reviewed in this thesis. This section will concentrate on CFD codes and methods that can be used to model the Pelton impulse turbine and tackle the problems associated with it. The main difficulties in simulating the performance of Pelton turbines are pressure losses, secondary flows, jets, film flow, free surfaces, spray formation, ventilation losses, unsteadiness and complex interaction between components (Sick, Keck et al. 2005). In addition to that, quasi-steady state approximations do not

work for flows in Pelton buckets, requiring completely unsteady time dependent simulations with rotor-stator interaction to be used, hence significantly adding to the already high computational demands. Fortunately, despite the difficulties explained above, the technology is being pushed forward making simulated results to agree with the experimental data satisfactorily and allowing the computed methods to be used for development of new designs or optimisation of the existing ones.

This section provides a review of the recent work done on modelling of Pelton turbines using various methods and codes. Simulations performed with ANSYS CFX or ANSYS Fluent will be discussed in more detail as these two codes seem to be producing the most accurate results within fairly reasonable timescales and are the most widely used. However, available alternatives will be provided as well.

2.2.1. Eulerian and Lagrangian Methods

There are two main ways to mathematically specify the flow field: Eulerian and Lagrangian (Batchelor 1973, Lamb 1994, Munson, Young et al. 2005). In CFD, the Eulerian methods solve the governing equations at the fixed positions in the domain, hence might require very fine meshes at regions where variables have high gradients, whereas Lagrangian methods follow the moving fluid particles.

In the Eulerian specification of the flow field the discretised space is called the grid or the mesh. The values at the non-mesh points are acquired by using interpolation schemes. From physical point of view, the flow is observed at fixed positions and calculations are performed at these positions in discrete timesteps. Being a discrete technique, the accuracy of CFD results highly depend on the level of space and time discretisation or in other words the mesh density and the timestep size. On the other hand, computational cost is also dependent on this level of discretisation. There are plenty of different commercial or open source CFD codes developed but the most popular Eulerian CFD codes used in turbo machinery are ANSYS CFX, ANSYS Fluent and OpenFOAM. Work performed on Pelton turbines using these codes will be reviewed later in this chapter.

Lagrangian specification of the flow field is an alternative way of solving the governing equations. The flow is observed by following of individual particles and tracking their trajectories. This method is especially attractive when modelling impulse turbines as it does not require the usage of a mesh which typically has to be very fine to capture the free surface jets and predict their interaction with the runner. Lagrangian methods are usually much faster but they are less developed therefore less accurate than the Eulerian CFD codes. The most popular Lagrangian techniques applied in modelling of impulse turbines are SPH, FLS and MPS. The application of these codes on modelling of Pelton turbines will be reviewed later in this chapter.

2.2.2. ANSYS CFX

The largest amount of publications on modelling of Pelton turbines use commercial code ANSYS CFX (Židonis and Aggidis 2015b). The capability of solving complex impulse turbine related problems that include multiphase flow with free surfaces has been demonstrated by a number of previous studies. CFX is an Eulerian code that uses cell vertex numerics (finite volume elements) to discretise the domain (Panthee, Neopane et al. 2014) and focuses on coupled algebraic multi grid approach to solve the governing equations of motion. In terms of multiphase modelling, CFX has two sub-models applicable for free surface simulations known as homogeneous and inhomogeneous indicating whether the velocity field of different phases is shared or separate respectively.

2.2.2.1. Inhomogeneous

In the inhomogeneous (or the inter-fluid transfer) model the interfacial transfer of momentum, heat and mass is directly dependent on the contact surface area between the two phases. The interfacial area per unit volume between the phases, known as the interfacial area density, characterises the contact surface area between the two phases. Note that it has dimensions of inverse length (ANSYS Inc. 2013b). The inhomogeneous model is based on the Euler-Euler approach and can be used together with several subsidiary models to model dispersed flow, mixtures of continuous fluids etc.

2.2.2.2. Homogeneous

In the homogeneous flow model a common flow field is shared by all fluids (in this thesis water and air). In addition to the flow field, other relevant fields such as temperature or turbulence are also shared. Therefore the multi-fluid model can be simplified. It becomes sufficient to solve for all the shared fields using bulk transport equations rather than solving individual phasic transport equations because all transported quantities except the volume fraction are shared in the homogeneous multiphase flow (ANSYS Inc. 2013b). However, the homogeneous multiphase model is prone to numerical diffusion if the discretization scheme of the domain (mesh) is of low resolution and the cells are not aligned with the flow (Soares, Noriler et al. 2013). Fig. 2.6 provides an example comparison between numerical diffusion on two meshes of different resolution.

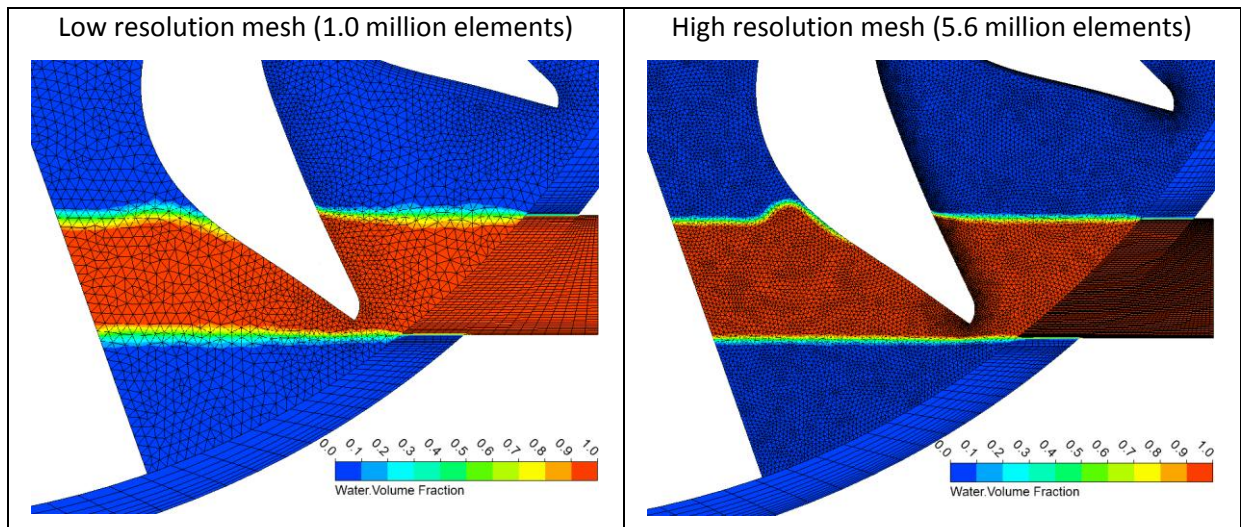


Fig. 2.6. Numerical diffusion on two meshes of different resolution.

2.2.3. ANSYS Fluent

A commercial alternative to ANSYS CFX is ANSYS Fluent. In terms of the amount of publications presenting accurate and reliable simulations of the free surface jets and Pelton turbines, ANSYS Fluent is a close second. Fluent is also an Eulerian code. However, there are some fundamental differences from CFX. Fluent uses cell-centred numerics (finite volumes) to discretise the domain (Panthee, Neopane et al. 2014) and offers more flexibility in choosing one of the three methods to solve the governing equations of motion: density based, segregated pressure based or coupled pressure based. In terms of multiphase modelling, Fluent uses Volume of Fluid (VOF) method for problems with free surface.

2.2.3.1. Volume of Fluid

The Volume of Fluid model is a free surface modelling technique that can model two or more immiscible fluids (Scardovelli and Zaleski 1999). It belongs to the Eulerian methods and can be applied to stationary or moving meshes. The VOF model solves a single set of momentum equations and tracks the volume fraction of each of the fluids throughout the domain (or a number of domains). For the simple 2D incompressible flow case the fluxes are defined on cell faces of a square mesh with constant grid spacing. The volume fraction function VF_{ij} represents the portion of the area of the cell (i, j) filled with phase 1. There is $0 < VF < 1$ in cells cut by the interface S and $VF = 0$ or 1 away from it. An example of a volume fraction function corresponding to a circle arc on a rectangular 2D grid is shown in Fig. 2.7. For an incompressible flow, conservation of volume ensures the conservation of mass. However, an explicit account needs to be taken of the special nature of the problem, which is entirely concentrated on the interface S. Moreover, validity of constraint $0 < VF < 1$ should be taken care of as the numerical errors can lead to values of VF outside the range of validity.

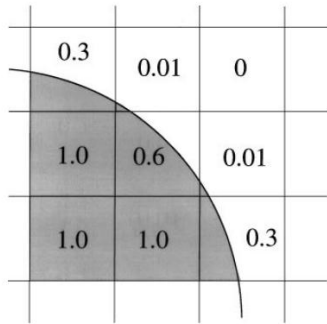


Fig. 2.7. The exact VOF model volume fraction function for a smooth circular arc over a square grid (Scardovelli and Zaleski 1999).

This model is widely used for the free surface jet simulations (Židonis and Aggidis 2015b) but can be used for other problems such as motion of large bubbles or flow motion after the dam break (ANSYS Inc. 2013c).

2.2.4. OpenFOAM

OpenFOAM (OpenFOAM Foundation 2012) is one of the most popular mesh based (Eulerian) open source codes used by the CFD community. Being a free and open source code it is attractive to many researchers and modellers. In some cases OpenFOAM is able to compete quite well with the commercial packages and various publications show that OpenFOAM is capable of modelling free surface flows (Schroeder, Kim et al. 2009, Rygg 2013, Shen and Wan 2014, Prasad, Hino et al. 2015). Being an open source code, OpenFOAM has seen implementation of all the multiphase models used by both CFX and Fluent: homogeneous, inhomogeneous and VOF.

2.2.5. Other Eulerian Solvers

In addition to the Eulerian codes like CFX, Fluent or OpenFOAM there were only few attempts to model Pelton turbines using alternative Eulerian solvers (Muggli, Zhang et al. 2000). There are more attempts to create alternative numerical methods that could be satisfactorily applied on Pelton turbines using Lagrangian flow specification as this would reduce the simulation time drastically and this area is less researched. The available Lagrangian techniques are presented in the following sections.

2.2.6. Smoothed Particle Hydrodynamics

Smoothed Particle Hydrodynamics (SPH) is a mesh free (Lagrangian) solver represented by the SPH European Research Interest Community (SPHERIC). Being a Lagrangian technique SPH is a promising tool for free surface, multiphase flow modelling as it does not require any mesh. However,

even the latest publications on modelling of a Pelton runner using SPH express concerns on the accuracy of the code (Marongiu, Leboeuf et al. 2010, Furnes 2013) or suggest that the method needs some further validation and development (Koukouvinis, Anagnostopoulos et al. 2010).

2.2.7. Fast Lagrangian Solver

Fast Lagrangian Solver (FLS) is another very interesting and promising mesh free modelling technique which was developed at the National Technical University of Athens to numerically develop and optimise impulse turbines at minimal computer cost (Anagnostopoulos, Koukouvinis et al. 2012). The main advantage of this technique is its speed making the time duration of the performance simulation almost negligible (Anagnostopoulos and Papantonis 2006). However, similar to the SPH, further development is needed to address the fundamental limitations of the FLS.

2.2.8. Other Lagrangian Solvers

Moving Particle Semi-implicit (MPS) method (Nakanishi, Fujii et al. 2009) is another Lagrangian method that could be used to model Pelton turbine performance. However only stationary bucket is modelled in this publication making it difficult to judge how accurate and fast it is when modelling a rotating runner.

2.3. Application of CFD on Pelton Turbines

There are four major sections of interest for efficiency analysis: distributor, nozzle, bucket and casing. The distributor and nozzle play an important role for the jet quality which is very important for both efficiency of the whole system (Staubli, Weibel et al. 2010) and the operational life of the runner as for high head application the nozzle dispersion can induce damages on buckets (Marongiu, Maruzewski et al. 2005, Sick, Keck et al. 2005, Peron, Parkinson et al. 2008). On the other hand, the efficiency of a turbine is affected by the bucket shape, which has already improved significantly since the original Pelton design. However, an accurate technique for modelling the flow in a rotating Pelton runner is required for further improvements and design validations as it is done for such turbines like Francis or Kaplan at the moment. Last but not least is the casing design, which is very important for Pelton turbines as it might cause flow energy losses due to disturbance of incoming jets interfering with water sheets that have not evacuated (Staubli, Weibel et al. 2010). Successful simulation of the whole system from the branchpipe to the casing is important but most probably not feasible to date because of such limiting factors like timescales or very high computational costs. That is why compromises are introduced to achieve an optimum effect within economically reasonable costs.

The studies performed can be grouped depending on the complexity as the ones that model only the bifurcation, injector and/or the jet (2.3.1 *Injector and Jet Simulations*), ones that model a jet interaction with a stationary bucket (2.3.2 *Stationary Bucket Simulations*) and finally the most complex ones that model a jet interaction with full or part of a runner in rotation (2.3.3 *Rotating Bucket Simulations*).

2.3.1. Injector and Jet Simulations

Early simulations on the free surface jet started around the year 2000. The codes used were CFX (Muggli, Zhang et al. 2000) and Fluent (Vesely and Varner 2001, Matthias and Promper 2004). Multiphase models used were homogeneous in CFX and VOF in Fluent. Usage of RANS turbulence models can be seen from the beginning until today. The model used in early CFD studies of the jets was k- ϵ . In more recent years more elaborate jet simulations were performed that included the branchpipe (Peron, Parkinson et al. 2008) or investigated the needle erosion using discrete particle model to track the sand particles (Chongji, Yexiang et al. 2014). CFX and Fluent were used for these studies respectively maintaining the usage of the same multiphase models. However, in terms of the turbulence model, k- ω SST model was used in CFX whereas k- ϵ RNG was used in Fluent.

The usage of CFD enabled the improvement of efficiency (Vesely and Varner 2001), identified a clear relationship between the efficiency of the runner and the jet dispersion caused by upstream bends (Peron, Parkinson et al. 2008) and allowed the prediction of the needle abrasion characteristics (Chongji, Yexiang et al. 2014).

2.3.2. Stationary Bucket Simulations

Injector simulations reviewed in the section above were performed using the Eulerian codes only. The stationary bucket simulations were also dominated by the usage of Eulerian codes however an attempt using a Lagrangian Moving Particle Semi-implicit (MPS) method code also exists (Nakanishi, Fujii et al. 2009). MPS is presented as an alternative to the Eulerian codes because it is expected to be a fast solver. However, no rotating runner simulations are available using the MPS making it difficult to judge how accurate and fast it is when modelling a rotating runner.

Again, ANSYS codes (CFX and Fluent) were dominating in the area and in most cases the same multiphase and turbulence models were used as in the jet simulations, i.e. homogeneous multiphase and k- ω SST model in CFX (Klemensten 2010, Gupta and Prasad 2012) and VOF multiphase and k- ϵ in Fluent (Zoppe, Pellone et al. 2006, Klemensten 2010). Both CFX and Fluent are very similar codes, therefore it is quite difficult to say which one is more suitable for modelling of Pelton turbines. There is a study performed by Klemensten (2010) that compares numerical results acquired using Fluent and

CFX to experimental data on a fixed Pelton bucket case. The study shows good consistency in terms of pressure distribution and the location of air-water interface. However, the comparison of the codes is not direct as the author had to use different settings to get the convergence. Moreover, no transient rotating runner simulations were performed therefore there is no information on the compared ability of Fluent or CFX to assess the hydraulic efficiency.

The scope of most of these stationary bucket studies was to compare the CFD results to the experimental measurements (Zoppe, Pellone et al. 2006, Klemensten 2010). Excellent agreement is reported except for the flow rate loss through the cutout (numerical results underestimate this loss). There was one study of a more theoretical nature where a circular and rectangular jet shape effect on the stationary bucket was investigated (Gupta and Prasad 2012).s

2.3.3. Rotating Bucket Simulations

Transient simulations where a rotating bucket or runner is interacting with a jet started around the year 2006 (Parkinson, Neury et al. 2006, Perrig, Avellan et al. 2006). Considering the number of publications ANSYS CFX is the absolute leader in this subject. However, there are few publications where simulations are performed using ANSYS Fluent and there is one attempt to model the Pelton turbine using OpenFOAM (Rygg 2013). The latter showed that the transient simulation of the rotating bucket is possible using OpenFOAM but the code needs to be further developed to become an alternative to the ANSYS products in this area. The simulation performed with OpenFOAM was overpredicting the torque on the bucket as compared to the results acquired experimentally or numerically using CFX. Moreover, the torque curve contained instabilities and did not coincide with the curve modelled in CFX. Finally, the required simulation time reported was almost 30 times larger than what was required by CFX.

All the rotating bucket simulations were transient as it is impossible to model the Pelton turbine using the steady state. Early CFX simulations were using the $k-\epsilon$ turbulence model (Perrig, Avellan et al. 2006) which was overtaken by the $k-\omega$ SST model at a later stage (Perrig 2007, Jošt, Lipej et al. 2008, Santolin, Cavazzini et al. 2009, Jošt, Mežnar et al. 2010, Barstad 2012, Gupta and Prasad 2012, Gupta, Prasad et al. 2014, Panthee, Neopane et al. 2014). In almost all cases the multiphase model used in CFX simulations was homogeneous with the exception of one study by Santolin, Cavazzini et al. (2009) where an inhomogeneous multiphase model was chosen. It was claimed that the inhomogeneous model showed higher stability even though other authors have not had any issues with the homogeneous model. Furthermore some previous studies showed that using homogeneous model a satisfactorily agreement between numerical and experimental results can be achieved (Janetzky, Göde et al. 1998, Kvicinsky, Kueny et al. 2002, Zoppe, Pellone et al. 2006). When modelling the rotating bucket or runner impacting with the jet in Fluent, the multiphase model used was VOF. In terms of the

turbulence model used it was the realizable $k-\varepsilon$ model (Xiao, Cui et al. 2012), the RNG $k-\varepsilon$ model (Wei, Yang et al. 2015) or the flow was modelled as inviscid (Koukouvinis, Anagnostopoulos et al. 2010).

As an alternative to using the Eulerian mesh based codes for Pelton turbine modelling there are publications on using Lagrangian meshless particle tracking techniques. The two Lagrangian techniques used were SPH and FLS. Due to their nature these techniques are much faster, therefore, can be used for the rotating runner simulations. However, even the latest publications on modelling of a Pelton runner using SPH expressed concerns on the accuracy of the code (Marongiu, Leboeuf et al. 2010, Furnes 2013) or suggested that the method needs some further validation and development (Koukouvinis, Anagnostopoulos et al. 2010). There is a publication on modelling of Turgo, another impulse turbine somewhat similar to Pelton from numerical modelling point of view, using SPH. It is claimed there that SPH has produced similar results to Fluent in much less time and therefore is a good alternative to the Eulerian methods (Koukouvinis, Anagnostopoulos et al. 2011). However, looking at the quality of the results in the comparison of the torque curves one can clearly see that SPH produced unwanted oscillations. In addition to that, no experimental validation of these results was provided. Finally, the blade geometry is represented as a surface rather than a solid geometry suggesting that this method was ignoring the negative pressure on the outside of the blade as it was entering the jet. This phenomenon is quite significant in Pelton turbines. Another Lagrangian code, FLS, is dealing with very similar problems as the SPH. Being extremely fast solver, FLS is seen as a very powerful tool for multi-parametric optimisation if coupled with some type of stochastic optimisation software (Anagnostopoulos and Papantonis 2007). However, the disadvantages of this technique are limitations on its accuracy and the need for some constants in the particle motion equation to be tuned depending on the application. Therefore, it cannot be used as a standalone CFD code without having experimental or numerical results from more accurate CFD solvers (Anagnostopoulos and Papantonis 2012). In addition to that, the main limitations of this approach is similar to the ones of SPH where only the inside surface of the bucket is modelled and no interaction between the buckets or negative pulling pressure on the outside of the bucket is taken into account. Therefore, according to the study done in collaboration with the developers of this code, FLS is very useful for early design stages when designing a turbine from scratch but when further developing or optimising a turbine of an already good performance, more accurate CFD methods should be used (Židonis, Panagiotopoulos et al. 2015).

Large computational cost of the simulations is the main factor why there is a lack of publications on CFD usage for optimisation Pelton turbines (Solemslie and Dahlhaug 2012). Therefore various authors made different simplifying assumptions in order to reduce this cost as much as possible and make Pelton optimisation possible. All available CFD simulations reviewed in this section were assuming

symmetry in the flow and therefore modelling only half of a runner or a bucket. Because of the periodic behaviour assumption, the majority of simulations used only a fraction of a runner with the number of buckets in the section modelled being 2, 3, 5, 7 or even 10. Fairly large amounts of buckets such as 5, 7 or 10 were used so that a periodic torque on the runner could be achieved (Perrig, Avellan et al. 2006, Perrig 2007, Gupta, Prasad et al. 2014). Other authors used only 3 consecutive buckets (Barstad 2012, Panthee, Neopane et al. 2014) where the torque was measured only on the bucket in the middle. This torque measured on a single bucket was then used to construct the torque on the runner assuming that every bucket would undergo identical loading. The first bucket was required to produce the back-splashing water that impacts the middle (or the second) bucket. The third bucket was required to realistically cut the jet when it is impacting the second bucket. Finally the lowest amount of buckets used in the simulations was 2 (Anagnostopoulos and Papantonis 2006, Koukouvini, Anagnostopoulos et al. 2010). However, these simulation were not including the back side of the buckets therefore could use only 2 buckets.

Some researchers have modelled the runner containing all the buckets (Parkinson, Neury et al. 2006, Jošt, Lipej et al. 2008, Santolin, Cavazzini et al. 2009, Jošt, Mežnar et al. 2010, Xiao, Cui et al. 2012, Xiao, Wang et al. 2014, Wei, Yang et al. 2015). To make it possible, super computers were used or extremely coarse meshes were created. Even though it was shown that it is possible to model the complete runner, this could be seen as unnecessary usage of computational resources. For instance, using the same computational resources and a reduced complexity simulation with only 2 buckets would allow simulations with better discretised grids (therefore improved accuracy) or analysing more operating points or design variations and enable the optimisation of Pelton turbine.

Last but not least is the validation of the simulations against experimental data. Most comparisons suggested that CFD is overpredicting the efficiency by 1.5 to 6 % (Perrig, Avellan et al. 2006, Santolin, Cavazzini et al. 2009, Barstad 2012) except for Gupta, Prasad et al. (2014) who showed that CFD was underpredicting the efficiency by 3.5%. The results of CFD could be overpredicting the efficiency because of the assumption that the runner is not bounded by the case. Another reason for the discrepancy between the numerical and experimental results was identified to be the inability to model the jet separation from the back side of the bucket where the Coanda Effect (Taylor 1980) takes place (Perrig, Avellan et al. 2006, Perrig 2007).

2.3.4. Summary of CFD Application on Pelton Turbines

Table 2.3 provides a summarised comparison of CFD codes that are applied to model the Pelton turbine together with the references to publications of each code being used to simulate the flow in different parts of the turbine at different level of complexity. Below is an index to the reference column of Table 2.3.

Index to the references of Table 2.3:

1	Muggli, Zhang et al. (2000)	16	Benzon, Židonis et al. (2015b)
2	Perrig, Avellan et al. (2006)	17	Veselý and Varner (2001)
3	Perrig (2007)	18	Matthias and Promper (2004)
4	Jošt, Lipej et al. (2008)	19	Zoppe, Pellone et al. (2006)
5	Santolin, Cavazzini et al. (2009)	20	Xiao, Cui et al. (2012)
6	Staubli, Abgottspon et al. (2009)	21	Chongji, Yexiang et al. (2014)
7	Jošt, Mežnar et al. (2010)	22	Wei, Yang et al. (2015)
8	Barstad (2012)	23	Rygg (2013)
9	Gupta and Prasad (2012)	24	Koukouvinis, Anagnostopoulos et al. (2010)
10	Gupta, Prasad et al. (2014)	25	Marongiu, Leboeuf et al. (2010)
11	Panthee, Neopane et al. (2014)	26	Furnes (2013)
12	Xiao, Wang et al. (2014)	27	Anagnostopoulos and Papantonis (2006)
13	Klemensten (2010)	28	Anagnostopoulos, Koukouvinis et al. (2012)
14	Židonis, Panagiotopoulos et al. (2015)	29	Nakanishi, Fujii et al. (2009)
15	Benzon, Židonis et al. (2015a)		

2.3.5. State of the Art in Modelling of Pelton Turbines

Numerical modelling of Pelton turbine performance is a challenging task. From the information provided in Table 2.3 it is clear that ANSYS CFX code is the most widely used CFD tool for simulating the jet interaction with a rotating runner. However, having in mind that Fluent is not very different from CFX it seems peculiar that there are very few publications applying it to model the jet-bucket interaction in Pelton turbines. The most recent publications on Pelton modelling with CFX use $k-\omega$ SST turbulence model and homogeneous multiphase model. Simplifications of the runner geometry are made to reduce the computational cost. These simplifications include introduction of symmetry plane and modelling of only few buckets of the runner. There are no publications on parametric optimization of the bucket using numerical modelling validated by experimental results. Lagrangian particle tracking methods are promising and attractive due to much lower computational cost but need to be further developed to be able to compete with commercial Eulerian codes like CFX.

Table 2.3. Comparison of CFD methods and software used for Pelton turbine modelling.

Code description			Problems analysed (Number of publications)			Capabilities		Usage in the field		Comment
Flow Field Specification	Name of code	Commercial	Injector and jet	Stationary bucket	Rotating bucket	Reliable accuracy*	Computational cost	Reference index**	Most recent publication	
Eulerian (mesh based)	CFX	Yes	4	2	11	Yes	High	1-16, 25	2015	<ul style="list-style-type: none"> • Good accuracy* • Suitable for optimisation • Most widely used for rotating bucket (runner) simulations
	Fluent	Yes	4	2	4	Yes	High	13-22	2015	<ul style="list-style-type: none"> • Good accuracy* • Suitable for optimisation
	OpenFOAM	No	-	-	1	No	High	23	2013	<ul style="list-style-type: none"> • Open source • No successful attempts to model impulse turbines
	Flow-3D	Yes	1	-	-	No	High	1	2000	<ul style="list-style-type: none"> • No recent publications on impulse turbine simulations
Lagrangian (mesh free)	SPH	No	-	-	3	No	Moderate	24-26	2013	<ul style="list-style-type: none"> • Open source • Useful for initial design stage
	FLS	No	-	-	3	No	Low	14, 27, 28	2014	<ul style="list-style-type: none"> • Useful for initial design stage
	MPS	No	-	1	-	No	Low	29	2009	<ul style="list-style-type: none"> • No recent publications on impulse simulations

*This assessment of accuracy is concentrating on modelling of Pelton turbines and is based on the findings of available publications.

** Index to the references is provided in the previous page.

Chapter 3. Computational Modelling

This chapter introduces to the CFD model chosen for this research based on the state of the art in modelling of Pelton turbines. The details of numerical models used and assumptions are described here together with the creation of modelling methodology that was developed to be used for turbine design analysis and optimisation. Moreover, this chapter includes verification of various assumptions introduced in the model to reduce the computational cost. Finally, the mesh refinement study is presented to quantify the discretization error.

3.1. ANSYS CFX

Various codes have been developed to numerically model the fluid dynamics. There is no single numerical technique that would be the overall best for all types of problems. Therefore, each application requires identifying the most suitable CFD code for the task. Based on the available literature reviewed in Chapter 2, ANSYS CFX is currently the most widely used and experimentally validated CFD code for Pelton turbine analysis where a jet is interacting with the rotating runner creating a problem that has to deal with multiphase, free surfaces, secondary flows, jets, film flow, spray formation, ventilation losses, unsteadiness and complex interaction between components. Simplifications and assumptions have to be used because of these challenges and also the fact that quasi-steady state approximations do not work for flows in Pelton buckets, requiring time dependent simulations with rotor-stator interaction to be used.

The actual version of CFX was 14.5 and it was used within ANSYS Workbench. Domain Geometries were created using SolidWorks 2013 and imported to the ANSYS Design Modeller. The meshes were created using ANSYS Mesher. An example of ANSYS Workbench project layout used for runner analysis is shown in Fig. 3.1.

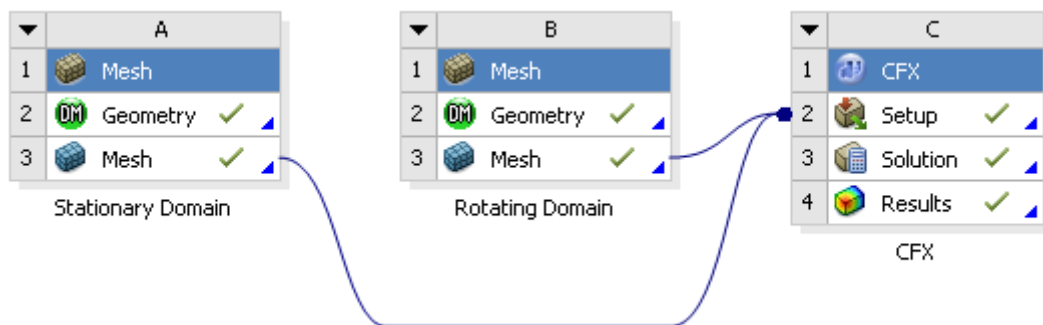


Fig. 3.1. Project layout in ANSYS Workbench.

3.2. Model Verification

Various assumptions were introduced in the CFD model to reduce the computational cost and make optimisation feasible. This section discusses the anticipated effect of these assumptions and provides justification for them. The assumptions were split into two distinct groups 3.2.1 *Geometry Decomposition* and 3.2.2 *Modelling Assumptions*.

3.2.1. Geometry Decomposition

Modelling of a complete turbine is vital if absolute accuracy is required. The efficiency of a Pelton turbine is expected to be affected by such features as turbine casing, interaction between the jets and the back splashing water, losses and secondary flows in the injector and the branchpipe, and similar. However, for optimisation purposes absolute accuracy is not required and it is well enough to have incremental accuracy. In order to optimise the runner it was very important to maintain good precision that allows comparison of different runner designs. Aiming for the incremental accuracy instead of the absolute accuracy has enabled the simplification of the problem to reduce the timescale. Using functional decomposition, the geometry of the computational domain was created removing the features that were assumed to have no or minor effect when comparing the runner designs. Fig. 3.2 provides the schematics of geometry decomposition and the assumptions made at each step will be described in the following sections.

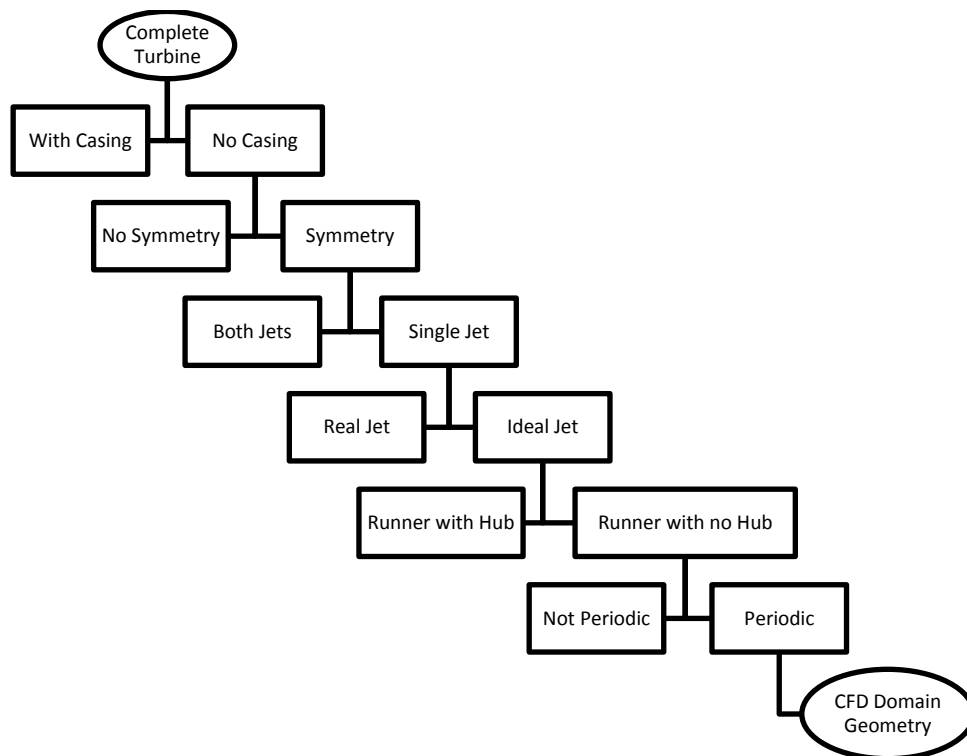


Fig. 3.2. Creation of the computational domain using functional decomposition.

3.2.1.1. No Casing

It was assumed that a runner without a casing has higher efficiency since there is no interference of the back splashing water. However, modelling of this effect is only important when aiming for the absolute accuracy but not the incremental analysis. To compare the runner designs, it is not required to quantify the effect of the casing. Assumption is made that if the runner efficiency is increased under conditions when the runner is open to the atmosphere the same would hold if the casing is included. The effect of this assumption was not quantified due to the computational cost limitations. Vast majority of publications reviewed in Chapter 2, section 2.3.3 *Rotating Bucket Simulations* were modelling the Pelton turbine without a casing except for publications by Marongiu, Leboeuf et al. (2010) and Wei, Yang et al. (2015).

3.2.1.2. Symmetry

Flow behaviour in the runner (with horizontal axis) was assumed to be symmetrical and therefore symmetry plane boundary was used. Fig. 3.3 presents an image of the rotating and stationary domains with the symmetry plane highlighted. A simulation with a mirrored mesh was performed to check if the flow is numerically symmetrical. An image of the mirrored domains is provided in Fig. 3.4. The difference between efficiencies calculated on the right hand side and on the left hand side of the bucket in the mirrored geometry simulation was 0.00 % or in other words no difference was observed. This proved that the flow is symmetrical.

The efficiency calculated on the same (right hand) side of the bucket with i) the symmetry plane boundary and ii) the left side being mirrored provided some difference of 0.01 % which is still negligible. Therefore it was verified that usage of the symmetry plane boundary has no noticeable effect on the accuracy.

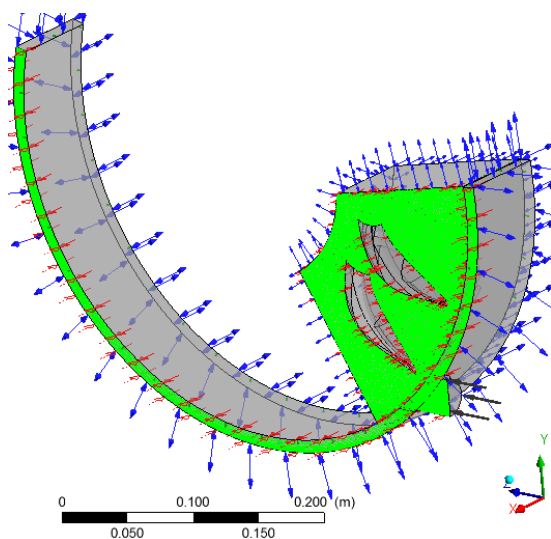


Fig. 3.3. CFX-Pre: screen capture of the rotating and the stationary domains with the symmetry plain boundary highlighted in green.

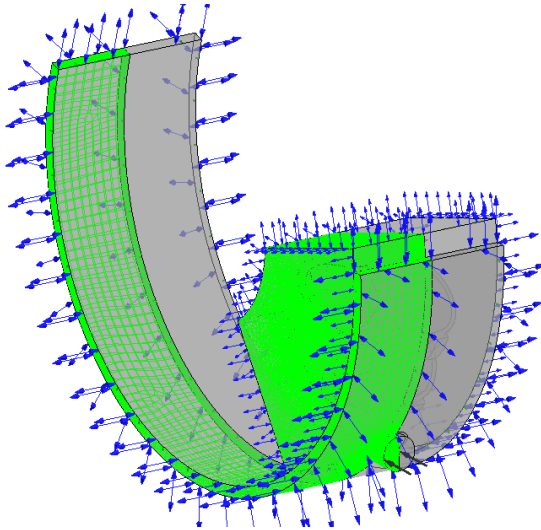


Fig. 3.4. CFX-Pre: screen capture of the rotating and the stationary domains with the mirrored mesh. Original part of the domain (right hand side) coloured in grey and the mirrored part (left hand side) highlighted in green.

3.2.1.3. Single Jet

It was assumed that hydraulic efficiency of the runner (not taking mechanical losses into account) with single jet is equal or higher than in the two jet operation since having more than one jet might create more unwanted flow interaction as shown by Wei, Yang et al. (2015). However, when comparing the designs this difference is irrelevant because if a runner is more efficient in a single jet operation the same is expected when both jets are in operation. Modelling of only the single jet operation was found in most of the publications reviewed in Chapter 2, section 2.3.3 *Rotating Bucket Simulations* (Perrig 2007, Santolin, Cavazzini et al. 2009, Koukouvinis, Anagnostopoulos et al. 2010, Anagnostopoulos and Papantonis 2012, Barstad 2012, Xiao, Cui et al. 2012, Furnes 2013, Rygg 2013, Panthee, Neopane et al. 2014, Xiao, Wang et al. 2014).

3.2.1.4. Jet Shape

Secondary flows caused by the bend upstream of the nozzle and the spear holding vanes as well as the jet velocity profile that develops as the water flows through the nozzle have an effect on the efficiency of Pelton runner (Peron, Parkinson et al. 2008, Staubli, Abgottspon et al. 2009, Staubli, Weibel et al. 2010). It was numerically shown that the ideal jet with uniform velocity provides approximately 0.6 % higher runner efficiency than the real jet with secondary flows and non-uniform velocity profile (Benzon, Židonis et al. 2015b). Presence of this velocity profile had larger effect than the secondary flows. However, this difference is expected to be systematic and cancel out when comparing the runner designs.

3.2.1.5. No Hub

A runner of a Pelton turbine is designed in such a way that the flow enters radially and fills the buckets in the region between the cutout and the root of the bucket and is then diverted by almost 180° and evacuates away from the runner. Therefore, if the runner is not bounded by the casing and is open to the atmosphere the flow will not be interacting with any other part of the runner except for the bucket. Hence, there is no need to include the hub into the CFD model. Vast majority of publications reviewed in Chapter 2, section 2.3.3 *Rotating Bucket Simulations* were modelling the Pelton turbine without including the hub. Except the publications by Marongiu, Leboeuf et al. (2010) and Wei, Yang et al. (2015) where a runner with a hub was modelled. However, these simulations were also modelling the casing that might cause the water to splash back towards the runner therefore the complete runner geometry was required for these simulations.

Fig. 3.5 provides images from simulations where the hub was ignored (Jošt, Mežnar et al. 2010). It shows that the flow evacuates the runner away from the buckets. However, there is a very unlikely possibility that during the optimisation process some modifications of the bucket might lead to the design where the flow is directed towards the hub. This would be captured instantly when analysing the flow patterns and prevented. Simulations presented later in this thesis show that the flow does not even reach the root of the bucket (Fig. 4.19).

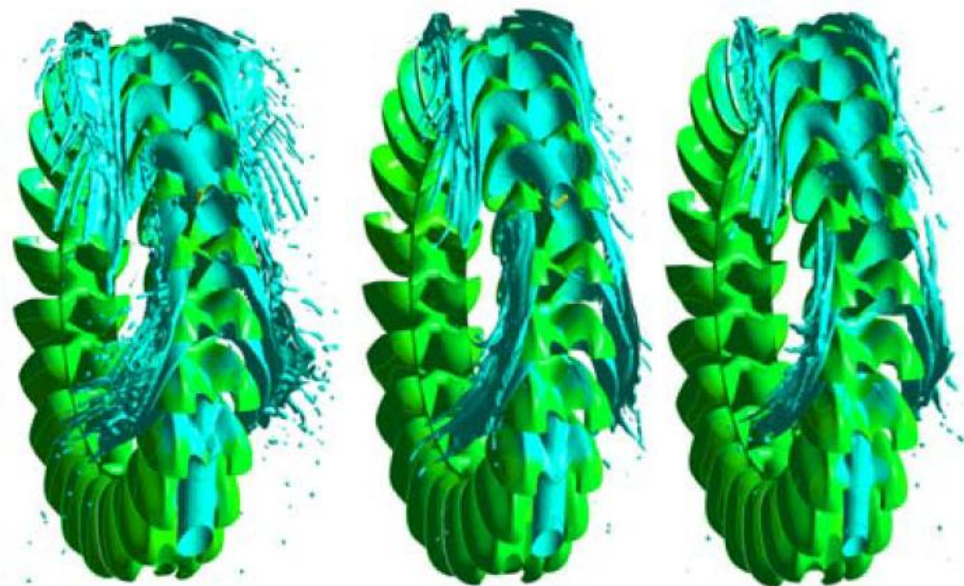


Fig. 3.5. Evacuating water sheets for different operating conditions (Jošt, Mežnar et al. 2010).

3.2.1.6. Periodic Torque

Torque in Pelton turbines is periodic as each bucket undergoes the same loading by the jet when operating in steady conditions. Therefore, many researchers used only a minimum number of buckets required to simulate the torque on a single bucket and then construct the torque on the complete runner

using periodicity. In the single jet operation, 3 buckets are enough to recreate the complete runner torque (Barstad 2012, Panthee, Neopane et al. 2014). The torque is measured on the reference bucket which is the bucket in the middle (or the second out of three). The first bucket is required to provide backslash that might impact the backside of the reference bucket and the third bucket is required to realistically cut the jet from impacting the reference bucket.

It was identified that the problem can be further simplified and usage of only two buckets to recreate the torque on the complete runner might be appropriate. This was based on the assumption that the flow inside of the bucket is not interacting with the flow on the outside of the same bucket. In that case, the reference surfaces to measure the torque become the inside surface of the first bucket and the outside surface of the second bucket. Any back splashing flow from the first bucket would be captured by the outside surface of the second bucket. The suction produced by the Coanda effect as the jet is cut by the bucket would be measured on the outside surface of the second bucket. Such approach was used in collaborative studies and is already published (Benzon, Židonis et al. 2015b, Židonis, Panagiotopoulos et al. 2015). This approach was tested by first calculating the torque in two different ways on a three bucket simulation, i.e. 1) the torque on the second bucket (both the inside and the outside) and 2) the torque on the inside of the first bucket and the torque on the outside of the second bucket. Finally, the torque was calculated using a simplified method 3) where a simulation with only two buckets was performed and the same measurements as in method 2) were taken. Fig. 3.6 provides a graphical explanation of the 3 methods used for comparison.

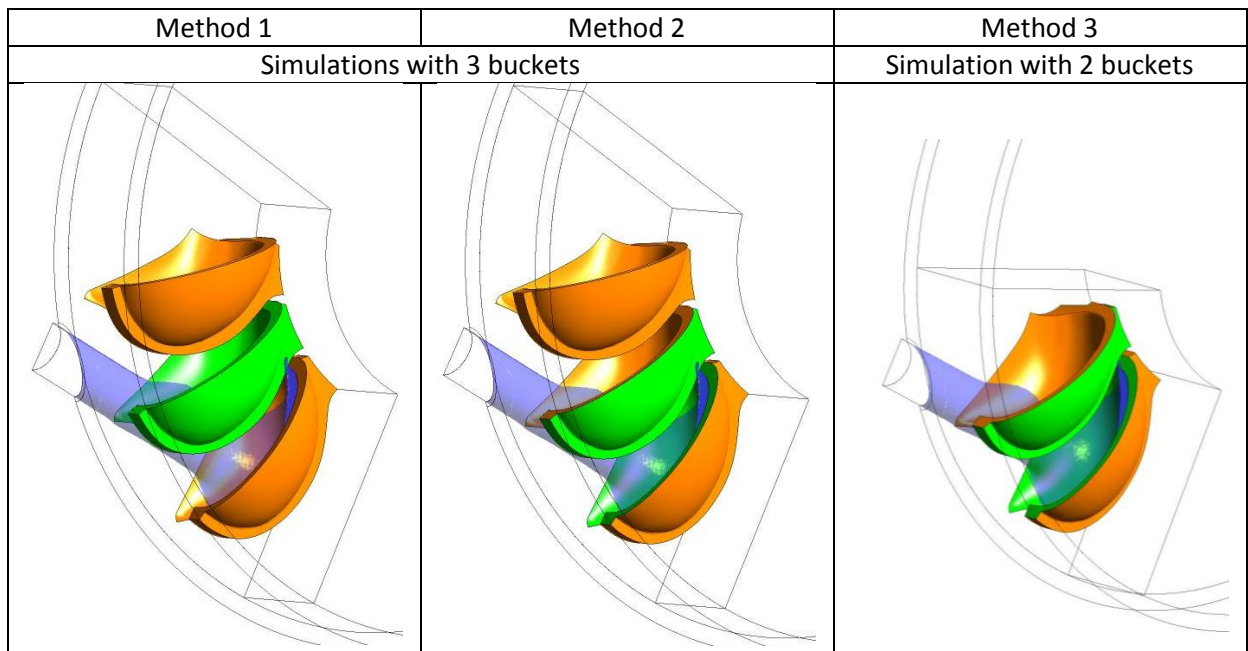


Fig. 3.6. Different torque measurement methods in simulations with three or two buckets. Reference surfaces contributing to the torque measurement are highlighted in green.

The torque curves acquired using all the three methods are presented in Fig. 3.7. These curves represent the torque on one bucket. For method 1 it is simply a sum of torque on the inside and the outside. For methods 2 and 3, before summing the readings, the outside torque was synchronised with the inside by shifting the outside torque curve along the abscissa by 20° (bucket spacing angle in the runner with 18 buckets). Visually the torque curves acquired using the three different methods look identical. Table 3.1 presents the calculated efficiency for each method. The difference between the methods was only 0.2 % therefore it was decided that method 3 is the most appropriate since running a simulation with 2 buckets instead of 3 requires lower computational resources.

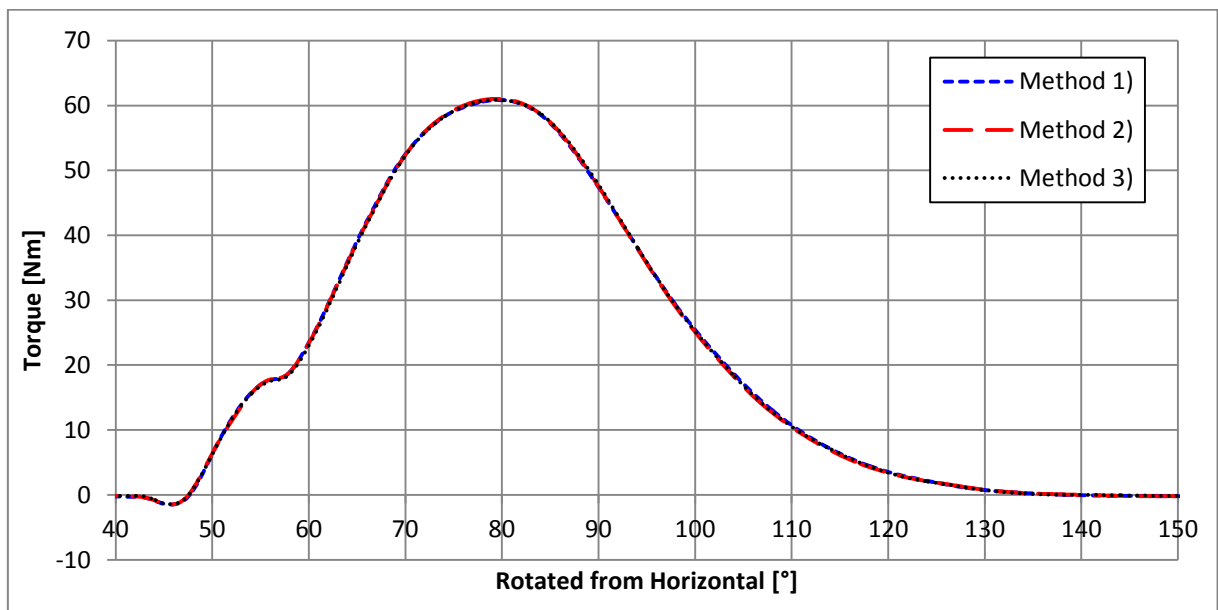


Fig. 3.7. Torque on one bucket acquired using different torque measurement methods.

Table 3.1. Efficiency calculated using different torque measurement methods. Efficiencies normalised to the result that was calculated using method 1.

Method	Normalised Efficiency [%]
1	100.0
2	99.8
3	99.8

3.2.2. Modelling Assumptions

Assumptions on the physics that define the problem and selection of the most suitable numerical schemes were made in addition to the assumptions made on the domain geometry. The justification for each selection and assumption is provided in this section based on the literature references or computational unit tests.

3.2.2.1. Multiphase Model

The Volume of Fluid or the homogeneous multiphase models are predominantly selected in Pelton turbine modelling when using the Eulerian specification of the flow field as reviewed in Chapter 2, Section 2.3 *Application of CFD on Pelton Turbines*. Both VOF and the Homogeneous models are very similar because all fluids share the same velocity fields as well as other relevant fields like temperature, turbulence, pressure, etc. CFX has an alternative multiphase model, the inhomogeneous model, where only the pressure field is shared by all the fluids. However, there is only one study that used the inhomogeneous multiphase model (Santolin, Cavazzini et al. 2009). Furthermore, previous studies have showed that an agreement between numerical and experimental results can be achieved using the homogeneous model (Janetzky, Göde et al. 1998, Kvicinsky, Kueny et al. 2002, Zoppe, Pellone et al. 2006). Therefore, based on the previous work, the homogeneous multiphase model was chosen in this research as oppose to the inhomogeneous multiphase model. Furthermore, in addition to the available publications, this selection can be justified fundamentally. The fluid interaction for the free surface flow was implemented using the volume fraction of each fluid. This approach is analogous to the VOF method. The turbine was modelled with no casing as described in section 3.2.1, *Geometry Decomposition*; therefore, no back splashing or any other violent free surface flow effect (such as sloshing, including wave breaking, vapour entrapment or cushioning) that could contradict the assumptions inherent in the homogeneous model (Brennen 2005) were present. Hence, it was assumed that it is appropriate to use the homogeneous multiphase with free surface model.

However, the homogeneous multiphase model is prone to numerical diffusion if the discretization scheme of the domain (mesh) is of low resolution and the cells are not aligned with the flow. Due to flow patterns that change with time as the frame of reference is rotating and usage of tetrahedral elements to mesh the complex geometry it was not possible to align the cells in the rotating domain. Therefore, mesh was required to be refined at the regions of interest to reduce the effect of numerical diffusion. The grid convergence study is provided in section 3.4.

3.2.2.2. Turbulence Model

Turbulence modelling is a complex process as it includes three dimensional, unsteady fluctuations in time and space that can be of many scales. In many cases turbulence involves length scales much smaller than the element sizing which can be practically used. Therefore, the Direct Numerical Simulation (DNS) of turbulence usually requires computational power that is much larger than currently available. Fortunately, large amount of research has been concentrating on creating turbulence models that predict the effect of turbulence on overall flow behaviour without modelling the details. Most of these methods are statistical turbulence models with two exceptions available in CFX: Large Eddy Simulation (LES) model and the Detached Eddy Simulation (DES). However, for problems such as modelling of Pelton turbines, statistical models based on Unsteady Reynolds

Averaged Navier-Stokes (URANS) Equations are used. The most widely used turbulence models are the Two-Equation Turbulence Models that provide a good compromise between computational cost and accuracy. The k- ϵ and k- ω models include additional separate equations to solve for turbulent kinetic energy (k) and turbulent dissipation rate (ϵ) or turbulence frequency (ω).

All the publications on modelling of the Pelton runner using Eulerian codes employed the URANS turbulence models since it was unnecessary to resolve the details of the turbulent fluctuations but the interest was on how the turbulence has affected the mean flow. Studies performed with CFX were using the k- ω SST except from one early publication by Perrig, Avellan et al. (2006) where the k- ϵ turbulence model was used as reviewed in Chapter 2, section 2.3.3 *Rotating Bucket Simulations*. However, usage of URANS turbulence models (k- ω SST in this case) requires a condition of scale separation to be met (Tucker 2014). I.e. the turbulence timescale must be much smaller than the resolved unsteadiness in the flow which in this case was the simulation time step. The turbulence timescale calculated using Eq. (3.1) was reaching values of 3 ms in the region where the flow was inside of the bucket (i.e. the most important region where the energy is transferred to the runner).

$$t_T = \frac{k}{\epsilon} \quad (3.1)$$

Whereas, the whole simulation time, during which the runner rotates 140°, was 30 ms. Therefore, it was impossible to provide a clear time scale separation no matter what timestep size was chosen as the whole duration of the simulated time was only 10 times larger than the turbulence timescale. This means that the turbulence fluctuations should be resolved if actual torque on one bucket per one passage is to be modelled and usage of URANS for such application is not appropriate. However, the interest is the periodic behaviour when each bucket undergoes the same mean loading and an infinite number of runner revolutions are made. This would represent the turbine operating at steady conditions. Therefore, it was decided that usage of k- ω SST was appropriate even though it was not feasible to measure its accuracy against other more computationally demanding models. Nevertheless, it was assumed that the uncertainty induced by the turbulence model was of systematic nature providing an offset in the results but not affecting the design comparison.

3.2.2.3. Buoyancy

The turbine was modelled with no casing as described in section 3.2.1, *Geometry Decomposition*. Therefore, the flow was free to leave the buckets and clear away from the runner without having any effect on the efficiency. Thus, there were no means for the gravity to have an effect on the performance as the water velocities were high. For instance, the distance from the simulation domain inlet to the pitch circle diameter was 185 mm. This means that it takes 5.5 ms for a water particle to travel this distance at a jet velocity of 33.3 m/s. The trajectory deviation due to the gravity during this time is 0.15 mm or 0.05° which is negligible.

To support this assumption, a computational unit test was performed to compare the efficiency when the buoyancy model is on and off. The buoyancy forces were based on difference in air and water density and the acceleration due to the gravity constant g (the direction of the vector being negative y direction). Buoyancy options as used in CFX-Pre are provided in Table 3.2. The difference in efficiency was 0.00 % or in other words no difference was observed.

Table 3.2. Buoyancy options as defined in CFX-Pre.

Buoyancy Model	
Option	Buoyant
Gravity x Direction	0
Gravity y Direction	-9.81 m/s ²
Gravity z Direction	0
Buoyancy Reference Density	1.2257 kg/m ³
Reference Location Option	Automatic

3.2.2.4. Surface Tension

Free surface option was chosen for the interphase transfer. No surface tension was modelled as it was assumed to have negligible effect. This assumption was verified numerically by performing a computational unit test. A simulation was performed where the surface tension was modelled. The surface tension coefficient value for water in contact with air at 15°C was 0.0735 N/m. The effect of not modelling the surface tension was 0.03 % of the original efficiency which is negligible.

3.2.2.5. Single Precision

It is advisable to use double precision if the simulation includes multiphase and free surface. However, running in double precision requires higher computational resources. Since the aim was to create a CFD model that is appropriate for design optimisation, the goal was to reduce the simulation time scale to the minimum. Therefore a computational unit test was performed to check what the difference in calculated efficiency using the single and double precision is. The difference in modelled efficiency was 0.00 % or in other words no difference was observed.

3.3. Setup and Post-Processing

The CFD model was created based on the assumptions verified in the previous sections. This section provides the details of setting up a simulation in ANSYS CFX, running it and analysing the results.

3.3.1. Computational Domain Geometry

Geometry of the computational domain was created based on the decomposition described in section 3.2.1. *Geometry Decomposition*. The stationary and rotating domains were created in Solidworks and imported into ANSYS Mesher via ANSYS Design Modeller. The geometries are presented in Fig. 3.8. Stationary domain contains half a cylinder for the inlet and a ring to accommodate an interface between the two domains. In CFX, the interface boundary becomes a wall boundary for the non-overlapping regions. Therefore this ring has to be long enough to allow water evacuation from the rotating domain during the rotation. Also, the stationary domain geometry was separated into 4 bodies of more basic shapes (showed in different colours) to assist the meshing process. The rotating domain geometry was constructed by subtracting the geometries of two consecutive buckets from a wedge shaped body. The geometry of this body was created to be as small as possible ensuring that there is just enough space around the bucket surface for the flow to leave the domain and also ensuring continuous jet entrance during the rotation until the jet is completely cut off by the second bucket. The stationary and rotating domains in relation to each other at the initial position are shown in Fig. 3.11.

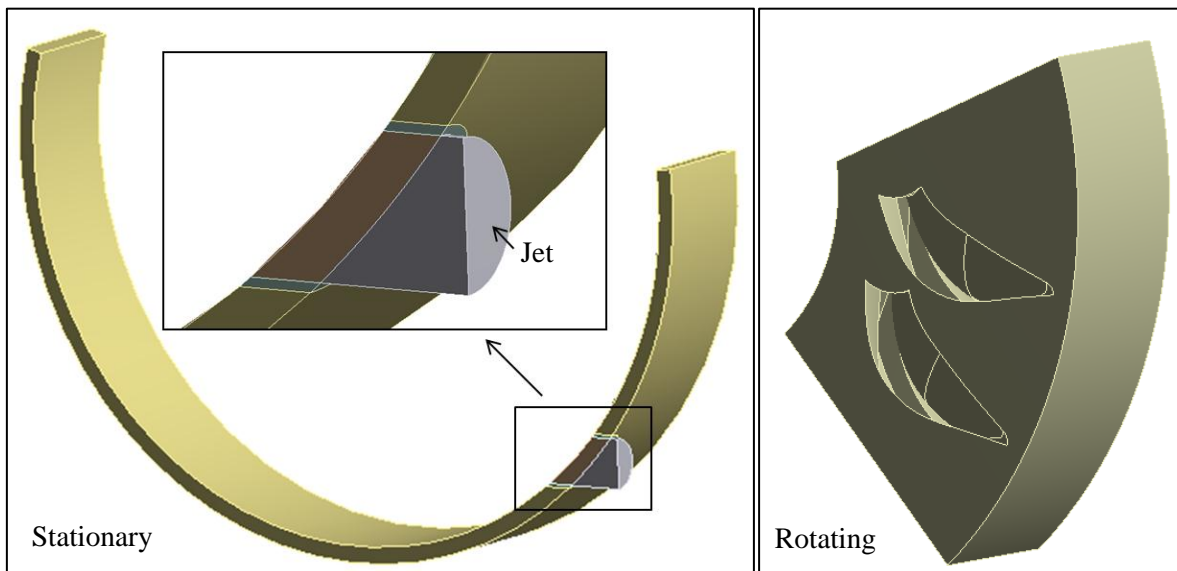


Fig. 3.8. Domain geometries as imported from Solidworks: stationary (left), rotating (right).

3.3.2. Mesh

CFX is a mesh based CFD technique that uses Eulerian fluid flow field specification. It discretises the domain using cell-vertex numerics (finite volume elements). It was possible to mesh the stationary domain using semi structured hexahedral elements because of its separation into the 4 basic shapes. However, unstructured tetrahedral elements were used for the rotating domain meshing because of more complex geometry to be captured by the mesh and also to allow automatic meshing for all the upcoming geometry modifications.

3.3.2.1. Stationary Domain

The stationary domain consisted of 0.34 million mesh elements (0.36 million nodes). All the elements were hexahedral and the sizing was controlled depending on the flow direction that was easily predictable in this domain. The skewness factor describing the quality of a hexahedral mesh was kept below 0.8 and the maximum aspect ratio was 38. Fig. 3.9 presents an image of the stationary domain mesh showing very dense mesh sizing at the inlet and the path of a jet and much larger elements where the flow details are outside of interest.

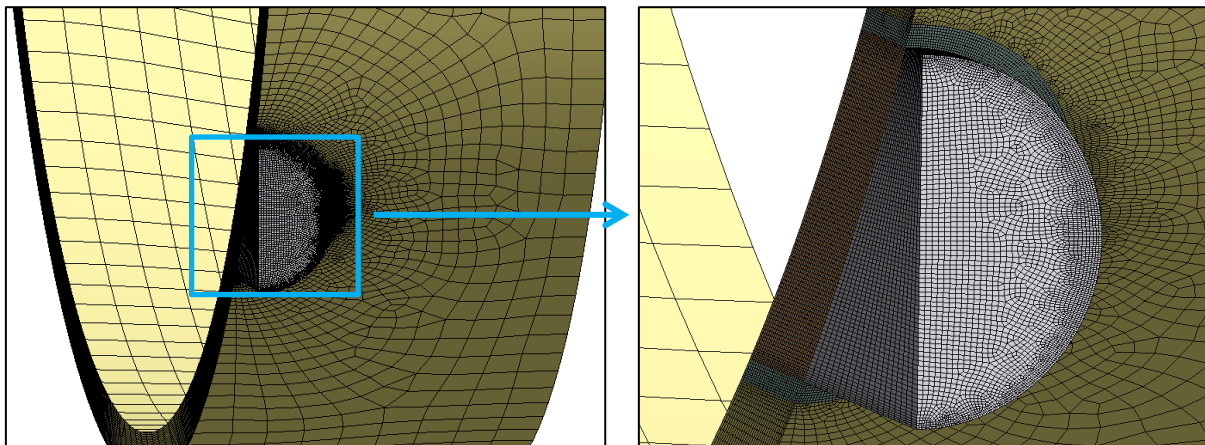


Fig. 3.9. Mesh of the stationary domain.

3.3.2.1. Rotating Domain

The rotating domain consisted of 3.3 million mesh elements (0.68 million nodes). The mesh was tetrahedral element based but also had wedge shaped and pyramid shaped cells that were created because of the inflation layer at the wall boundaries. The orthogonal quality was kept higher than 0.1 and the maximum aspect ratio was 58. The inflation layers shown in Fig. 3.10 were applied on the surfaces of interest which were the inside of the first bucket and the outside of the second bucket. Data of the modelled torque was taken at these two surfaces to construct the overall torque as described in section 3.3.5 *Post-Processing the Results*. The inflation consisted of 5 layers.

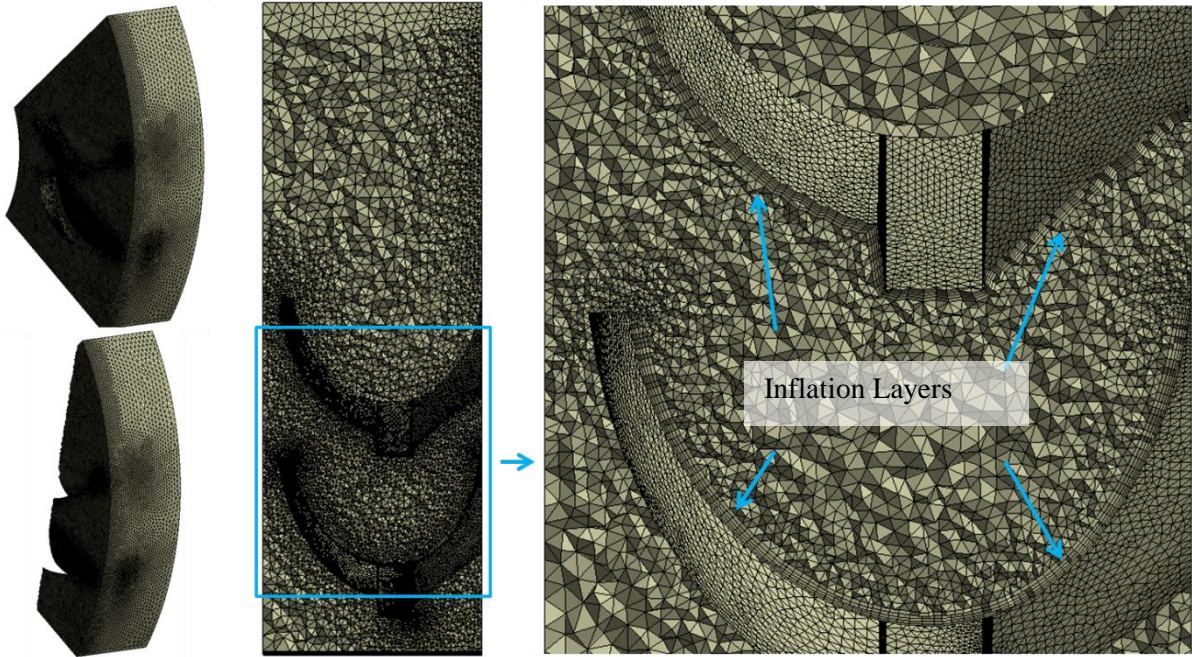


Fig. 3.10. Mesh of the rotating domain.

3.3.3. Physics Definition

The definition of physics was performed in CFD-Pre which is a pre-processor for ANSYS CFX. After creating the meshes they were imported into CFX-Pre where physical models were selected. In this project, named selections were created for each boundary in Solidworks and retained through the Solidworks – Design Modeler – ANSYS Mesher - CFX-Pre importing process. The named selections are given in Table 3.3. Complete physics definition for this CFD model in CFX Comand Language is provided in Appendix B. The details of each selected physics model are described in this section. Fig. 3.11 shows both stationary and rotating domains as they are imported into CFX-Pre which is a first step of the physics definition.

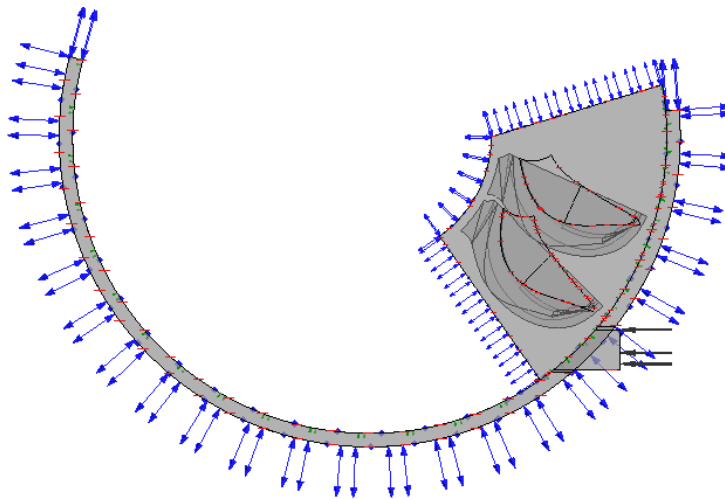


Fig. 3.11. Rotating and stationary domains in CFX-Pre.

Table 3.3. List of named selections in the domain geometries.

Selection Name	Description
Stationary Domain	
NS_SInlet	Inlet face
NS_SWall	Cylindrical face adjacent to the inlet
NS_SSymmetry	Symmetry face
NS_SOpening	All the remaining faces of the domain that are open to the atmosphere
Rotating Domain	
NS_RBucket1In	Inside faces of bucket 1
NS_RBucket1Cut	Cutout faces between inside and outside of bucket 1*
NS_RBucket1Out	Outside faces of bucket 1
NS_RBucket2In	Inside faces of bucket 2
NS_RBucket2Cut	Cutout faces between inside and outside of bucket 2*
NS_RBucket2Out	Outside faces of bucket 2
NS_RSymmetry	Symmetry face
NS_ROpening	All the remaining faces of the domain that are open to the atmosphere

* - When setting up the boundaries, these faces were assigned to the inside surfaces as it was anticipated that the cutout face will be blended into the inside surface during the optimisation. However, it was decided to have a separated selection for this face to be able to monitor its effect separately.

3.3.3.1. User Defined CEL Expressions

First of all, a number of expressions were defined to automate the process of preparing a simulation for each design change and to control the simulation. Some expressions were simply user controlled constant variables and some were relationships between different variables or data readings from the simulation. These expressions are explained in this section.

`FrozenTime = 0.005 [s]`

Defines how long the rotating domain is frozen before it starts rotating.

`FrozenTimestep = FrozenTime/nFrozen`

Calculates the timestep size to be used in frozen mode.

`JetR = (29.7/2) [mm]`

Radius of the jet.

`JetVel = VolumeFlow/(0.5*pi*JetR^2)`

Calculates jet velocity based on volumetric flow rate.

`JetVelVar = JetVel*((-(1/50)*atstep+1050/50)*step(1050-atstep)*step(atstep-1000)+step(1000-atstep))`

Controls gradual switching off of the jet (velocity) depending on the number of timesteps.

`MassFlowIn = 2*(Water.massFlow()@SInlet)`

Reads the mass flow rate at the inlet.

MassFlowOut = -2*(Water.massFlow()@SOpening+Water.massFlow()@ROpening)
 Reads the mass flow rate at all the openings.

MeanVel = areaAve(Velocity)@SInlet
 Reads the average velocity at the inlet.

Omega = 942.5 [rev/min]
 Rotational speed of the runner and the rotating domain.

OmegaVar = -step((Time-FrozenTime-0.5*TimeStep)/1[s])*Omega
 Controls the rotational speed of the rotating domain during the simulation.

TimeStep = dOmega/Omega
 Calculates the timestep size.

TimeStepVar = step((-Time+FrozenTime-0.5*TimeStep)/1[s])*
 FrozenTimestep+step((Time-FrozenTime+0.5*TimeStep)/1[s])*TimeStep
 Controls the timestep size during the simulation.

Torque1Cut = -2*torque_x()@NS_RBucket1Cut
 Torque1In = -2*torque_x()@NS_RBucket1In
 Torque1Out = -2*torque_x()@NS_RBucket1Out
 Torque2Cut = -2*torque_x()@NS_RBucket2Cut
 Torque2In = -2*torque_x()@NS_RBucket2In
 Torque2Out = -2*torque_x()@NS_RBucket2Out
 Reads the torque on different named selection.

VFWaterVar = (- (1/50)*atstep+1000/50)*step(1000-atstep)*
 step(atstep-950)+step(950-atstep)
 Controls gradual switching off of the jet (water volume fraction) depending on the number of timesteps.

VolumeFlow = 0.5*0.0231 [m³/s]
 Defines the volumetric flow rate.

dOmega = 0.05 [degree]
 Defines the angle to rotate during one time step.

nFrozen = 200
 Defines the number of timesteps for the rotating domain to be frozen before it starts rotating.

3.3.3.2. Materials

Two materials were defined: air and water at 15°C. Isothermal conditions were assumed therefore constant fluid properties were specified as given in Table 3.4. The morphology option for both fluids was Continuous fluid.

Table 3.4. Constant material properties of air and water used in CFX.

Fluid	Density [kg/m ³]	Dynamic Viscosity [Pa s]
Water	998.78	1.108 * 10 ⁻³
Air	1.2257	1.797 * 10 ⁻⁵

3.3.3.3. Domain Interface

The interface type between the stationary and rotating domains was Fluid-Fluid. Interface model for this type was General Connection and the Transient Rotor Stator option was selected for Frame Change/Mixing Model. For Pitch Change option Specified Pitch Angles of 360° were chosen as the rotating domain is simply an arbitrary cut from the runner rather than a periodic segment.

3.3.3.4. Boundary Conditions

To solve the governing differential equations they have to be closed by specifying boundary conditions. This section contains a list of boundaries and their conditions (Table 3.5 and Table 3.6).

Table 3.5. Boundary conditions in Stationary domain.

Domain: Stationary			
Name (Location)	Boundary Type	Boundary Details	Fluid Values
SIlet (NS_SIlet)	Inlet	Flow regime Option: Subsonic Mass and momentum: Option: Normal Speed Value: JetVelVar Turbulence Option: Medium (Intensity = 5%)	Air Volume Fraction Value: 1-VFWaterVar Water Volume Fraction Value: VFWaterVar
SOpening (NS_SOpening)	Opening	Flow regime Option: Subsonic Mass and momentum: Option: Entrainment Relative Pressure Value: 0 [Pa] Turbulence Option: Zero Gradient	Air Volume Fraction Value: 1 Water Volume Fraction Value: 0
SSymmetry (NS_SSymmetry)	Symmetry	n/a	n/a
SWall (NS_SWall)	Wall	Mass and momentum: Option: Free Slip Wall	n/a
Domain Interface 1 Side 2 (NS_SInterface)	Interface	Mass and momentum: Option: Conservative Interface Flux Turbulence Option: Conservative Interface Flux	n/a

Table 3.6. Boundary conditions in Rotating domain.

Domain: Rotating			
Name (Location)	Boundary Type	Boundary Details	Fluid Values
ROpening (NS_ROpening)	Opening	Frame type Option: Rotating Mass and momentum: Option: Entrainment Relative Pressure Value: 0 [Pa] Turbulence Option: Zero Gradient	Air Volume Fraction Value: 1 Water Volume Fraction Value: 0
RSymmetry (NS_RSymmetry)	Symmetry	n/a	n/a
RWall1 (NS_RBucket1In, NS_RBucket1Cut, NS_RBucket1Out)	Wall	Frame type Option: Rotating Mass and momentum: Option: No Slip Wall Wall Roughness Option: Smooth Wall	n/a
RWall2 (NS_RBucket2In, NS_RBucket2Cut, NS_RBucket2Out)	Wall	Frame type Option: Rotating Mass and momentum: Option: No Slip Wall Wall Roughness Option: Smooth Wall	n/a
Domain Interface 1 Side 1 (NS_RInterface)	Interface	Mass and momentum: Option: Conservative Interface Flux Turbulence Option: Conservative Interface Flux	n/a

3.3.3.5. Initial Conditions

In the beginning of the simulation both domains are full of air with 0 m/s velocity. Therefore, the given initial conditions are 0 m/s for all the three Cartesian Velocity Components and 0 Pa for Relative pressure. Initial Water volume fraction is 0 and initial Air volume fraction is 1.

3.3.3.6. Timestep

Timestep is an important parameter in transient simulations. The optimum timestep can be adjusted by observing the Courant Number which in a one-dimensional grid is expressed as:

$$Courant\ number = \frac{udt}{dx} \quad (3.2)$$

The Courant number calculated in CFX is a multidimensional generalisation of this one-dimensional equation and is written in the output file for every timestep of a transient simulation. It is suggested to

keep this number below 1 which means that the flow does not jump more than one cell during one timestep. This also means that meshes with smaller elements require smaller timesteps for problems with identical velocities. Timestep used in this CFD model was chosen so that the RMS Courant Number is approximately equal to 0.5 and equivalent to some physically convenient angle of rotation during one timestep. Therefore, the timestep size during rotation was $8.8 \text{ * } \mu\text{s}$ and the rotated angle during one timestep was 0.05° .

3.3.4. Solver Definition

3.3.4.1. Solver Control

This paragraph contains the settings for solver control. The chosen advection scheme was High Resolution as according to the CFX Modelling Guide (ANSYS Inc. 2013a) it gives a good compromise between robustness and accuracy. Second Order Backward Euler option was selected for the Transient Scheme as it is generally recommended for most transient runs in CFX. The Convergence Criteria found to be producing accurate results within reasonable timescales was RMS Residual Target = 0.0001 and the range for number of coefficient loops per timestep was from 3 to 10.

3.3.4.2. Solver Settings

It was found that single precision provides almost identical results to double precision (section 3.2.2.5) and reduces the time duration noticeably. Therefore single precision was used. Chosen Run Mode was Platform MPI Local Parallel with 4 partitions. All simulations were carried out using quad core Intel Xeon, 3.4GHz with 16GB memory RAM. The simulation time was 1.5 million CPU seconds which is approximately 4.5 days when running in parallel mode on 4 cores.

3.3.5. Post-Processing the Results

After the simulation is finished, the post-processing of the results takes place. As described in section 3.3.1. *Computational Domain Geometry* only a part of the runner was modelled to replicate the performance of a complete runner. Therefore, torque readings acquired on the inside surface of the first bucket and the outside surface of the second bucket have to be converted into power output. Fig. 3.12.a presents the torque curves as acquired during the simulation.

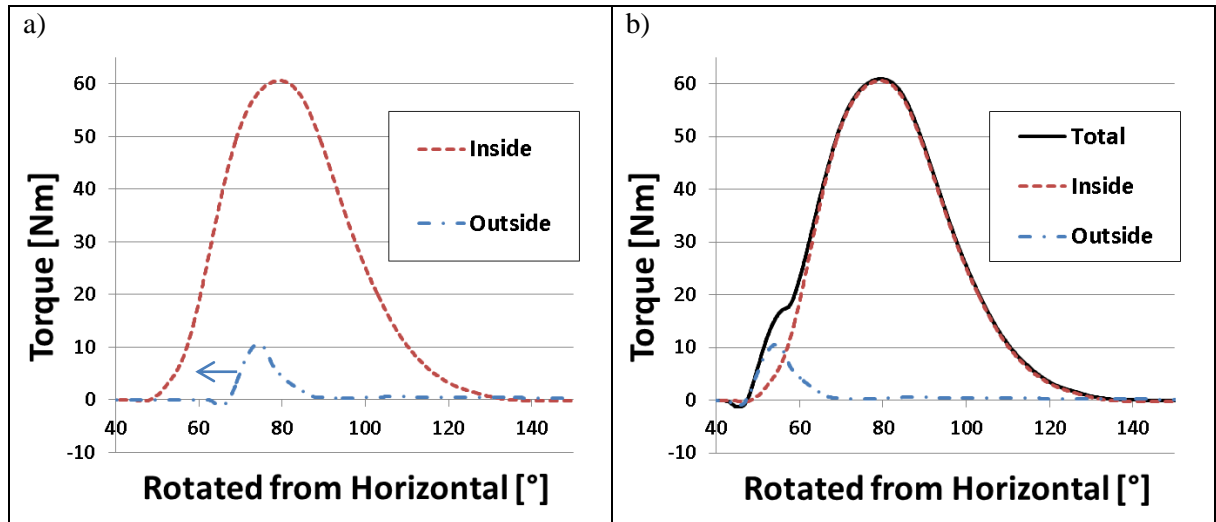


Fig. 3.12. Simulated results: a) inside and outside torque curves as acquired, b) inside torque curve summed with the synchronised outside torque curve to produce a curve of total torque on one bucket.

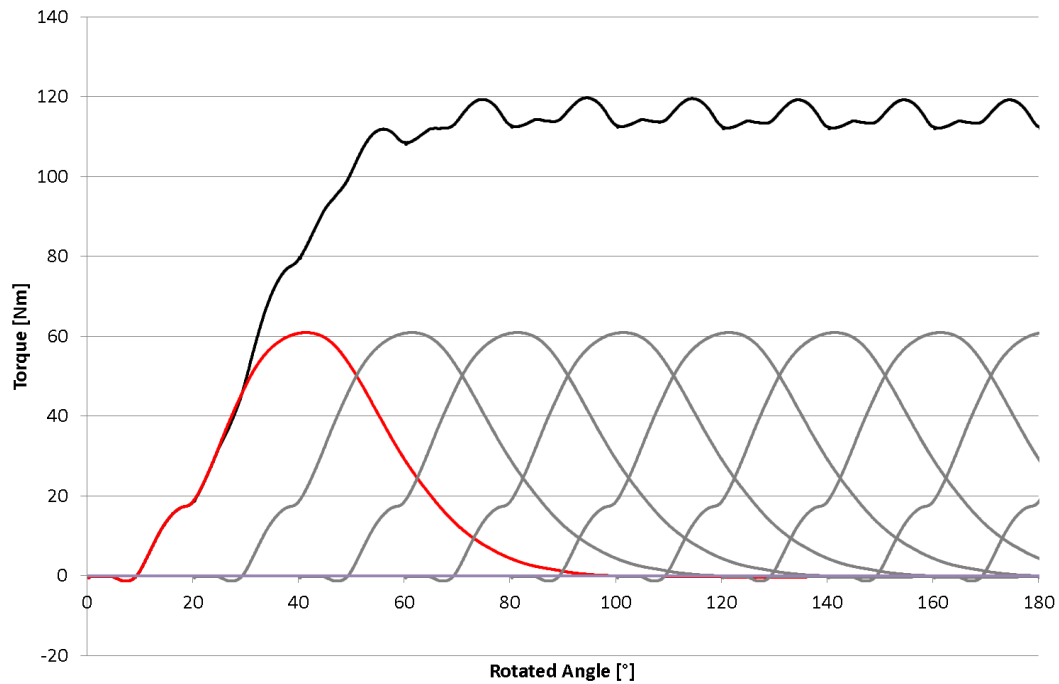


Fig. 3.13. Runner torque construction from a torque data acquired on a single bucket.

One way is to synchronise these readings of the inside and outside torque by shifting the outside torque curve along the abscissa. To become of the same phase the outside torque readings have to be shifted by the angle that is separating the buckets (e.g. 20° for runner with 18 buckets). Then by adding the inside torque readings to the synchronised outside torque readings, total torque produced by one bucket can be calculated as shown in Fig. 3.12.b. Assuming that at stable conditions every bucket is producing identical torque periodically the total torque curve can be copied in steps equal to the spacing between the buckets and by summing all the resulting curves the runner torque can be calculated as shown in Fig. 3.13.

This runner torque can then be used for power output calculations by taking the average value. Methods of calculating the power output from a single bucket torque readings similar to the described above are quite common and can be found in the literature (Barstad 2012). However, this method requires the timestep to be constant throughout the whole simulation. If for any reason the timestep was changed, interpolation or extrapolation has to be used.

Alternative method, that is more flexible and can accommodate the timestep changes, is to use numerical integration. When the rotated angle is expressed in radians, area under the torque curve is work produced by that surface (i.e. inside or outside) during one revolution. This work can be calculated by using the trapezoid rule to numerically integrate the torque as defined in Eq. (3.3).

$$W = \int_a^b M(\theta) d\theta = \frac{1}{2} \sum_{i=1}^N (\theta_{i+1} - \theta_i) (M(\theta_{i+1}) + M(\theta_i)) \quad (3.3)$$

Work produced by a single bucket during one revolution can be calculated by simply adding the work produced by the inside surface to the work produced by the outside surface (3.4) disregarding their phase.

$$W_B = W_{IN} + W_{OUT} \quad (3.4)$$

Then work produced by the runner during one revolution is:

$$W = N_B W_B \quad (3.5)$$

Time of one revolution can be found from the rotational speed expressed in rad/s (3.6) or revolutions per minute (3.7). The latter is more often used in engineering.

$$t = \frac{2\pi}{\omega} \quad (3.6)$$

$$t = \frac{60 [s]}{n} \quad (3.7)$$

Finally, power produced by the runner can be calculated:

$$P_{out} = \frac{W}{t} \quad (3.8)$$

The integration method was chosen for power output calculations because of its flexibility. However, both methods give nearly identical results.

To calculate the efficiency, power input has to be calculated as well which for a complete turbine is calculated (3.9) using two variables describing the flow conditions: the net pressure head and the flow rate (Aggidis and Židonis 2014).

$$P_{inT} = \rho g H Q \quad (3.9)$$

However, power of a free jet is taken as power input when looking at the runner efficiency. For an ideal jet with uniform velocity power input is:

$$P_{in} = \frac{\rho Q \bar{u}^2}{2} = \frac{\dot{m} \bar{u}^2}{2} \quad (3.10)$$

Therefore, runner efficiency in this model was calculated using Eq. (3.8) for power output and Eq. (3.10) for power input:

$$\eta = \frac{P_{out}}{P_{in}} \quad (3.11)$$

3.3.6. Simulation Sequence

The simulation models a very short segment of the whole operating cycle. In physical terms it models a rotation of 140° which is less than 1 revolution and the simulation time is just 30 ms. This is enough to calculate or in other words construct the total torque produced by the runner at steady conditions assuming periodic behaviour. User defined monitor points showing the flow rate and the velocity at the inlet and the torque at various bucket locations are provided in Fig. 3.14. Note that the mass flow rate at the inlet drops to 0 before the inlet velocity, because the water volume fraction at the inlet is gradually reduced to 0 before reducing the velocity. This way the convergence and robustness of the simulation is improved.

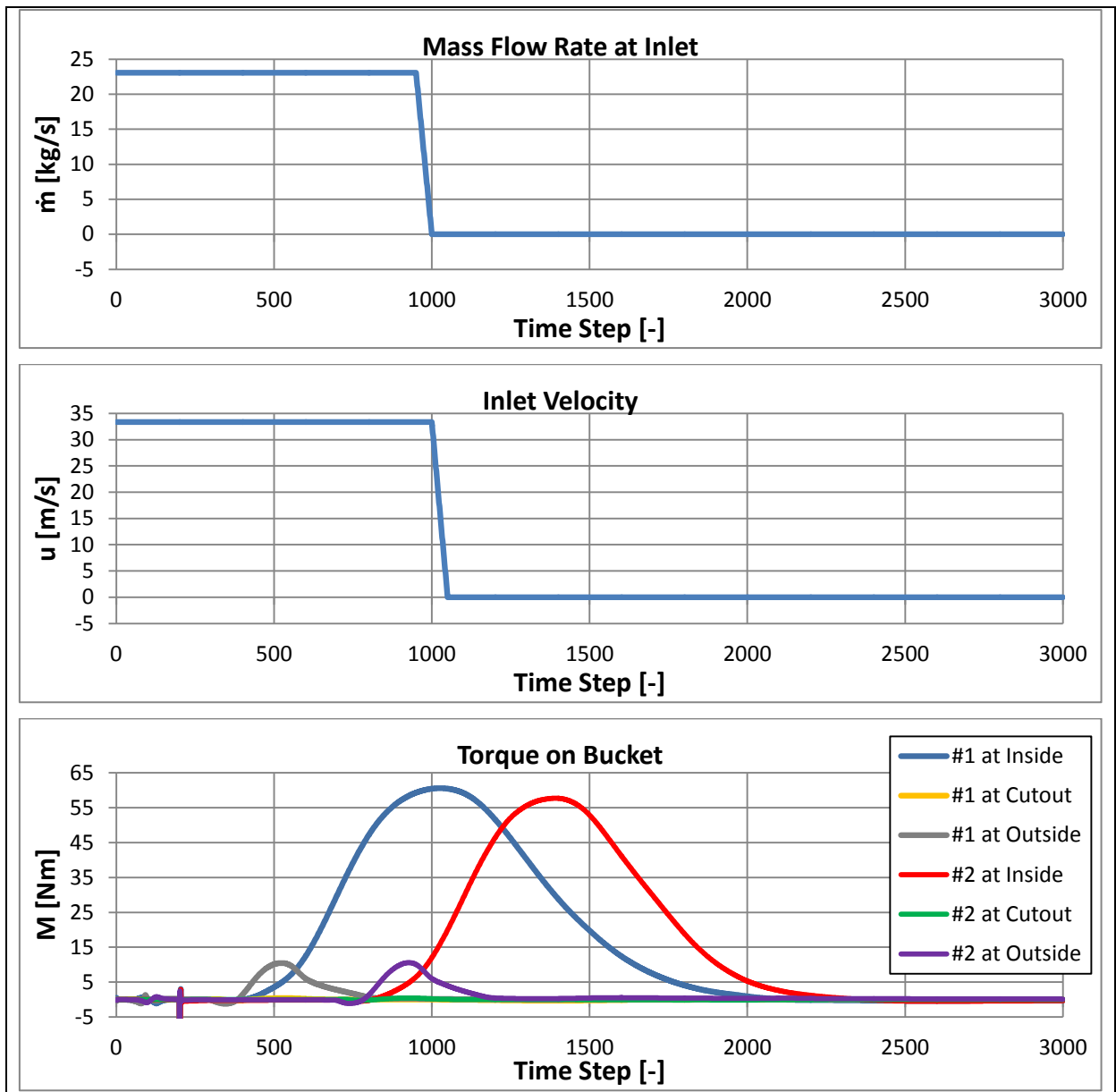


Fig. 3.14. User defined monitor point variables against the accumulated timestep number of the complete simulation.

The whole simulation can be separated into 3 main stages:

- 1) **Jet initialisation.** During this stage, the rotating domain has 0 [rpm] velocity and is waiting until the jet initialises (i.e. travels through both domains). 5 timeframes showing this initialisation are presented in Fig. 3.15.

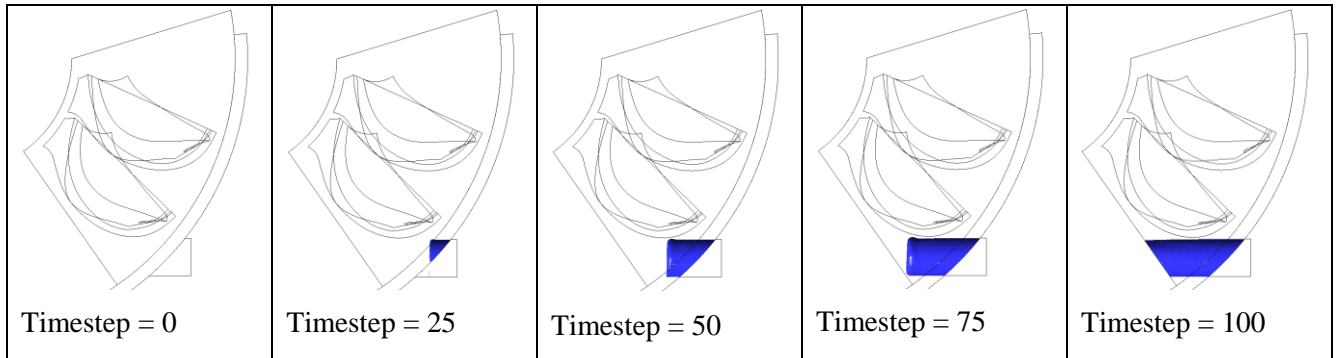


Fig. 3.15. Timeframes of jet initialisation while the rotating domain is frozen.

- 2) **Jet entering the first bucket.** During this stage the rotating domain starts rotating and the jet enters the first bucket. The jet force transferred to the bucket starts increasing until approximately the same time when it is being cut off by the second bucket. This stage ends when the jet is gradually switched off (velocity and water volume fraction turns to 0 at the inlet boundary) to avoid hitting the interface between the domains at non overlapping conditions. It was found to increase the robustness of the simulation and to improve the convergence. Fig. 3.16 shows the timeframe images of this stage.

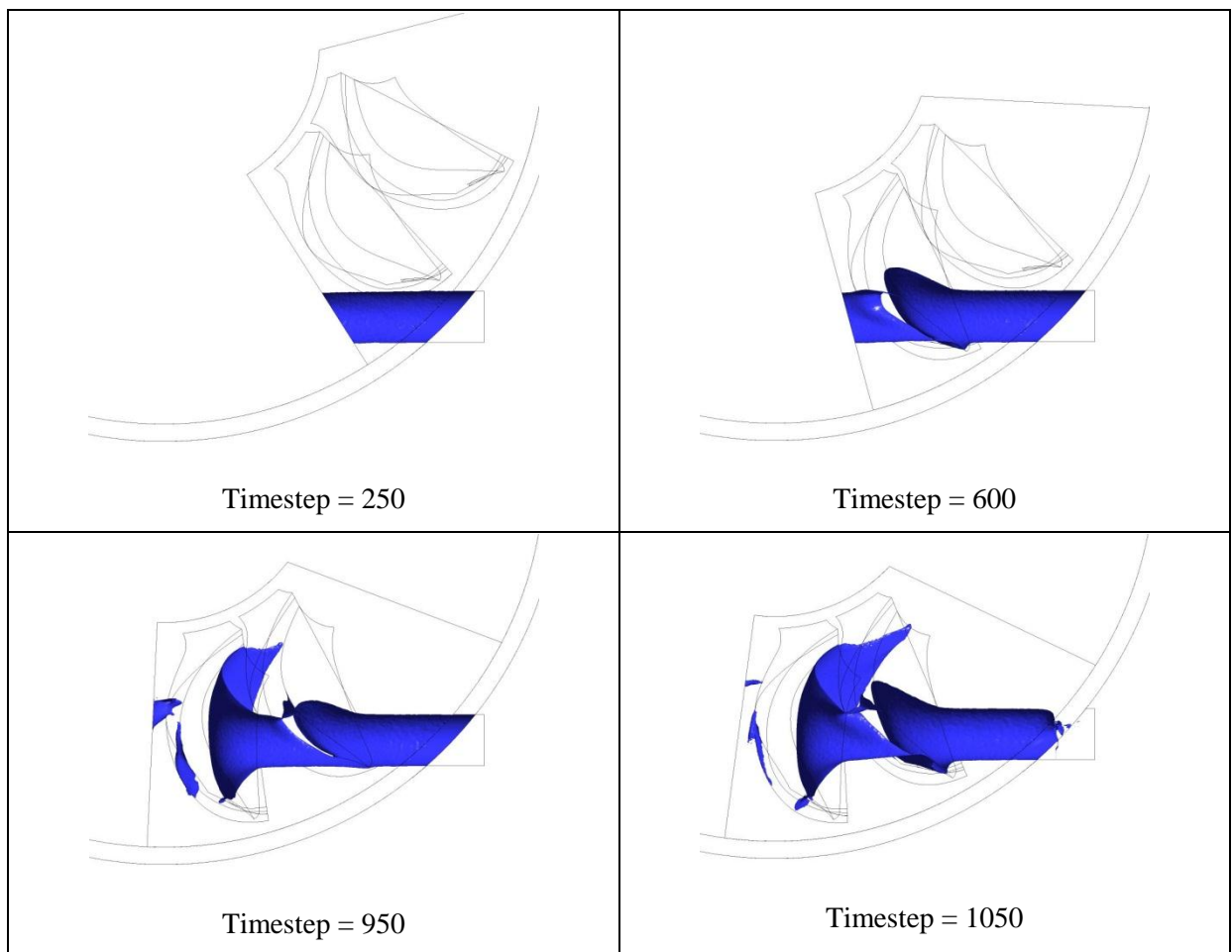


Fig. 3.16. Timeframes of the jet entering the bucket until being completely switched off.

- 3) **Water leaving the first bucket.** During this stage the jet that was entering the first bucket is completely cut off and is continuing to transfer its kinetic energy into the bucket. This stage ends when the water completely clears the first bucket and the torque drops to 0 Nm. The simulation ends together with this stage.

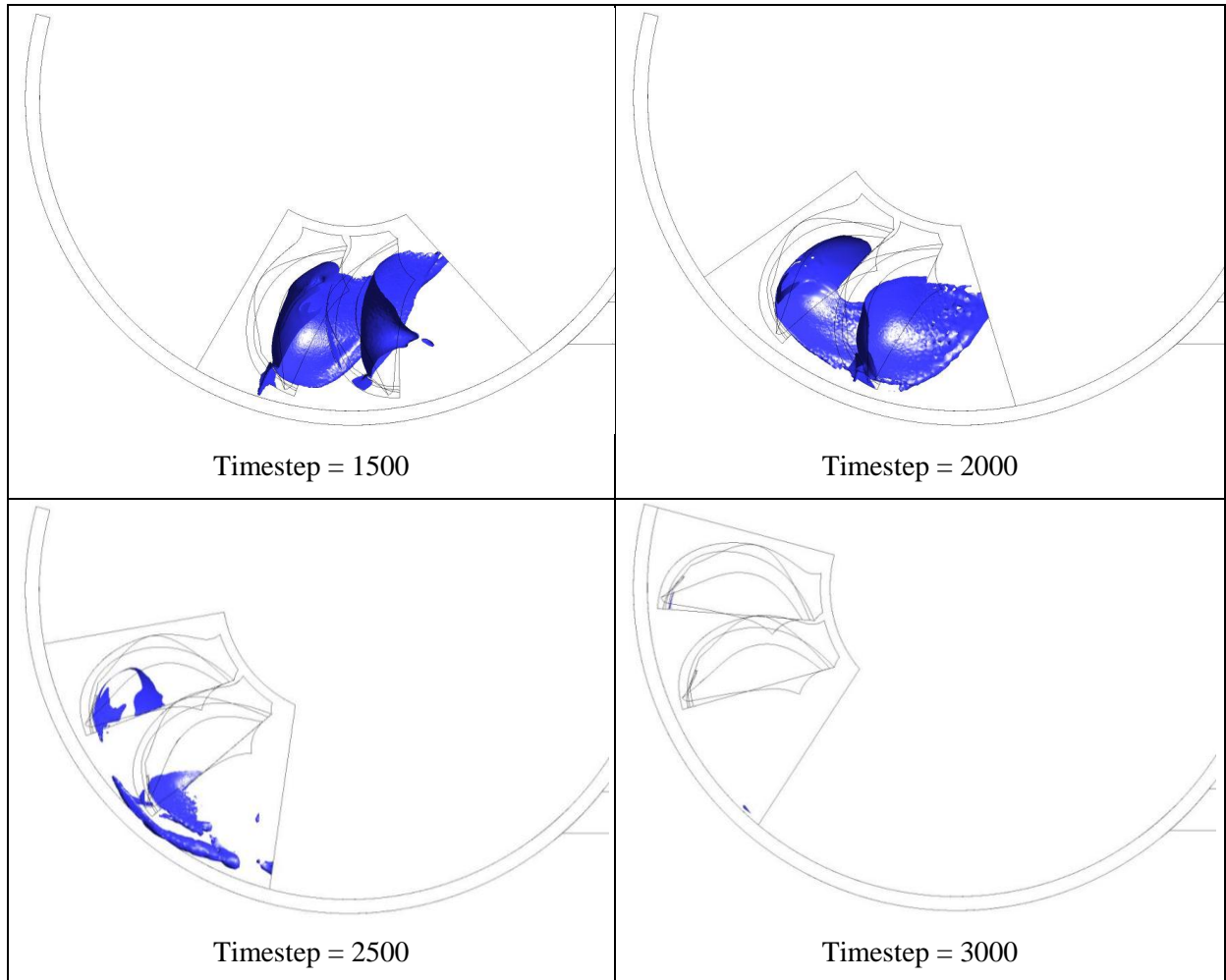


Fig. 3.17. Timeframes of water completely clearing the first bucket.

3.4. Model Validation

3.4.1. Mesh Convergence Study

A mesh convergence study was performed to evaluate the spatial discretisation error and find the resolution required to achieve mesh independent results. Grid Convergence Index (GCI) suggested by Roache (1994) for consistent analysis of grid convergence was used. The flow field was computed on three grids with the refinement ratio $r = 1.1$. The finest mesh consisted of 1.9 million nodes. Table 3.7 indicates the grid information and the resulting modelled runner efficiency normalised to the coarsest grid result. Each solution was properly converged with respect to iterations.

Table 3.7. Grid convergence results normalised to the coarsest grid (#3).

Grid	Normalised grid spacing [-]	Number of nodes [-]	Normalised efficiency [%]
#1	0.83	1910449	100.49
#2	0.91	1431136	100.26
#3	1.00	1037902	100.00

Efficiency modelled using different grid spacing is provided in Fig. 3.18. The modelled efficiency approaches asymptotic zero grid spacing value as the grid spacing is reduced. Using Eq. (3.12) the order of convergence can be determined:

$$p_c = \frac{\ln\left(\frac{\eta_3 - \eta_2}{\eta_2 - \eta_1}\right)}{\ln(r)} \quad (3.12)$$

In this case η_i is the efficiency of simulations with different grid spacing where index 1 denominates the finest grid and index 3 denominates the coarsest grid.

After the order of convergence is known, it is possible to obtain an estimate of the efficiency at zero grid spacing using Richardson extrapolation and two finest grid results:

$$\eta_{h=0} = \eta_1 + \frac{\eta_1 - \eta_2}{2^{p_c} - 1} \quad (3.13)$$

This estimated zero grid spacing efficiency is also shown in Fig. 3.18.

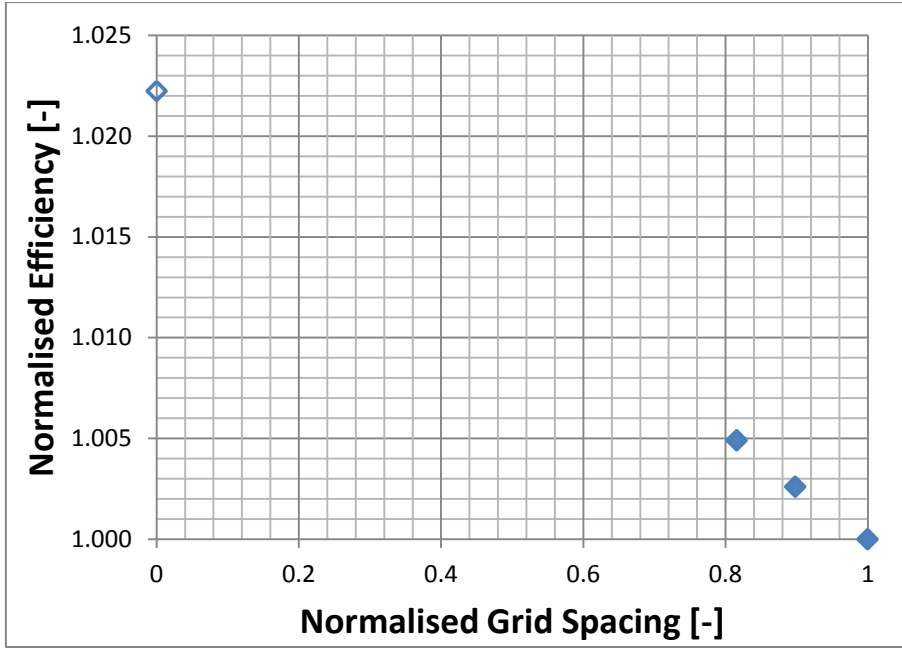


Fig. 3.18. Mesh refinement study results. Grid spacing of each case is normalised by the grid spacing of the coarsest grid. Efficiency is normalised by the result acquired using the coarsest grid.

The Grid Convergence Index (GCI) can now be calculated using Eq. (3.14) and Eq. (3.15).

$$GCI_{12} = \frac{F_s(\eta_1 - \eta_2)/\eta_1}{r^{p_c} - 1} \quad (3.14)$$

$$GCI_{13} = \frac{F_s(\eta_1 - \eta_3)/\eta_1}{r^{p_c} - 1} \quad (3.15)$$

Roache (1994) suggests using the factor of safety $F_s = 1.25$ if three grids are used to estimate the order of convergence p_c .

Table 3.8. Grid convergence criteria.

Refinement ratio	r	1.1
Order of convergence	p_c	1.31
Safety factor	F_s	1.25
GCI for grids 1 and 2	GCI_{12}	2.16 %
GCI for grids 2 and 3	GCI_{23}	2.45 %
GCI for grids 1 and 3	GCI_{13}	4.60 %

Finally it can be checked if the solutions were in the asymptotic range of convergence:

$$\frac{GCI_{23}}{r^{p_c} \cdot GCI_{12}} = 1.002$$

The result is approximately 1 which indicates that the solutions were well within the asymptotic range.

Normalised torque curves of this study are provided in Fig. 3.19. The scaled in area of where the mesh refinement had the biggest influence on the torque curves is provided in Fig. 3.20. The error is of very systematic nature and the coarser meshes simply underpredict the peak torque. Based on the available computational resource limitations it was decided to use mesh #3 for the comparison of the designs. The simulation with mesh #3 took almost 5 days on the PC used during the research (Intel Xeon CPU E3-1240 V2 @ 3.40GHz GHz with 16 GB RAM). The absolute error band of this simulation was 4.6% as presented in Table 3.8. However, when comparing the designs it was assumed that this systematic error would cancel.

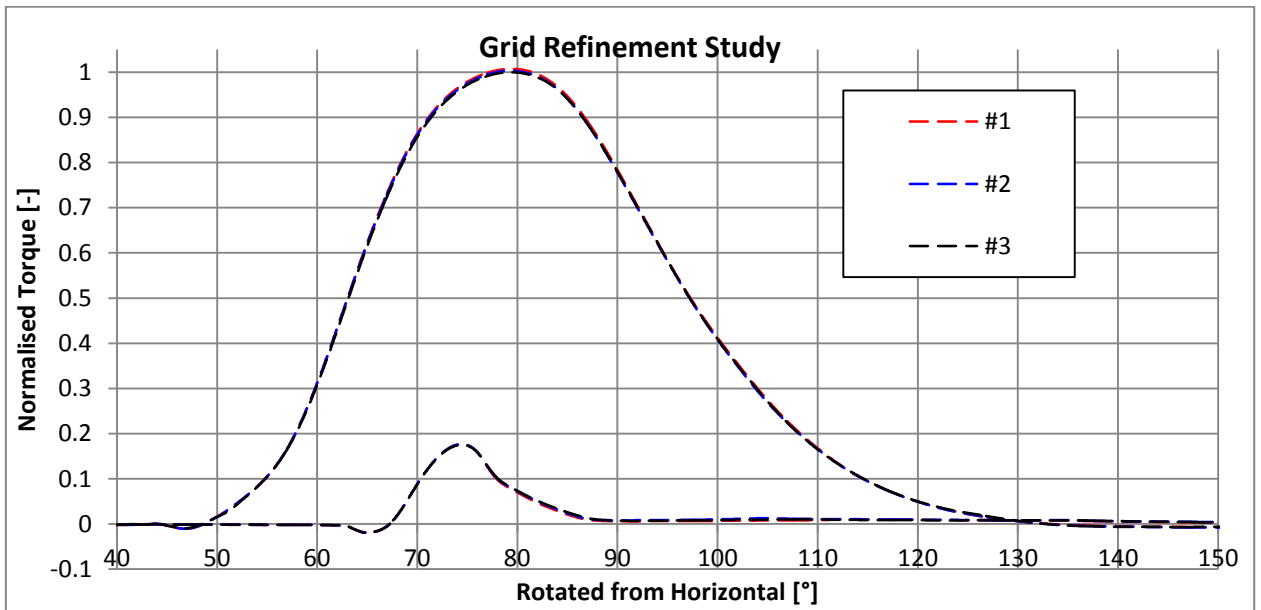


Fig. 3.19. Normalised torque curves of the grid refinement study.

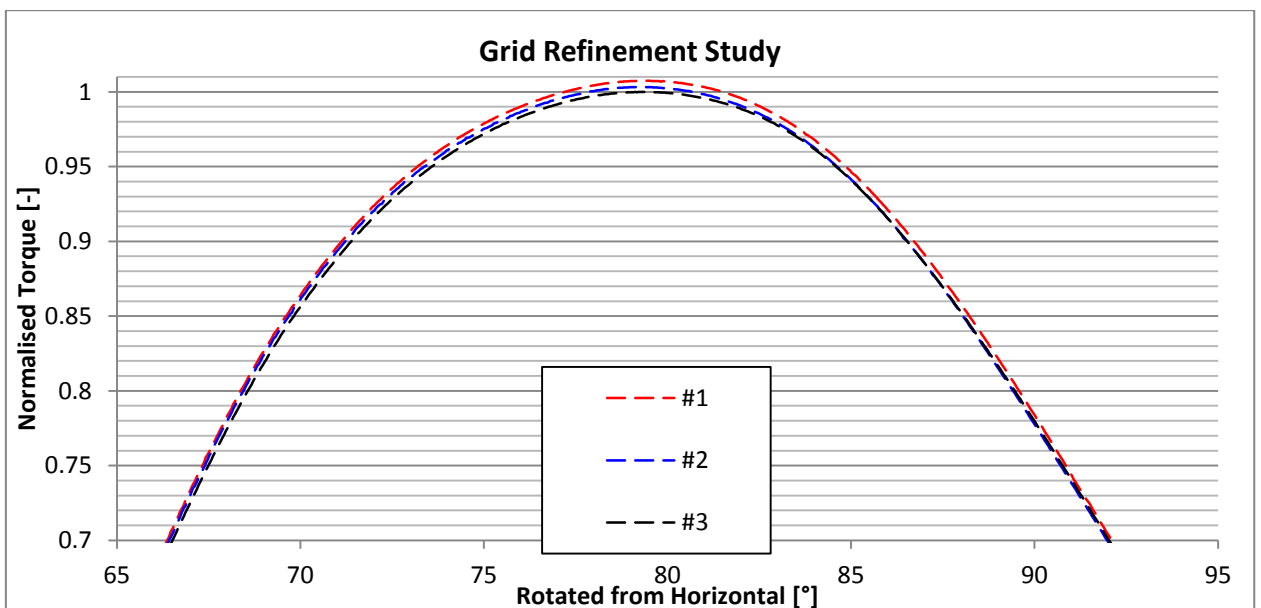


Fig. 3.20. Region of the normalised torque curves of the grid refinement study where the main difference was observed.

3.4.2. Fine and Coarse Mesh Simulations

The time duration to solve the simulation using the mesh sizing selected in the previous section was acceptable for design comparison but inappropriate for parametric study. Therefore it was decided to use this sizing only to verify the key design changes. Simulations that used mesh sizing #3 were called the *fine mesh* simulations.

For the parametric study where a large number of simulations were going to be analysed, a mesh with larger (coarser) mesh sizing was required. Using Eq. (3.16) the required grid resolution can be estimated based on the grid convergence study results and the required accuracy.

$$r^* = \left(\frac{GCI^*}{GCI^{23}} \right)^{1/p_c} \quad (3.16)$$

Following the ideas of Benek, Kraft et al. (1998) the application of CFD can be categorised into three levels depending on the required accuracy: 1) absolute quantities (most accurate), 2) incremental quantities and 3) qualitative information. Absolute quantities were out of the scope of this study since the efficiency of the existing design was known and the aim was to increase it. Therefore only the incremental quantities and qualitative information was required for optimisation. This meant that the error estimated in the previous section would cancel out. Consequentially, it was assumed that for back to back comparison of small changes in the design under identical conditions much larger absolute error band can be allowed. Therefore using Eq. (3.16) and $GCI^* = 10\%$ the required grid resolution was estimated to be $r^* = 2.93$ which results in a mesh containing approximately 40000 nodes. Using this sizing, the duration of the simulation was reduced noticeably. Moreover, larger timesteps could be used with larger elements, as explained in section 3.3.3.6 Timestep, reducing the time duration even further. The new time duration achieved was 20 hours. This type of simulation was called the *coarse mesh* simulation and was used for parametric design optimisation described in Chapter 4. Each key design change achieved using parametric optimisation was then verified using the *fine mesh* simulation before taking the design to the next optimisation stage.

3.5. Summary of Computational Modelling

This chapter presented the relevant working principles of the CFD code and model used in this research. Moreover, details of preparing the simulation, model setup, solving process and post-processing were provided here. Assumptions and their justification were explained in this chapter. Verification of these assumptions was provided where possible by comparing them to more complex CFD models from physical point of view but also more demanding from computational cost point of view. Table 3.9 provides the relative numerical error band δ for the assumptions that were tested in this chapter. The total numerical error calculated using the root-sum-square method is also provided in this table. It should be mentioned that there are more possible sources of error that were not tested in this chapter but can cause uncertainties. These are the turbulence model, the boundary layer resolution or the multiphase model. However, it was expected that these uncertainties are of systematic nature that create an offset in absolute efficiency but do not compromise the direct comparison of design modifications.

Table 3.9. Known relative numerical error band introduced by various assumptions.

Source of Error	Numerical Error Band δ [%]
Symmetry	0.02
Jet shape	0.60
Periodic Torque	0.20
Buoyancy	0.00
Surface Tension	0.03
Single Precision	0.00
Domain Discretization (Mesh)	4.60
Total (Root-Sum-Square)	4.6

Chapter 4. Design Optimisation

This chapter describes the optimisation process and the improvement in performance calculated numerically using CFD. Experimental results validating this improved efficiency are provided in the following Chapter 5. The process of geometry parameterisation and identification of key parameters is described in this chapter. Different design optimisation stages employing the design of experiments technique or analytical development are described here in detail.

4.1. Preparation

Before starting the optimisation, bucket design was simplified to ease the geometry parameterisation process. The key concentration when simplifying the geometry was to maintain the hydraulic efficiency at the same or higher level than the original. Reduction in strength was not of the highest concern at this stage and no strength analysis was performed here as the bucket design was expected to undergo severe geometry changes during the optimisation process anyway. Nevertheless, attention was paid to make feasible modifications and avoid unrealistic shapes of almost no thickness in material, etc. Fig. 4.1 provides an image of the bucket geometry with the key features labelled.

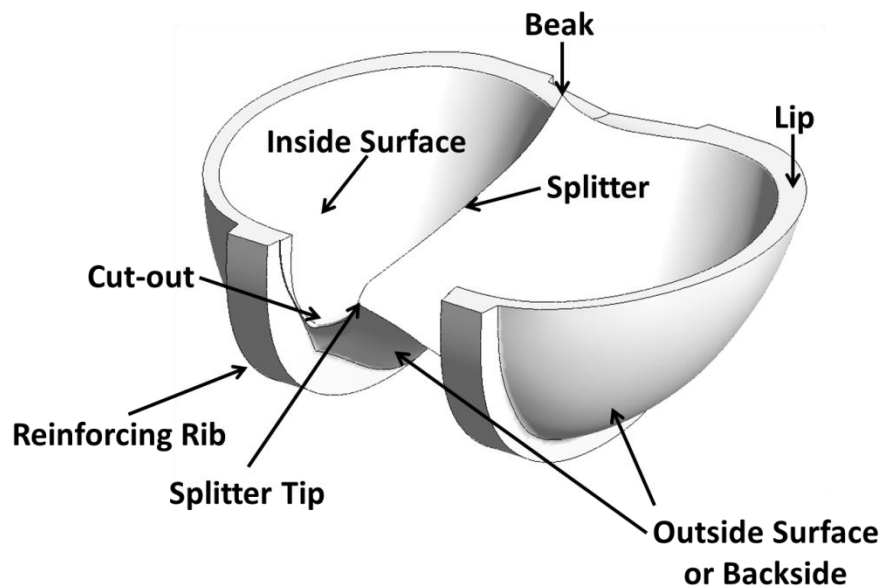


Fig. 4.1. Bucket geometry with definition of key features.

4.1.1. Removing of the Bucket Reinforcing Ribs

The original bucket geometry contained ribs to reinforce the bucket strength. However, these ribs were undesirable from the manufacturing point of view as they made this process more complex. Also a rounded surface was preferable when parameterising the geometry which was the next step in preparation for optimisation. Therefore, first step was to remove the ribs by thickening the whole bucket uniformly. Fig. 4.2 shows both the original and modified geometries. Fine mesh CFD simulations were performed to show that this modification had no negative effect on the performance. According to CFD, removing the ribs had increased the efficiency by 0.1 % as shown in Fig. 4.60.

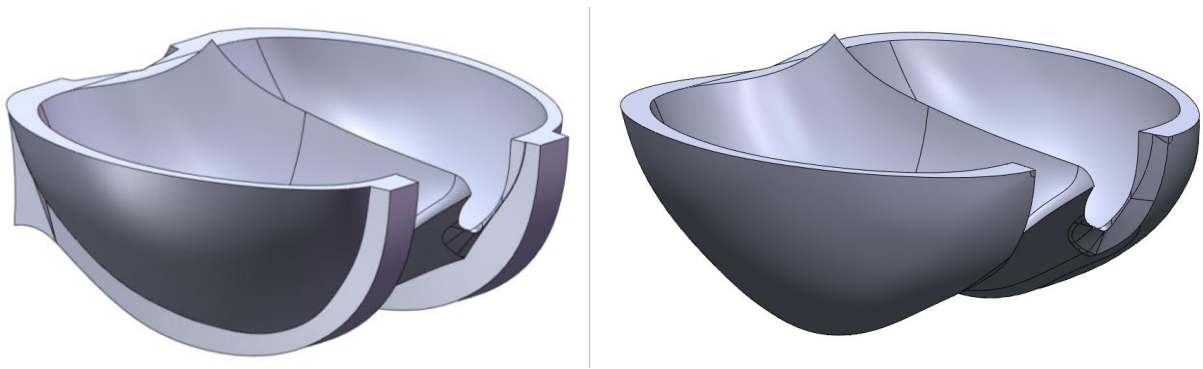


Fig. 4.2. Original geometry with the reinforcing ribs (left), reinforcing ribs removed (right).

4.1.2. Geometry Parameterisation

After the inside and the outside surfaces of the bucket were rounded the geometry was parameterised. The chosen method was to fit control curves in Solidworks that allow flexible semi-automatic modification of the geometry. This method was preferred over other fully automatic surface parameterisation methods like NURBS or similar because of the relatively low amount of modifications to be investigated. Having the time cost of each CFD simulation in mind, it was apparent that the number of modifications is going to be less than hundreds. Therefore complete automation was not required. On the other hand, knowing the cost of each simulation this parameterisation method ensured that each modification is sound and logical and that the computational resources are used efficiently. Fig. 4.3 shows the inside and the outside surfaces and their control curves. An example of a control curve is provided in Fig. 4.4. These parametric surfaces are then combined together by filling in the missing surfaces (Fig. 4.5) at the cutout and the lip. At this point all the surfaces enclose a finite volume which can be converted into a solid body. The whole parameterisation process has caused minor changes in the geometry. However, the fine CFD analysis showed no difference in the efficiency (Fig. 4.60).

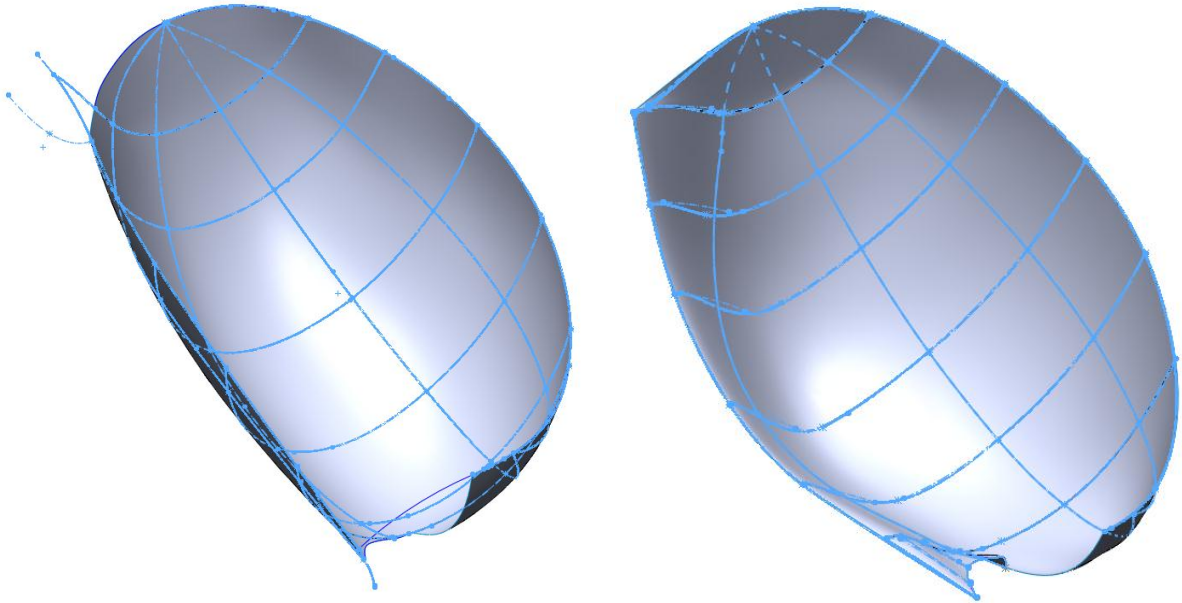


Fig. 4.3. Inside (left) and outside (right) surfaces of one half of the bucket and their control curves.

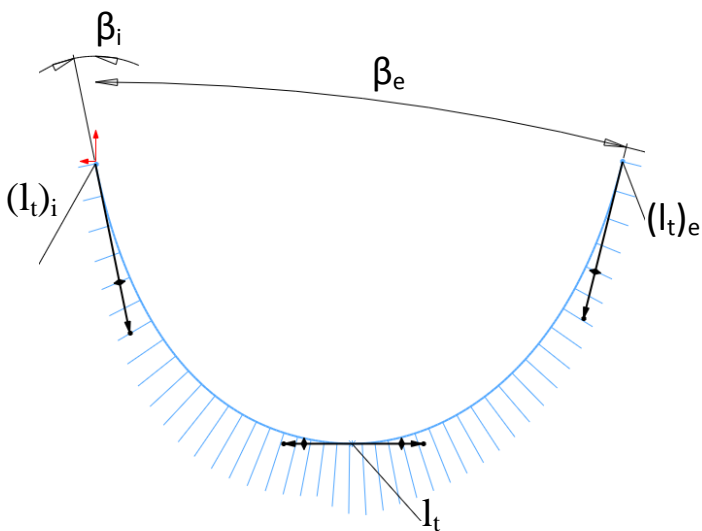


Fig. 4.4. Control curve of one bucket profile specifying the inlet (β_i) and exit (β_e) angles and the tangential length (l_t) at three key points of the spline.

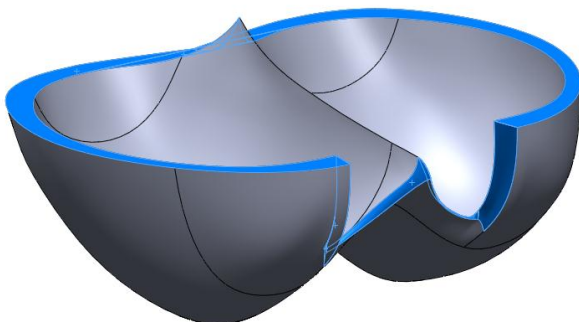


Fig. 4.5. Parameterised bucket geometry with the connecting surfaces highlighted in blue.

4.1.3. Splitter Simplification

The next preparatory step was to simplify the splitter geometry by removing the protruding beak that was present at the furthest point from the cutout. Geometries before and after this simplification are provided in Fig. 4.6. It was known that this protrusion was designed to relieve the stress concentration from the splitter edge when the bucket is bent backwards by the jet force or stretched by the centrifugal forces or both. However, similar as in the previous section 4.1.1 *Removing of the Bucket Reinforcing Ribs*, strength was not of the key importance at this early stage and the concentration was on the hydraulic design and geometry simplification to assist the parametric optimisation process. Again, fine mesh CFD simulation was performed to ensure that the performance was not reduced. CFD results showed no difference in the efficiency at all (Fig. 4.60). The geometry was ready for the parametric study.

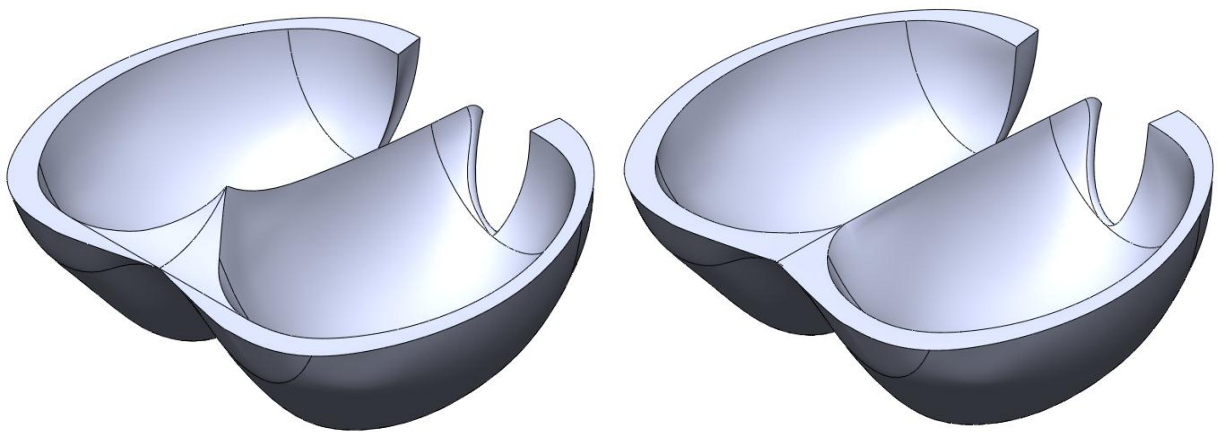


Fig. 4.6. Bucket geometry before (left) and after (right) the splitter shape was simplified.

4.2. Design Parameters

Performance of the Pelton runner can be reduced or increased by various changes in the design that have an effect on different phenomena. That is why before modifying the design it was important to identify the parameters that could be quantified and therefore correlation between the modification made and the change in performance could be analysed. 12 design parameters were selected that were expected to influence the runner efficiency. 9 of these parameters control the shape of the bucket and 3 control the position of the bucket. Naturally, all of the parameters were expected to be related between themselves to a higher or lower extent, however, due to the current time cost limitations of CFD they were separated into smaller groups based on the level of interrelation.

P1 Bucket length to width ratio (L/B):

proportions of the bucket are changed by varying its length. The width is kept constant since it is related to the jet diameter which depends on the operating conditions.

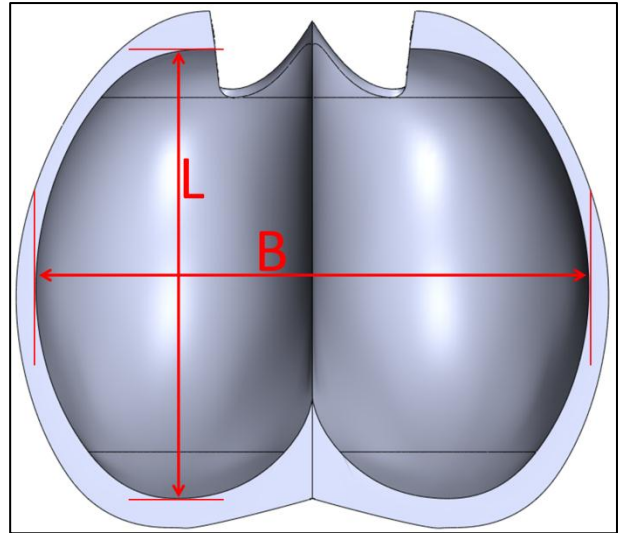


Fig. 4.7. Design Parameter P1 Bucket length to width ratio (L/B).

P2 Bucket depth to width ratio (H/B):

the bucket width is constant as in P1 while the depth is varying.

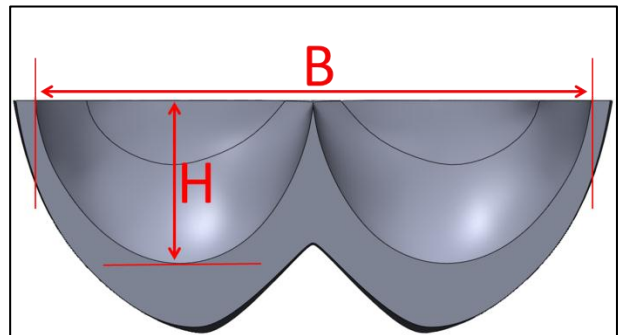


Fig. 4.8. Design Parameter P2 Bucket depth to width ratio (H/B).

P3 Bucket exit angle (β_e):

is measured in the plane that is perpendicular to the edge of the lip. It controls at what angle the flow leaves the bucket. It would be ideal to divert the jet direction by 180° and have it leaving the bucket vertically meaning that the power of the jet was utilised completely, however then the leaving water would interfere with the next bucket. That is why optimisation of this parameter is required.

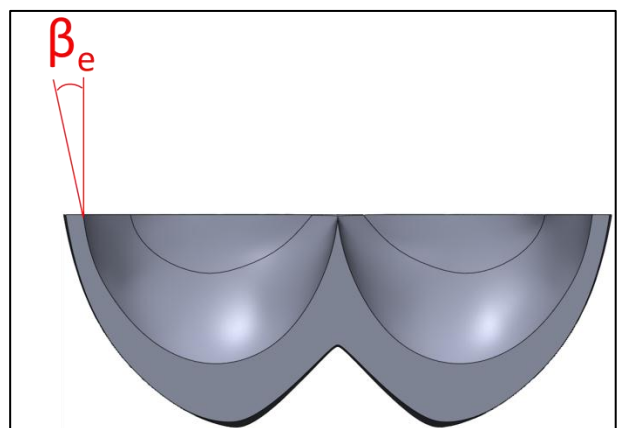


Fig. 4.9. Design Parameter P3 Bucket exit angle (β_e).

P4 Splitter inlet angle (β_i): it was expected that the angle at which the jet is divided into two might have an influence on the performance by affecting the pressure distribution on the inside surface of the bucket.

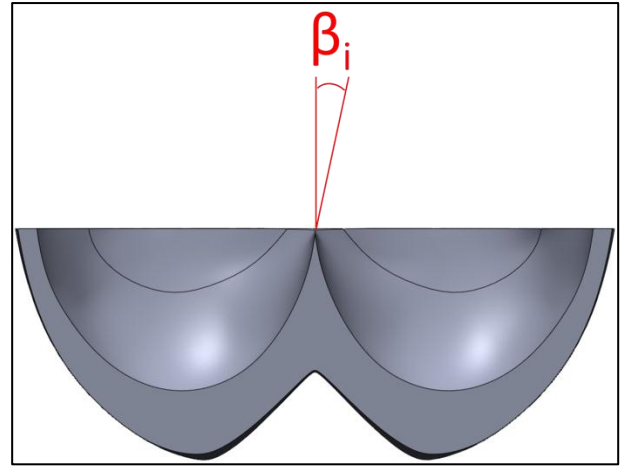


Fig. 4.10. Design Parameter P4 Splitter inlet angle (β_i).

P5 Inclination angle (α): in various runner designs, buckets are mounted at different angles. It was decided to look into this parameter to optimise the angular positioning. The angle α is changed while keeping the radial distance R_t (splitter tip to the axis of rotation O) constant.

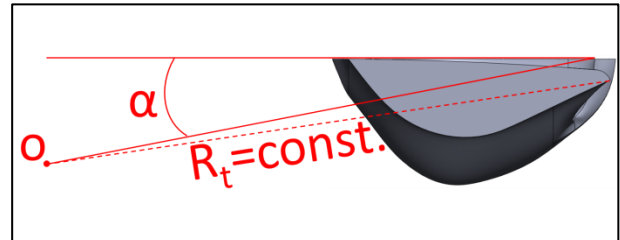


Fig. 4.11. Design Parameter P5 Inclination angle (α).

P6 Radial distance (R_t): within certain limits bucket can be moved radially. For a developed design this position is expected to be very close to its optimum. However, this parameter becomes very important when looking at new designs or if the original geometry of the bucket has been noticeably modified. The pitch circle diameter (D_p) and the inclination angle (α) are kept constant while describing this parameter.

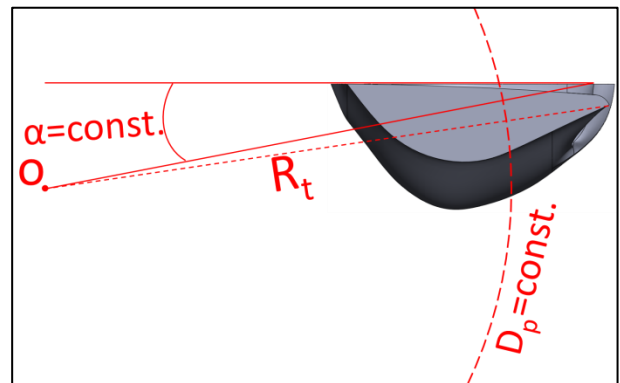


Fig. 4.12. Design Parameter P6 Radial distance (R_t).

P7 Number of buckets (N_b): as the geometry of the bucket and its positioning is changed the spacing between the buckets might be no longer at its optimum. I.e. if the size of the bucket was increased perhaps fewer buckets are needed or vice versa.

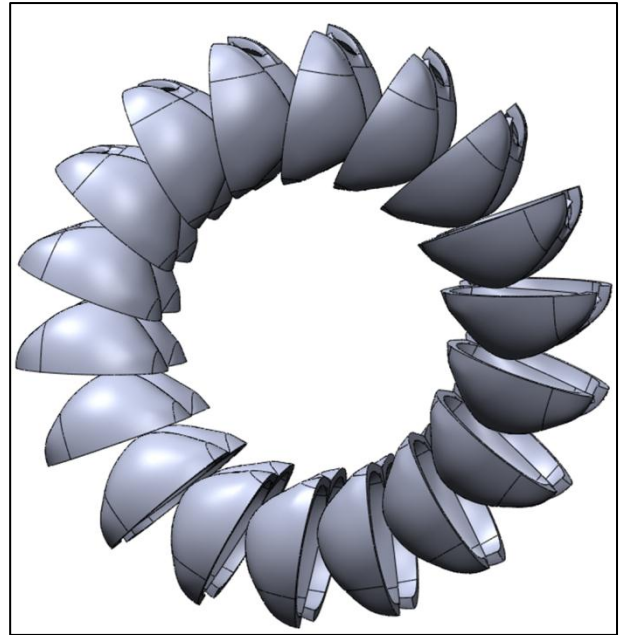


Fig. 4.13. Design Parameter P7 Number of buckets (N_b).

P8 Splitter level (H_s): there is a noticeable variation of the splitter level between various Pelton bucket designs. Therefore it was decided to look at the effect of this parameter.

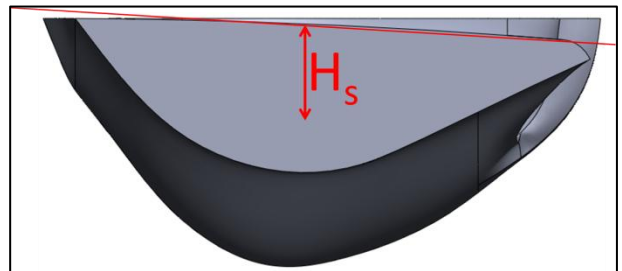


Fig. 4.14. Design Parameter P8 Splitter level (H_s).

P9 Splitter edge angle (β_s): the edge of the splitter is at different angle in different bucket designs. Therefore it was decided to study the importance of this angle.

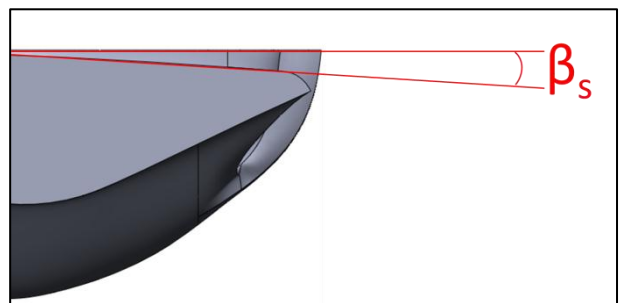


Fig. 4.15. Design Parameter P9 Splitter edge angle (β_s).

P10 Backside of the splitter: due to the Coanda effect (Taylor 1980, Perrig 2007), the backside of the splitter can produce useful torque as the suction produced by the jet is pulling the bucket. However, if some energy is taken from the jet at this point, less energy reaches the inside of the neighbouring bucket. Therefore it was decided to study this part of the bucket carefully to increase the overall efficiency.

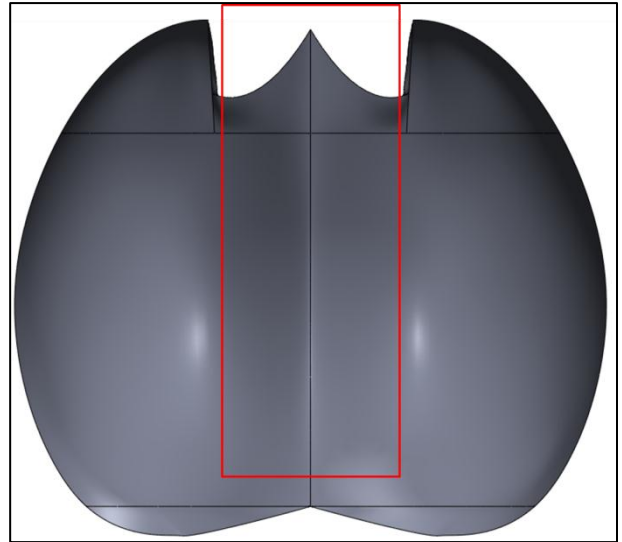


Fig. 4.16. Design Parameter P10 Backside of the splitter.

P11 Cutout Shape: all modern Pelton buckets have the cutout in the front to ensure smooth flow transition as the runner is rotating. The shape of this cutout is limited by two factors: 1) the cutout has to be wide enough to accommodate the jet at the maximum flow rate, 2) if the cutout is too wide some part of the flow will leave the bucket in high velocity without transferring its energy to the runner.

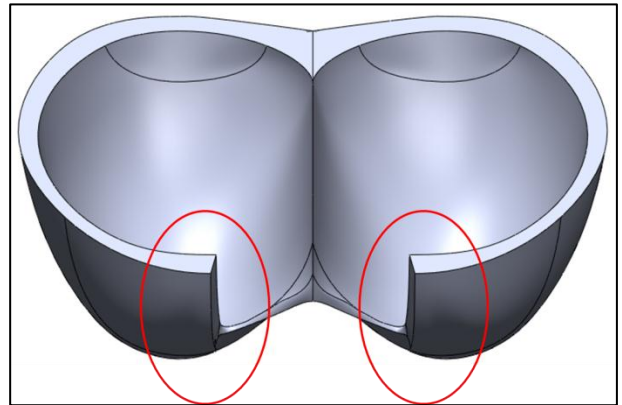


Fig. 4.17. Design Parameter P11 Splitter edge angle (β_s).

P12 Splitter tip geometry: splitter tip is most often the first part of the bucket that interferes with the jet. Therefore it is very important to cause as little disturbance in the jet as possible during this impact.

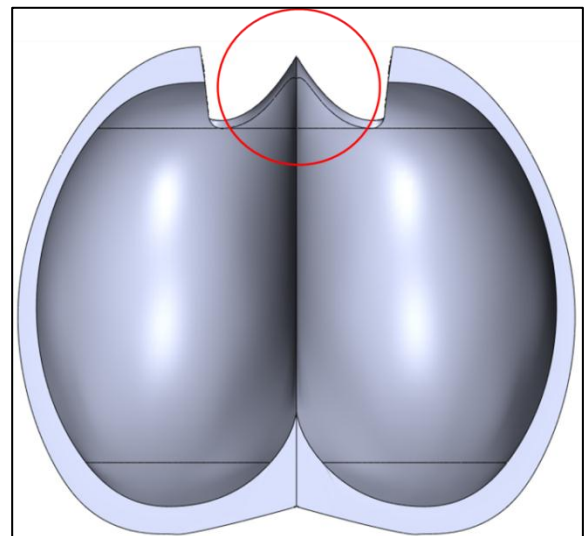


Fig. 4.18. Design Parameter P12 Splitter tip geometry.

4.3. Design of Experiments Optimisation

Coarse mesh CFD simulations were used during this study and only the key output geometries from this study were verified using the fine mesh simulations. However, even using the coarse mesh simulations, computational cost was too high to examine all of the parameters at the same time to achieve the geometry that gives the total highest efficiency and investigate the interaction between these parameters. Therefore, the parameters were grouped into sets according to the anticipated level of interaction between them. There were two sets of parameters that were approached using Design of Experiments (DOE) technique:

- **DOE Study 1** – analysed 4 parameters (P1-P4) simultaneously. These parameters were the ratios L/B and H/B , exit angle (β_e) and inlet angle (β_i). This way bucket shape proportions and the flow angles were controlled. It was assumed that all 4 parameters are highly related because when changing (scaling) the length or depth of a bucket the angles are changing as well.
- **DOE Study 2** – when the bucket proportions were optimised it was decided to look at its positioning in the runner. Therefore this study was simultaneously looking at three parameters (P5-P7) that describe the position of the bucket: radial distance (R_d), inclination angle (α) and the number of buckets (N_b).

Design Expert 9 software (Stat-Ease 2014) was used to create the test plans and select the optimum values after simulations in the test plan were completed. The remaining design parameters (P8-P12) were not suitable for parametric optimisation and therefore they were optimised analytically observing the flow behaviour and trying to solve the identified problems.

The chosen method for DOE analysis was Response Surface Designs (RSD). To reduce the number of runs to a minimum it was decided to use the Small Central Composite Design (Draper and Lin 1990), which is available for 4 factors and can be used to analyse quadratic behaviour. More details on this method can be found in the documentation of the Design Expert 9 with the relevant extract provided in Appendix C.

4.3.1. P1-P4: DOE Study 1 (L/B, H/B, β_e , β_i)

Design limits for these 4 parameters are provided in Table 4.1. The range for the study was created around the initial design values (confidential data of Gilkes) acquired after the original geometry was simplified and parameterised in section 4.1 *Preparation*.

Table 4.1. Design ranges for parameters L/B, H/B, β_e , β_i .

Design Parameter		Lower Limit	Upper Limit
P1	L/B	0.75	1.05
P2	H/B	0.275	0.325
P3	β_e	15°	21°
P4	β_i	7°	16°

Because of specifying the angles before the scaling, the real angles were different than the control angles. Moreover, a clear relationship between the ratio H/B and the control angles was expected. E.g. for a constant control exit angle, the real exit angle would decrease if the ratio H/B was increased. However, knowing the real angles were not important during the optimisation as the response surface was produced for the control angles.

Also, it is important to describe the definition and the location of the control angles since the exit or inlet angles might be varying around the lip or along the splitter. It can be seen from Fig. 4.19 that at the peak torque on the inside of the bucket (coloured in white) most of the flow is leaving at the far end of the bucket (closest to the axis of runner rotation). Moreover, the flow there has the highest velocity, meaning that the losses are the highest at that location. Finally, looking at the distribution of the exit angle measured in the plane intersecting the jet axis and rotated around this axis from 45° to 120° as shown in Fig. 4.20., distribution of the exit angles is provided in Fig. 4.21 and the effect on the losses if the flow was leaving at the identical angle to the bucket exit angle is provided in Fig. 4.22. The effect was calculated using Eq. (4.1) and measured at 120° it was almost 10 times higher than at 90°. Therefore, based on all of these observations it was decided to be specifying the exit angle at the location of measurement plane equal to 120°. The splitter inlet angle was uniform along the edge in the region that was in contact with water at one time or another throughout the duty cycle.

$$1 - \eta = 1 - \cos \beta_e \quad (4.1)$$

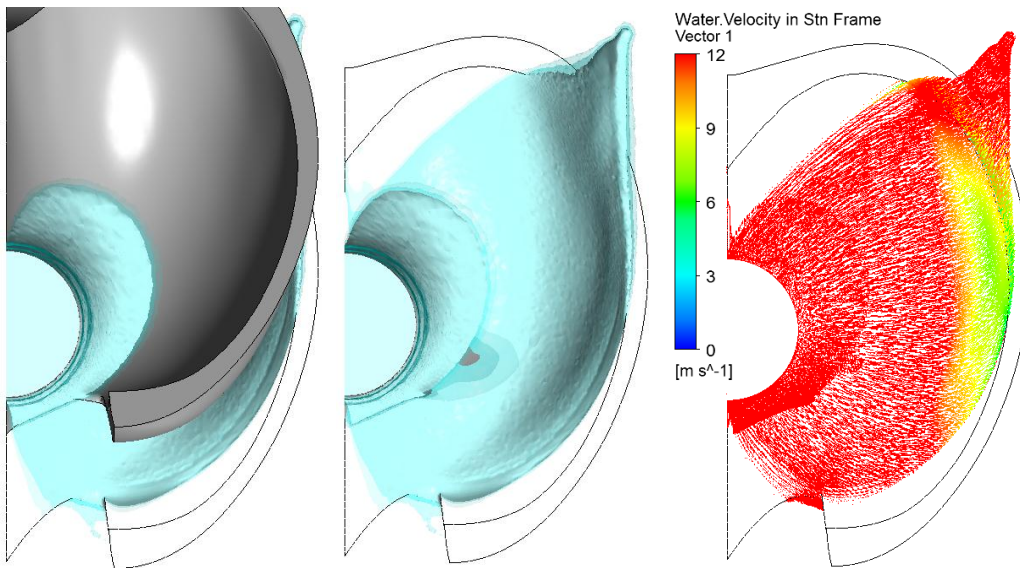


Fig. 4.19. Jet impacting bucket 1 (white) at the peak inside torque.

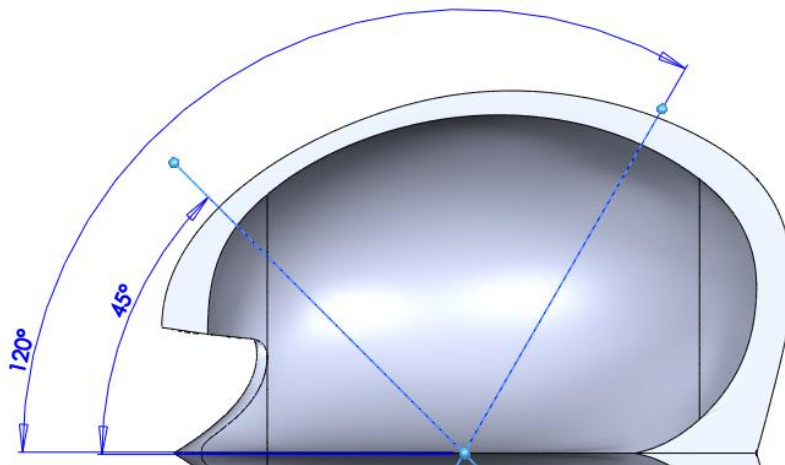


Fig. 4.20. Range for the locations of the plane where the exit angle was measured.

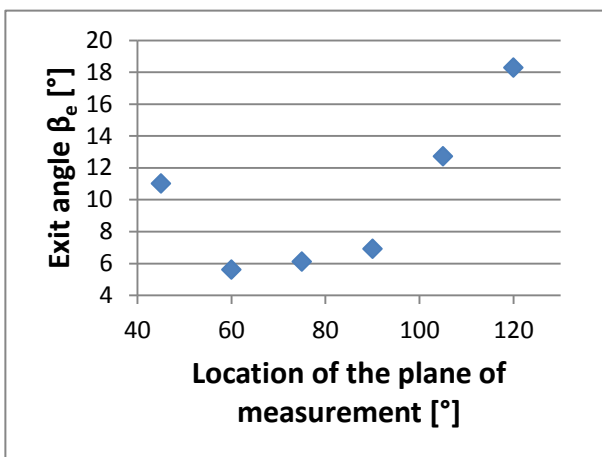


Fig. 4.21. Distribution of the exit angle (β_e).

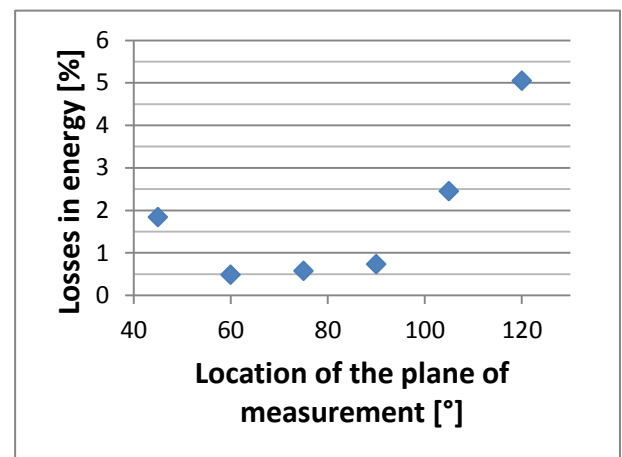


Fig. 4.22. Distribution of the losses caused by the exit angle (β_e).

The test plan consisted of 17 initial design variations to be analysed plus 4 repetitions of the centre point. The purpose of repeating the measurements at the centre point comes from the experimental

approach to assess the repeatability. Since CFD was used in the particular case, there was no repeatability error at all. That is why the centre point values were simply copied meaning that only 17 simulation runs were required to complete the test plan. Same procedure of copying the centre point values was done for all the DOE studies. These 17 design points together with the simulated efficiency normalised to the maximum efficiency of the test plan Eq. (4.2) are provided in Table 4.2 under iteration 1.

$$\eta_{norm} = \frac{\eta}{\eta_{max}} \quad (4.2)$$

After performing these 17 simulations the peak efficiency was discovered to be outside of the design range for parameter P2 (H/B). Therefore it was decided to run 3 more simulations (iteration 2) at higher H/B ratios and add them to the test plan. Values for parameters P1, P3 and P4 were selected from the response surface that was already available. The results were inserted into the data to update the response surface. Parameter values for the simulation in Iteration 3 were taken from the response surface at the predicted peak efficiency. According to the response surface it was expected to be 0.1 % higher than the already acquired maximum (modification a-12). However, the simulation results showed that it was 0.5 % lower than a-12. The data was updated. Again, the predicted peak was only 0.1 % higher than a-12. Therefore it was decided to take a-12 as the final modification of the DOE Study 1. It can be seen from the table that a-19 had the same efficiency as a-12. However, the latter was preferred as its ratios L/B and H/B were smaller, meaning that it was a smaller size bucket than a-19 but with the same efficiency.

Fine mesh simulation was performed to verify the improvement in the efficiency achieved during the DOE study 1. The predicted efficiency improvement was 0.9 % of the initial efficiency as shown in Fig. 4.60. This was achieved by stretching the initial bucket shape lengthwise by a factor of 1.11 and depth wise by a factor of 1.17 while keeping the width constant and adjusting the exit angle to divert the flow as close as possible to 180°. As explained in the beginning of this section the real exit angles are different from the control angles due to the sequence in which the geometry is controlled. The real exit angles and the theoretical losses caused by these angles are provided in Fig. 4.23 and Fig. 4.24 respectively. The inlet angle was found to have very little influence on the performance. Visual comparison is provided in Fig. 4.25, Fig. 4.26 and Fig. 4.27.

Table 4.2. Test plan for parameters L/B, H/B, β_e , β_i .

Iteration	Modification Name	L/B [-]	H/B [-]	β_e [°]	β_i [°]	η_{norm} [-]
1	a-1	0.648	0.300	18.0	11.5	0.967
	a-2	0.750	0.275	15.0	7.0	0.985
	a-3	0.750	0.275	15.0	16.0	0.981
	a-4	0.750	0.325	21.0	7.0	0.982
	a-5	0.750	0.325	21.0	16.0	0.983
	a-6	0.900	0.258	18.0	11.5	0.989
	a-7	0.900	0.300	18.0	3.9	0.997
	a-8	0.900	0.300	13.0	11.5	0.992
	a-9	0.900	0.300	18.0	11.5	0.997
	a-10	0.900	0.300	23.0	11.5	0.989
	a-11	0.900	0.300	18.0	19.1	0.991
	a-12	0.900	0.342	18.0	11.5	1.000
	a-13	1.050	0.275	21.0	7.0	0.972
	a-14	1.050	0.275	21.0	16.0	0.967
	a-15	1.050	0.325	15.0	7.0	0.986
	a-16	1.050	0.325	15.0	16.0	0.982
	a-17	1.152	0.300	18.0	11.5	0.980
2	a-18	1.030	0.420	32.0	16.5	0.975
	a-19	0.930	0.350	17.5	9.8	1.000
	a-20	0.930	0.375	17.5	9.8	0.998
3	a-21	0.960	0.350	21.0	10.5	0.995

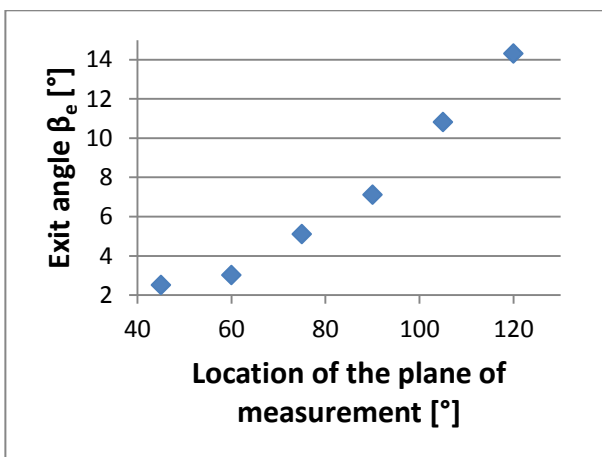


Fig. 4.23. Distribution of the real exit angle (β_e) after the DOE Study 1.

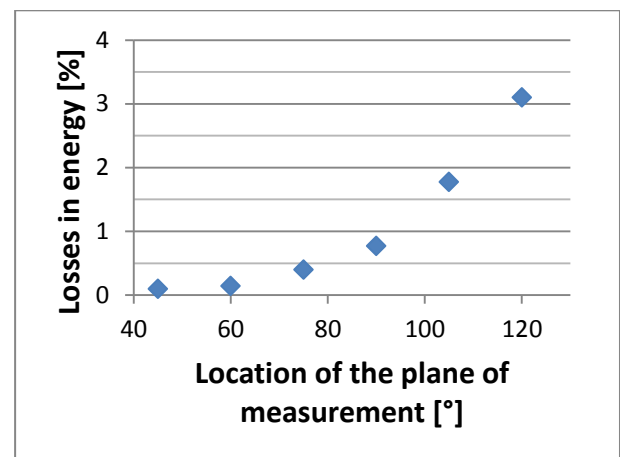


Fig. 4.24. Distribution of the losses caused by the exit angle (β_e) after the DOE Study 1.

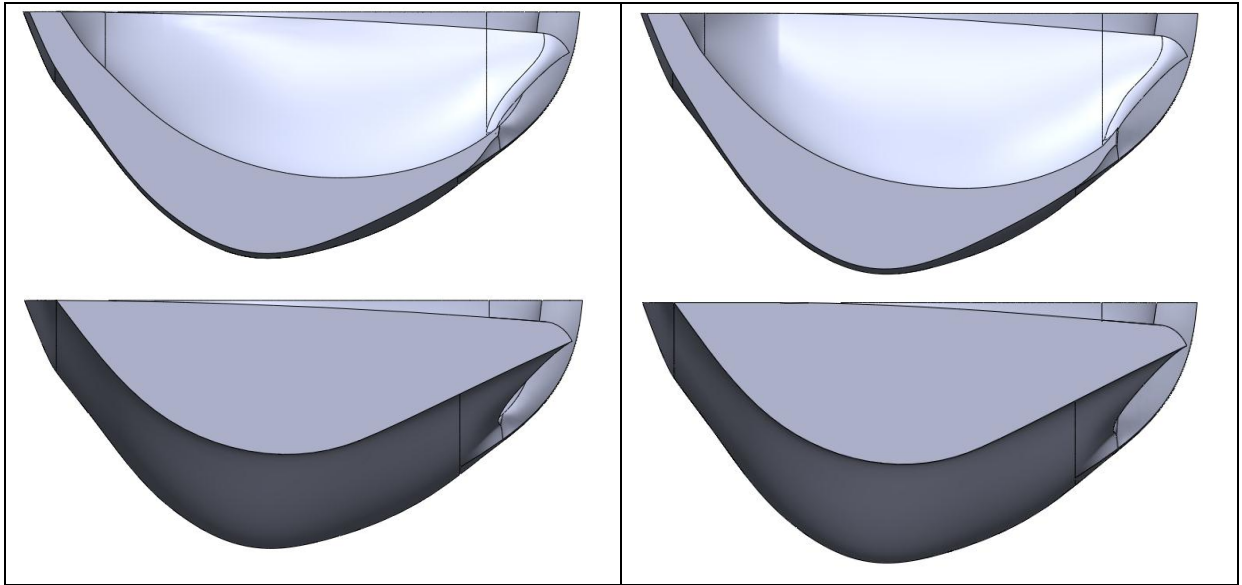


Fig. 4.25. Side view of the bucket geometry before (left) and after (right) the DOE Study 1.

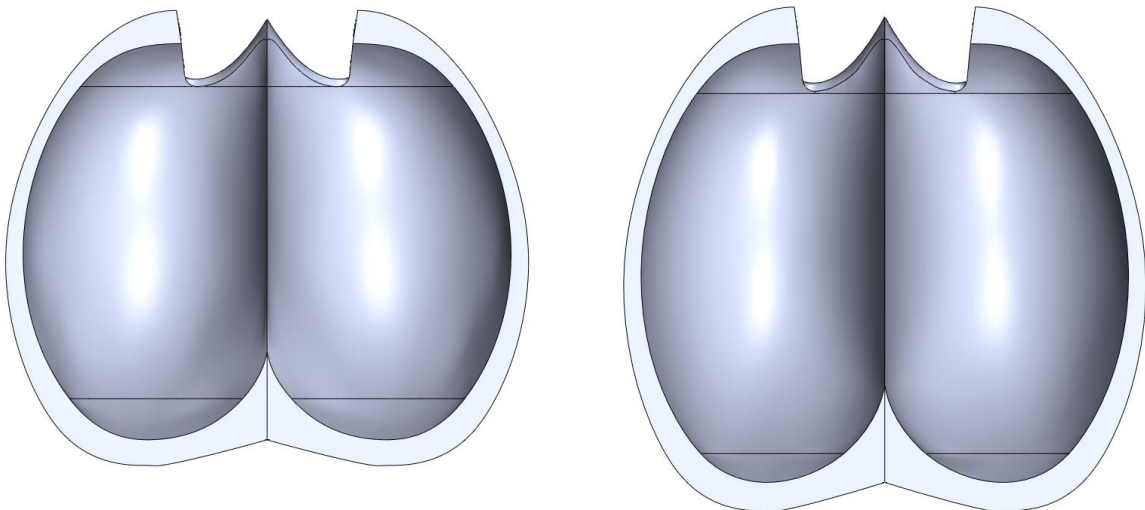


Fig. 4.26. Top view of the bucket geometry before (left) and after (right) the DOE Study 1.

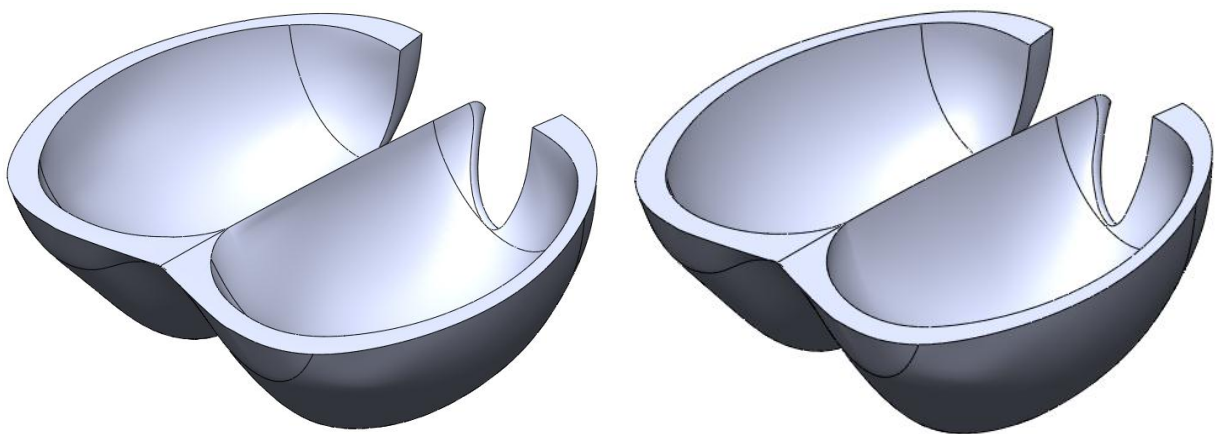


Fig. 4.27. Bucket geometry before (left) and after (right) the DOE Study 1.

Looking at the interaction between the flow that leaves the bucket and the backside of the next bucket it can be seen that the optimum exit angle is such that the exiting flow is sliding on the back of the following bucket as shown in Fig. 4.28. This phenomenon was observed in other designs as well (Perrig 2007, Židonis, Panagiotopoulos et al. 2015).

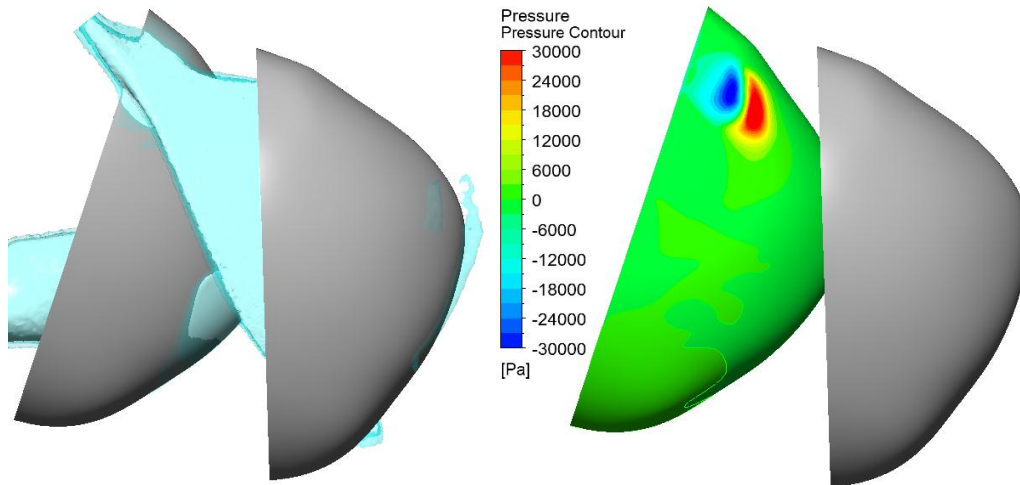


Fig. 4.28. Water exiting the bucket sliding on the back of the following bucket.

4.3.2. P5-P7: DOE Study 2-1 (α , R_t , N_b)

Design limits for these 3 parameters are provided in Table 4.3. The range of investigation for parameters α and R_t was created around the initial design values (confidential data of Gilkes) acquired after the geometry was modified in DOE Study 1 (previous section). For parameter N_b , the number of buckets, it was expected that increasing the number might increase the efficiency as less water particles would be lost during the transition of the jet from one bucket to another. In the original design, the amount of buckets was at its limit in terms of manufacturing because of the complex shaped splitter and the ribs. Now, that the bucket geometry was simplified (sections 4.1.1 and 4.1.3) it was possible to fit more buckets on the runner.

Table 4.3. Design ranges for parameters α , R_t and N_b .

Design Parameter		Lower Limit	Upper Limit
P5	α	2°	12°
P6	R_t/R_p^*	1.30	1.43
P7	N_b	18	20

*radial distance is presented in relation to the pitch circle radius R_p .

The test plan consisted of 11 initial design variations to be analysed plus 4 repetitions of the centre point. As explained before, the purpose of repeating the measurements at the centre point comes from the experimental approach to assess the repeatability. Like in the DOE Study 1, CFD was used hence there was no repeatability error at all. That is why the centre point values were simply copied meaning that only 11 simulation runs were required to complete the test plan. These 11 design points together

with the simulated efficiency normalised to the maximum efficiency of the test plan Eq. (4.2) are provided in Table 4.4 under iteration 1.

Table 4.4. Test plan for parameters α , R_t and N_b .

Iteration	Modification Name	α [°]	R_t/R_p [-]	N_b [-]	η_{norm} [-]
1	b-1	12	1.43009	18	0.942
	b-2	14	1.363574	19	0.970
	b-3	7	1.363574	17	0.991
	b-4	2	1.297059	18	0.985
	b-5	2	1.43009	20	0.939
	b-6	7	1.363574	21	0.982
	b-7	0	1.363574	19	0.976
	b-8	7	1.335638	19	0.993
	b-9	7	1.265796	19	0.956
	b-10	12	1.297059	20	0.968
	b-11	7	1.363574	19	0.987
2	b-12	4.2	1.340959	18	0.995
	b-13	7	1.363574	16	0.995
	b-14	0	1.330316	16	0.988
	b-15	7	1.335638	19	0.993
	b-16	4.94	1.340959	17	0.998
	b-17	4.25	1.339629	16	0.998
	b-18	3.57	1.336968	15	1.000
	b-19	2.9	1.33484	14	0.996
	b-20	5.65	1.342289	18	0.995

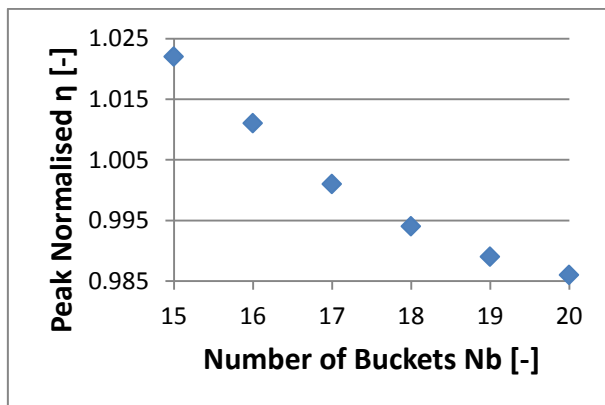


Fig. 4.29. Peak efficiency for different number of buckets N_b (DOE Study 2-1 Iteration 1).

Contrary to the expectations, increasing the amount of buckets has reduced the efficiency. Moreover, the response surface suggested that reducing the number of buckets below the original value would increase the efficiency. In fact the most optimum combination of these 3 parameters was outside of the investigation range for parameter N_b , the number of buckets. The peak efficiency for each number of buckets is presented in Fig. 4.29. A clear drop in the efficiency can be observed within the range of study (18-20 buckets) as the number of buckets is increased. The extrapolated results outside of the

range showed that this increase would persist if the number of buckets was further reduced. Fig. 4.31 provides efficiency contours for each number of buckets to give more details. Clear relationship between these 3 parameters α , R_t and N_b can be observed in the contours suggesting that in order to successfully identify the optimum number of buckets, the inclination angle α and the radial distance R_t should be adjusted as it was done in this study.

Since the predicted efficiency according to the response surface was increasing outside of the range of the study, it was decided to extend the range by including additional points to the original test plan. The additional points are provided in Table 4.4 under iteration 2. It can be seen from Fig. 4.30 that after these additional points were included, it was possible to locate the optimum number of buckets which according to the response surface was 16 or 17 buckets.

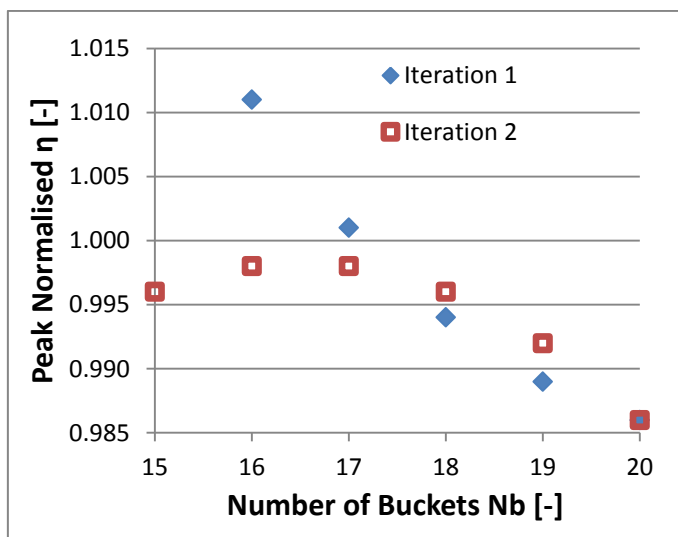


Fig. 4.30. Peak efficiency for different number of buckets N_b (DOE Study 2-1 Iterations 1 and 2).

However, due to this chaotic creation of the test plan where 10 additional points were included far outside of the initial range, the accuracy of such a response surface was not of highest reliability. The highest simulated efficiency was at the design point b-18, where the number of buckets $N_b = 15$ and the normalised efficiency $\eta_{norm} = 1$, which was 0.4 % higher than the predicted peak efficiency at $N_b = 15$. Therefore it was decided to perform a new study of these 3 parameters α , R_t and N_b with the ranges refined around the peak area. This new DOE Study 2-2 is presented in the following section.

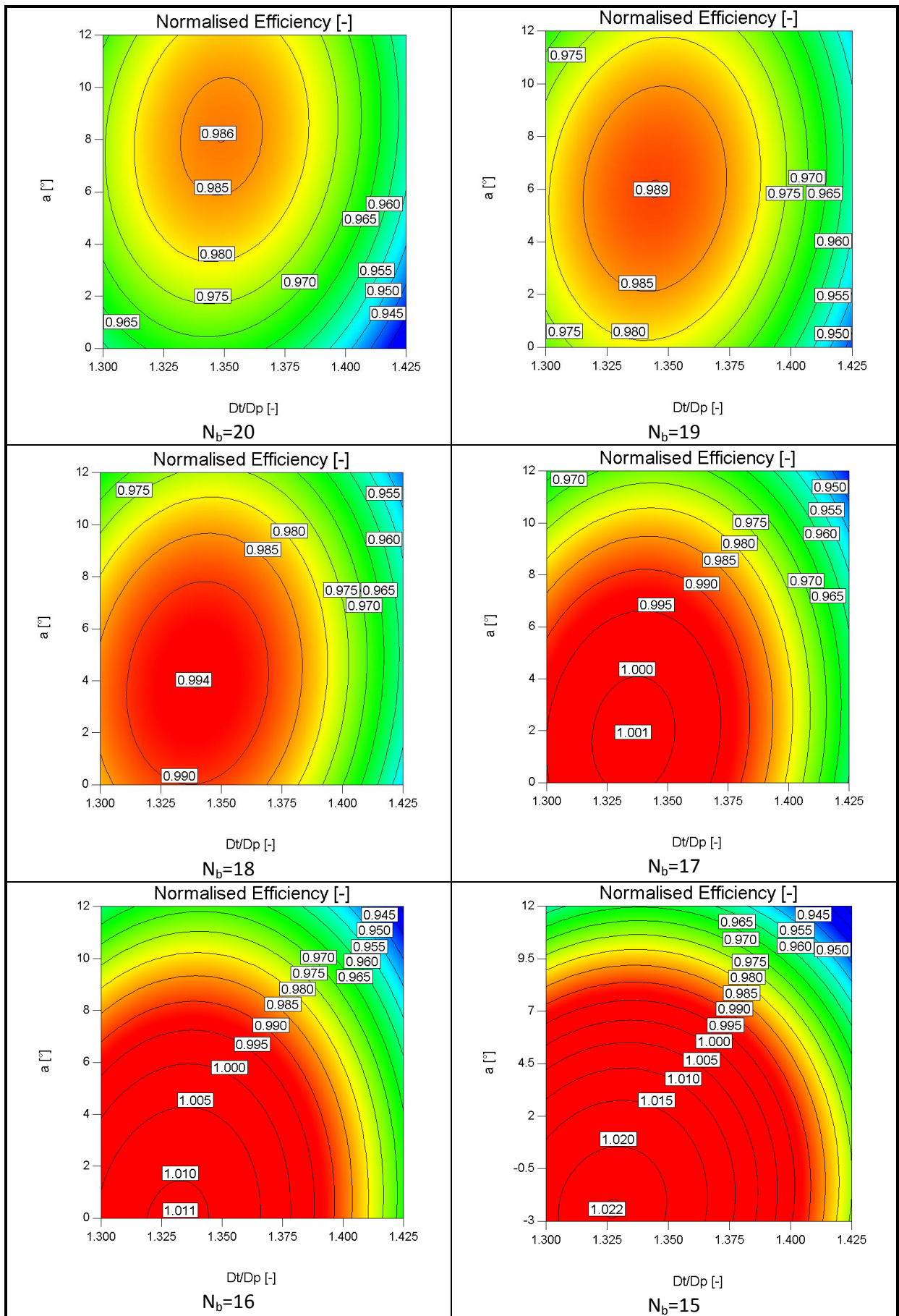


Fig. 4.31. Normalised efficiency contours for different N_b (DOE Study 2-1 Iteration 1).

4.3.3. P5-P7: DOE Study 2-2 (α , R_t , N_b)

Not only the number of buckets provided by the DOE Study 2-1 response surface to achieve the best efficiency was unexpected, but also it was in disagreement with industrial experience and most of the suggestions found in the available literature. Table 4.5 provides suggestions on the number of buckets calculated using the dimensions of the runner and bucket used in this research with more details published in a paper concentrating on identifying the optimum number of buckets (Židonis and Aggidis 2015a). It is important to note, that the bucket shape used in that paper is of later modification stage therefore the optimum N_b presented in that paper might be different to the results of DOE Study 2-1 or DOE Study 2-2. Nevertheless, the main dimensions like the jet or pitch circle diameter were identical therefore suggestions provided in Table 4.5 are applicable at this stage as well.

Table 4.5. Suggestions on the amount of buckets found in the available literature.

Author	Suggested N_b
M. Nechleba (1957)	18 to 21
M. Eisenring (1991)	17
I. U. Atthanayake (2009)	26
B. A. Nasir (2013)	18

Only Eisenring suggested smaller amount of buckets than in the original design which had 18 buckets. However, the number suggested by him, $N_b = 17$, was still higher than found in the DOE Study 2-1. Moreover, the optimum performance values from the DOE Study 2-1 were outside of the initial investigation range of the study and raised some doubts about the accuracy of the response surface. Therefore, to have more confidence in the results provided by the DOE Study 2-1 it was decided to repeat the DOE study of parameters α , R_t and N_b in the new range presented in Table 4.6. The study was refined around the optimum design values suggested in DOE Study 2-1.

Table 4.6. Design ranges for parameters α , R_t and N_b .

Design Parameter		Lower Limit	Upper Limit
P5	α	2°	7°
P6	R_t/R_p^*	1.317	1357
P7	N_b	15	17

*radial distance is presented in relation to the pitch circle radius R_p .

The test plan is presented in Table 4.7. Very similar procedure to DOE Study 2-1 Iteration 1 was used. 11 design points c-1 to c-11 were investigated to create the initial response surface. Using this surface, 4 new design points c-12 to c-15 were added to the test plan. These new points were selected by choosing the optimum combination of the parameters α and R_t for each number of buckets N_b from 15 to 18 based on the response surface from iteration 1. Comparison of the simulated performance and the predicted performance is provided in Fig. 4.32-A. Since the disagreement between the simulated and predicted efficiencies was substantial it was decided to run more iterations until the predicted and

simulated results achieve agreement. Therefore using the response surface acquired after the iteration 2 more design points c-16 to c-19 were added to the test plan. This time the predicted and simulated results were in much better agreement as can be seen in Fig. 4.32-B.

After including the design points of iteration 3 and their simulated performance results into the test plan, the response surface remained almost unchanged and the predicted peak efficiencies with and without design points c-16 to c-19 (iteration 3) were within 0.1 % as shown in Fig. 4.33.

Table 4.7. Test plan for parameters α , R_t and N_b .

Iteration	Modification Name	α [°]	R_t/R_p [-]	N_b [-]	η_{norm} [-]
1	c-1	7.0	1.317	17	0.989
	c-2	2.0	1.317	15	0.994
	c-3	7.0	1.357	15	0.995
	c-4	4.5	1.309	16	0.988
	c-5	4.5	1.365	16	0.997
	c-6	4.5	1.337	14	0.994
	c-7	1.0	1.337	16	0.995
	c-8	4.5	1.337	16	0.998
	c-9	4.5	1.337	18	0.996
	c-10	2.0	1.357	17	0.989
	c-11	8.0	1.337	16	0.992
2	c-12	3.5	1.348	15	0.999
	c-13	5.1	1.350	16	0.999
	c-14	6.7	1.353	17	0.995
	c-15	8.3	1.356	18	0.992
3	c-16	3.6	1.350	15	1.000
	c-17	4.2	1.345	16	0.998
	c-18	4.8	1.340	17	0.997
	c-19	5.3	1.334	18	0.994

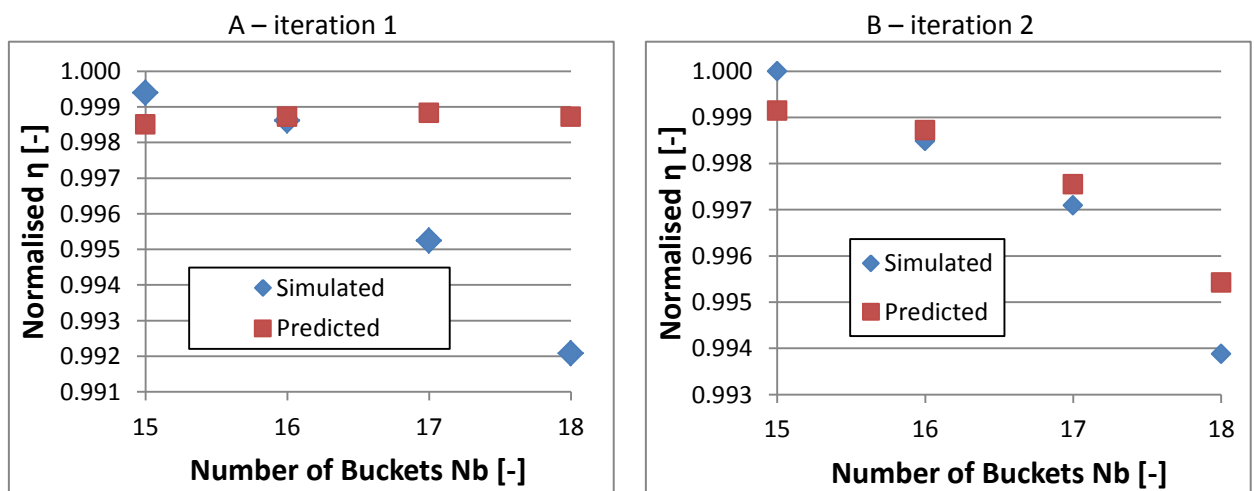


Fig. 4.32. Comparison of the predicted peak efficiency and the simulated result for different number of buckets N_b . A: DOE Study 2-2 Iteration 1, B: DOE Study 2-2 Iteration 2.

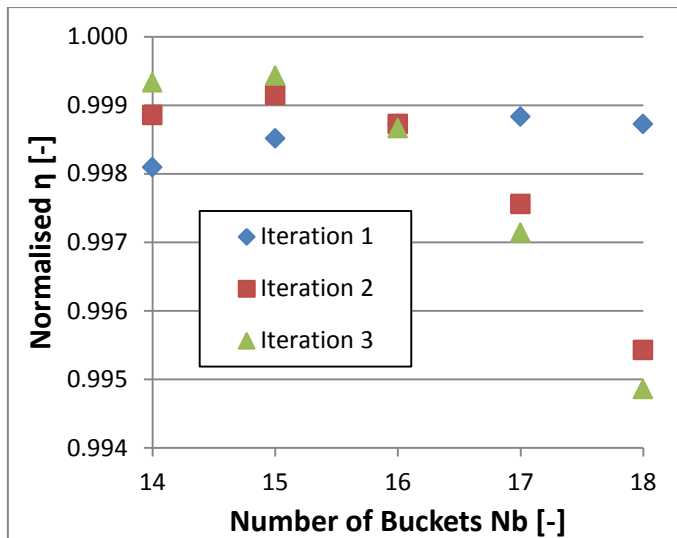


Fig. 4.33. Peak efficiency for different number of buckets N_b (DOE Study 2-2 Iterations 1, 2 and 3).

The repeated study of the bucket positioning parameters α , R_t and N_b also suggested that the same drastic reduction in the number of buckets from $N_b = 18$ to $N_b = 15$ while adjusting the positioning parameters α and R_t would increase the efficiency. The guidelines on the optimum number of buckets found in the available literature disagree among themselves and also do not provide any experimental testing or numerical modelling data on which these guidelines are based (Židonis and Aggidis 2015a). Moreover, those theoretical calculations disregard the fact that for each number of buckets different combination of α and R_t are required to find the optimum. Fig. 4.34 shows α vs R_t efficiency contour plots for different N_b where the combination of α and R_t for the peak efficiency is clearly dependent on the N_b . Taking into account the limitations of the available guidance, a decision was made to trust the results of DOE Study 2-2 and reduce the number of buckets to 15. Design point c-16 was taken for further optimisation as the output of this study since it provided highest simulated efficiency and was very close to the predicted by the response surface.

Fine mesh simulation was performed to verify the improvement in the efficiency achieved during the DOE study 2. Even though the performance was improved by only 0.1 % of the initial efficiency as shown in Fig. 4.60, the design was simplified by reducing the amount of buckets from 18 to 15. Therefore the achievement of this study could be summarised as design simplification while maintaining the same efficiency. The cross-section views at the symmetry plane of the original runner design, the design after the DOE Study 1 and the design after DOE study 2 are provided in Fig. 4.35.

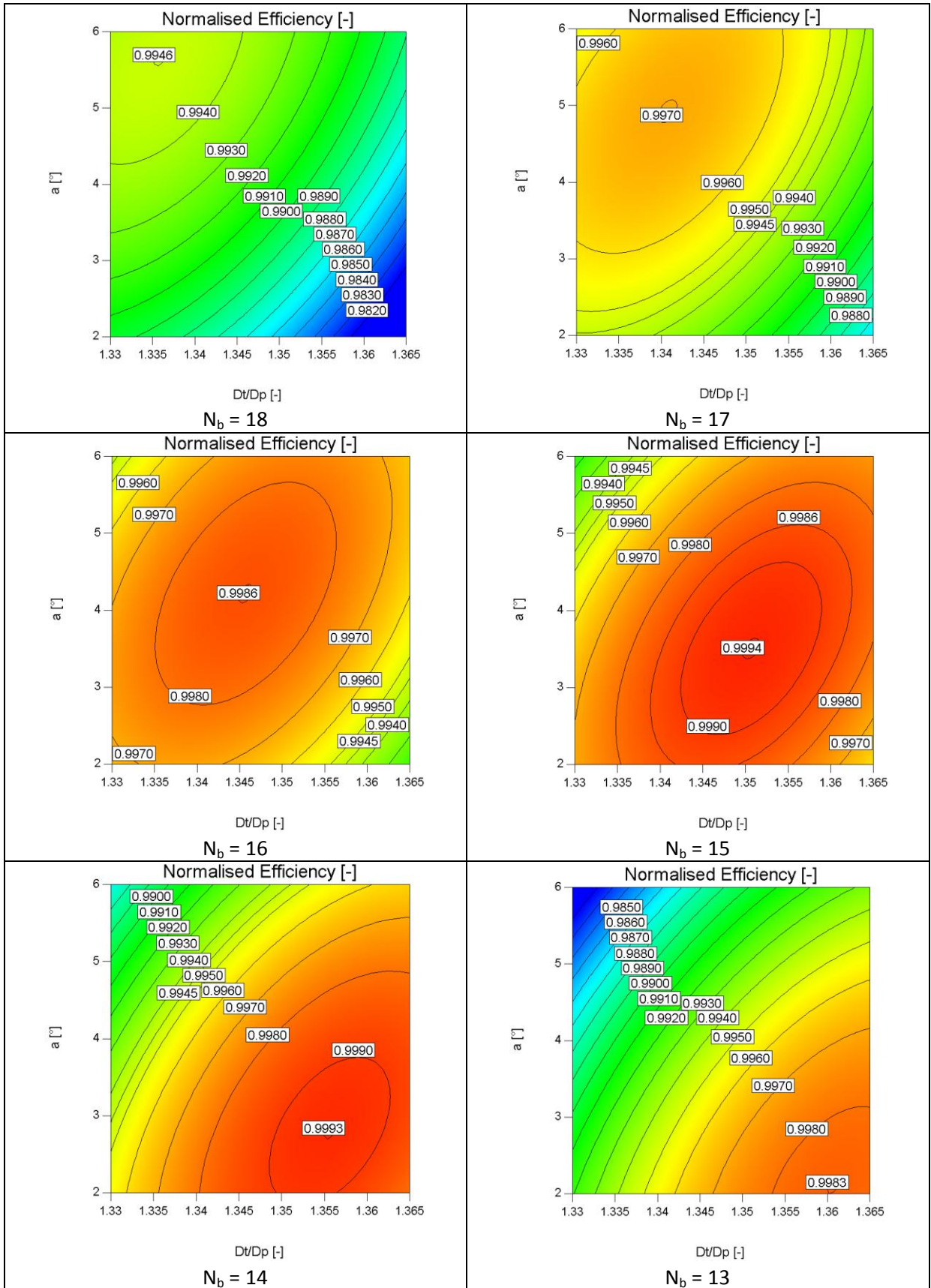


Fig. 4.34. Normalised efficiency contours for different N_b (DOE Study 2-2 Iteration 3).

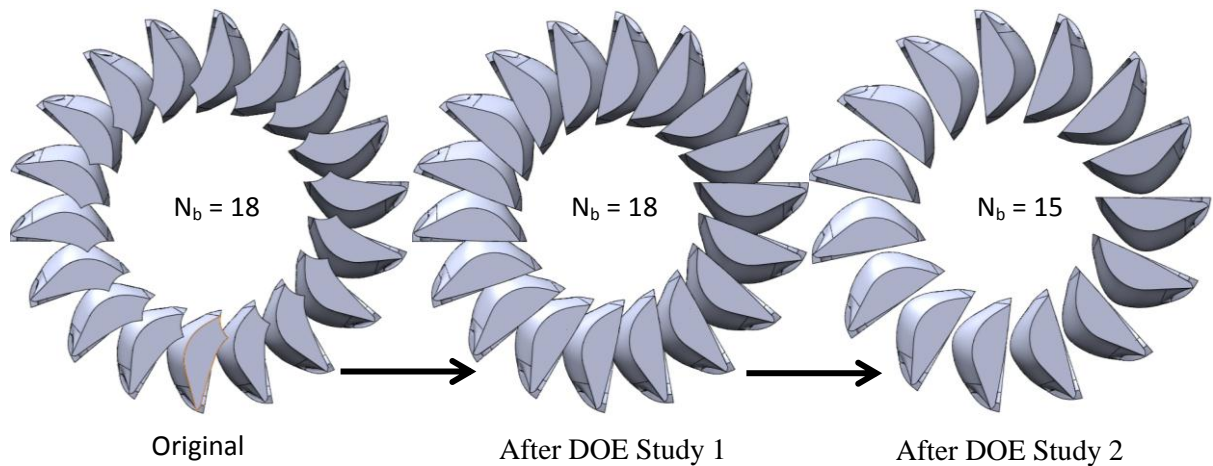


Fig. 4.35. Peak efficiency for different number of buckets N_b (DOE Study 2-2 Iterations 1, 2 and 3).

Every time the jet enters a bucket some unwanted disturbance is caused to the jet suggesting that fewer buckets would reduce these disturbances. On the other hand there is a natural concern to ensure that no water particles are lost during the transition from one bucket to another when the number of buckets is reduced. However, looking at the CFD results it seems that much less than 18 buckets were required for that. Flow behaviour inside two consecutive buckets of interest in a runner with 15 buckets is shown in Fig. 4.36 at two different time selections: when the jet has just been cut off from the first bucket by the consecutive bucket and when the last water particles have reached the first bucket. It can be seen that no water particles were lost in this runner with $N_b = 15$. Even in a runner with as low as 12 buckets (Fig. 4.37) no water particles were lost by failing to hit the bucket during the transition. Some amount of the flow was lost through the cutout but this problem can be solved by modifying the cutout shape which was done later in the optimisation procedure.

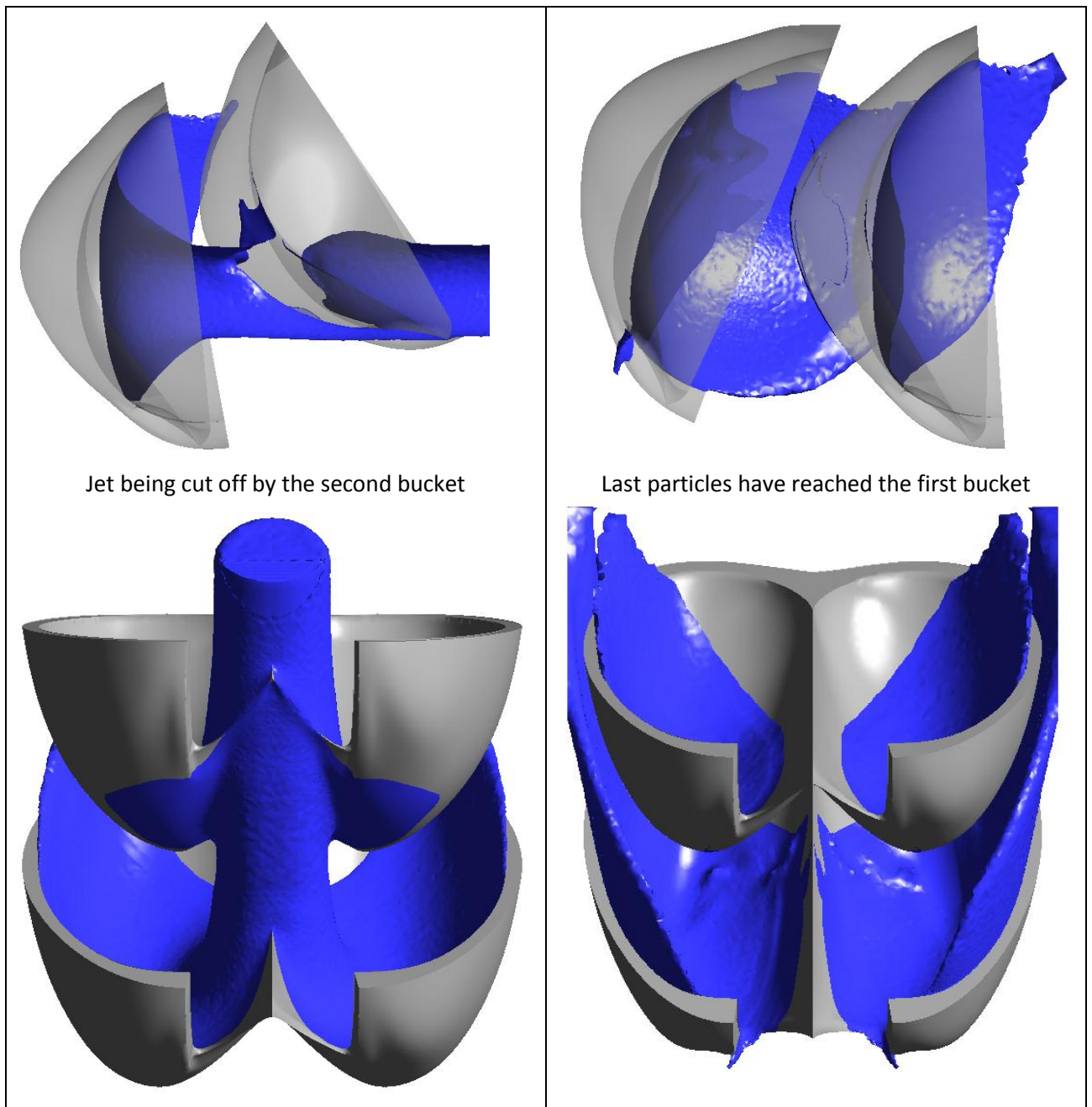


Fig. 4.36. Various views of flow behaviour inside two buckets of interest showing that no water particles were lost in the runner with 15 buckets.

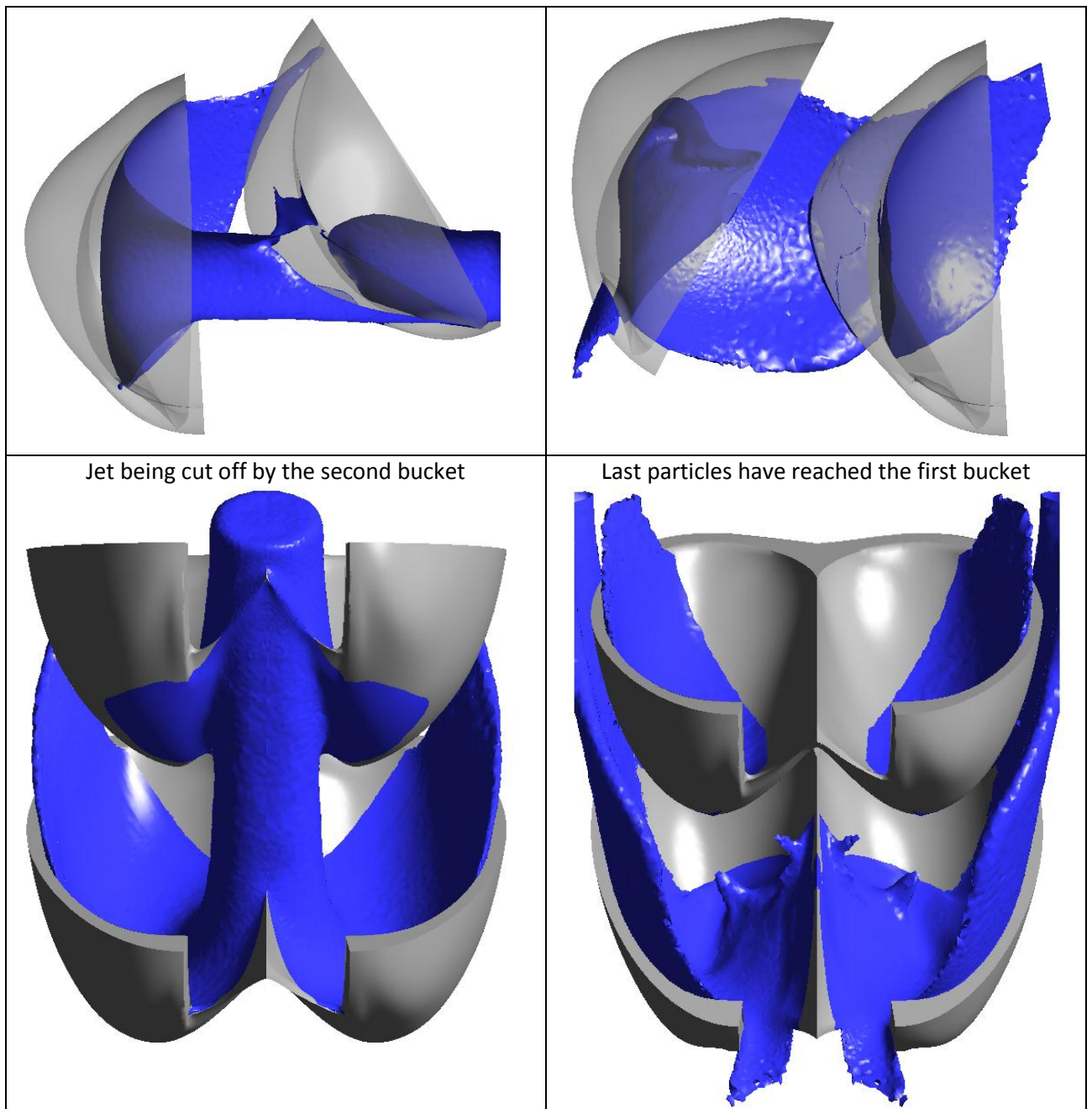


Fig. 4.37. Various views of flow behaviour inside two buckets of interest showing that no water particles are lost in the runner with only 12 buckets.

4.4. Analytical Optimisation

Analytical optimisation was performed after the first 7 parameters were optimised in two groups using the design of experiments technique as described in the previous section. The rest 5 design parameters were modified analytically by observing the flow behaviour and trying to lead the water in more efficient way.

- 1) First of all, readjusting of parameter P3, the bucket exit angle (β_e), was investigated assuming that smaller exit angle can be used since the spacing between the buckets was increased.
- 2) Parameter P10, the backside of the splitter, was modified aiming to reduce the counter torque caused when the bucket is cutting into the jet.
- 3) Modifying parameter P11, the cutout shape, to reduce the amount of the flow that leaves through the cutout with high velocity without being utilised.
- 4) Further modifying the cutout shape P11 together with the splitter tip geometry P12.

Similar to the Design of Experiments optimisation presented previously, coarse mesh simulations were used for performance evaluation and the output geometries from this study were verified using the fine mesh simulations. Based on previous studies of having low impact on the efficiency (Židonis, Panagiotopoulos et al. 2015) and the time constraints of the whole PhD research, parameters P8 and P9 were modified only as a result of other modifications without examining closely their effect on performance.

4.4.1. P3: Exit Angle β_e

The exit angle was to be readjusted after it was decided to reduce the number of buckets in the DOE Study 2. It was anticipated that the angle can be reduced from its initial value. 5 simulations were performed to investigate the efficiency response to the exit angles in steps of 2° and then the step was refined to 1° around the peak efficiency. These simulations showed that even though the number of buckets was reduced the optimum exit angle remained unchanged as presented in Fig. 4.38. No verification by fine mesh simulation was required since the design was not changed and the initial exit angle was retained.

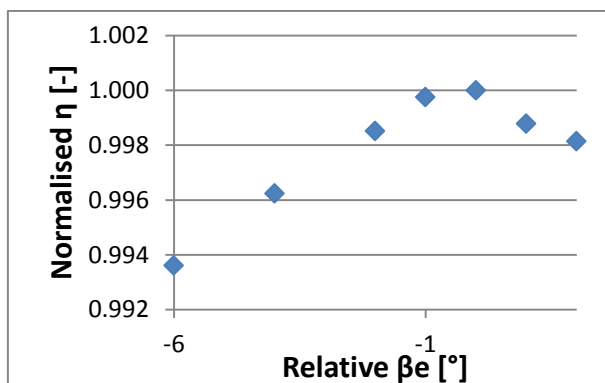


Fig. 4.38. Normalised runner efficiency η vs. the relative exit angle β_e .

4.4.2. P10: Backside of the Splitter

Next step was to modify the backside of the splitter (P10) to reduce the counter-torque and utilise more energy on the inside of the bucket. Even though the overall efficiency was improved during the Design of Experiments Optimisation stage, the counter-torque has increased. Moreover, large amount of energy was being utilised on the backside of the bucket rather than on the inside (Fig. 4.39) compared to the torque curves of the original design (Fig. 3.19). Therefore 7 design modifications described in Table 4.8 were made to investigate the efficiency response. The images of these modifications are provided in Fig. 4.40 and Fig. 4.41.

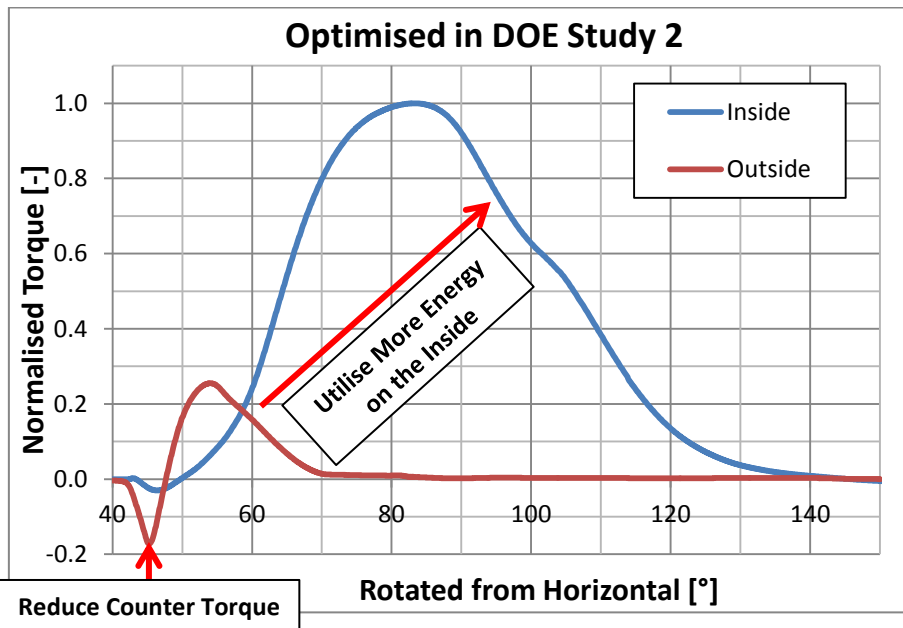


Fig. 4.39. Normalised torque curves of a runner after the DOE Study 2 (modification c-16).

Table 4.8. Design modifications of the backside of the splitter geometry. Efficiency normalised to the latest modification c-16.

Iteration	Modification Name	Description	η_{norm} [-]
1	d-1	Cutout edge modified	0.998
	d-2	Curved backside of the splitter	0.976
	d-3	Straight backside edge of the splitter moved in by 5° rotating it around the splitter tip	1.002
	d-4	Straight backside edge of the splitter moved out by 5° rotating it around the splitter tip	0.978
2	d-5	Straight backside edge of the splitter moved in by 10° rotating it around the splitter tip	1.003
3	d-6	Curved backside edge of the splitter moved in by 10° rotating it around the splitter tip	0.998
	d-7	Straight backside edge of the splitter moved in by 10° rotating it around the splitter tip and the splitter edge modified	1.001

3 out of these 7 modifications have improved the efficiency as well as reduced the counter torque and shifted a noticeable amount of positive torque to be utilised on the bucket inside. Modification d-5 was the one with the highest efficiency and predicted an improvement of 0.26 % (using coarse mesh) compared to the initial c-16.

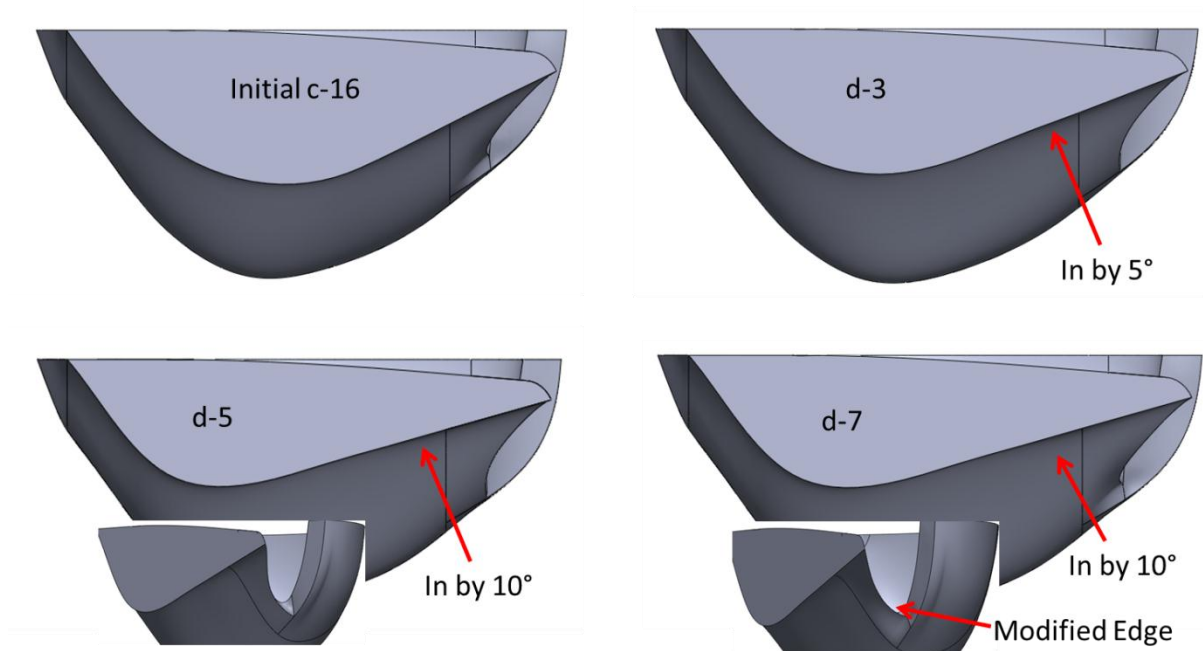


Fig. 4.40. Backside of the splitter modifications that have improved the efficiency.

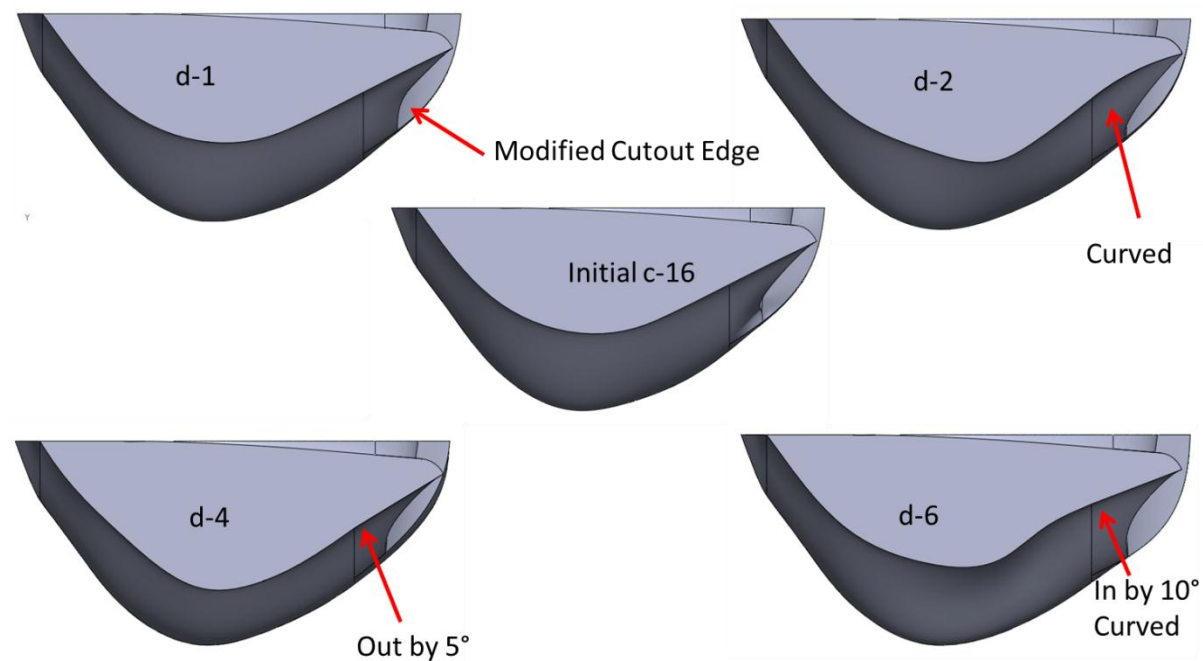


Fig. 4.41. Backside of the splitter modifications that have reduced the efficiency.

However, this modification d-5 made the geometry to be very thin at few regions. Therefore, the original minimum thickness was restored by adding some material on the inside of the splitter. Based

on the parametric study of two Pelton designs (Židonis, Panagiotopoulos et al. 2015) it was assumed that slightly modifying the inside will have minor effect on the efficiency. The material was added by keeping the splitter inlet angle constant and reducing the tangency value as shown in Fig. 4.42.

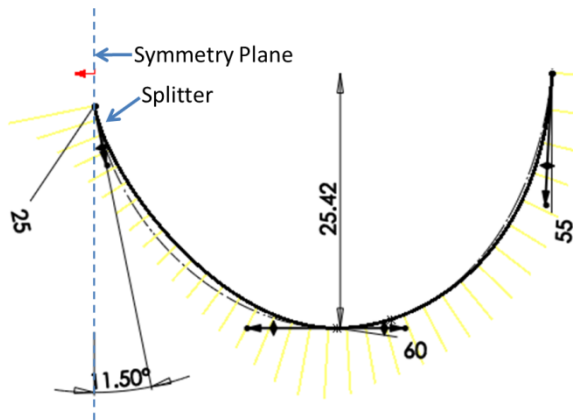


Fig. 4.42. Bucket shape control curve (dashed line: before the modification, solid line: modified)

The efficiency of this corrected geometry d-5.1 with restored thickness was 0.15 % (coarse mesh) higher than the initial c-16 and what is more important the counter-torque was reduced noticeably and most of the energy was utilised on the inside of the bucket (Fig. 4.43).

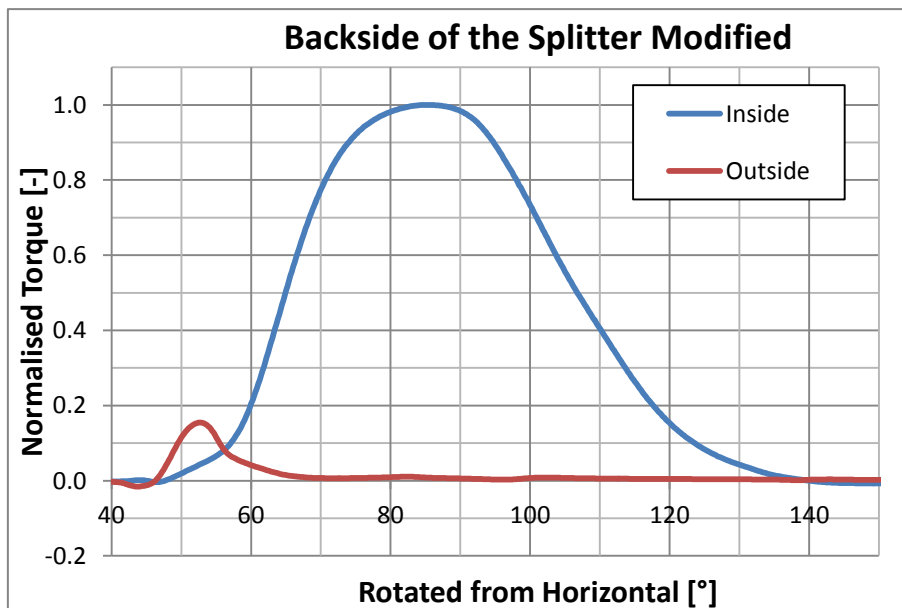


Fig. 4.43. Normalised torque curves of a runner after the backside of the splitter was modified and the thickness restored (modification d-5.1).

Fine mesh simulation was performed to verify the improvement in the efficiency achieved by modifying the backside of the splitter (P10). The performance was improved by 0.7 % of the initial efficiency as shown in Fig. 4.60.

4.4.3. P11: Cutout Shape

The next modification performed in this analytical optimisation stage was the shape of the cutout (P11). The cutout shape was modified to reduce the amount of flow leaving with high velocity through the cutout as presented in Fig. 4.44. Not only the available energy was lost through this cutout but also the water particles with high velocity caused unwanted splashing. Fig. 4.45 provides a comparison of the cutout shape before (d-5.1) and after (e-0) this modification. According to the coarse mesh simulation results this modification of the cutout has improved the efficiency by 0.4 %. However, modifying the cutout to further reduce the escaping flow was very difficult due to the complex geometry and the need for the cutout face to blend into the thick wall of the bucket.

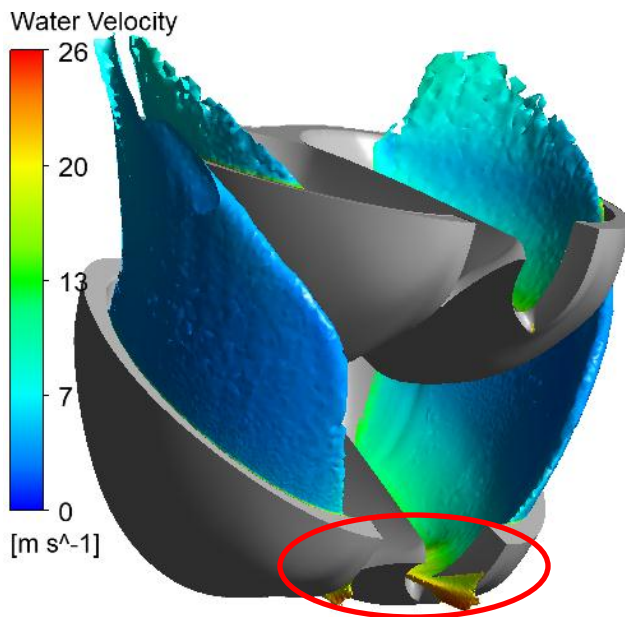


Fig. 4.44. Flow leaving through the cutout with high velocity

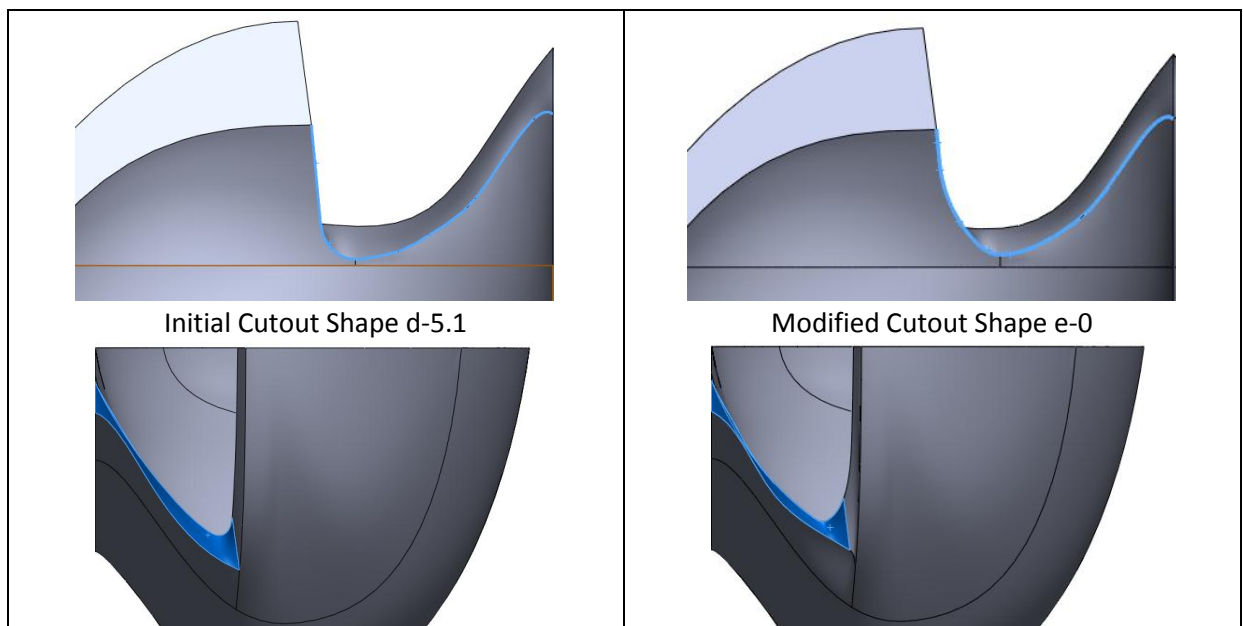


Fig. 4.45. Cutout shape modification.

Fine mesh simulation was performed to verify the improvement in efficiency achieved by modifying the cutout shape (P11). The performance was improved by 0.3 % of the initial efficiency as shown in Fig. 4.60. It shows that fairly large amount of energy was lost through the cutout. However, some amount of water was still leaving through the cutout even after its geometry was modified. There were 2 main difficulties in modifying it further to stop the water from leaving through the cutout:

- 1) complex geometry conditions where the cutout surface had to connect the inside and the outside surfaces of the bucket and also blend into the thick wall of the bucket,
- 2) not to cause negative disturbances on the flow when the jet is entering the bucket.

Therefore a question was raised if such a thick bucket wall is required in this region which does not add any strength when the bucket is fully loaded. The structural Finite Element Analysis (FEA) and further optimisation is presented in the following section.

4.4.4. P11-P12: Splitter Tip and Cutout Shape

As explained in the previous section more resource in efficiency improvement by diverting the flow from the cutout was identified. However, reducing the amount of this unutilised flow was difficult due to the complex geometry where the cutout face had to connect the inside and outside faces of the bucket and also blend into the thick wall at the side. Moreover, the shape of the cutout had to be modified in such way that it stops the unwanted leakage of the flow at the end of bucket's duty cycle but does not cause any negative effect at the beginning of this duty cycle as the jet is entering the bucket. Looking at the original shape of the cutout (Fig. 4.46) it seems as if the cutout was designed by almost literally cutting out a piece of material from the closed bucket. Afterwards, when the reinforcing ribs were removed (section 4.1.1), the wall thickness was increased uniformly. However, the region where the cutout joined this wall remained almost unchanged. This inherited arrangement was the reason for complex geometry surface highlighted in blue in Fig. 4.47. Therefore it was decided to perform the structural Finite Element Analysis (FEA) to investigate if some of the material could be removed without reducing the strength of the bucket.

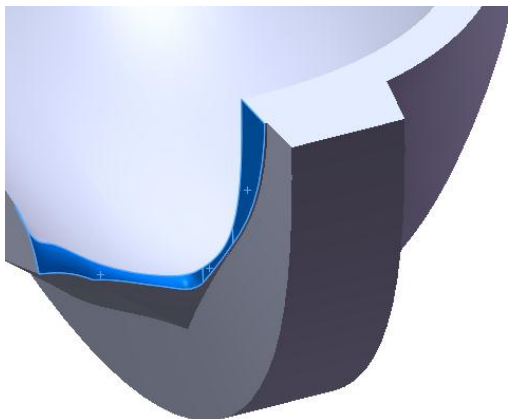


Fig. 4.46. Cutout in the original bucket design (face of the cut highlighted in blue).

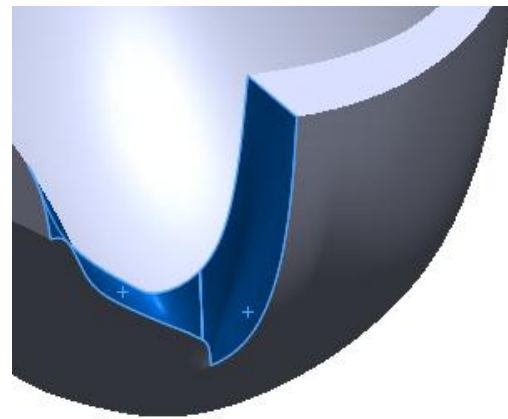


Fig. 4.47. Cutout in the modification e-0 (face of the cut highlighted in blue).

Assumption was made that in terms of the stress, cutout region is the most affected by the centrifugal forces present at the runaway speed whereas the jet loading is affecting the root of the bucket or the splitter edge. Therefore at this stage only runaway conditions were analysed using FEA. More detailed structural analysis that considered other loading conditions was performed at the final optimisation stage and is presented in section 4.5.1.

Stress contours in the original and the so far modified (e-0) bucket designs under the runaway conditions are presented in Fig. 4.48. The stress probes in the stress concentration region at the cutout show that the modified design has reduced the maximum value. Moreover it was identified that this stress concentration was caused by having this thick piece of material which was trying to ‘unpeel’ due to inertia at the runaway conditions (Fig. 4.49). Therefore reducing the thickness of that wall would increase the strength of the bucket as well as simplify the geometry and allow more flexibility for modifications.

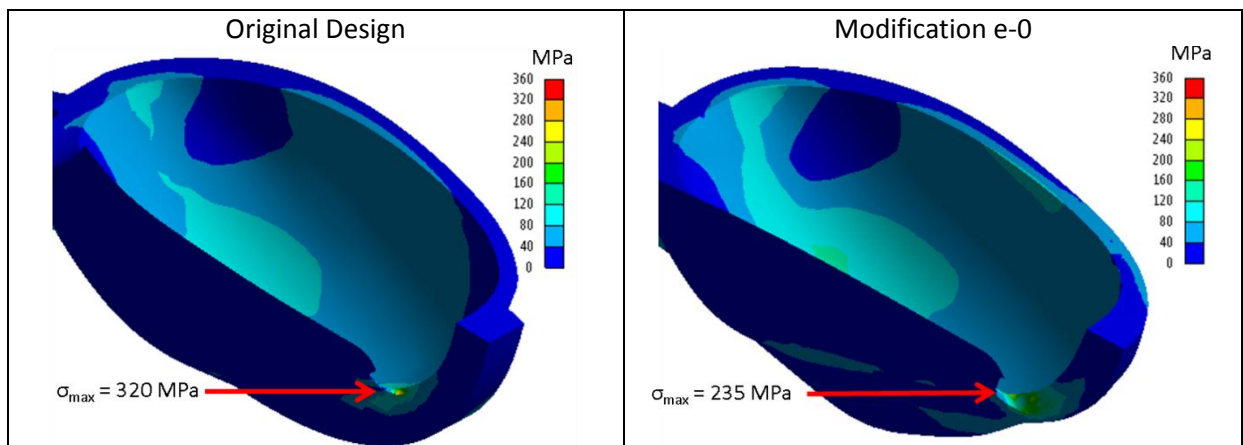


Fig. 4.48. Equivalent (Von-Mises) stress contours for the original (left) and e-0 (right) bucket design under runaway conditions.

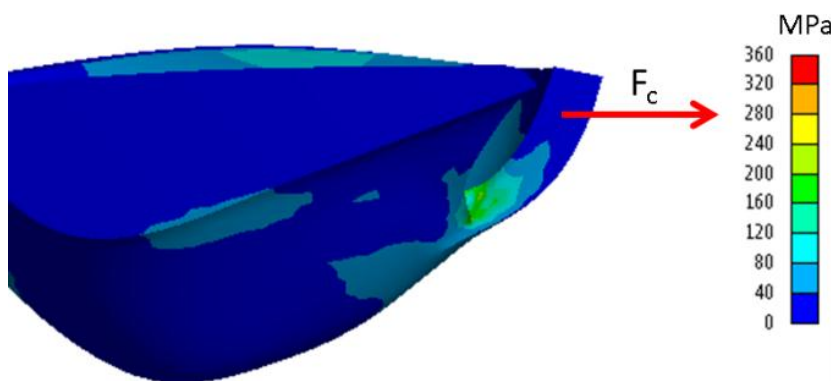


Fig. 4.49. Stress concentration at the cutout caused by the inertial force F_c of the thick bucket wall. Modification e-0.

Based on these FEA results few bucket modifications were made with reduced amount of material to reduce the inertial force. Quick FEA analysis at runaway conditions was performed to check if the maximum stress is acceptable (i.e. lower than in the original design) before passing that design to the

coarse mesh CFD analysis. Modifications that passed the FEA check are provided in Table 4.9. At first 3 initial modifications e-1, e-2 and e-3 were made to analyse the efficiency response. These initial modifications are presented in Fig. 4.50.

Table 4.9. FEA approved design modifications around the cutout.

Modification Name	Based on	Description	η_{norm} [-]
e-0	n/a	n/a	0.995
e-1	e-0	Material that was causing the bucket to 'unpeel' at runaway removed. Inside and outside surfaces blend into an edge.	0.996
e-2	e-0	Material that was causing the bucket to 'unpeel' at runaway removed. Inside and outside surfaces blend into a narrow face.	0.996
e-3	e-0	Material that was causing the bucket to 'unpeel' at runaway removed. Transition face between inside and outside surfaces removed. Splitter tip shortened.	0.998
e-4	e-3	Shallower cutout.	0.996
e-5	e-3	Splitter tip further shortened and backside splitter edge curved back.	0.996
e-6	e-3	Splitter tip further shortened and backside splitter edge kept straight.	0.992
e-7	e-6	Shallower cutout.	0.995
e-8	e-6	Different cutout shape at the splitter tip region.	0.991
e-9	e-3	Extremely curved splitter edge.	0.996
e-10	e-3	Thickened outside wall.	0.999
e-11	e-10	Straight splitter edge.	1.000

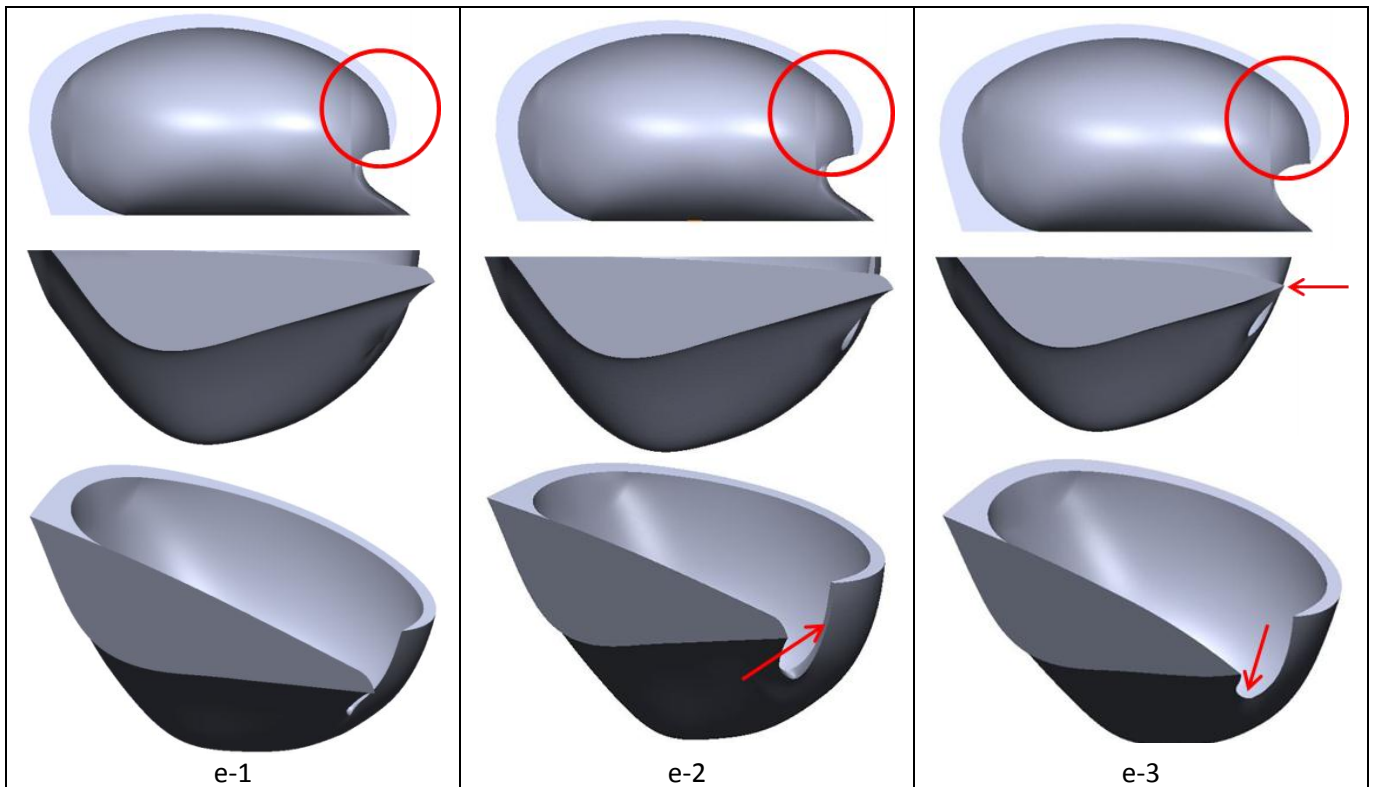


Fig. 4.50. Three initial FEA approved modifications of the cutout and the splitter tip.

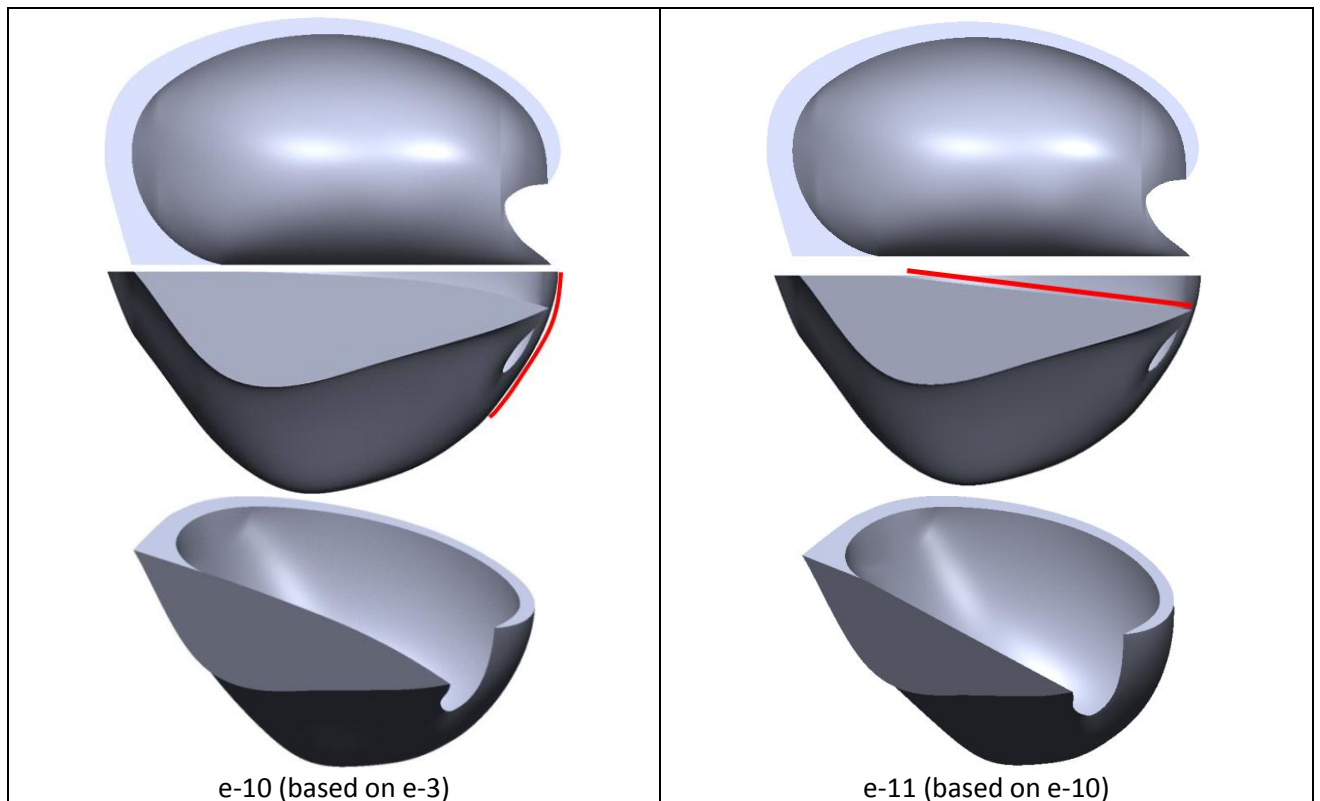


Fig. 4.51. Two final FEA approved modifications of the cutout and the splitter tip. Modified regions highlighted in red.

Modification e-3 was taken as the base for further modifications not only because it showed the best improvement in the efficiency but also because it was the most sound from the designing point of view. Modifications e-1 and e-2 had the splitter tip sticking outside since the wall thickness was reduced. Out of all further modifications only two e-10 and e-11 showed further improvement in efficiency from e-3. Thus e-10 and e-11 provided in Fig. 4.51 were taken for further development.

4.5. Finalising

All 12 design parameters described in section 4.2 were evaluated. 7 of them (P1-P7) were modified using parametric design of experiments approach, 3 (P10-P12) were modified analytically and 2 (P8-P9) were modified only as a result of other modifications without examining closely their effect on performance. This latter decision was made due to the time constraints of the whole PhD research project and previous studies showing low impact on the efficiency. All modifications were made from the hydraulic design point of view based on CFD results without performing any structural analysis (with an exception of FEA at runaway conditions performed for parameters P11-P12 and presented in section 4.4.4). Therefore going towards the end of design modification phase it was decided to perform detailed Finite Element Analysis (FEA) since the bucket shape was changed significantly compared to the original design. This analysis and required structural modifications are described in the following section 4.5.1. After final modifications on the bucket shape were made it was decided to readjust its positioning parameters by performing DOE Study 3 (α , R_t) provided in section 4.5.2.

4.5.1. Structural Analysis

Operating conditions of interest for the structural analysis were identified:

- 1) Runaway speed – when there is no load on the shaft and flow rate is at its maximum. At these conditions runner is rotating at its maximum speed and therefore almost no jet force is present. However, the centrifugal forces are at their maximum.
- 2) Normal running – jet induced force on the bucket at the peak torque from the nominal operating point.
- 3) Jet entering the bucket - jet induced force at the nominal operating point on the bucket as it is entering the bucket and all the force is concentrated around the splitter tip.

Before performing the FEA analysis at all the 3 operating conditions which would include running CFD simulations and coupling them to the FEA analysis for points 2) and 3) it was decided to do a visual comparison between the original design and modifications e-10 and e-11. Few potentially weak locations were identified where the thickness of the modified design was noticeably lower compared to the original as presented in Fig. 4.52 and Fig. 4.53. Therefore some thickness was added to e-10 and e-11 making them e-10.1 and e-11.1. As expected this increase in thickness caused a slight trade off with the efficiency. Coarse mesh predicted reduction was 0.08 % and 0.15 % respectively.

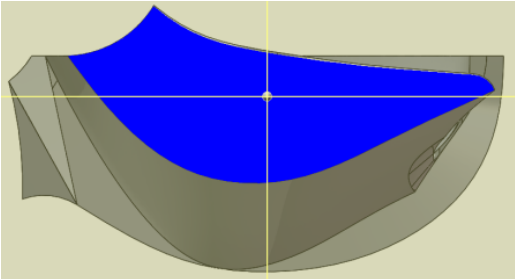
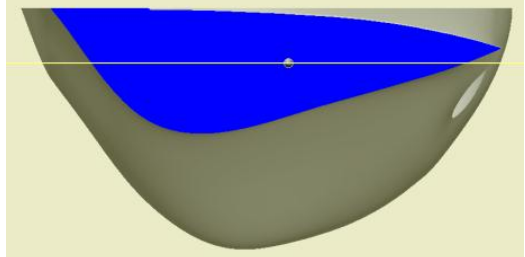
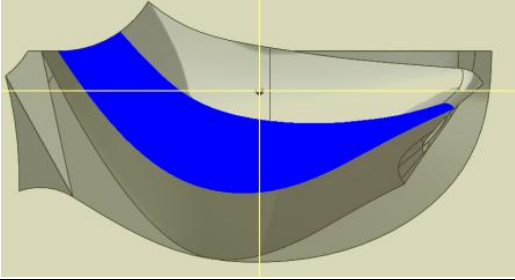
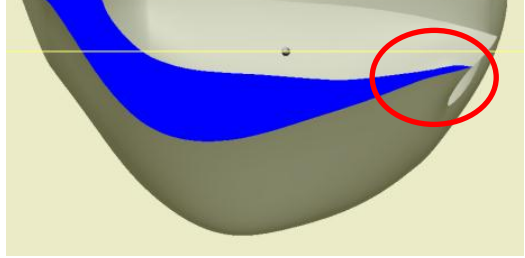
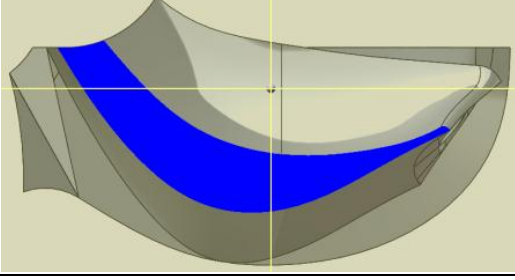
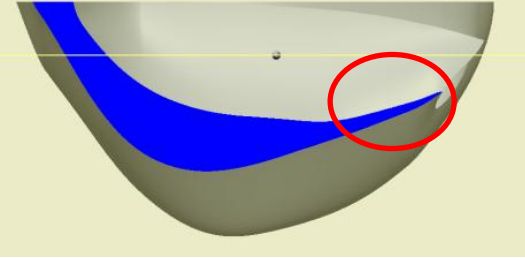
s [mm]	Original Design	Modification e-10
0		
5		
10		

Fig. 4.52. Thickness comparison of the original and modification e-10 designs at 3 different cross-section locations expressed as distance s from the symmetry plane.

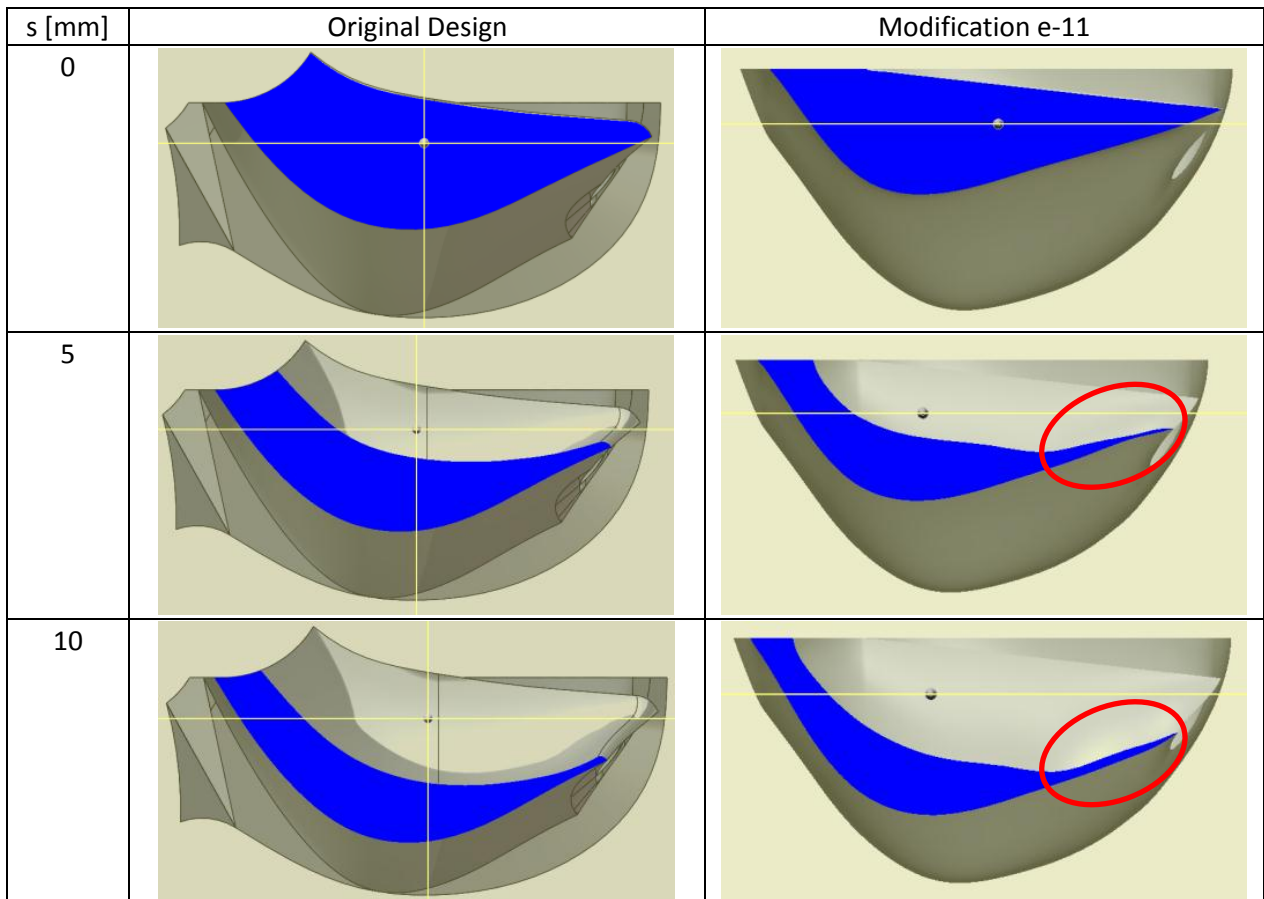


Fig. 4.53. Thickness comparison of the original and modification e-11 designs at 3 different cross-section locations expressed as distance s from the symmetry plane.

Complete FEA analysis was performed on the original design and modifications e-10.1 and e-11.1. The details for nominal and runaway operating conditions are provided in Table 4.10. These conditions were supplied by Gilkes based on the requirements for their product. Fig. 4.54 presents the FEA results under the nominal operating conditions at different rotating angles. This figure represents the peak torque at the cutout edge (on the left hand side) and the splitter edge (on the right hand side) as the jet is entering the bucket and until the peak torque is reached.

Table 4.10. Operating conditions for FEA analysis.

	H	750	m
	D_p	415	mm
	N_i	1	
	B	118	mm
Nominal	n₁₁	40	rpm
	Q_{11k}	310	l/s
	n	2640	rpm
	Q	118.4	l/s
	d	36.3	mm
Runaway	n₁₁	70	rpm
	n	4619	rpm

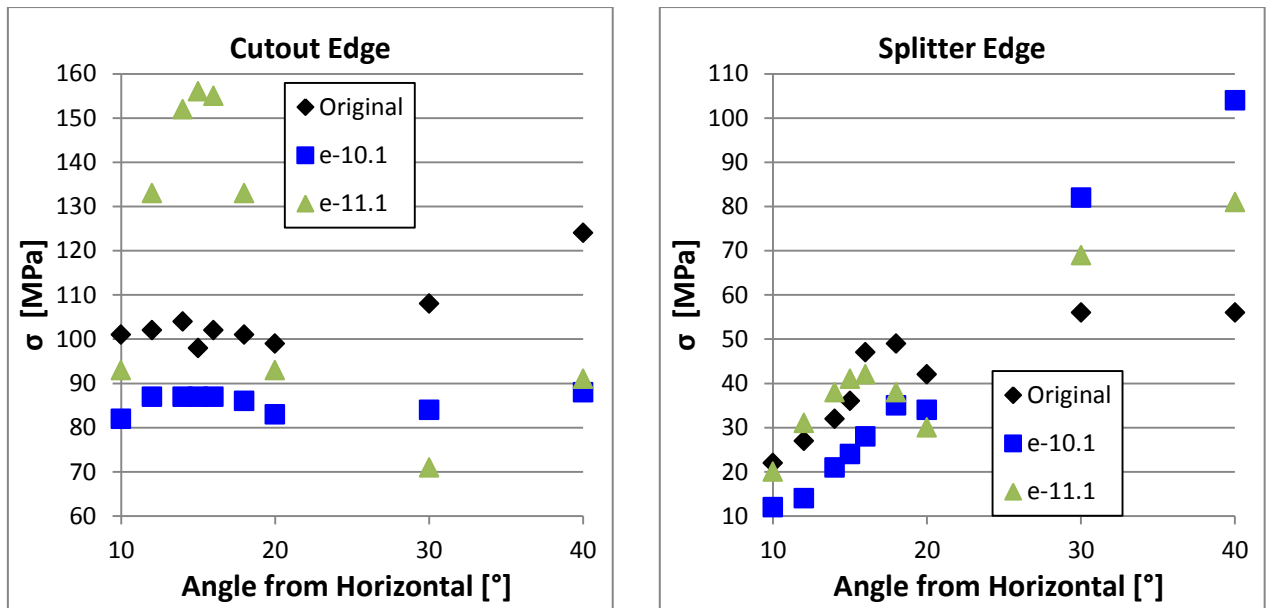


Fig. 4.54. FEA results at various bucket angular positions under the nominal operating conditions. Left: peak stress at the cutout edge, right: peak stress at the splitter edge.

The stress at the cutout edge of e-10.1 was lower than in the original bucket for all angular positions analysed. The stress at the splitter edge of bucket modification e-10.1 has reached higher values than in the original design. However, it was still lower than the maximum stress observed in the original bucket design at the cutout therefore this modification was accepted.

Modification e-11.1 was not acceptable as the stress at the cutout has peaked noticeably higher than the maximum stress in the original bucket. The peak stress was in the angular position ranging from 10° to 20° rotated from horizontal. At this stage the jet is entering the bucket. Even though this is far from the peak overall torque on the bucket but the jet force is concentrated on the region around the splitter tip. This peak in the stress at the cutout edge shows that the thickness needs to be further increased. However it was already showed that increasing the thickness reduces the efficiency. Therefore modification e-11.1 was withdrawn taking e-10.1 for further development.

Bucket size has increased noticeably throughout the modifications, especially when parameters P1 and P2 were modified during DOE Study 1. Therefore, it was decided to remove some amount of material from the bottom of the bucket because of two reasons:

- the modified bucket was thicker than the original (Fig. 4.55) suggesting that less thickness would be acceptable,
- more space between the buckets (Fig. 4.56) is always preferable from the manufacturing point of view.

The comparison of this modified bucket e-10.2 where the part of material was removed to the initial FEA approved shape e-10.1 is provided in Fig. 4.56. It can be seen from Fig. 4.57 that this removal of material has not changed the structural performance significantly at the locations of interest. Therefore this modification e-10.2 was taken further.

Fine mesh simulation was performed to verify the improvement in the efficiency achieved by modifying the cutout shape and the splitter tip (P11-P12) and also after strengthening the bucket at the critical regions indicated by the FEA structural analysis. The performance was improved by 0.2 % of the initial efficiency as shown in Fig. 4.60.

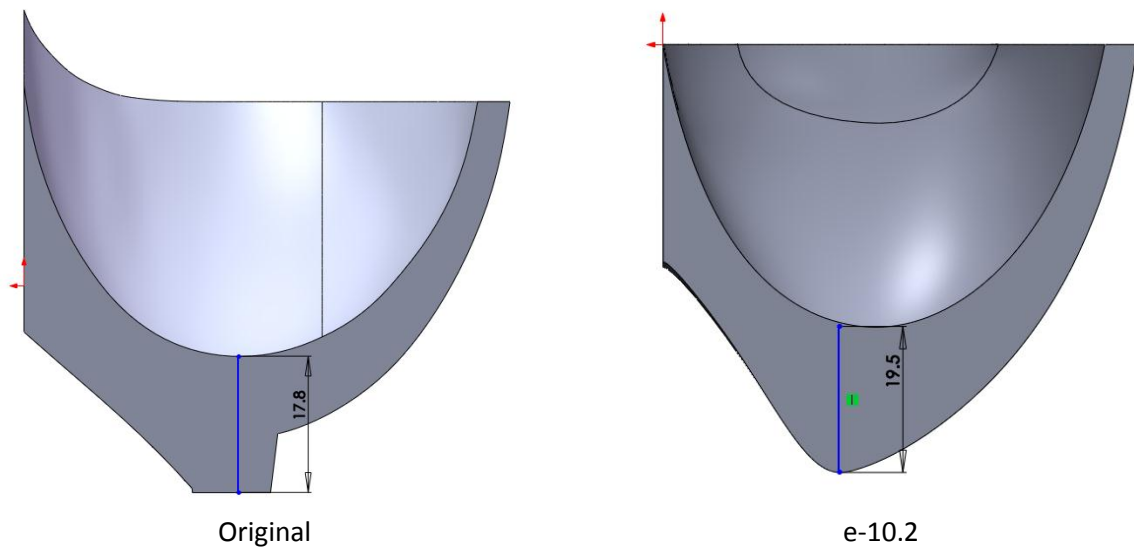


Fig. 4.55. Maximum thickness comparison of the original and modification e-10.1.

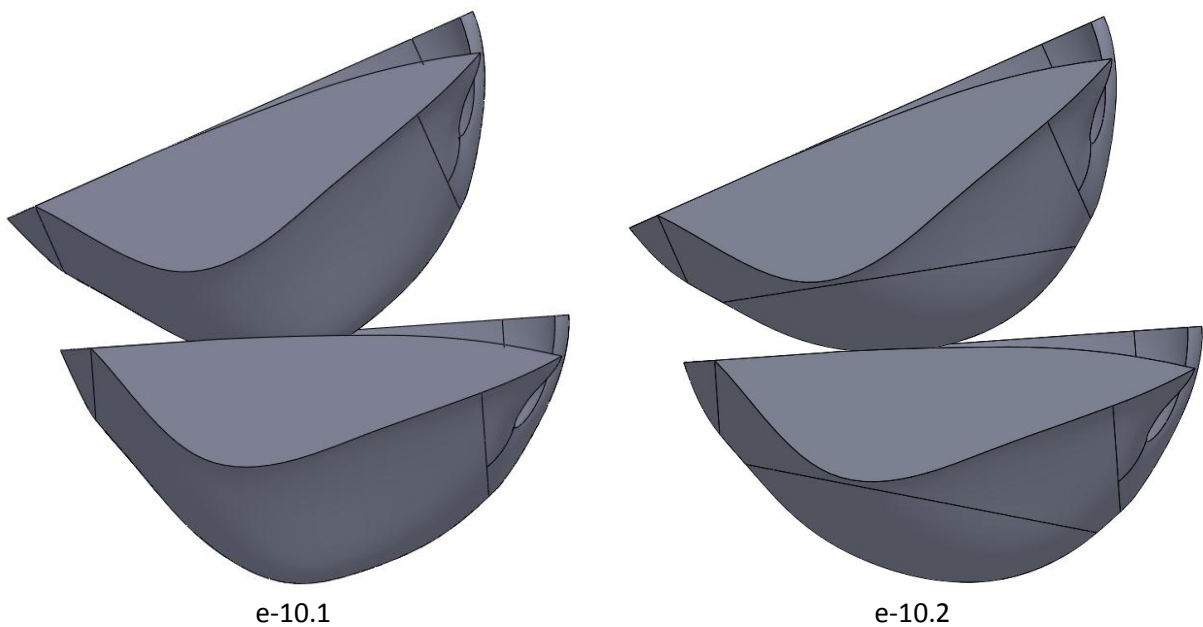


Fig. 4.56. Removed material from the bottom of e-10.1.

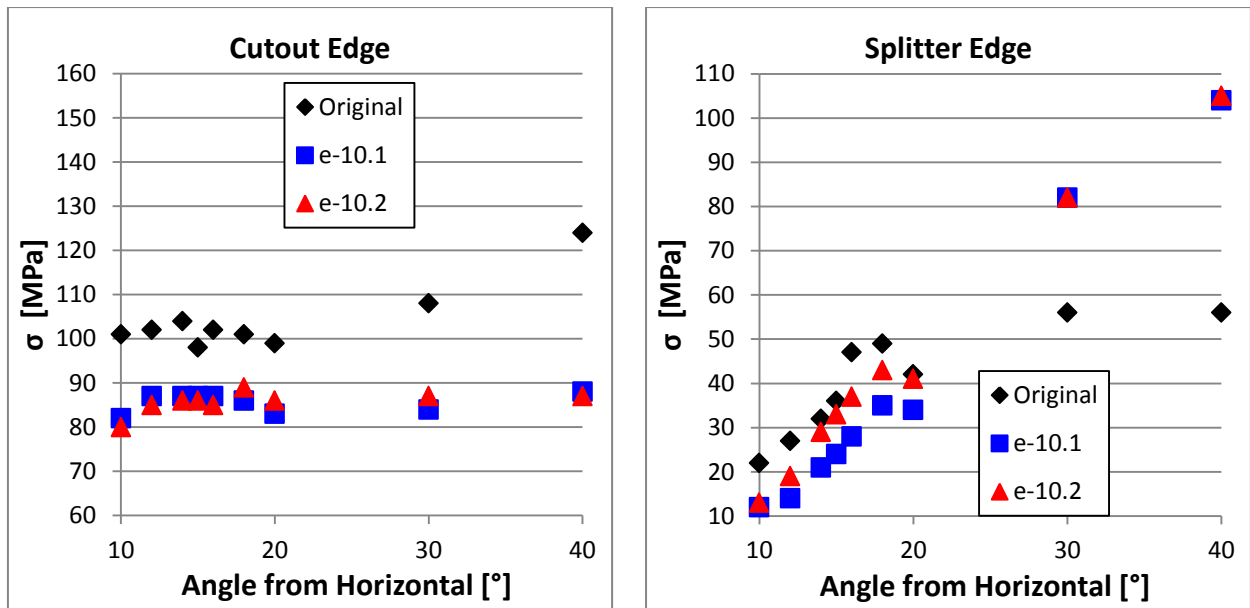


Fig. 4.57. FEA results at various bucket angular positions under the nominal operating conditions. Left: peak stress at the cutout edge, right: peak stress at the splitter edge.

4.5.1.1. Comments on the FEA

- 1) At first these designs might seem highly over engineered as the peak stresses are much lower than the yield strength of stainless steel. However, Pelton buckets are subject to fatigue as they are loaded with high frequency during their operation (Brekke 2010). Detailed structural analysis that includes the fatigue analysis was considered to be outside of the scope of this PhD that concentrates on the numerical optimisation of the hydraulic performance. Therefore it was decided to maintain similar stress levels within the bucket to the original design that was tested over time as a reliable product. The FEA analysis provided in this thesis was to ensure that the design is sensible from the structural point of view. The aim was to minimise the risk of producing a geometry that was hydraulically improved but unfeasible from the manufacturing point of view.
- 2) To modify the specific speed of Pelton turbine while keeping constant number of jets, the bucket of constant size and width can be mounted on different diameter hubs. It is different to the uniform scaling using the Affinity laws which does not change the specific speed. In a way modifying this B/D_p ratio can be considered as creating a new turbine.
 It was specified by the manufacturers to optimise the hydraulic performance using the highest B/D_p ratio (or the highest specific speed) of their product range. However, for the structural analysis most critical loads were required. Therefore the FEA was performed on the runner that had 1.3 times lower B/D_p ratio (lower specific speed).

4.5.2. P5-P6: DOE Study 3 (α , R_t)

Various bucket shape modifications were made since adjusting its radial position R_t and the inclination angle α in the DOE Study 2. Therefore it was expected that readjusting the position of the bucket on the runner might further increase the efficiency. Moreover, in DOE Study 2, the number of buckets was reduced noticeably. To be able to isolate the effect of bucket shape from the change in the number of buckets when performing experiments it was decided to produce 3 runners for testing:

- 1) Original runner – original bucket design, 18 buckets on the runner. Testing this runner provided the datum point to assess the efficiency improvement.
- 2) Optimised runner 1 – optimised bucket design, 18 buckets on the runner. Testing this runner provided the information on the efficiency improvement due to the bucket design.
- 3) Optimised runner 2 – optimised bucket design, 15 buckets on the runner. Testing this runner provided the information on the effect on efficiency due to the number of buckets.

Hence, in addition to further improving the efficiency, readjusting of the angular and the radial position allowed fairer comparison between 18 and 15 bucket runners knowing that the buckets were in the optimum position. Also, removing the thick layer of material at the front of the bucket (the remains of the ribs) and shortening the splitter tip allowed increasing the radial position without increasing the original outer diameter if needed.

Two Design of Experiments studies containing 9 design points to construct the response surfaces were performed to optimise the bucket positioning for Optimised runner 1 and Optimised runner 2.

4.5.2.1. Optimised Runner with 15 Buckets

Design limits for the two bucket positioning parameters P5 and P6 are provided in Table 4.11. The range of investigation for parameters α and R_t was created based on the initial values taken from modification e-10.2. Range for the angular position α was taken around the initial value of 3.6° and the range for the radial distance R_t was taken by selecting the initial value $R_t / R_p = 1.313$ to be the minimum bound expecting to increase the efficiency by increasing the radial distance. Table 4.12 provides the details of the 9 design points where the first design point named f-0-15B-1 is the same as e-10.2. Results are presented in the efficiency contours provided in Fig. 4.58. It suggests a small increase of 0.1 % in the efficiency according to the coarse mesh results by increasing the radial distance R_t by 0.9 %. Design point f-0-15B-9 was very close to the predicted peak therefore it was decided to use the positioning of this design point for an optimised runner with 15 buckets.

Fine mesh simulation was performed to verify the improvement in the efficiency achieved by readjusting the positioning parameters (P5-P6). The performance was improved by 0.2 % of the initial efficiency as shown in Fig. 4.60.

Table 4.11. Design ranges for parameters α , R_t , where $N_b = 15$.

Design Parameter		Lower Limit	Upper Limit
P5	α	1°	6°
P6	R_t/R_p^*	1.316	1.334

*radial distance is presented in relation to the pitch circle radius R_p .

Table 4.12. Test plan for parameters α and R_t , where $N_b = 15$.

Modification Name	α [°]	R_t/R_p [-]	η_{norm} [-]
f-0-15B-1	3.6	1.313	0.999
f-0-15B-2	6.0	1.334	0.999
f-0-15B-3	6.0	1.316	0.998
f-0-15B-4	7.0	1.325	0.997
f-0-15B-5	3.5	1.338	0.998
f-0-15B-6	0.0	1.325	0.993
f-0-15B-7	1.0	1.334	0.995
f-0-15B-8	1.0	1.316	0.996
f-0-15B-9	3.5	1.325	1.000

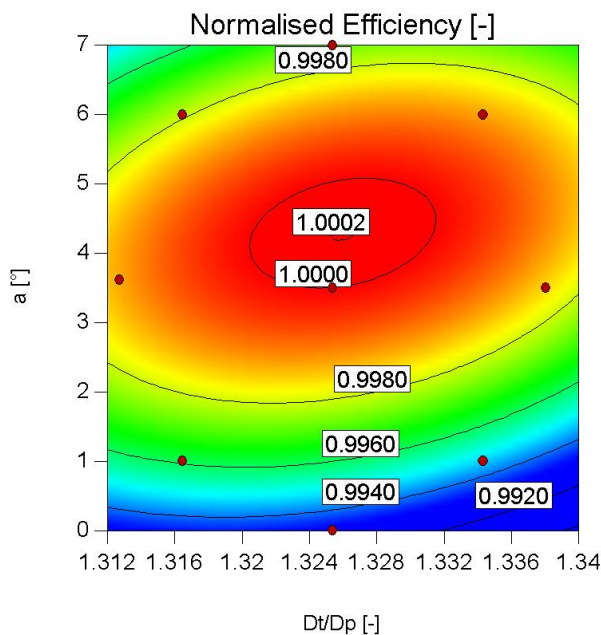


Fig. 4.58. Normalised efficiency contours for $N_b = 15$.

4.5.2.1. Optimised Runner with 18 Buckets

It was not unexpected that repositioning of the bucket in the runner where $N_b = 15$ has increased the efficiency by very little as the bucket was optimised in the 15 bucket arrangement since the DOE study 2 where it was showed that a runner with 15 buckets is the most optimum. However, optimum positioning of the bucket where $N_b = 18$ was not known. It was very important to find the optimum positioning for this runner so that runners with different amount of identical geometry buckets could be compared. The design limits for the two bucket positioning parameters P5 and P6 are

provided in Table 4.13. The details of the 9 design points are provided in Table 4.14 and the results are presented in the efficiency contours provided in Fig. 4.59. Design point f-0-18B-8 was very close to the predicted peak therefore it was decided to use the positioning of this design point for an optimised runner with 18 buckets.

Fine mesh simulation was performed to verify the effect on the efficiency achieved by adjusting the positioning parameters (P5-P6) for the runner with 18 buckets. The runner with 18 optimised buckets was expected to be 0.2 % less efficient than the runner with 15 optimised buckets as shown in Fig. 4.60.

Table 4.13. Design ranges for parameters α , R_t , where $N_b = 18$.

Design Parameter		Lower Limit	Upper Limit
P5	α	2.9°	7.1°
P6	R_t/R_p^*	1.303	1.334

*radial distance is presented in relation to the pitch circle radius R_p .

Table 4.14. Test plan for parameters α and R_t , where $N_b = 18$.

Modification Name	α [°]	R_t/R_p [-]	η_{norm} [-]
f-0-18B-1	5.3	1.297	0.9963
f-0-18B-2	7.1	1.334	0.9982
f-0-18B-3	7.1	1.303	0.9959
f-0-18B-4	8.0	1.319	0.9957
f-0-18B-5	2.0	1.319	0.9955
f-0-18B-6	2.9	1.334	0.9938
f-0-18B-7	2.9	1.303	0.9964
f-0-18B-8	5.0	1.319	1.0000
f-0-18B-9	5.0	1.341	0.9952

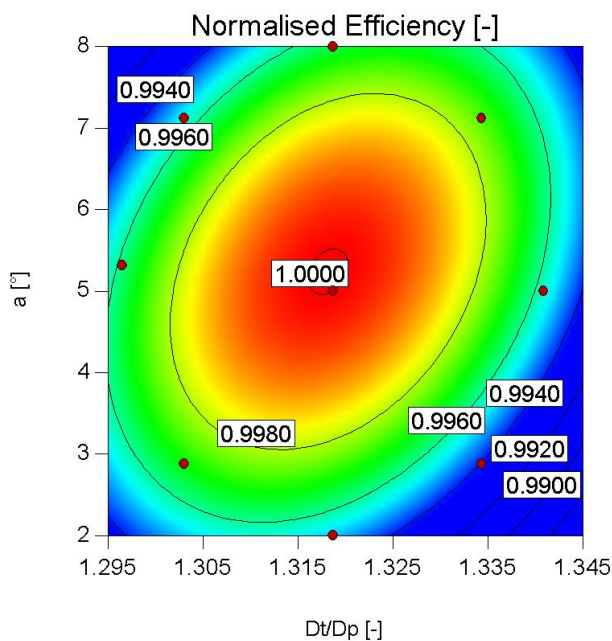


Fig. 4.59. Normalised efficiency contours for $N_b = 18$.

4.5.3. Final Design Approved for Manufacturing

The modifications f-0-15B-9 and f-0-18B-8 were passed to the design engineers of Gilkes. These modifications were integrated into the mono-block runner design, to check if there are no issues from the manufacturing point of view and few minor modifications were made. These modifications were checked and approved by the fine mesh CFD simulation. At this stage the bucket design was frozen giving it the name Z120. Total efficiency improvement predicted by the CFD fine mesh simulations was 2.5 % of the original efficiency for a runner with 15 buckets and 2.1 % for a runner with 18 buckets as shown in Fig. 4.60. Experimental testing of these optimised runners against the original runner is presented in the following Chapter 5.

4.6. Summary of Design Optimisation (Fine Mesh Results)

Summary of the fine mesh simulation results for each key design modification is provided in Fig. 4.60. The results are provided as the efficiency increase from the original design normalised to the original efficiency.

$$\Delta\eta_{norm} = \frac{\eta - \eta_0}{\eta_0} \quad (4.3)$$

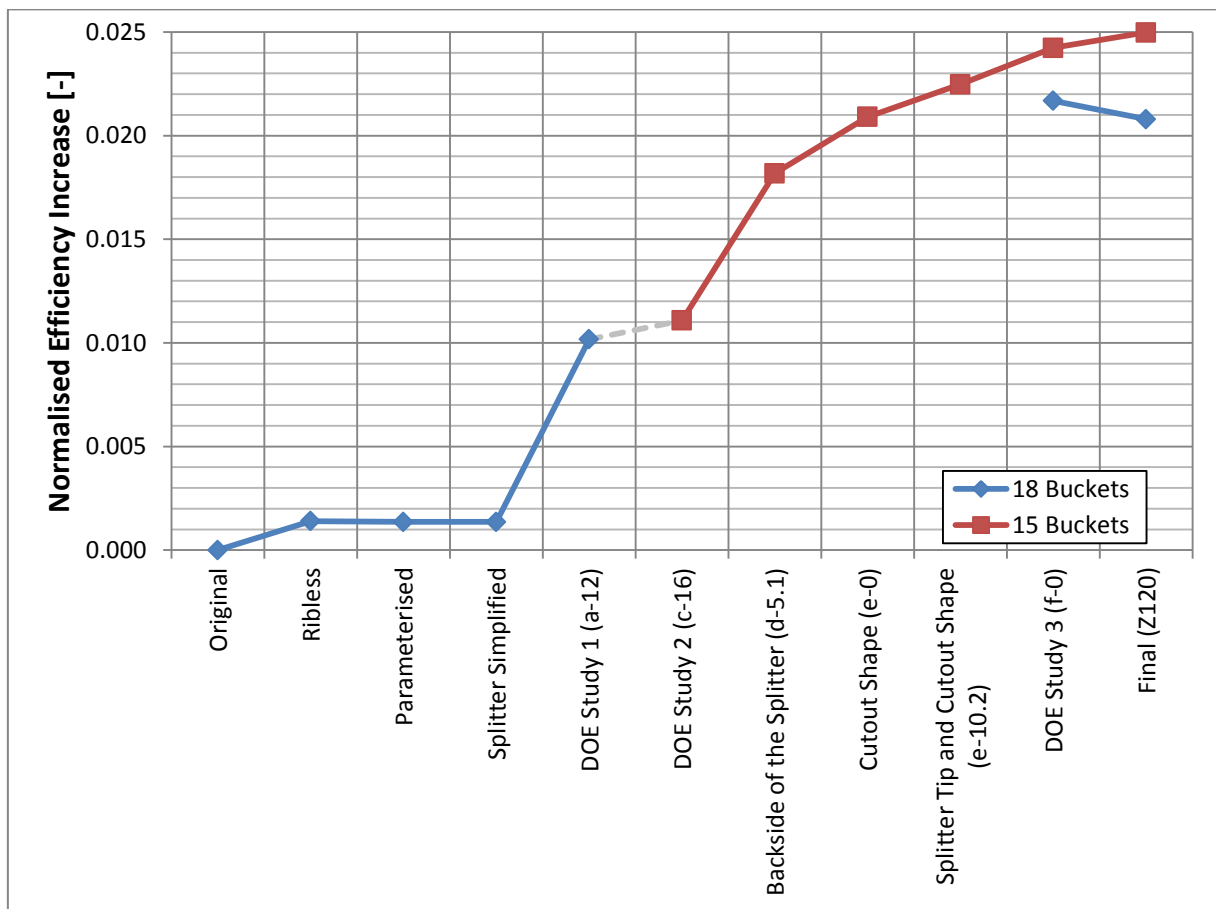


Fig. 4.60. Summary of efficiency improvements during key development stages according to fine mesh CFD simulations.

Chapter 5. Experimental Testing

This chapter provides information on the experimental testing of the numerically optimised runners. Experiments were taking place at the National Technical University of Athens (NTUA) Laboratory of Hydraulic Machines. Three turbine models were tested: original design and two numerically optimised runners to support the numerical study. Experimental process and turbine performance hill charts of all the three runners (initial and two modifications) are provided in this chapter.

5.1. Overview

Experimental testing was performed at the NTUA Laboratory of Hydraulic Machines which was contracted by Gilkes. The contract allowed Gilkes or research students funded by Gilkes to use the Laboratory facilities under the supervision of NTUA staff. Brand new testing stand was manufactured for these tests and some instruments or related items were upgraded. The new items were:

- Turbine casing.
- Injectors.
- Branchpipe.
- Flow straightener inside the pipe that leads to the branchpipe.
- Wiring of the instruments.
- Signal processing circuits and units.

Two sets of tests were performed:

- 1) 1st Set of Tests included the runner tests of the Original runner and the Optimised runner with 18 Z120 buckets (original number of buckets). A decision was made by the funders to first identify the effect of the optimised bucket shape design without changing the original number of buckets. It was agreed that if the improvement in the efficiency showed by CFD is successfully proved experimentally, additional runner with 15 buckets can be made and tested as the next step.
- 2) 2nd Set of Tests included the runner tests of the Original runner with 18 and 15 Z120 buckets. After the increase in efficiency caused by the bucket design was proved experimentally to have met the expectations a decision was made to produce a new runner with 15 optimised design buckets. The old torque meter was upgraded before these tests as some unwanted scatter in the readings was observed in the 1st set of tests. This meant that the Optimised runner with 18 buckets had to be retested so that the systematic error is cancelled out when comparing it to the Optimised runner with 15 buckets.

Details of the tests and preparation for them will be provided later in this chapter.

5.2. Manufacturing

Commercial Pelton runners are usually made as mono-block units to have very long life cycle (Vesely and Varner 2001, Wang, Liu et al. 2010, Ferreño, Álvarez et al. 2011, Padhy and Saini 2011). However for testing purposes the runners were made as segmented units of bolted-on buckets on the hub. An image of the segmented runner with 15 numerically optimised (Z120) buckets is provided in Fig. 5.1. The hubs and the bush were manufactured from stainless steel and all the buckets were CNC machined from aerospace grade aluminium alloy. Fig. 5.2 provides an image of a single Z120 bucket.



Fig. 5.1. Segmented Pelton runner with 15 numerically optimised (Z120) buckets used for experimental testing.



Fig. 5.2. Z120 bucket CNC machined from aerospace grade aluminium alloy.

The pitch circle diameter D_p of the model turbine was 320 mm and the bucket width B was 120 mm. Fig. 5.3 and Fig. 5.4 show the complete assembly of the Gilkes Pelton turbine testing facility installed at the NTUA Laboratory of Hydraulic Machines.

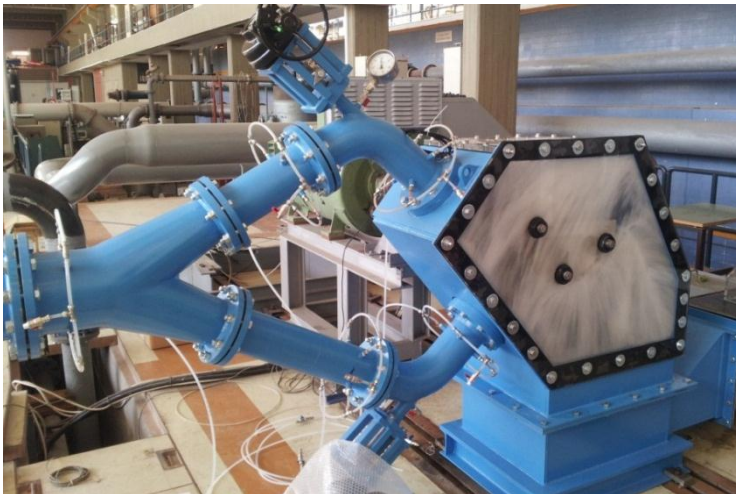


Fig. 5.3. Gilkes Pelton turbine testing facility at the Laboratory of Hydraulic Machines (NTUA).

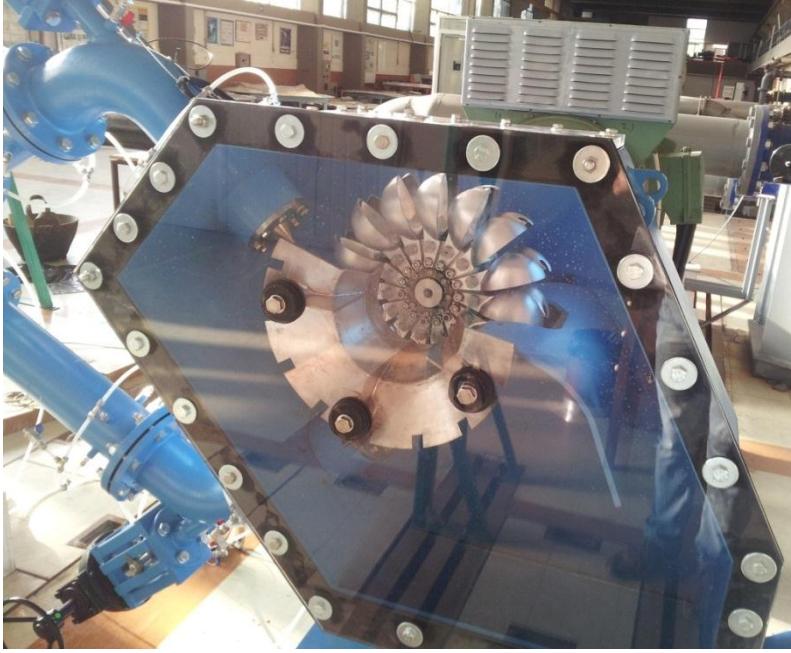


Fig. 5.4. Inside view of the Pelton turbine casing.

5.3. Turbine Characteristic Equations

This section provides equations used to define the characteristics of a turbine and present the results. These equations are based on the Affinity laws (Nechleba 1957, Aggidis and Židonis 2014) and most of them can be found in the international turbine testing standards (IEC 60193:1999). Few additional equations derived for specific analysis are also provided here.

Efficiency of a turbine is the ratio of the mechanical power provided by a shaft of a turbine to the power generator (output power) divided by the hydraulic power (input power):

$$\eta = \frac{P_{out}}{P_{in}} \quad (5.1)$$

where

$$P_{out} = M\omega \quad (5.2)$$

and

$$P_{in} = \rho QgH \quad (5.3)$$

Turbine characteristics are presented by the efficiency η at different combinations of the unit speed n_{11} Eq. (5.4) and the unit flow rate Q_{11} Eq. (5.5).

$$n_{11} = \frac{n \times D}{\sqrt{H}} \quad (5.4)$$

$$Q_{11} = \frac{Q}{D^2 \times \sqrt{H}} \quad (5.5)$$

In the international turbine testing standards (IEC 60193:1999) the minimum model size of Pelton turbine is specified in terms of bucket width as oppose to the reference diameter as it is done for other turbines. This suggests that bucket width represents the Pelton turbine better and therefore following the same logic additional unit flow rate definition was made to allow more generic comparison of Pelton runners. This equation of unit flow rate specified to the bucket width and one jet allows comparison between different specific speed Pelton runners:

$$Q_{11k} = \frac{Q/N_j}{B^2 \times \sqrt{H}} \quad (5.6)$$

5.4. Testing Procedure

The chosen measurement method for testing was to use a constant head by setting the rotational speed of the test rig pump. The operating point was adjusted by changing the rotational speed of the runner. Measurements were taken for different flow rates by setting the spear position followed by an adjustment of the pump speed to maintain the constant head. Two sets of measurements were taken for each runner to test their operation with both jets and with single jet (lower injector).

The measurement procedure is summarized below:

1. Turn on all instruments to be used and allow a preheat time of at least 30 min before initiating measurements.
2. Check the hydraulic circuit to ensure the flow is guided to the necessary section of the test rig and that there are no visible leaks in the system.
3. Set the initial spear position in the first nozzle to be used.
4. Start-up of the brake at low rotational speed.
5. Start-up of the laboratory pump and set the speed to produce the required head for the measurements.
6. Set the turbine rotational speed to the required value.
7. Allow sufficient time for the flow conditions to be stabilized (60 seconds were found to be adequate).
8. Obtain measurements continuously for 120 seconds.
9. Increase the speed of the turbine.
10. Repeat steps 7-9.
11. Once the full range of speed has been obtained, change the spear position.
12. Adjust the pump rotational speed to maintain the head constant.
13. Repeat steps 6-12.

The procedure to produce the hill charts is summarised here:

1. Obtain measurements from the data logging equipment (using LabVIEW).
2. Store measurements in .txt files.
3. Import measurement data in a suitable data processing software (Excel).
4. Use the calibration curves to calculate the physical parameters measured.
5. Calculate the performance parameters (n_{11} , Q_{11k} , η).
6. Use the calculated data to draw the hill charts (using Matlab).

The test plan in form of Q_{11k} vs n_{11} values is provided in Fig. 5.5 with the operating point used for CFD optimisation coloured in green. Each set of measurements consisted of 61 data points: 6 rotational speeds for each of 10 flow rates plus one data point at the expected best efficiency point, i.e. operating conditions that were used for runner optimisation in CFD ($n_{11} = 39.8$ rpm, $Q_{11k} = 0.221$ m³/s).

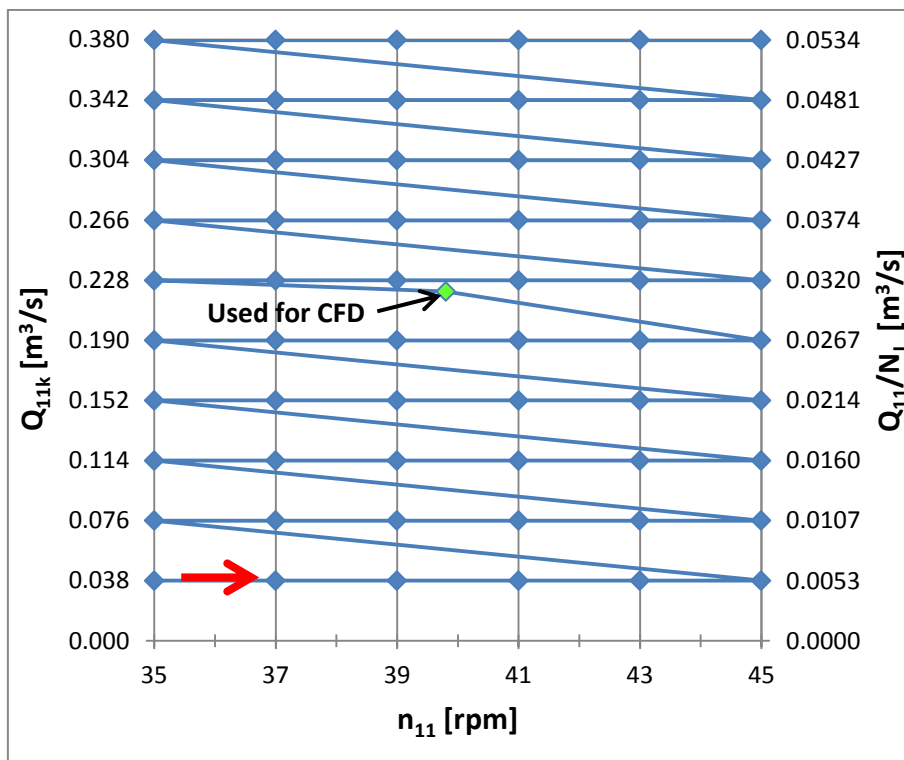


Fig. 5.5. Test plan and testing sequence.

5.5. 1st Set of Tests

This set of tests includes the tests of the Original runner and the Optimised runner with 18 buckets. These tests were made to evaluate the efficiency increase caused by the optimised bucket geometry (Z120). Experienced problems and recommendations are provided in section 5.5.6.

1st set of tests was performed in June 2014.

5.5.1. Instruments and Calibration

Details of the instruments used for testing and their calibration are provided in this section. Testing and calibration procedures were following the guidelines of the international testing standard *IEC 60193 Hydraulic turbines, storage pumps and pump-turbines – Model acceptance tests* (IEC 60193:1999).

5.5.1.1. Physical Constants

The density of water ρ and the acceleration due to gravity g were calculated according to the tables provided in the international standard (IEC 60193:1999). These tables are provided in the Appendix A. The location of the experimental testing was at altitude $h = 200$ m and latitude $\phi = 37.978^\circ$ which according to the Table A. 1 gave the gravity constant value $g = 9.7994$ m/s². Density was calculated for each test individually depending on the pressure and water temperature readings according to Table A. 2.

5.5.1.2. Error Definitions

Absolute error Eq. (5.7) is the difference between the reference value and the measured (readout) value.

$$\Delta = X_{ref} - X_m \quad (5.7)$$

Relative error Eq. (5.8) is the absolute error divided by the reference value.

$$\delta = \frac{\Delta}{X_{ref}} * 100 \% \quad (5.8)$$

5.5.1.3. Pressure Transducers

Pressure head was measured at 5 different reference locations as indicated in Fig. 5.6. Only pressure p_1 located before the bifurcation was used for efficiency calculations. Pressure readings from locations p_2 to p_5 were made to allow additional analysis or backup the readings of p_1 .

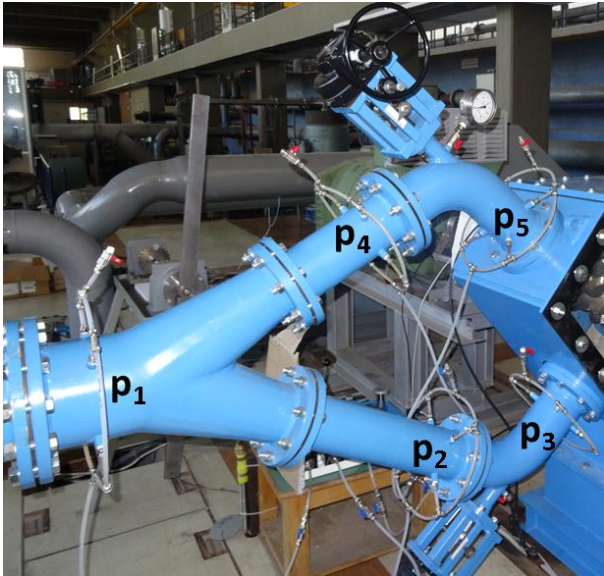


Fig. 5.6. Reference locations for pressure readings p_1 to p_5 .

Four axisymmetric pressure taps were made for each reference location and connected to the pressure transducer using the ring manifold as suggested by the international testing standards (IEC 60193:1999). Schematics of the arrangement are provided in Fig. 5.7-B.

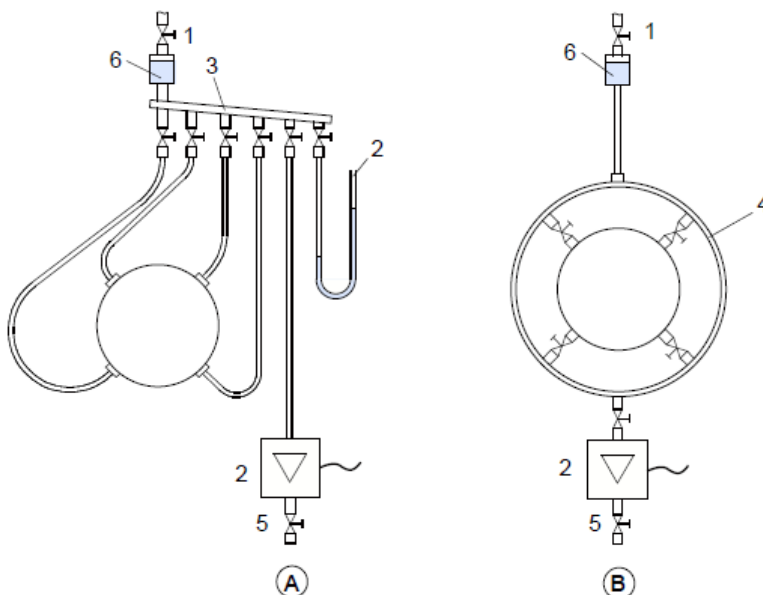


Fig. 5.7. Types of pressure manifolds (IEC 60193:1999). 1) vent, 2) pressure measuring instrument, 3) manifold, 4) ring manifold, 5) drain and 6) gas-collecting chamber.

Pressure transducers (0 to 10 bar range, manufacturer: ESI Technology Ltd., model: Ellison-Pr3200) were calibrated using a dead weight tester made by TRADINCO® instruments. The calibrated weights of this tester indicate applied pressure in bar if gravity constant $g = 9.80665 \text{ m/s}^2$. Since the value of the gravity constant at the laboratory was different, when corrected for altitude and latitude as explained in section 5.5.1.1 Physical Constants, the calibration weights had to be corrected as well by the factor $9.7994 / 9.80665 = 0.9993$.

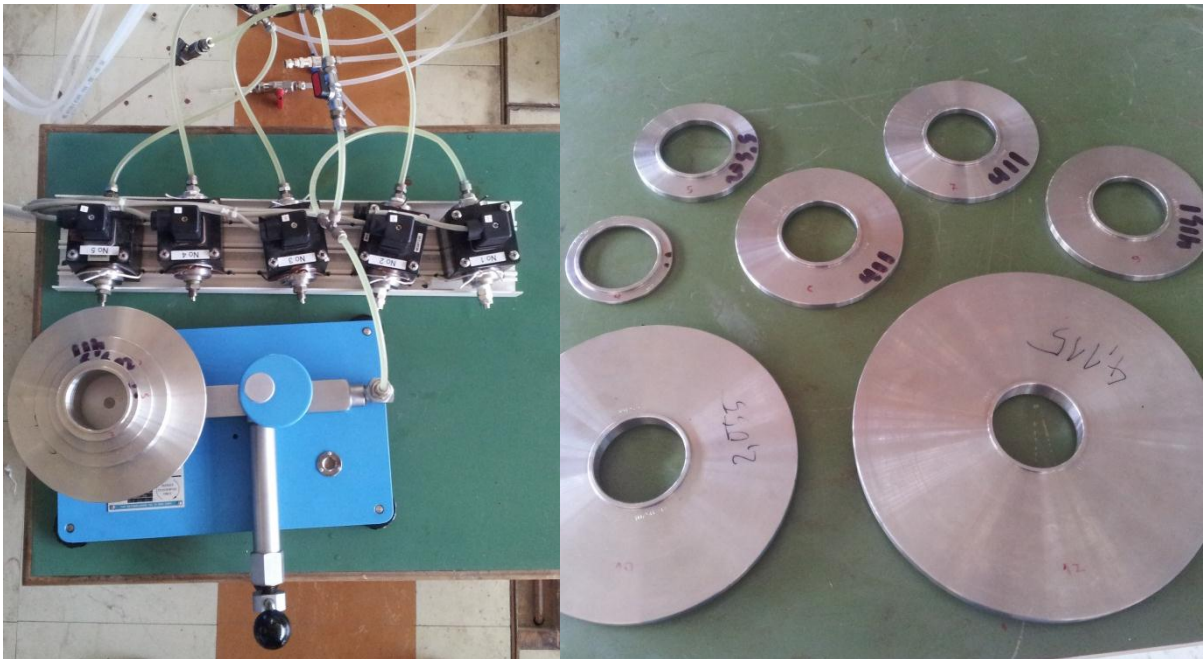


Fig. 5.8. Dead weight tester connected to the pressure transducers (left) and the calibrated weights (right).

Calibration curve and the relative error are provided in Fig. 5.9. The relative error around the testing pressure corresponding to the pressure head of 60 metres was less than $\pm 0.1 \%$.

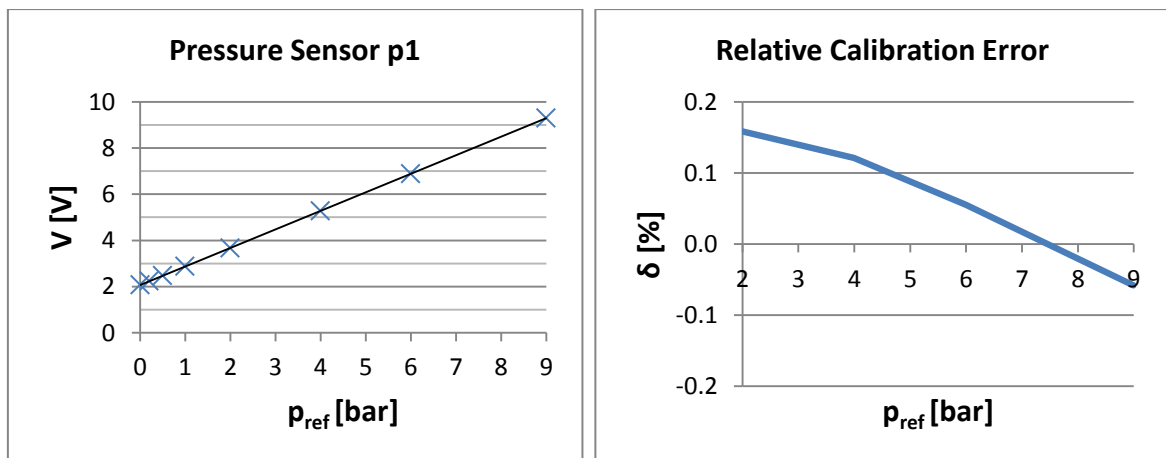


Fig. 5.9. Calibration curve and the relative error of the pressure transducer p_1 .

5.5.1.4. Flow Meter

The flow meter was calibrated using the volumetric tank (Fig. 5.10). The usable depth of the tank was up to 6 metres and the area was around 20 m² giving the total volume of 120 m³. The depth in the tank was measured using an immersed pressure sensor (0 to 1 bar range, manufacturer: Vega, model: VEGA-139A). Details of the area vs. elevation in the volumetric tank measured in steps of 0.5 m were provided by the laboratory and shown in Fig. 5.11.

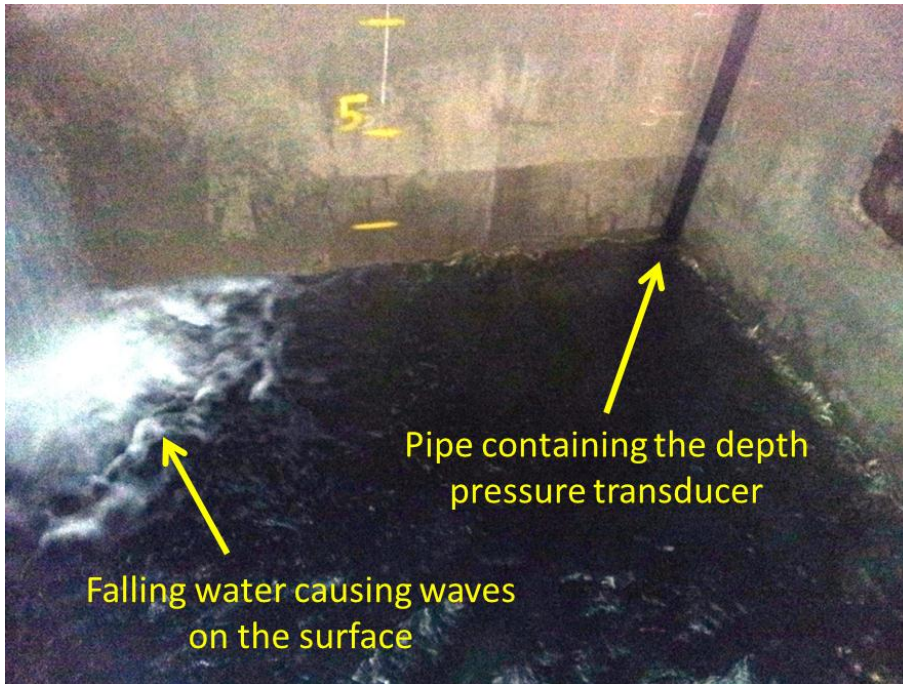


Fig. 5.10. Inside of the volumetric tank used to calibrate the flow meter.

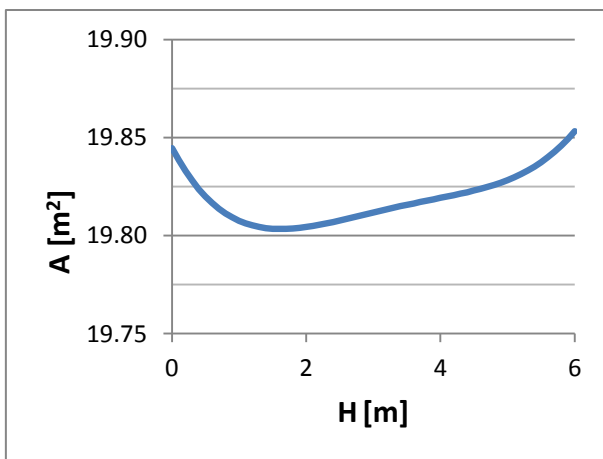


Fig. 5.11. Cross-sectional area of the volumetric tank vs. the elevation curve.

The depth pressure sensor was calibrated in similar way to the pressure sensors p_1 to p_5 . Calibration curve and the relative error are presented in Fig. 5.12. During the calibration of the flow meter the level in the volumetric tank was kept above 2 m to reduce the oscillations in the depth pressure readings created by the waves on the surface. These waves were caused by the falling water as it was

pumped into the tank (Fig. 5.10). Therefore the relative error of the depth pressure sensor is provided in the range of 0.2 to 0.6 bar and the error was within $\pm 0.1\%$.

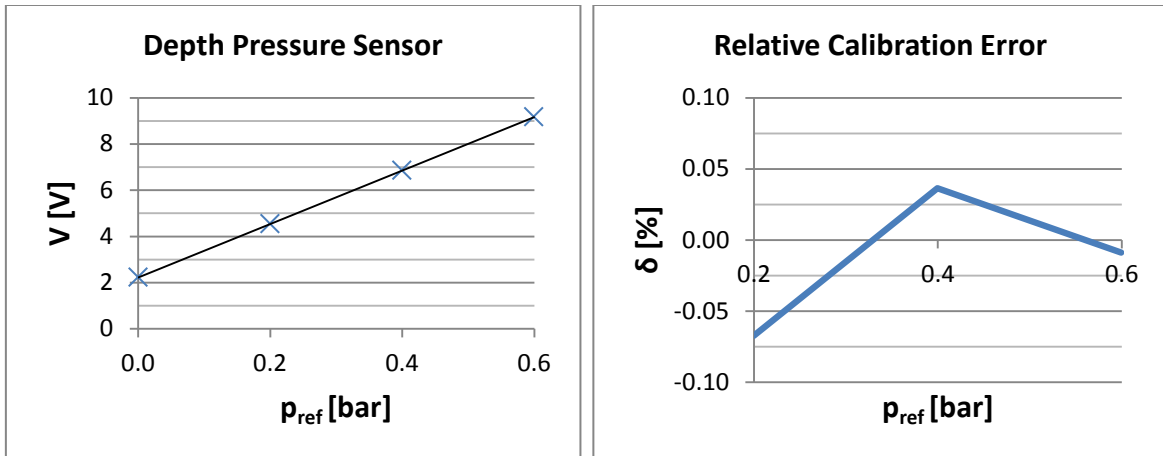


Fig. 5.12. Calibration curve and the relative error of the depth pressure sensor.

Flow rate was measured using the electromagnetic flow meter with the range of 0 to 600 m^3/h (manufacturer: ABB, model: DE41F). The flow meter was located in the inlet pipe upstream of the bifurcation and downstream of the pump. An image of the flow meter is provided in Fig. 5.13.

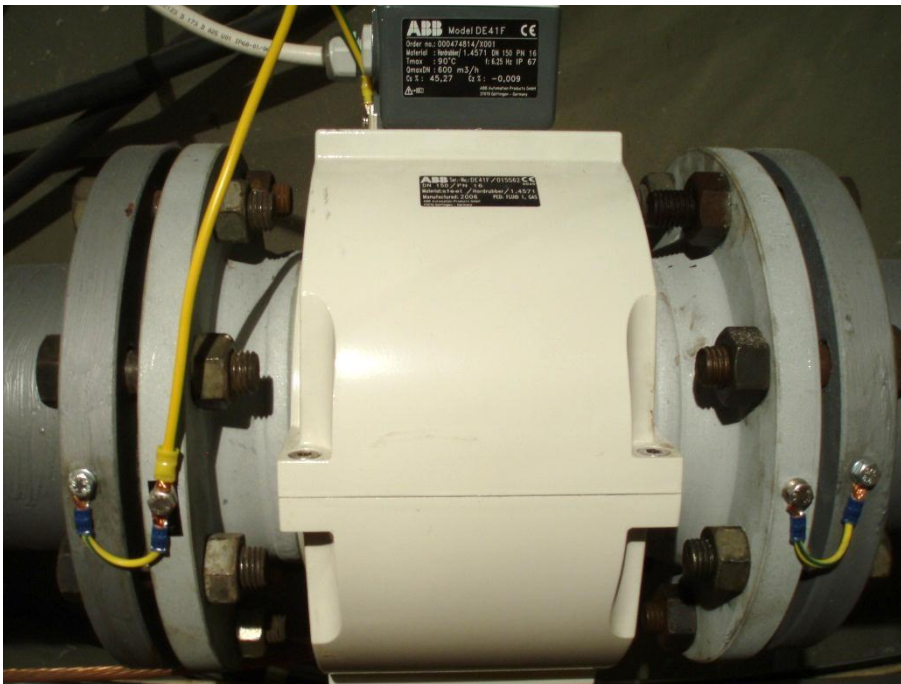


Fig. 5.13. Electromagnetic flow meter.

During the calibration all the flow was diverted from the turbine to the volumetric tank. For each flow rate water was pumped at constant rate over some period of time while taking the depth pressure readings in the intervals of 1 s. The time period was ranging from 2 min for high flow rates ($> 200 m^3/h$) to 10 min for the lowest flow rate ($\sim 12 m^3/h$). Fig. 5.14 presents a curve of water tank

elevation vs. time as the water is pumped at constant rate of $11.7 \text{ m}^3/\text{h}$. A linear fit was made and used to calculate the average flow rate during the time of pumping (10 min in this instance). Oscillations on the surface were present and were visible in the readings of the depth pressure sensor (red curve). The linearity of calibration using this method was affected by these oscillations that were dependent on the initial water level in the tank and control of the flow rate produced by the pump. Therefore there was inevitable factor of human error in achieving calibration linearity.

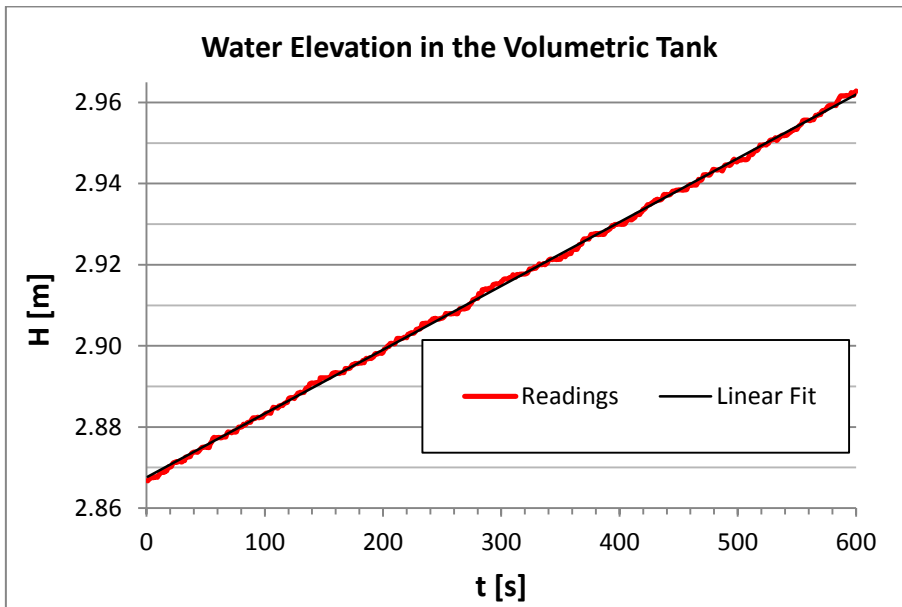


Fig. 5.14. Water elevation in the tank vs. time curve and its linear fit for $Q = 11.7 \text{ m}^3/\text{h}$.

Calibration curve and relative error of the flow rate sensor are provided in Fig. 5.15. The relative error was within $\pm 0.5 \%$.

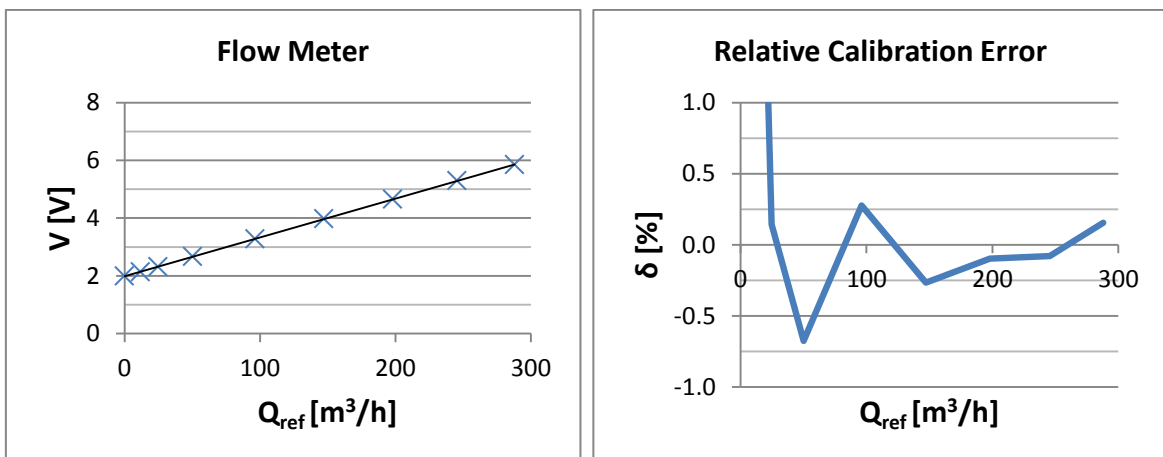


Fig. 5.15. Calibration curve and the relative error of the flow meter.

5.5.1.5. Torque Meter

The torque meter arrangement used in the testing was “a bearing of rotating parts not in balance” (IEC 60193:1999). Schematics of such arrangement are presented in Fig. 5.16. An image of the torque meter, which was a torque transducer with a strain gage sensing (manufacturer: Kyowa, strain gauge model: DPM-611A, torque transducer model: TP-50KMxCB) used during the testing is provided in Fig. 5.17.

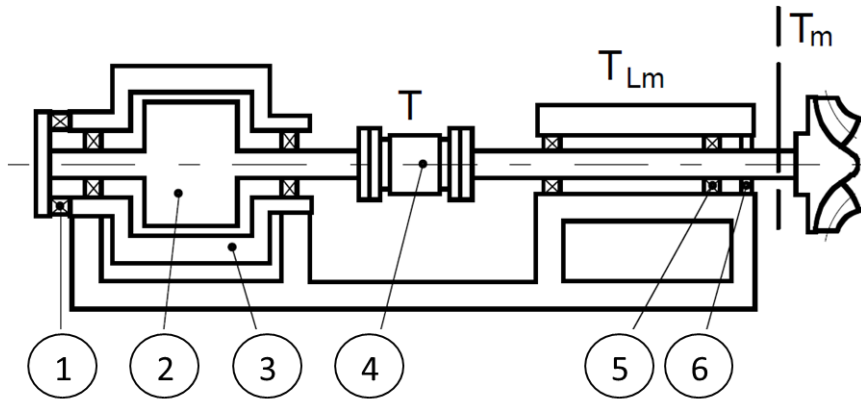


Fig. 5.16. Arrangement using a torque meter with machine bearings and seals not in balance (IEC 60193:1999). 1) axial thrust bearing, 2) rotating part, 3) stationary part, 4) torque meter, 5) bearing of rotating part not in balance 6) mechanical seal of rotating part not in balance.

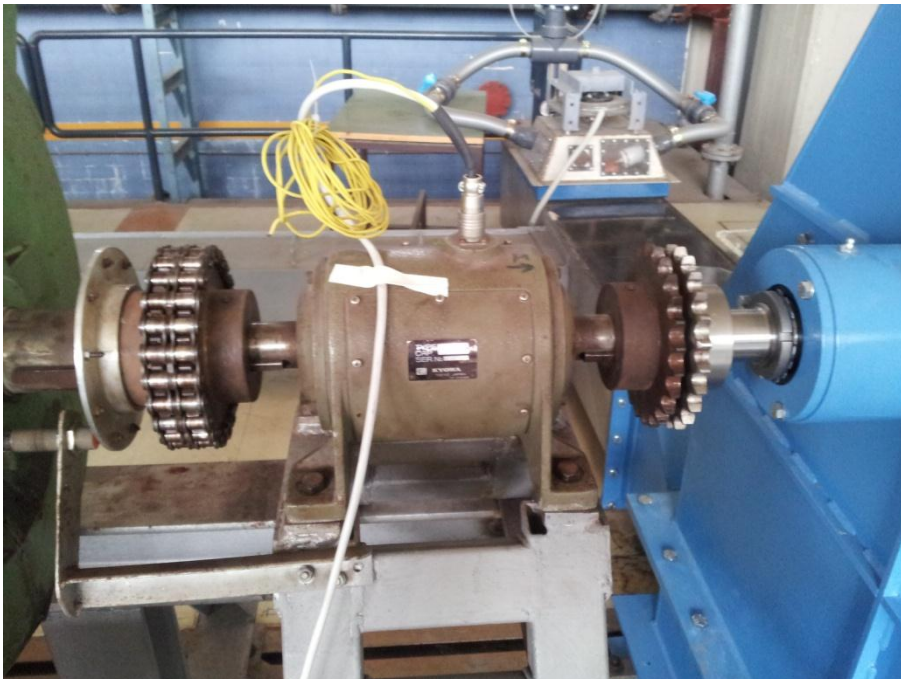


Fig. 5.17. Torque meter.

This torque meter was calibrated using the brake lever and the calibrated weights as presented in Fig. 5.18. Calibration curve and the relative error are provided in Fig. 5.19. The relative error for this sensor was within $\pm 0.05\%$.



Fig. 5.18. Calibration of the torque meter.

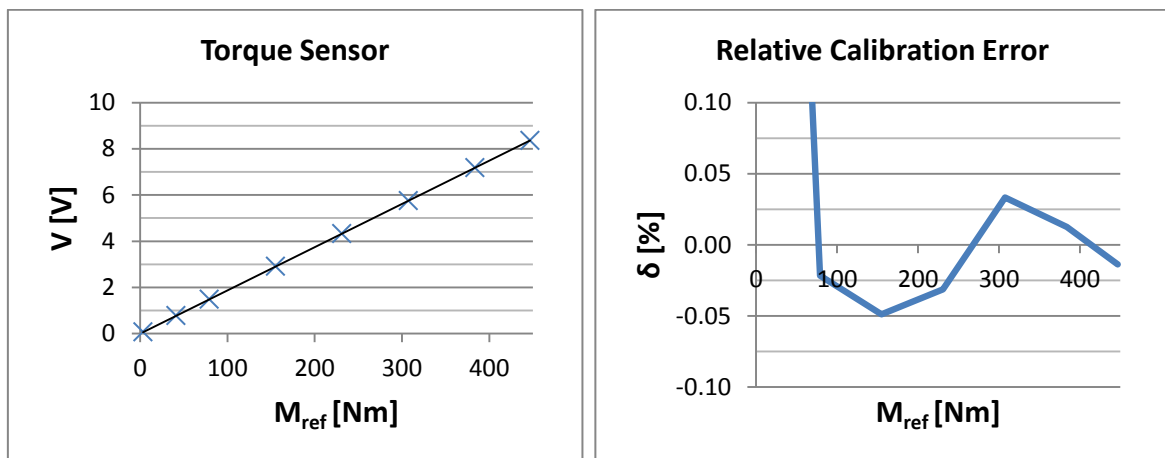


Fig. 5.19. Calibration curve and the relative error of the torque meter.

In addition to calibrating the torque meter, sensitivity and speed tests were carried out as required by the standards (IEC 60193:1999).

Sensitivity test:

Sensitivity test was performed by placing very small weights on top of the existing weights shown in Fig. 5.18 and observing what is the lowest mass (or corresponding torque) that can be measured with this system. The lowest torque that could be measured was 0.06 Nm (8 g mass on 0.78 m lever) which was acceptable according to the standard.

Speed test:

The shaft was disconnected to verify that the torque remains 0 Nm at all the speeds. In Fig. 5.17 the right hand side of the torque meter (the turbine side) is uncoupled from the shaft by removing the coupling chain.

5.5.1.6. Rotational Speed Sensor

The rotational speed was measured using a magnetic pulse meter (manufacturer: Efectron, model: GA3005-ANKG). The resolution of 10 pulses per revolution was available because there were 10 screws on the plate (Fig. 5.20). Usually the speed measuring device is not truly calibrated because of its digital nature. The readings of this rotational speed sensor were checked using a stroboscope and a hand held tachometer. The latter is presented in Fig. 5.21. According to the standards (IEC 60193:1999) the systematic uncertainty of aforementioned instrumentations is expected to be within $\pm 0.01\%$ to 0.05% . The value of $\pm 0.05\%$, which is a maximum expected uncertainty, was taken for uncertainty analysis.

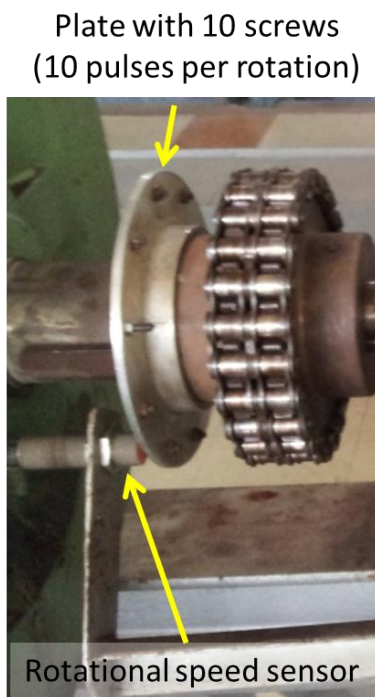


Fig. 5.20. Rotational speed sensor



Fig. 5.21. Checking the readings with a hand held tachometer.

5.5.1.7. Calibration Error Summary

The error of each instrument arising from calibration is provided in Table 5.1. It can be seen that the highest source of error was the flow meter.

Table 5.1. Systematic error of each instrument.

Instrument	Relative Error δ [%]
Pressure (p_1)	± 0.1
Pressure (Depth)	± 0.1
Flow Rate	± 0.5
Torque	± 0.05
Rotational Speed	± 0.05

5.5.2. Estimation of the Uncertainty

5.5.2.1. Systematic Uncertainty

The total calibration error for hydraulic efficiency $(\delta_{\eta h})_s$ calculation was determined by combining the uncertainties of the component measurements by the root-sum-square method Eq. (5.9). The total error in the calibration becomes a systematic error in the measured quantity when this calibration is used for subsequent model tests (IEC 60193:1999). Therefore using Eq. (5.9) systematic uncertainty in hydraulic efficiency $(\delta_{\eta h})_s$ was equal to ± 0.5 %.

Uncertainty related to the density $(\delta_{\rho})_s$ was assumed to be less or equal to ± 0.1 %. This was done because the density of water changes by only 0.1 % in the whole range of water temperatures observed during all the tests, which was 20° to 24° at 60 m pressure head.

$$(\delta_{\eta h})_s = \sqrt{(\delta_p)_s^2 + (\delta_Q)_s^2 + (\delta_{\rho})_s^2 + (\delta_{\omega})_s^2 + (\delta_M)_s^2} \quad (5.9)$$

5.5.2.2. Random Uncertainty

The uncertainty was determined by repeating measurements at one operating point. The operating point was the best efficiency point of the original runner. Using the best efficiency point conditions ensured that the system is at its most stable state. A total of 5 samples were taken for this analysis. The procedure described in Annex L (*Analysis of random uncertainties for a test at constant operating conditions*) of the international testing standard (IEC 60193:1999) was followed and presented in Table 5.2.

Table 5.2. Calculating the random uncertainty.

#	Measured Values Y_i^*	$\bar{Y} - Y_i$	$(\bar{Y} - Y_i)^2$
1	1.0016	-0.001598	2.55228×10^{-6}
2	1.0014	-0.001399	1.95711×10^{-6}
3	0.9972	0.002778	7.71661×10^{-6}
4	0.9993	0.000689	4.75349×10^{-7}
5	1.0005	-0.000471	2.21634×10^{-7}
	$\bar{Y} = 1$	n/a	$\Sigma = 1.29230E \times 10^{-5}$

*Normalised to the average $\bar{\eta}$

Estimated standard deviation of the observations:

$$s_Y = \sqrt{\frac{\Sigma(\bar{Y} - Y_i)^2}{n - 1}} = 0.001797$$

Random uncertainty associated with the mean value at the 95 % confidence level:

$$(\Delta_Y)_r = \pm \frac{t \cdot s_Y}{\sqrt{n}} = \pm 0.002231$$

$$(\delta_Y)_r = \frac{(\Delta_Y)_r}{\bar{Y}} \times 100 \% = \pm 0.2 \%$$

5.5.2.3. Total Uncertainty

The total uncertainty of this experimental testing:

$$\delta_t = \pm \sqrt{\delta_s^2 + \delta_r^2} = \pm \sqrt{0.5^2 + 0.2^2} = \pm 0.6 \%$$

The total uncertainty of $\pm 0.6 \%$ was considered to be acceptable. Moreover, since the main objective of this project was to improve the efficiency of an existing original design and the optimised design was compared to the original design under the same conditions it is the random uncertainty $(\delta_Y)_r$ which actually matters.

5.5.3. Datum for Normalising the Results

All efficiencies measured during the 1st set of tests that are presented in the following section are normalised to the measured peak efficiency of the original runner operating with both jets (Fig. 5.23).

5.5.4. Test Results

5.5.4.1. Original Runner Both Jets Operation

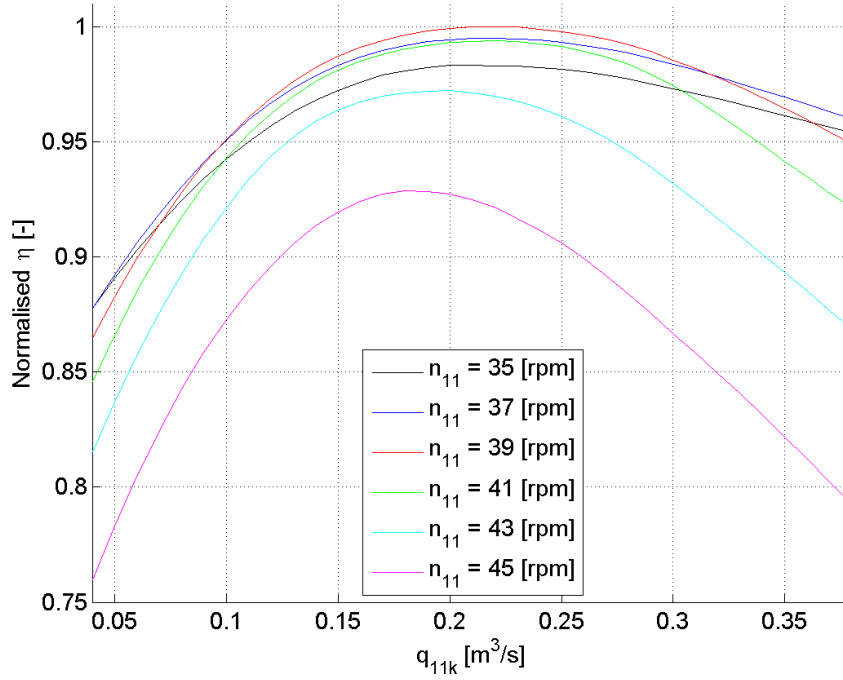


Fig. 5.22. Original runner in both jets operation: normalised efficiency vs. specific flow rate curves.

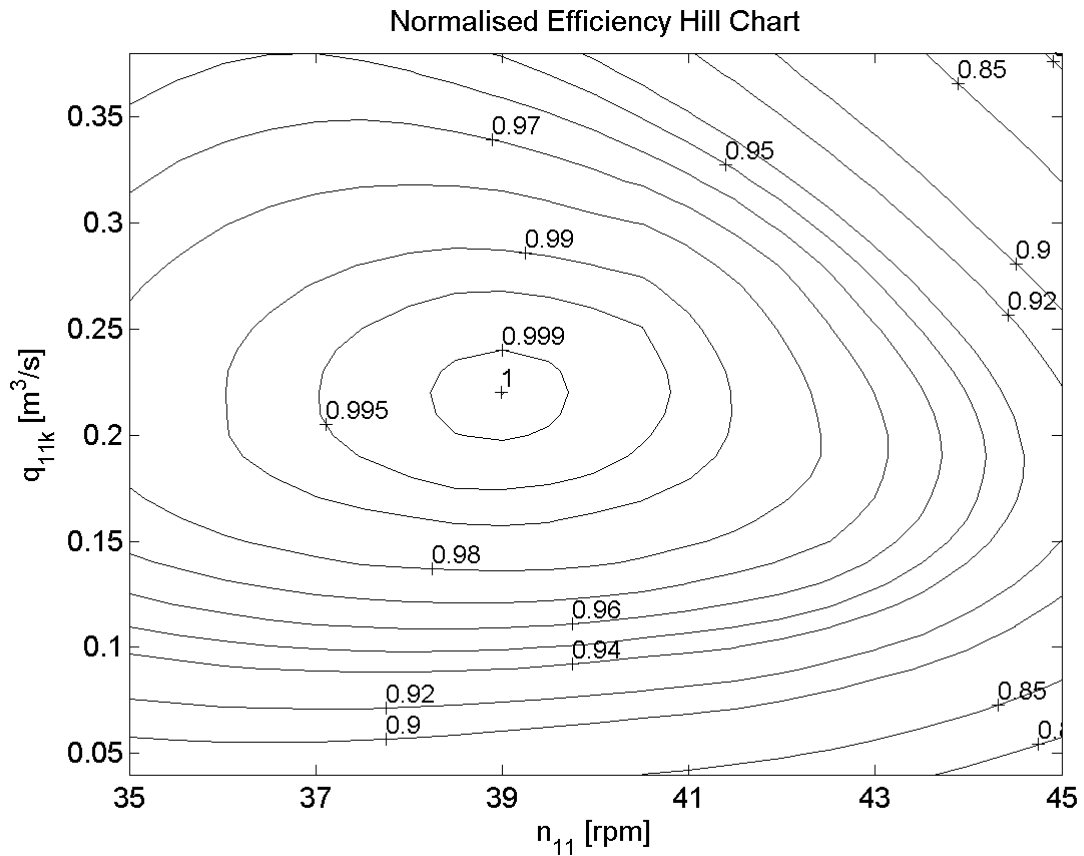


Fig. 5.23. Original runner in both jets operation: normalised efficiency hill chart.

5.5.4.2. Original Runner Single Jet Operation

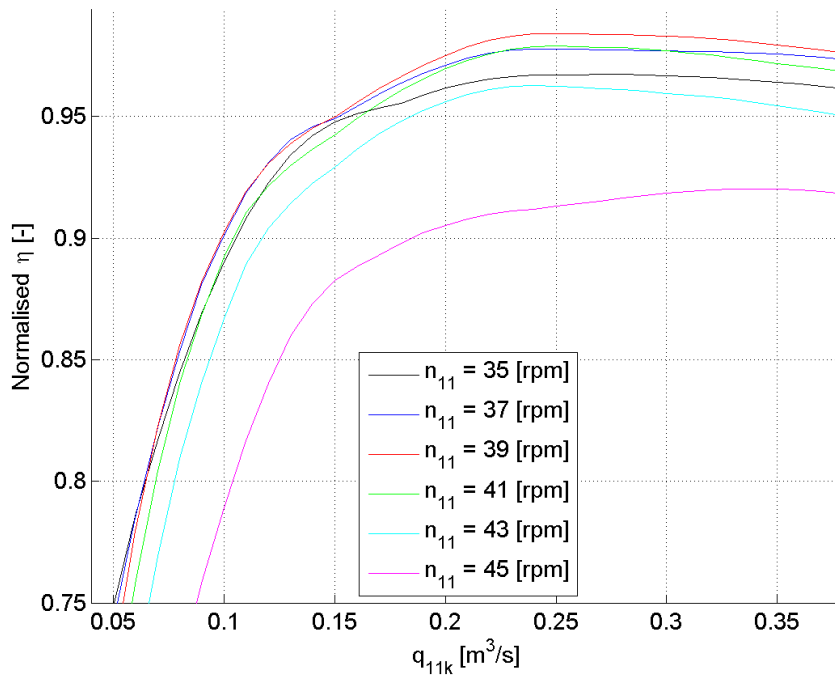


Fig. 5.24. Original runner in single jet operation: normalised efficiency vs. specific flow rate curves.

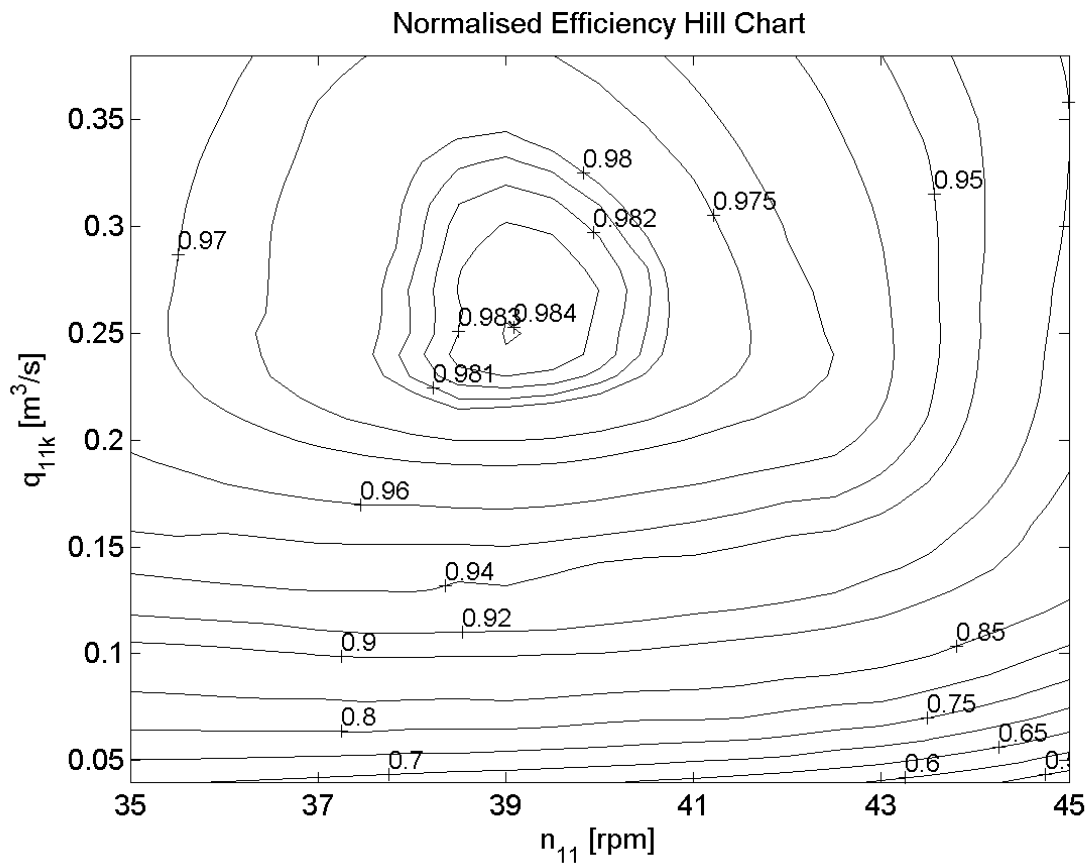


Fig. 5.25. Original runner in single jet operation: normalised efficiency hill chart.

5.5.4.3. Optimised Runner with 18 Buckets Both Jets Operation

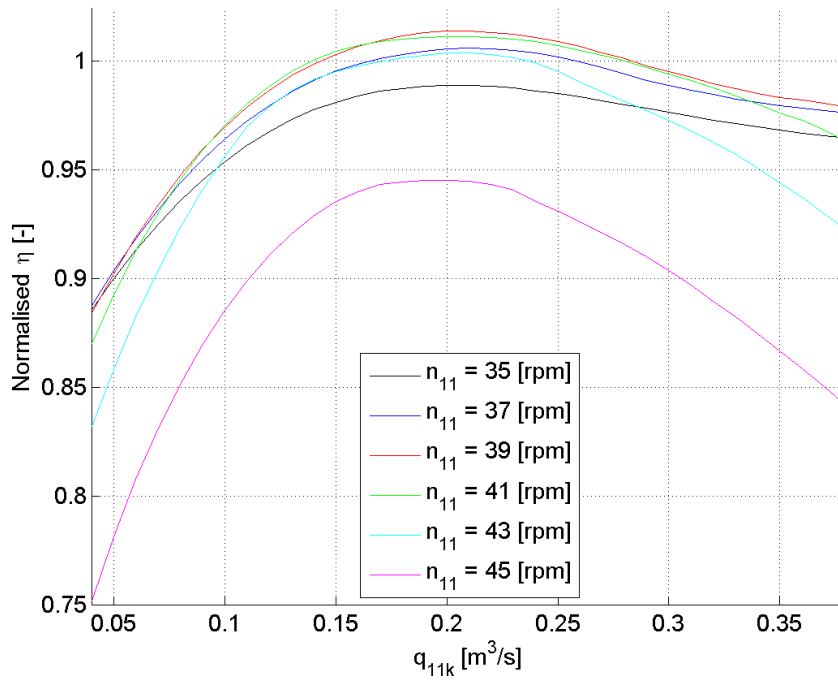


Fig. 5.26. Optimised runner with 18 buckets in both jets operation: normalised efficiency vs. specific flow rate curves.

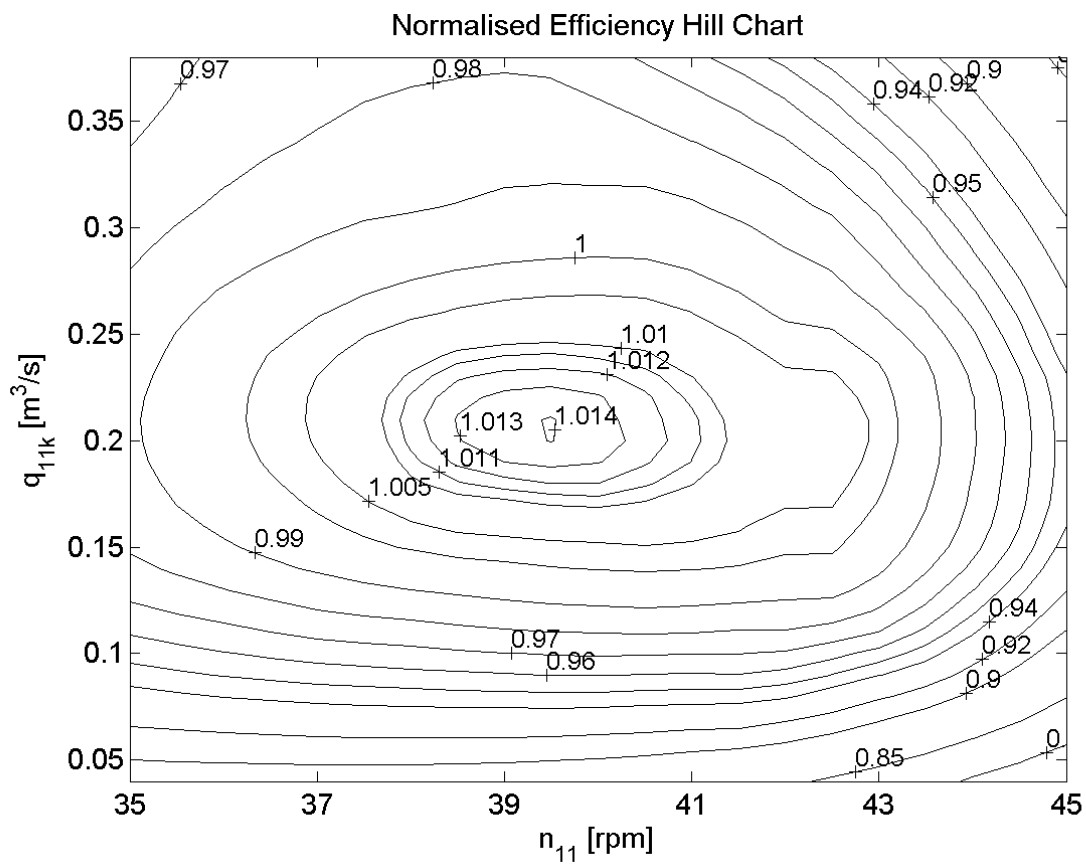


Fig. 5.27. Optimised runner with 18 buckets in both jets operation: normalised efficiency hill chart.

5.5.4.4. Optimised Runner with 18 Buckets Single Jet Operation

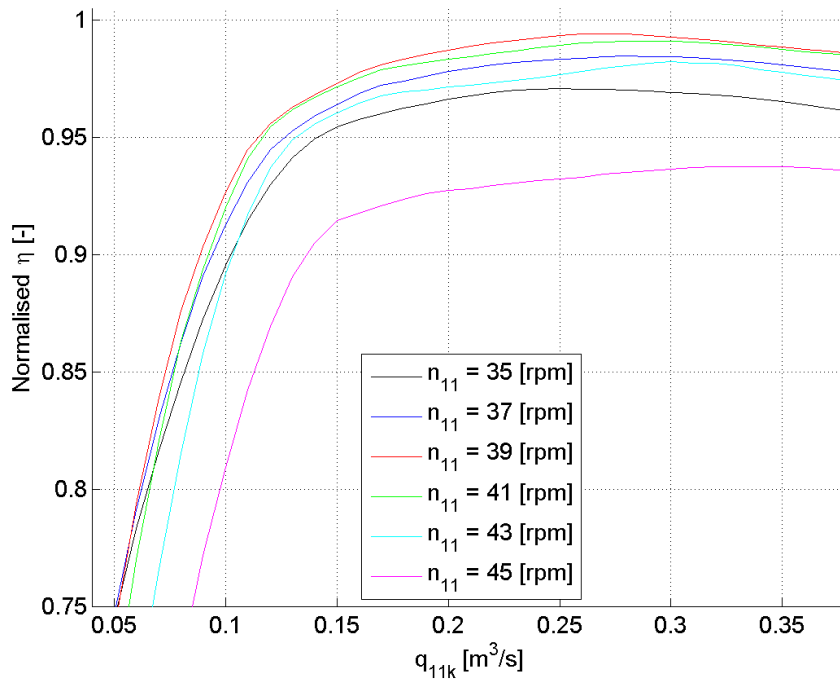


Fig. 5.28. Optimised runner with 18 buckets in single jet operation: normalised efficiency vs. specific flow rate curves.

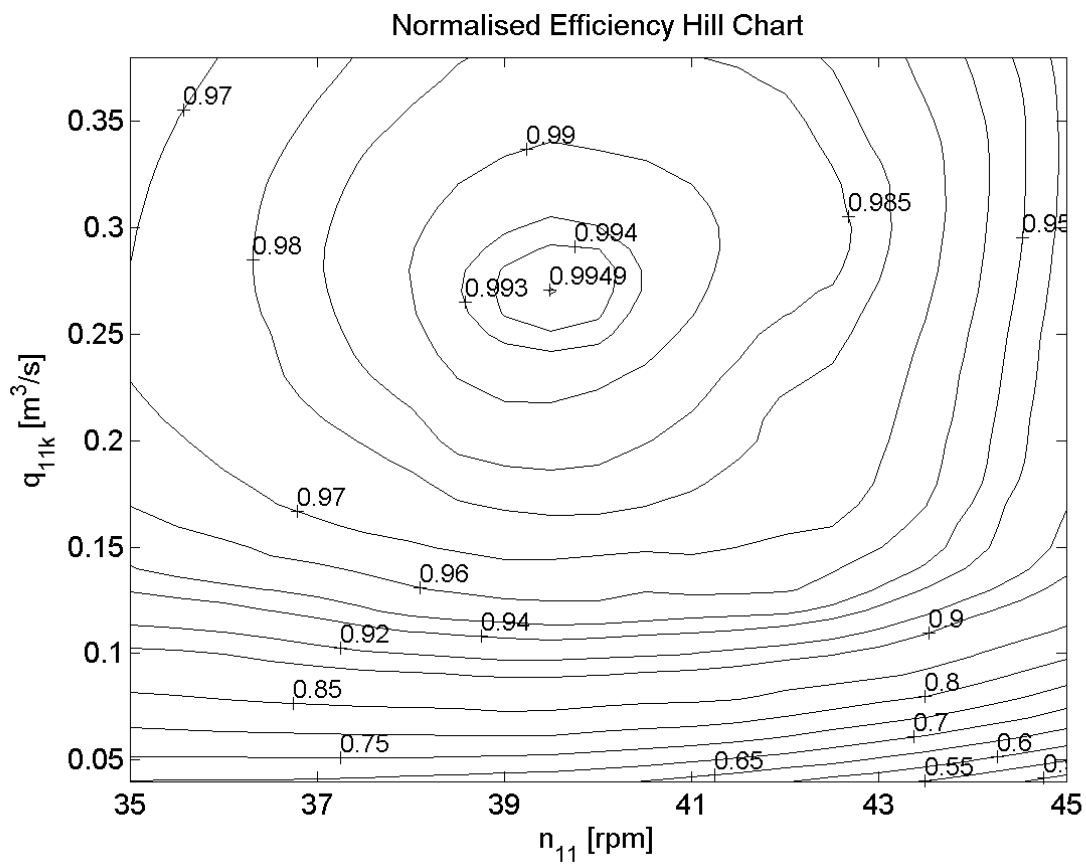


Fig. 5.29. Optimised runner with 18 buckets in single jet operation: normalised efficiency hill chart.

5.5.4.5. Summary of 1st Set of Testing Results

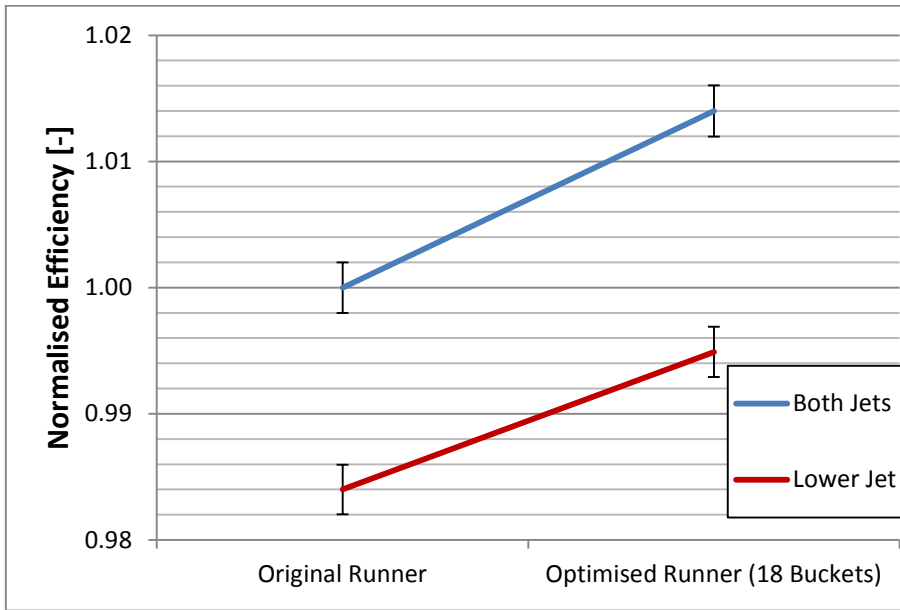


Fig. 5.30. Summary of best efficiency point results for each design tested.

5.5.5. Estimation of the Mechanical Losses

The mechanical losses have to be estimated to allow comparison of the experimentally measured results and the numerical results. Torque measuring device with “bearing of rotating parts not in balance” provides measurements of the shaft torque M_s that has to be corrected for the friction torque M_f . Torque on the runner M_m used to calculate the hydraulic efficiency can be found using equation (5.10).

$$M_m = M_s + M_{Lm} \quad (5.10)$$

The disk friction losses and leakage losses (volumetric losses) are included and are considered here as hydraulic losses (IEC 60193:1999). The disk friction losses are the friction losses of the outer surfaces of the runner not in contact with the flow passing the blades. For Pelton turbine, disc friction losses are the friction losses caused by the air drag on the rotating runner. Two methods were used to estimate the friction losses.

5.5.5.1. Estimation Method 1

In Pelton turbine mechanical losses can be measured by rotating the runner without injecting any water ($Q = 0 \text{ m}^3/\text{s}$). This way torque caused by the bearing friction and the disc friction can be measured for different range of rotating speeds as presented in Fig. 5.31 (blue curve). However, this does not provide separate information on the amount of disc friction torque and the bearing friction

torque. Therefore, having only this data it is impossible to correct for the bearing friction losses while including the disc friction losses into the hydraulic efficiency calculation or in other words consider it as the hydraulic losses.

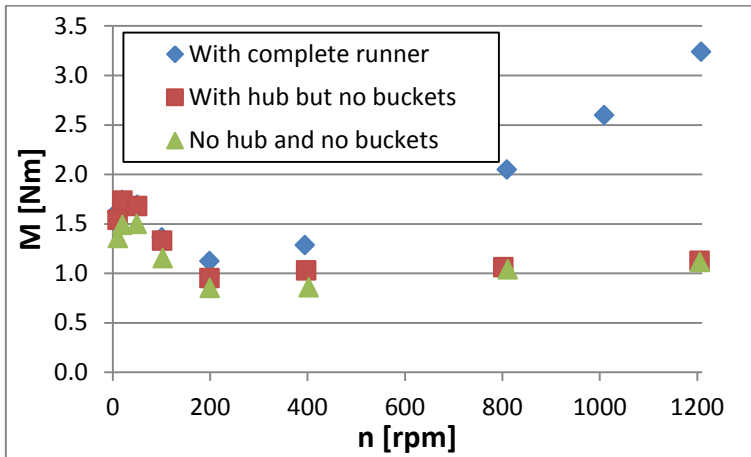


Fig. 5.31. Friction torque vs. the rotational speed when $Q = 0 \text{ m}^3/\text{s}$.

That is why it was decided to measure the torque against the rotational speed at $Q = 0 \text{ m}^3/\text{s}$ with only the hub but no buckets (Fig. 5.31 red curve) as shown in Fig. 5.32 and with no hub on the shaft whatsoever (Fig. 5.31 green curve). It can be seen that adding a hub of $m = 9.6 \text{ kg}$ at the end of a shaft did not affect the friction torque in the region of relevant rotational speeds (850 to 1100 rpm). Therefore it was assumed that the difference in the measured friction torque between a complete runner and a hub with no buckets is the disc friction torque.



Fig. 5.32. Friction torque measurements with only a hub but no buckets.

Bearing friction losses and the disc friction losses for single jet and both jets operation at the best efficiency point are provided in Fig. 5.33 and Fig. 5.34 respectively. Using this method the lower limit of the bearing friction losses can be estimated assuming that increasing the loading on the runner by the jet loading can only increase this friction torque or have minor effect but not reduce it. The estimated bearing friction losses at the best efficiency point are 0.4 % for the single jet operation and 0.7% for the operation with both jets.

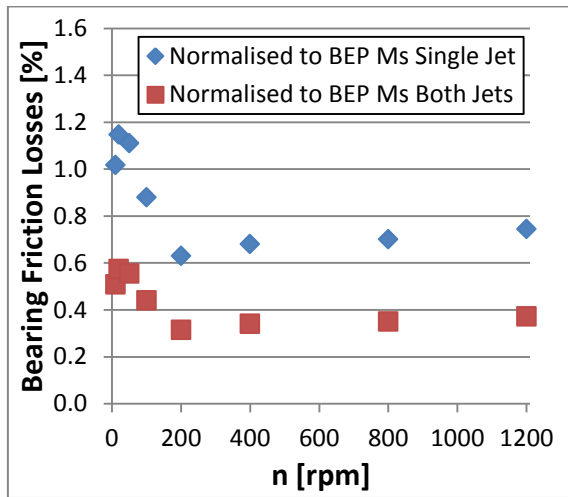


Fig. 5.33. Bearing friction losses calculated using the measured torque at the BEP.

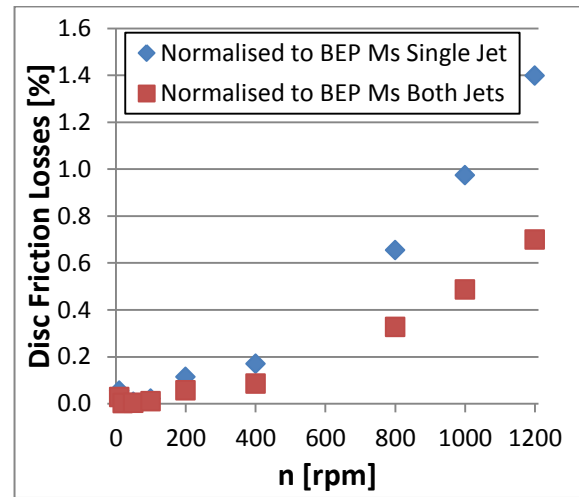


Fig. 5.34. Disc friction losses calculated using the measured torque at the BEP.

5.5.5.2. Estimation Method 2

Another way to estimate the friction losses is by analysing the efficiency difference in single jet and both jets operation. Efficiency increase in both jets operation was observed. This is because the bearing friction torque and the disc friction torque remain unchanged or almost unchanged whereas the torque on the runner caused by the jets is doubled meaning that the friction losses are now shared between the two jets. This way the friction torque M_{Lm} can be calculated:

Friction torque is a sum of the bearing friction torque and the disc friction torque.

$$M_{Lm} = M_B + M_D \quad (5.11)$$

To calculate the torque measured on the shaft M_s the friction torque has to be subtracted from the torque caused by the jets M_J and multiplied by number of jets N_J .

$$(M_s)_{N_J} = N_J M_J - M_{Lm} \quad (5.12)$$

The measured efficiency for different number of jets is equal to the torque measured on the shaft times the rotational speed and divided by the input power of one jet and the number of jets.

$$\eta_{N_J} = \frac{M_s \omega}{N_J P_{in}} \quad (5.13)$$

Then the ratio between the measured efficiency using both jets and one jet can be expressed as:

$$\frac{\eta_2}{\eta_1} = \frac{(M_s)_2}{2P_{in}} \cdot \frac{P_{in}}{(M_s)_1} = \frac{(M_s)_2}{2(M_s)_1} = \frac{2M_J - M_{Lm}}{2(M_s)_1} = 1 + \frac{M_{Lm}}{2(M_s)_1} \quad (5.14)$$

Rearranging it the friction torque can be found.

$$M_{Lm} = 2(M_s)_1 \left(\frac{\eta_2}{\eta_1} - 1 \right) \quad (5.15)$$

For the original runner operating at the best efficiency point, the friction torque was found equal to 4.6 Nm (at $n = 945$ rpm). Expressed as a ratio between the friction torque and the measured torque it was:

$\frac{M_{Lm}}{(M_s)_1} = 3.6\%$ for the single jet operation and $\frac{M_{Lm}}{(M_s)_2} = 1.8\%$ for the operation with both jets. The friction values calculated using method 1 at the rotational speed $n = 945$ rpm provide ratios of 1.9 % and 0.9 % respectively (using friction torque data measured with complete runner provided in Fig. 5.31).

There are three possible explanations for this mismatch:

- 1) The disc friction losses increase as the runner is in operation as oppose to when it is rotating at the same speed but with no flow. When the runner is rotating the drag is caused by the air. When the turbine is in operation in addition to the air the drag force maybe caused by the splashing water and mist created as a result.
- 2) The assumption that jet loading and the weight of buckets do not increase the bearing friction torque is not correct.
- 3) Measurements of such low torque values were inaccurate.

5.5.6. Problems and Recommendations

Some problems were experienced during the testing. The main issue was the amount of spurious errors causing scattered results or even temporary drops in efficiency for a group of consecutive data points. Control points in the test plan were used to indicate these problems and suggest when the test or part of the test in between the control points needs to be repeated. Fig. 5.35 provides an example of control points that indicate problems in the test. The power output readings were indicated as the source of error. Since the rotational speed measurements were double checked by additional instruments as described in section 5.5.1.6 Rotational Speed Sensor it was suggested to replace the old torque meter with a brand new one to increase the stability in future tests. Even though the calibration linearity of the old torque meter was excellent attention has to be made that the torque meter was calibrated in

static conditions as oppose to its operation at high rotational speeds. Assumption was made that unreliable results were successfully removed by using these control points and repeating the suspicious data points.

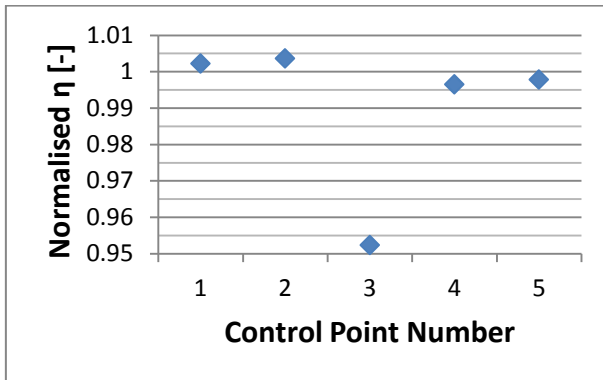


Fig. 5.35. Example of control points indicating problems in the testing.

5.6. 2nd Set of Tests

This set provides results of the Optimised runners with 18 buckets and 15 buckets. This set was performed after the results of the 1st set of tests showed that the bucket geometry was successfully optimised. The Optimised runner with 18 buckets was retested to become a baseline for comparison with the Optimised runner with 15 buckets. Establishing of the new baseline was required to cancel out the systematic uncertainty and to allow the back to back comparison after the torque meter was upgraded. The new torque meter was a rotary torque transducer (manufacturer: Datum electronics, model: M425) and is shown in Fig. 5.36.

2nd set of tests was performed in January 2015 giving half a year difference from the 1st set of tests.



Fig. 5.36. New torque meter.

5.6.1. Calibration

Identical procedure of instrument calibration was performed as in the 1st set of tests. The error of each instrument arising from calibration is provided in Table 5.3.

Table 5.3. Systematic error of each instrument.

Instrument	Relative Error δ [%]
Pressure (p_1)	± 0.1
Pressure (Depth)	± 0.1
Flow Rate	$\pm 1^*$
Torque	± 0.1
Rotational Speed	± 0.05

*As explained in section 5.5.1.4 the calibration linearity and therefore systematic error of the flow meter was inevitably prone to the human error. That is why the systematic error of the flow meter was so different between the 1st (Table 5.1) and 2nd sets of tests.

5.6.2. Estimation of the Uncertainty

5.6.2.1. Systematic Uncertainty

The total calibration error for hydraulic efficiency $(\delta_{\eta})_s$ was determined in the same way as it was done for the 1st set of tests. I.e. it was calculated by combining the uncertainties of the component measurements by the root-sum-square method Eq. (5.9). Therefore using this equation and the data provided in Table 5.3, the systematic uncertainty in hydraulic efficiency $(\delta_{\eta})_s$ for the 2nd set of tests was found to be equal to $\pm 1\%$.

5.6.2.2. Random Uncertainty

The random uncertainty was determined by repeating measurements at one operating point. The chosen operating point was the control point (single jet) which is close to the best efficiency point of the optimised runner with 18 buckets. A total of 12 samples were taken for this analysis. The procedure described in Annex L (*Analysis of random uncertainties for a test at constant operating conditions*) of the international testing standard (IEC 60193:1999) was followed.

Table 5.4. Calculating the random uncertainty.

#	Measured Values Y_i^*	$\bar{Y} - Y_i$	$(\bar{Y} - Y_i)^2$
1	1.0000	-0.00003	7.40215×10^{-10}
2	1.0024	-0.00242	5.87839×10^{-5}
3	1.0001	-0.00014	1.92516×10^{-8}
4	0.9998	0.00021	4.27361×10^{-8}
5	1.0001	-0.00014	1.92744×10^{-8}
6	0.9982	0.00179	3.18723×10^{-6}
7	1.0000	-0.00003	8.23546×10^{-10}
8	1.0006	-0.00062	3.79995×10^{-7}
9	1.0000	0.00002	3.14222×10^{-10}
10	1.0000	-0.00002	3.53085×10^{-10}
11	0.9989	0.00109	1.17731×10^{-6}
12	0.9997	0.00030	8.90882×10^{-8}
	$\bar{Y} = 1$	n/a	$\Sigma = 1.07955 \times 10^{-5}$

*Normalised to the average \bar{Y}

Estimated standard deviation of the observations:

$$s_Y = \sqrt{\frac{\sum(\bar{Y} - Y_i)^2}{n - 1}} = 0.000991$$

Random uncertainty associated with the mean value at the 95 % confidence level:

$$(\varepsilon_Y)_r = \pm \frac{t \cdot s_Y}{\sqrt{n}} = \pm 0.00063$$

$$(\delta_Y)_r = \frac{(\varepsilon_Y)_r}{\bar{Y}} \times 100 \% = \pm 0.1 \%$$

5.6.2.3. Total Uncertainty

The total uncertainty of this experimental testing:

$$\delta_t = \pm \sqrt{\delta_s^2 + \delta_r^2} = \pm \sqrt{1.0^2 + 0.1^2} = \pm 1.0 \%$$

The systematic uncertainty in this set of tests was higher than in the 1st set of tests. However, the main objective of this set of tests was to compare the optimised runners with 18 and 15 buckets against each other. For this reason only the random uncertainty was really important and it was reduced to $\pm 0.1 \%$.

5.6.3. Datum for Normalising the Results

All efficiencies measured during the 2nd set of tests that are presented in the following section are normalised to the measured peak efficiency of the optimised runner with 18 buckets operating with both jets (Fig. 5.38).

5.6.4. Test Results

5.6.4.1. Optimised Runner with 18 Buckets Both Jets Operation

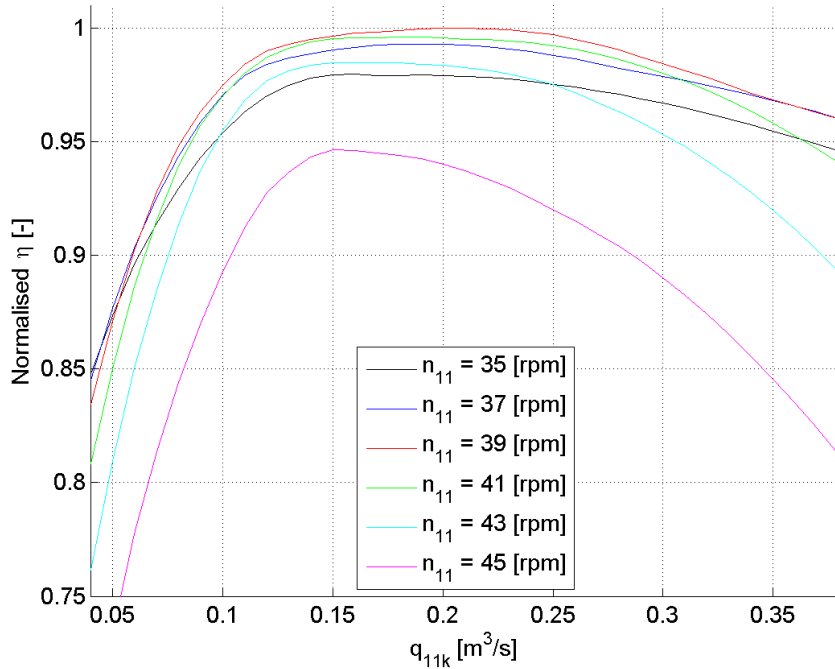


Fig. 5.37. Optimised runner with 18 buckets in both jets operation: normalised efficiency vs. specific flow rate curves.

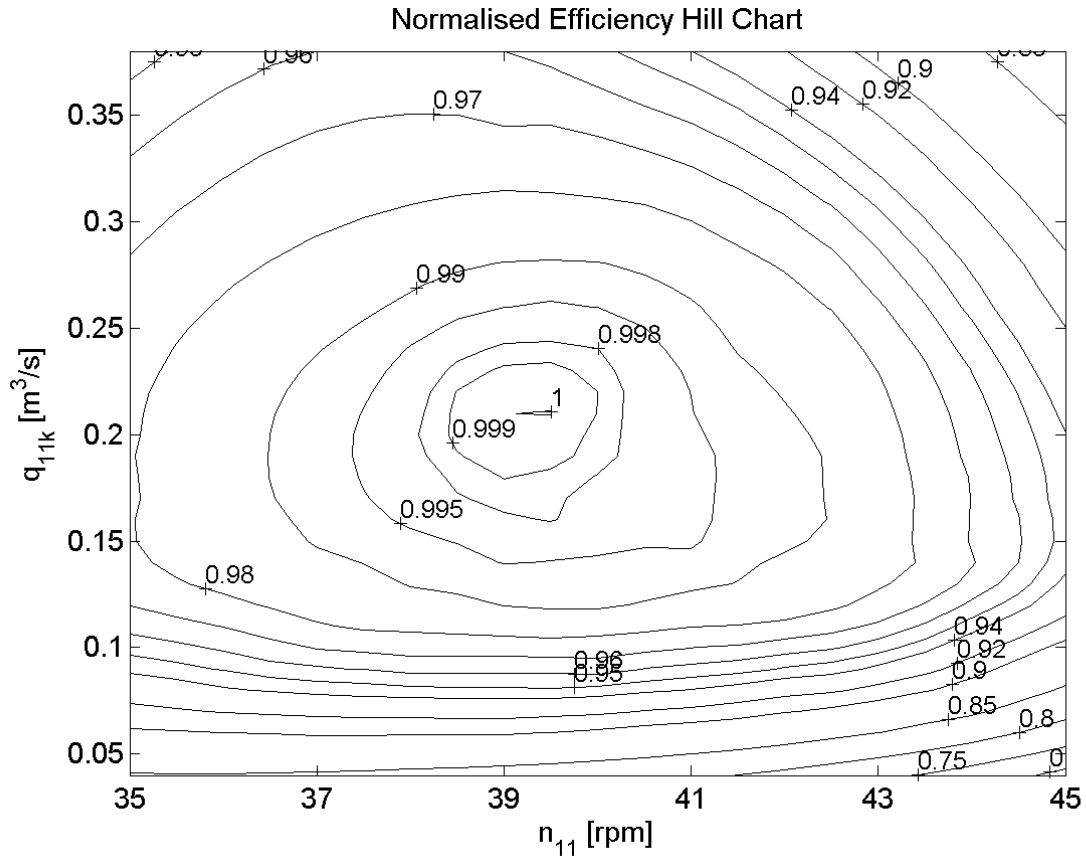


Fig. 5.38. Optimised runner with 18 buckets in both jets operation: normalised efficiency hill chart.

5.6.4.2. Optimised Runner with 18 Buckets Single Jet Operation

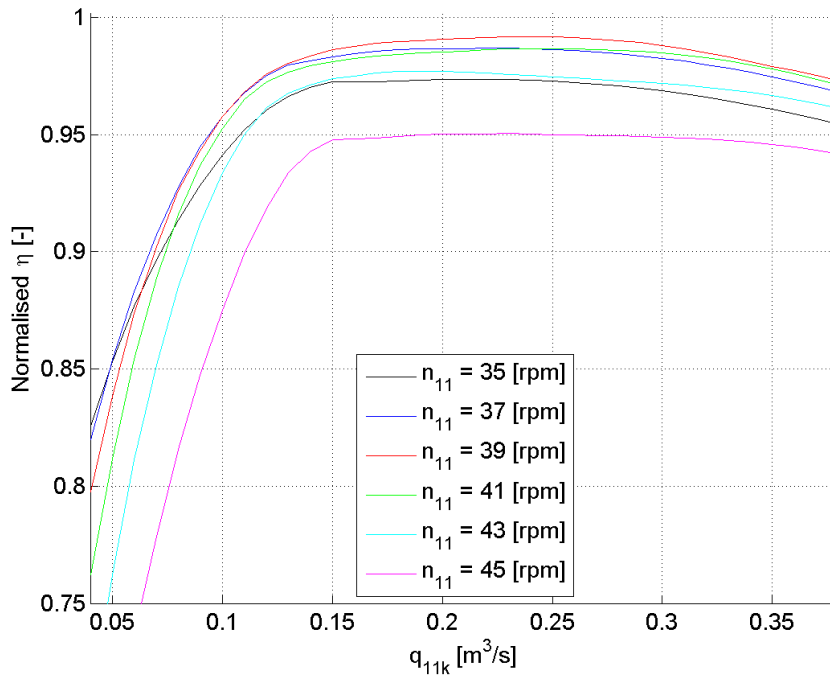


Fig. 5.39. Optimised runner with 18 buckets in single jet operation: normalised efficiency vs. specific flow rate curves.

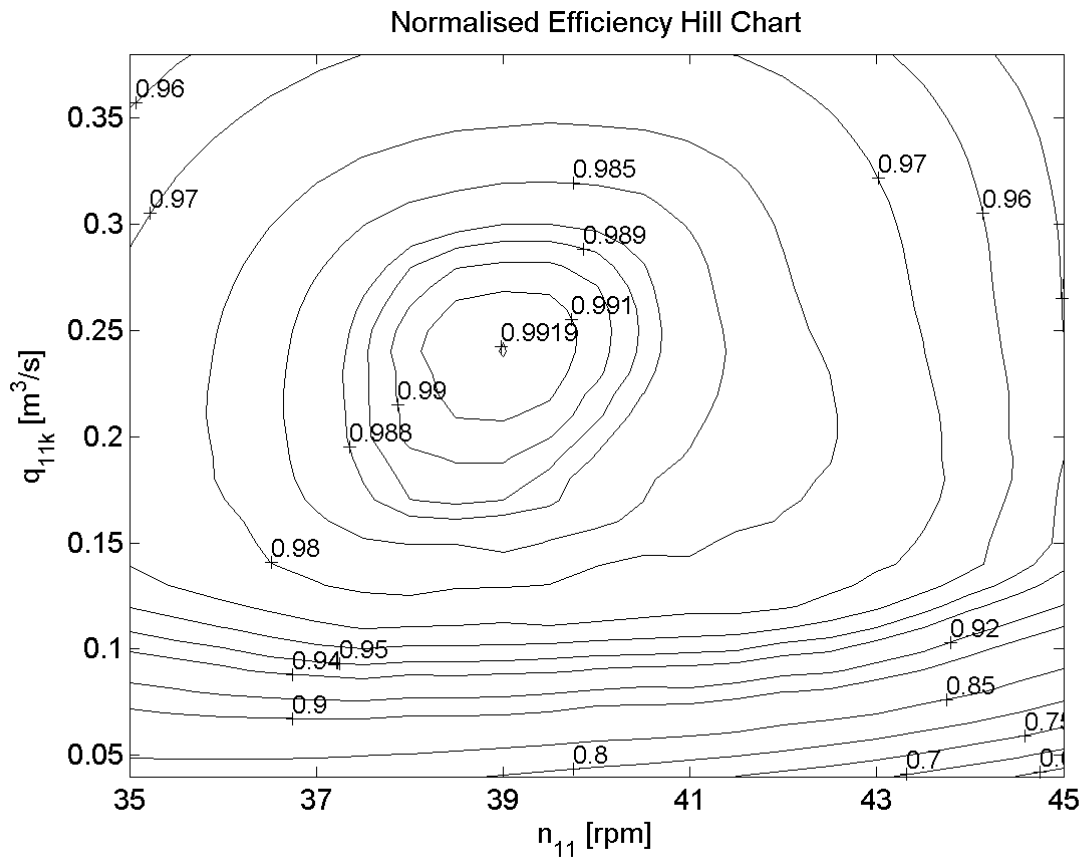


Fig. 5.40. Optimised runner with 18 buckets in single jet operation: normalised efficiency hill chart.

5.6.4.3. Optimised Runner with 15 Buckets Both Jets Operation

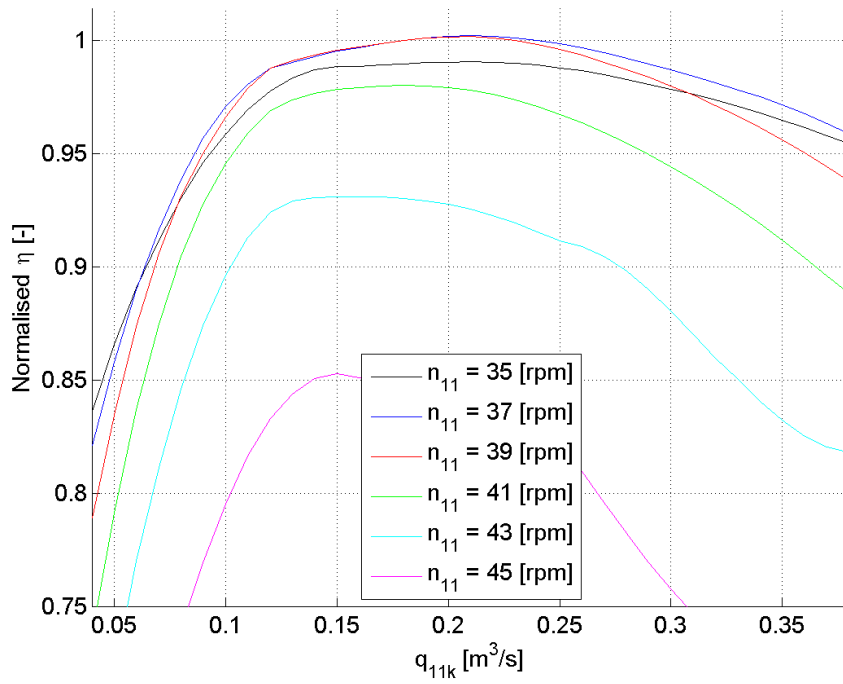


Fig. 5.41. Optimised runner with 15 buckets in both jets operation: normalised efficiency vs. specific flow rate curves.

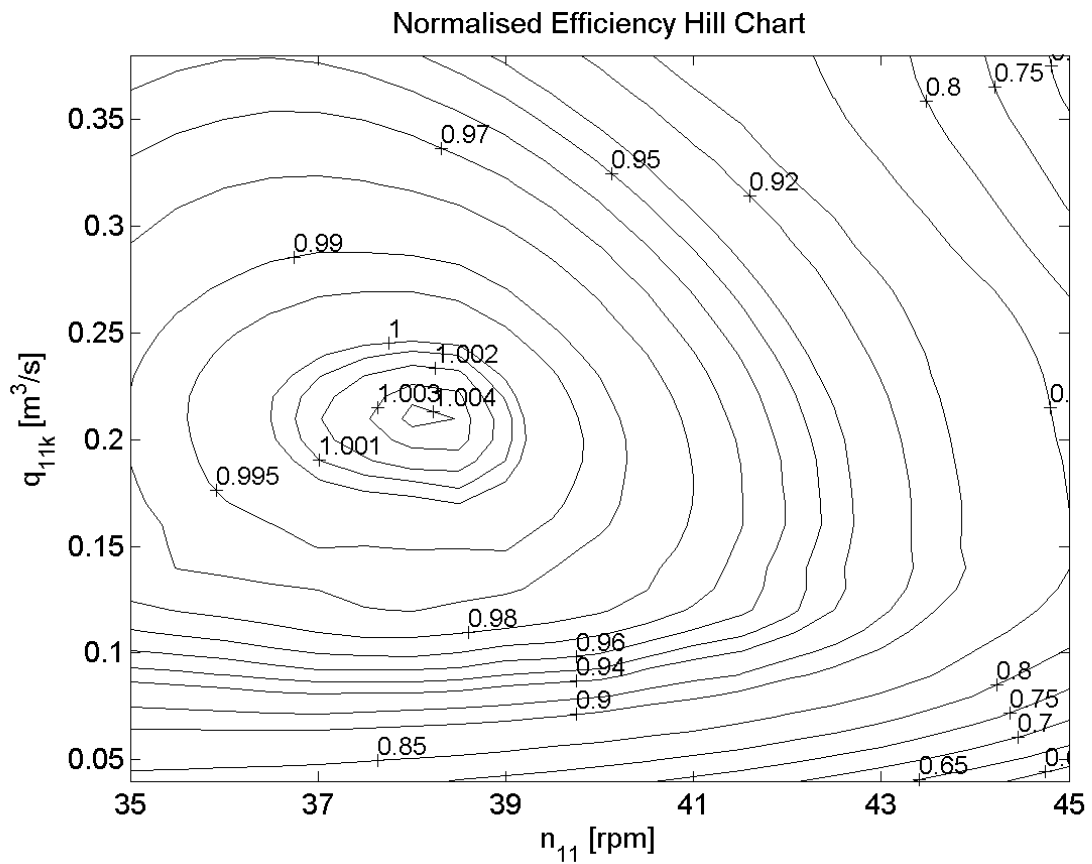


Fig. 5.42. Optimised runner with 15 buckets in both jets operation: normalised efficiency hill chart.

5.6.4.4. Optimised Runner with 15 Buckets Single Jet Operation

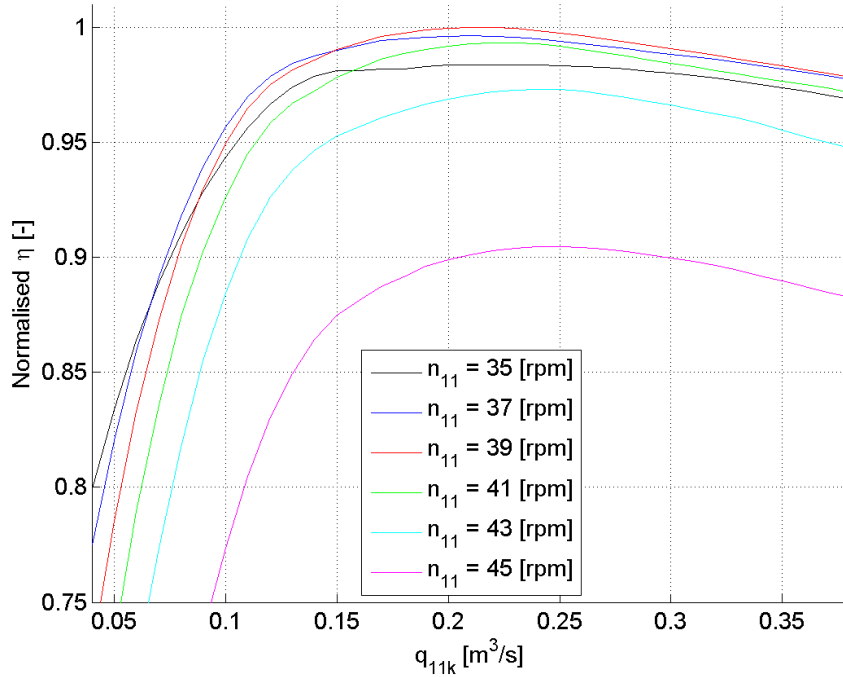


Fig. 5.43. Optimised runner with 15 buckets in single jet operation: normalised efficiency vs. specific flow rate curves.

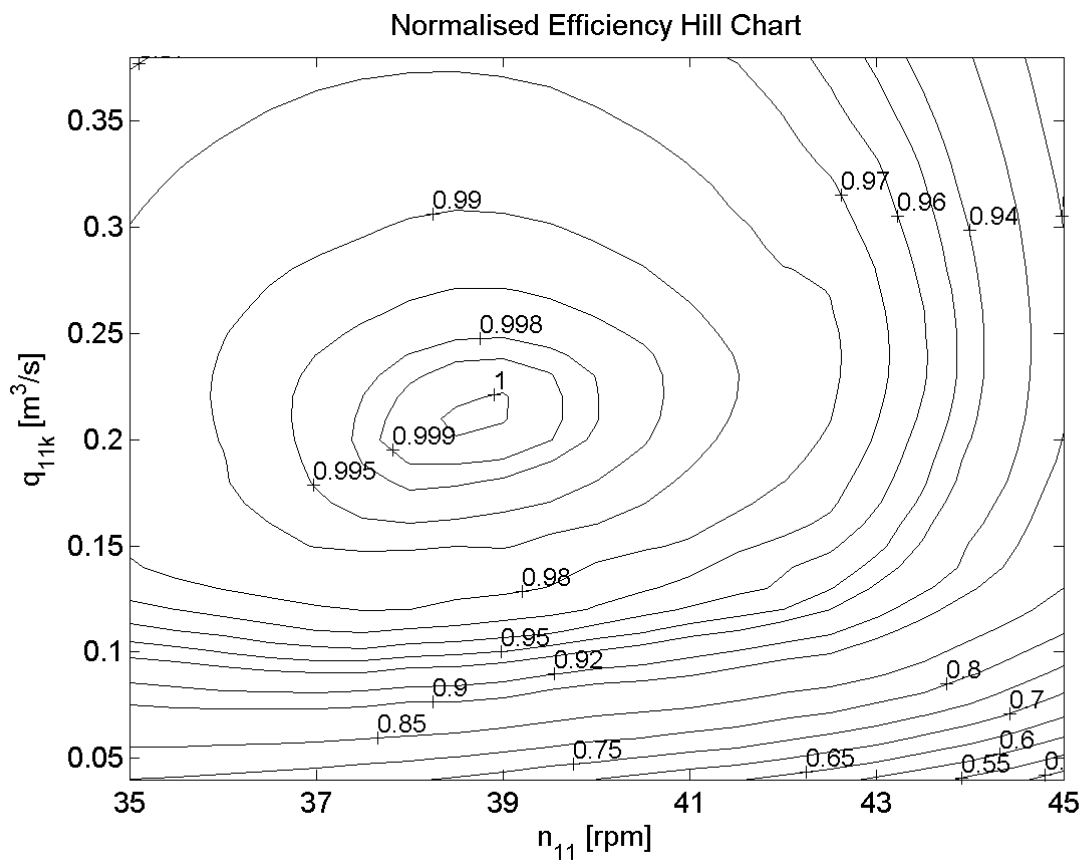


Fig. 5.44. Optimised runner with 15 buckets in single jet operation: normalised efficiency hill chart.

5.6.4.5. Summary of 2nd Set of Testing Results

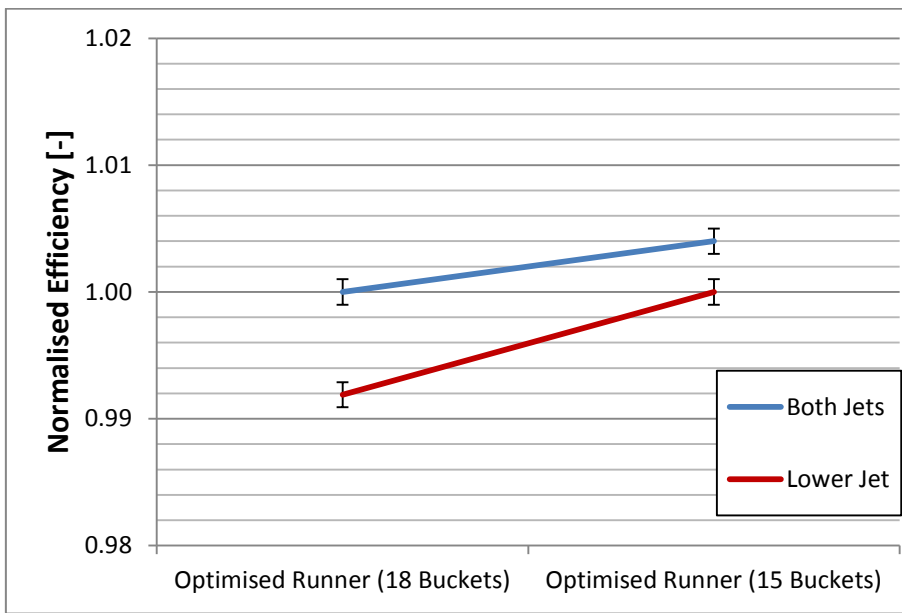


Fig. 5.45. Summary of best efficiency point results for each design tested.

Chapter 6. Results and Discussion

This chapter provides a discussion on the achieved results and includes comparisons of numerical and experimental results and original and optimised runner performance. Limitations of the numerical model and optimisation technique developed during this research are also provided in this chapter.

6.1. Comparison of Numerical and Experimental Results

During the optimisation stage simulations were performed at the original best efficiency point operating conditions that were known from previous testing ($n_{11} = 39.8$ rpm, $q_{11k} = 0.221$ m³/s). Only the single jet operation was modelled assuming that increasing the efficiency in the single jet operation would increase the performance with both jets in operation as well. Therefore a comparison of numerical and experimental results was performed at this operating point using the single jet results.

To compare the CFD simulation results to the experimental data, different sources of the hydraulic and mechanical losses should be taken into consideration. Losses that were present in the experimental testing but were not modelled are:

- Bearing friction losses,
- Disc friction losses,
- Injector losses,
- Water interference due to the casing.

The amount of mechanical losses (bearing and disc friction) was estimated in Chapter 5, section 5.5.5.2 and equal to 1.9 % of the measured efficiency for the single jet operation.

Nozzle losses according to various sources can vary from 0.5 % to 3.4 % (Zhang and Casey 2007, Sharma, Kothari et al. 2011, MESA Associates and Inc. and Oak Ridge National Laboratory 2012, Benzon, Židonis et al. 2015a). To narrow this range and have a better estimation, results from full injector assembly simulations using CFX and Fluent will be used (Benzon, Židonis et al. 2015b) where the estimated losses for a similar design injector at similar spear travel were found to be around 2 %.

It is very difficult to estimate the effect of water interference due to the casing; therefore, the losses from this source were unknown. A comparison of numerical and experimental results is provided in Table 6.1. Results are normalised to the experimentally measured efficiency that was corrected for the estimated mechanical and injector losses. The CFD result taken for comparison is the estimated efficiency at zero grid spacing calculated using Richardson extrapolation (please see Chapter 3, section 3.4.1 *Mesh Convergence Study* for details).

Numerically predicted efficiency was overpredicting the efficiency by 1.8 % compared to the values measured experimentally and corrected for the losses. Considering the error bands for the CFD and the experimental results which were ± 2.3 % and ± 0.3 % respectively, this overprediction is within the error range. Nevertheless, it was expected that CFD results would overpredict the efficiency since the splashing and water interference effect caused by the casing was not included in the CFD model.

Table 6.1. Comparison of CFD and experimental results at $n_{11} = 39.8$ rpm, $q_{11k} = 0.221$ m³/s normalised to the experimentally measured efficiency that was corrected for the estimated mechanical and injector losses.

Normalised CFD η [%]	Normalised Experimental η [%]
	96.2 Measured
	98.0 Corrected for mechanical losses
101.8	100.0 Corrected for injector and mechanical losses

Numerical and experimental results were further examined by comparing the efficiency improvement predicted by CFD to the experimentally measured. In the efficiency improvement values the systematic uncertainty is cancelled out. Therefore this comparison shows an effect that the random uncertainty has on the results.

Fig. 6.1 provides a comparison made at the operating point used for optimisation. Both CFD and experimental results agree that at these conditions efficiency was increased by optimising the bucket shape and then further increased by reducing the number of buckets. However, the predicted magnitude is different from the experimental observations. CFD has overpredicted the effect of the bucket shape (+2.1 % against +1.0 % experimental) and underpredicted the effect of reduced number of buckets (+0.4 % against +0.8 % experimental). Overall the total increase predicted by CFD was 2.5 % whereas the experimentally measured increase at these operating conditions was 1.9 %.

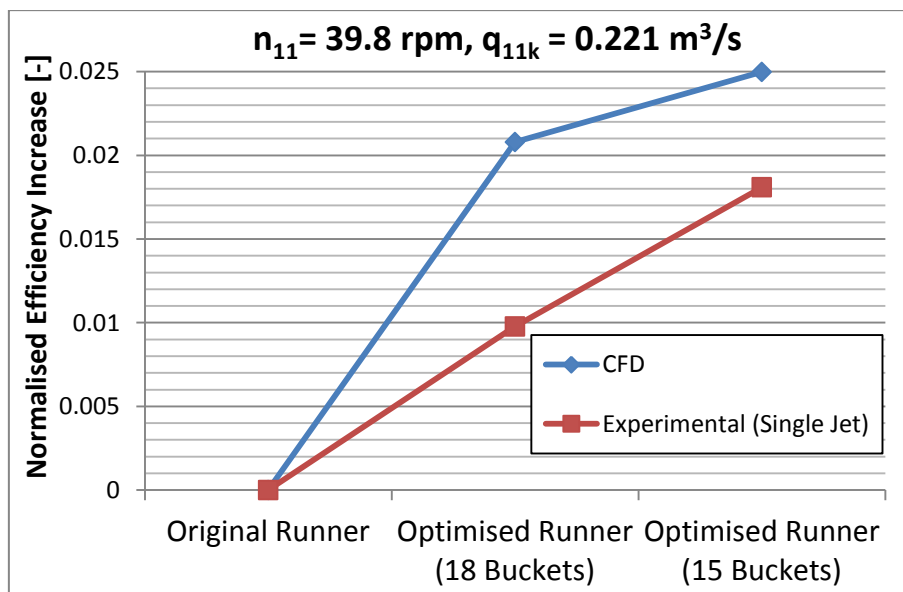


Fig. 6.1. Comparison of efficiency improvement predicted by CFD and measured experimentally at operating point used for optimisation.

The CFD model was based on a number of assumptions that simplified the problem and allowed simulation of Pelton turbine performance within reasonable timescales that were acceptable for optimisation. These assumptions and the expected effect on accuracy were provided in Chapter 3. Further discussion of numerical limitations that could have caused this disagreement between CFD and experimental results will be provided later in this chapter in section 6.3 *Limitations of the CFD Model*.

Comparison provided in Fig. 6.1 shows the experimentally measured improvement at a single operating point. However, experimental results presented in the previous chapter suggest that in some cases the location of the best efficiency point has changed and therefore the overall improvement in the efficiency is different to what is shown in Fig. 6.1. Moreover, Fig. 6.1 presents only the single jet experimental results. Therefore, more detailed analysis of the efficiency and performance improvement based on the experimental results is provided in the following section.

6.2. Comparison of Runner Designs

As discussed previously, the simulations were performed at constant operating conditions of the original best efficiency point using the single jet only. On one hand, this created a risk of optimising the runner only locally, i.e. to improve its efficiency at the BEP conditions but reduce the performance over the whole range of flow rates. On the other hand, there was a chance that outside of the BEP, the efficiency improvement was even higher than at the BEP. Finally, the effect achieved at the single jet operation might have been different to the effect when both jets are in operation. To know the overall improvement, efficiencies of each modification were compared at their best efficiency point disregarding the change of its location. This comparison is presented in Fig. 6.2.

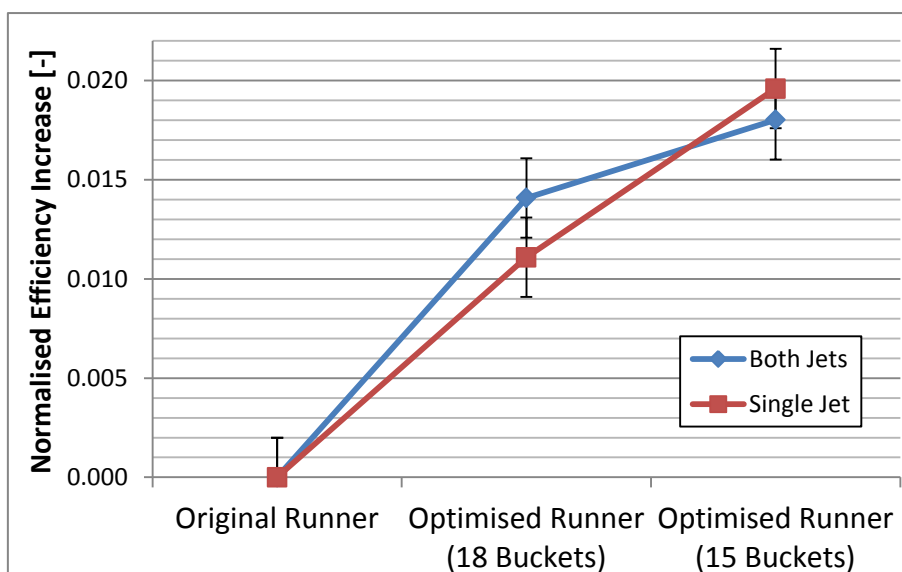


Fig. 6.2. Overall efficiency improvement of each runner compared at their best efficiency point operating conditions – experimental results.

The efficiency improvement achieved was identical within the random uncertainty limits for single and both jets in operation. The overall improvement was approximately 1.9 % of the original efficiency. Individual effects of the bucket shape modification and the reduction in the number of buckets are discussed in the following sections 6.2.1 and 0.

6.2.1. Effect of the bucket shape design modifications

The modified bucket design has increased the best efficiency point performance by 1.4 % of the original efficiency according to the experimental results with both jets in operation (Fig. 6.3) and 1 % according to the single jet results (Fig. 6.4). In both figures three η vs. Q_{11k} curves are presented:

black – original bucket shape performance at the best efficient n_{11} value,

blue – optimised bucket shape performance at the original best efficient n_{11} value,

red – optimised bucket shape performance at the best efficient n_{11} value for the optimised design.

Efficiencies were normalised to the BEP of the original runner in operation with both jets.

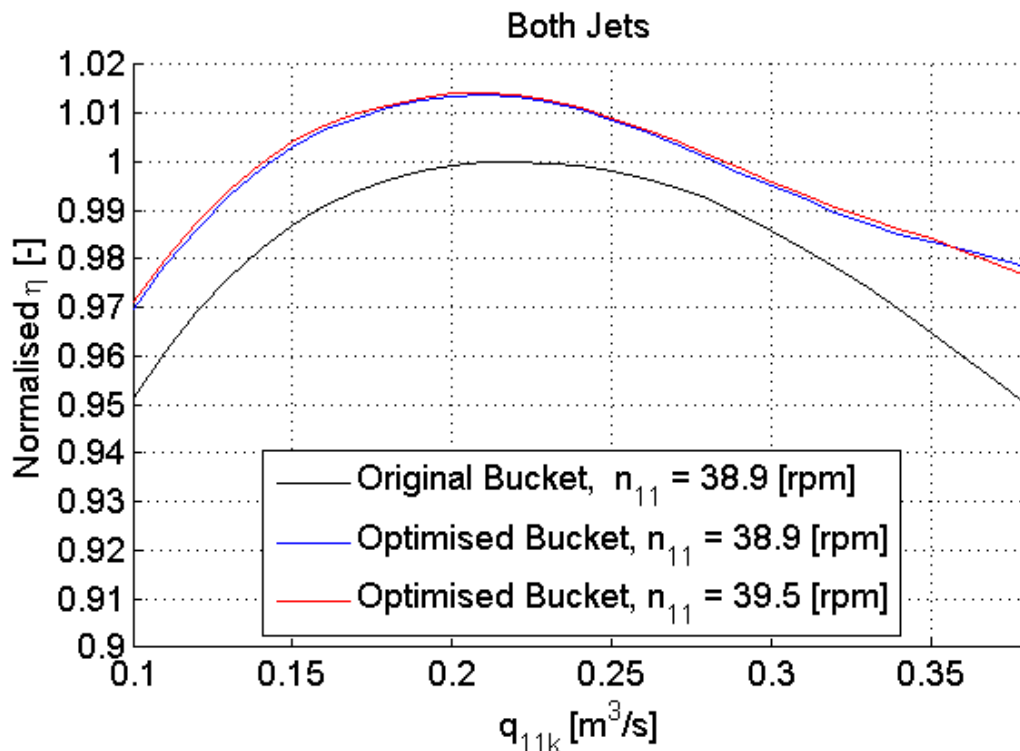


Fig. 6.3. Comparison of runner performance at the best efficient n_{11} using original and optimised bucket designs – both jets in operation.

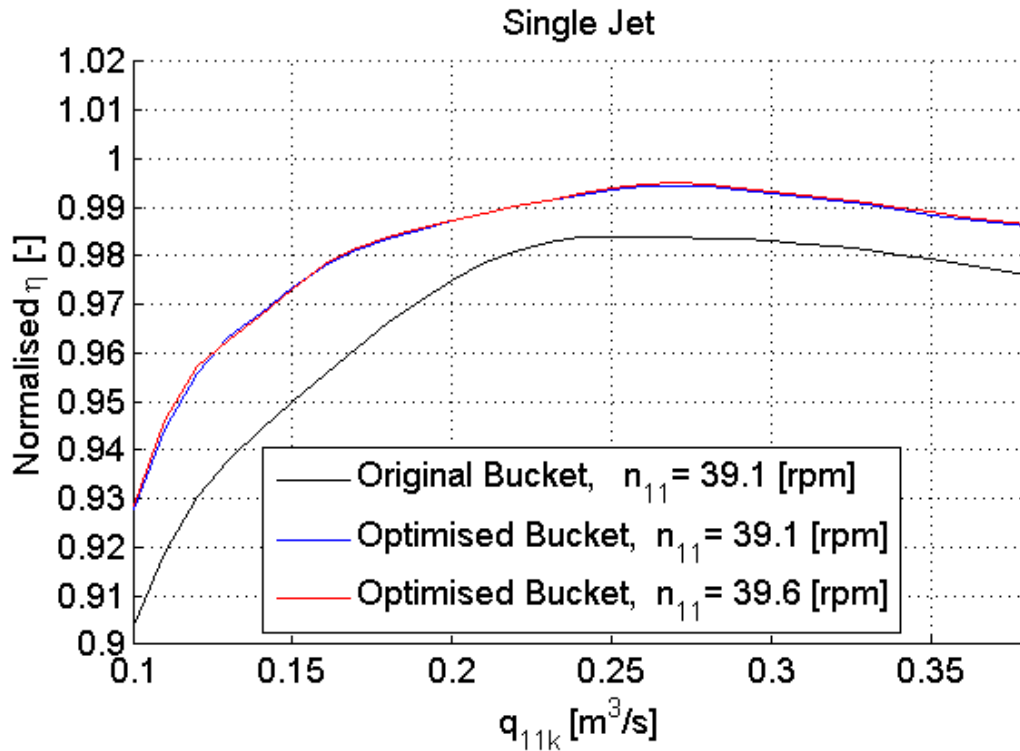


Fig. 6.4. Comparison of runner performance at the best efficient n_{11} using original and optimised bucket designs - single jet operation.

The main design changes, described in detail in Chapter 4 that caused this improvement were:

- The increased length and depth of the bucket.
- Major changes in the cutout shape and the shape of the splitter tip.
- Major changes of the backside of the bucket.
- Readjustment of the bucket position in terms of the radial distance and the inclination angle.

Due to the high computational costs, during the optimisation process the numerical evaluation of the efficiency was performed only at the best efficiency point conditions. Therefore there was a risk of improving the efficiency at the best efficiency point but reducing it over the whole range of flow rates which might be not acceptable. However, Fig. 6.3 and Fig. 6.4 show that the efficiency was successfully improved over the whole range of flow rates. Moreover, in the operation with both jets, the efficiency of the runner with the optimised bucket design is dropping slower than the original giving more than 2.5 % improvement at full capacity. Finally, the optimum rotational speed remained almost unchanged.

6.2.2. Effect of the reduced number of buckets on the runner

After the bucket shape design was improved, the number of buckets was reduced to 15 from the original number of 18. According to various different design guidelines, that usually take into account the ratio between the jet diameter and the runner pitch circle diameter, the minimum suggested number of buckets for Pelton runner used in this case was 17 or 18 (Table 4.5). In any available guidance, the number of 15 buckets on the runner is not suggested for any Pelton runner with any specific speed. However, these guidelines are based on theoretical calculations that include various assumptions that simplify the problem. No publically available experimental or CFD studies identifying the optimum number of buckets were found. That is why the CFD study was performed in this PhD research and is described in detail in Chapter 4, sections 4.3.2 and 4.3.3.

Experimental results suggest that this reduction has increased the efficiency by additional 0.4 % for the operation with both jets (Fig. 6.5) and 0.8 % for the single jet operation (Fig. 6.6). This does not mean that the original runner had too many buckets. Most probably the increase in the bucket size (described in Chapter 4, section 4.3.1) has created this need to reduce the number of buckets for the optimised runner.

Analogically to the η vs. Q_{11k} charts presented in the previous section, 3 curves are presented in each figure. For the single jet operation there is almost no difference in the best efficient n_{11} of the runners with 18 and 15 buckets. However, when both jets are operating, the best efficient n_{11} for 18 and 15 buckets is quite different. I.e. there is a reduction in the best efficient n_{11} for the runner with 15 buckets.

Higher improvement in the efficiency for the single jet operation and the reduction of the best efficient n_{11} indicate that the runner with 15 buckets is experiencing some problems in the two jet operation. The identified problem was the jet interference during the operation with both jets. As the number of buckets is reduced the angle between the buckets is increased. This means that the first jet is entering the bucket for slightly longer time before it gets cut off by the following bucket. Consequently the water from the first jet stays longer in the bucket as presented in Fig. 6.7. Therefore there is a possibility that the second jet starts entering the bucket before the water from the first jet has cleared. The problem of jet interference in the two jet operation was investigated by Wei, Yang et al. (2015) and showed reduction in torque produced by the second jet in the case where the angle between the jets is too small (Fig. 6.8).

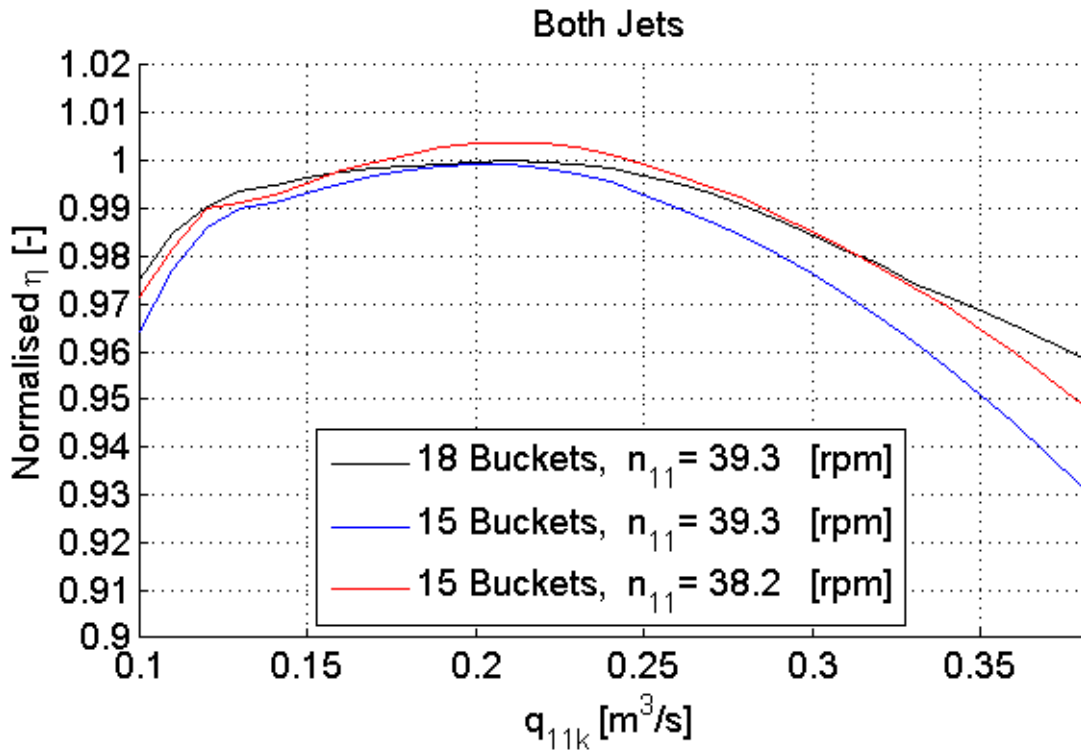


Fig. 6.5. Comparison of the optimised runner performance at the best efficient n_{11} using 18 and 15 buckets – both jets in operation.

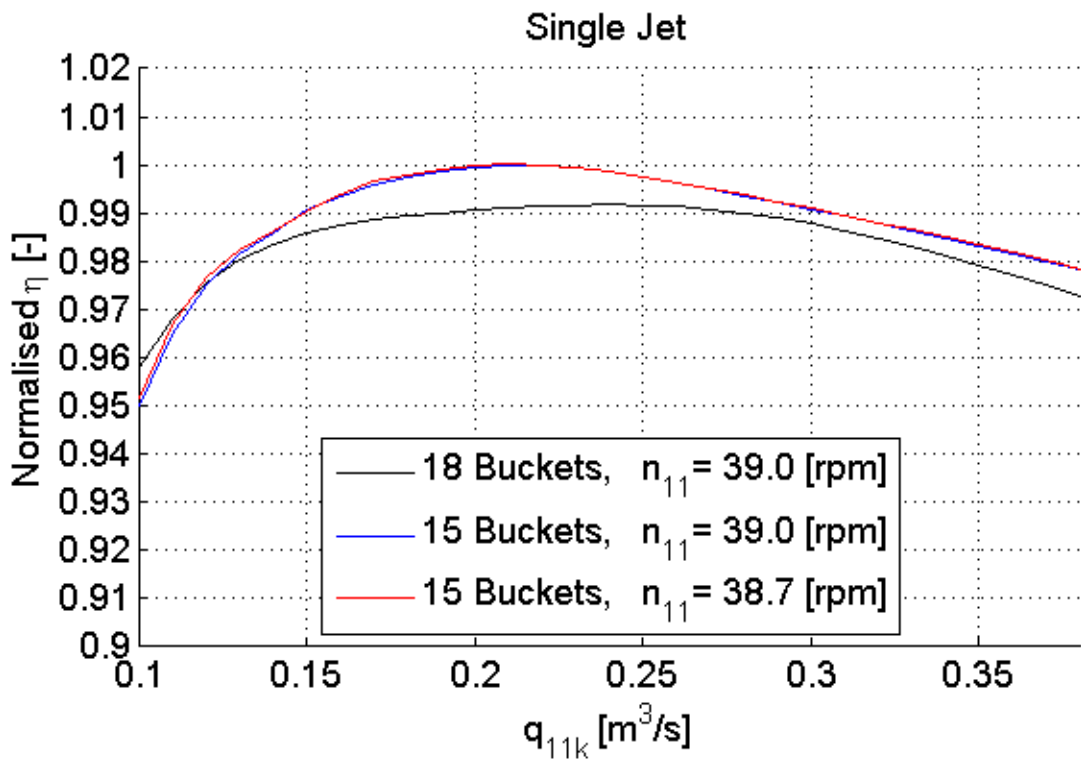


Fig. 6.6. Comparison of the optimised runner performance at the best efficient n_{11} using 18 and 15 buckets – single jet operation.

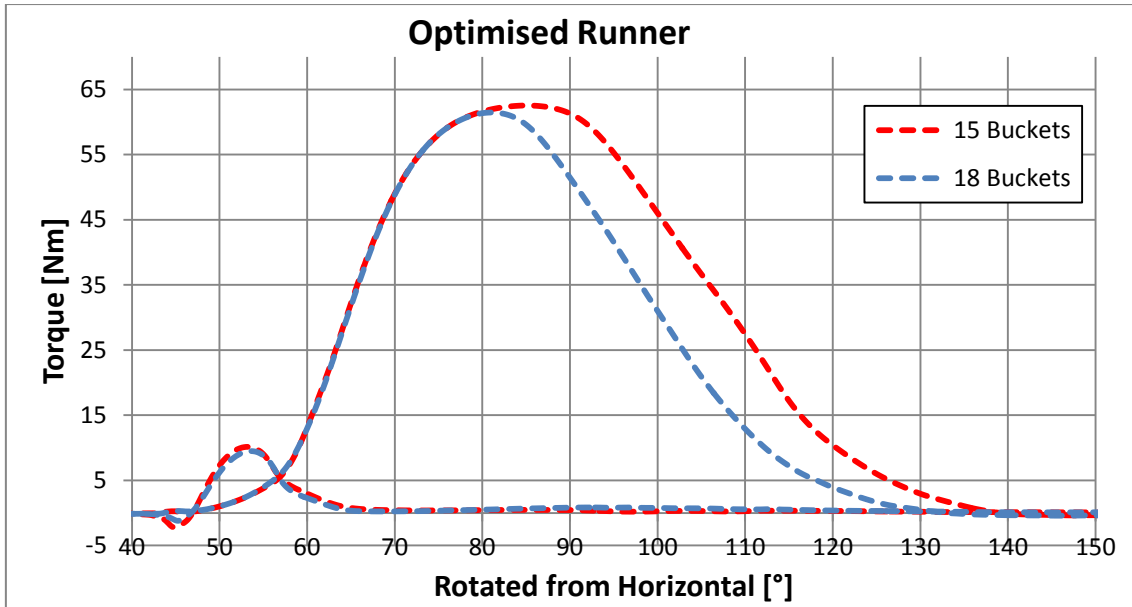


Fig. 6.7. Torque curves on a single bucket in an optimised runner with different amount of buckets.

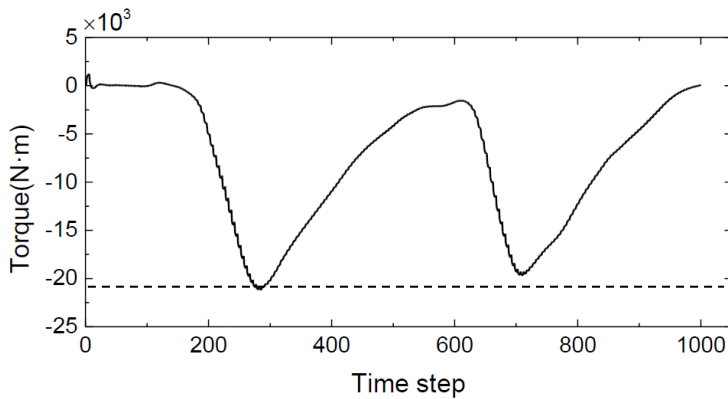


Fig. 6.8. Two inverted torque peaks generated by two jets (Wei, Yang et al. 2015).

To check if there is a possibility for the jet interference when both jets are operating, the torque curve from a single jet operation was copied and shifted by 80° which was the angle between the jets in the test rig. Fig. 6.9 presents the two torque curves on the original runner. As expected, the transition from the 1st jet to the 2nd was smooth, i.e. the water from the 1st jet has left the bucket just before the 2nd jet was entering. This shows that the angle between the jets was correctly chosen for the Original runner. Fig. 6.10 indicates that in the Optimised runner with 18 buckets the transition between the jets was also smooth since the number of buckets remained unchanged.

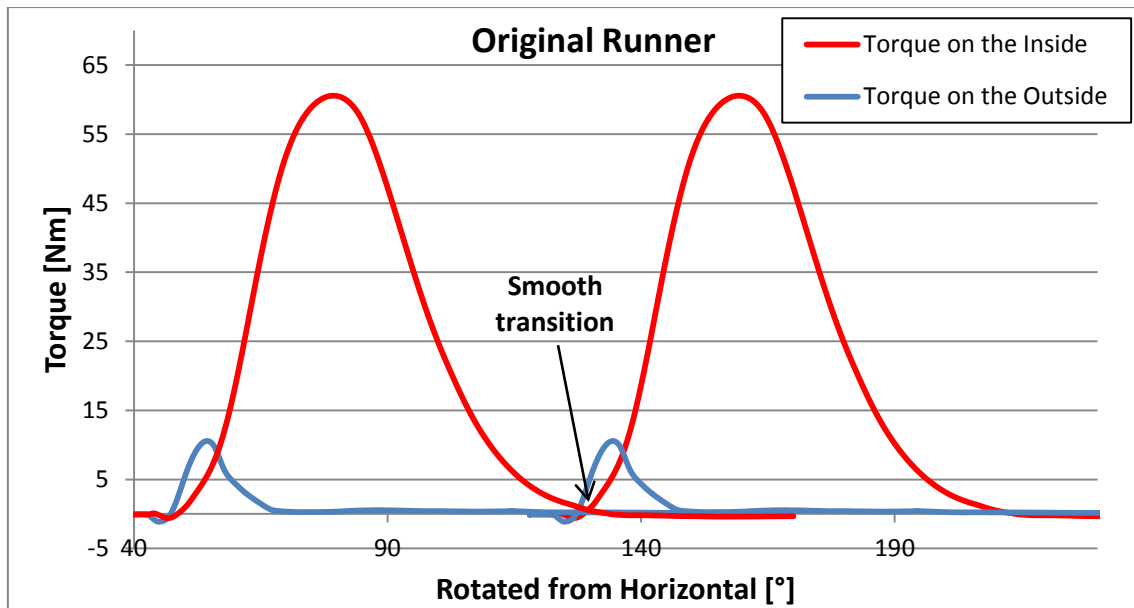


Fig. 6.9. Two torque peaks taken from the single jet simulation and manually shifted by the angle between the jets (80°). Original runner.

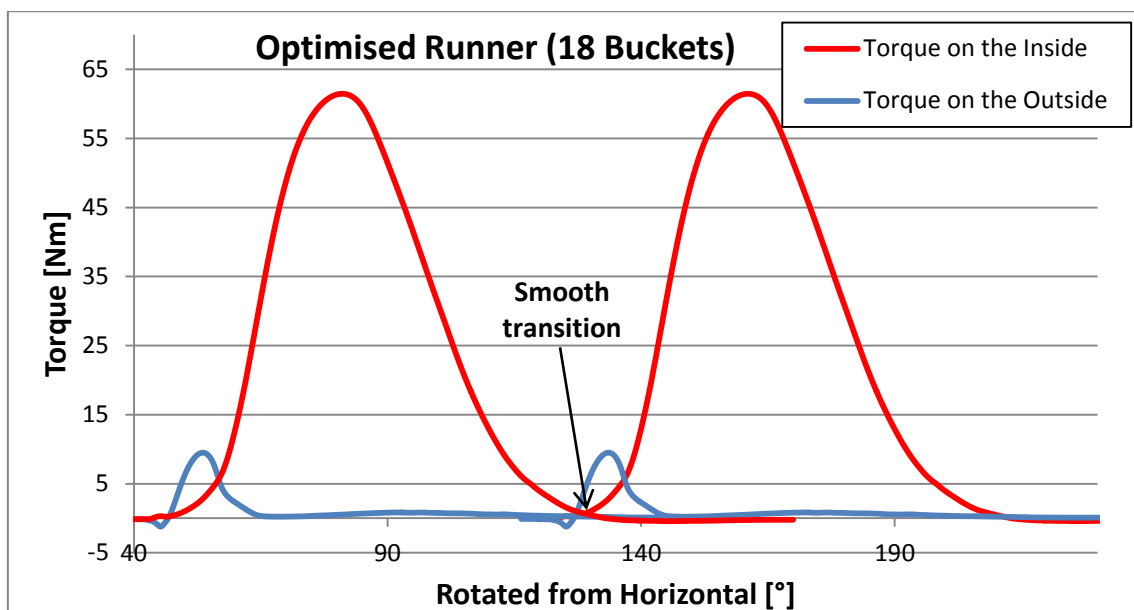


Fig. 6.10. Two torque peaks taken from the single jet simulation and manually shifted by the angle between the jets (80°). Optimised runner with 18 buckets.

However, looking at the torque curves provided in Fig. 6.11 some potential interference between the 1st jet and the 2nd jet can be observed. To assess the effect that this interference might have on the torque created by the 2nd jet and to quantify this effect in terms of efficiency, simulations with two jets were performed for all the three runners. Fig. 6.12 provides an image of a two jet simulation setup with the Original runner. This time a third bucket was added so that the jet is cut off realistically. Otherwise, using only two buckets for a two jet simulation caused a problem when the water from the inside of the second bucket was interfering with the second jet in an unrealistic fashion.

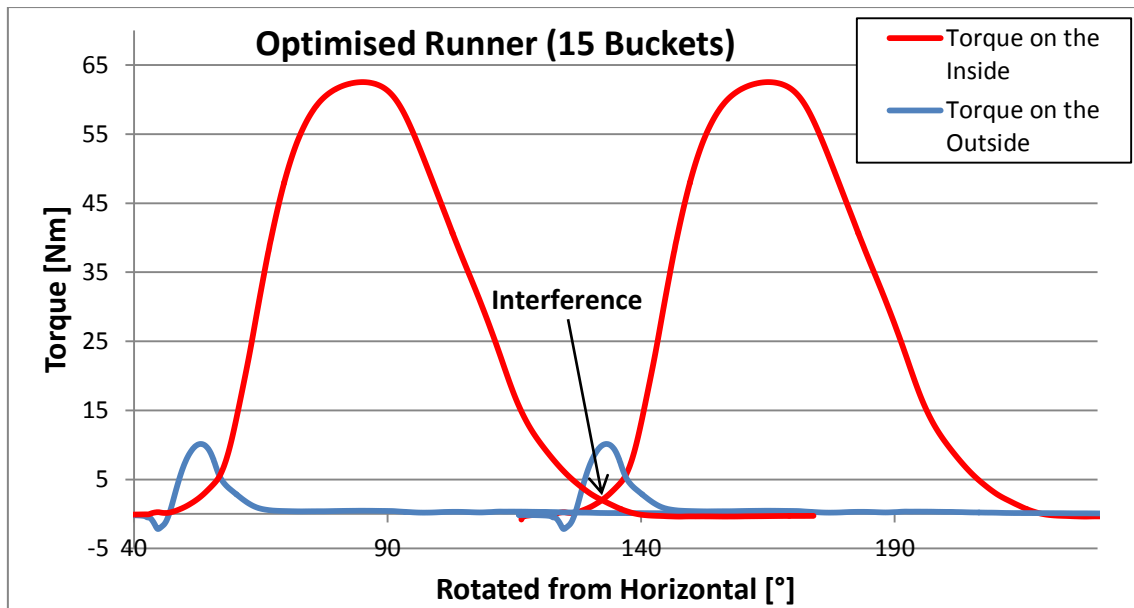


Fig. 6.11. Two torque peaks taken from single jet simulation and manually shifted by the angle between the jets (80°). Optimised runner with 15 buckets.

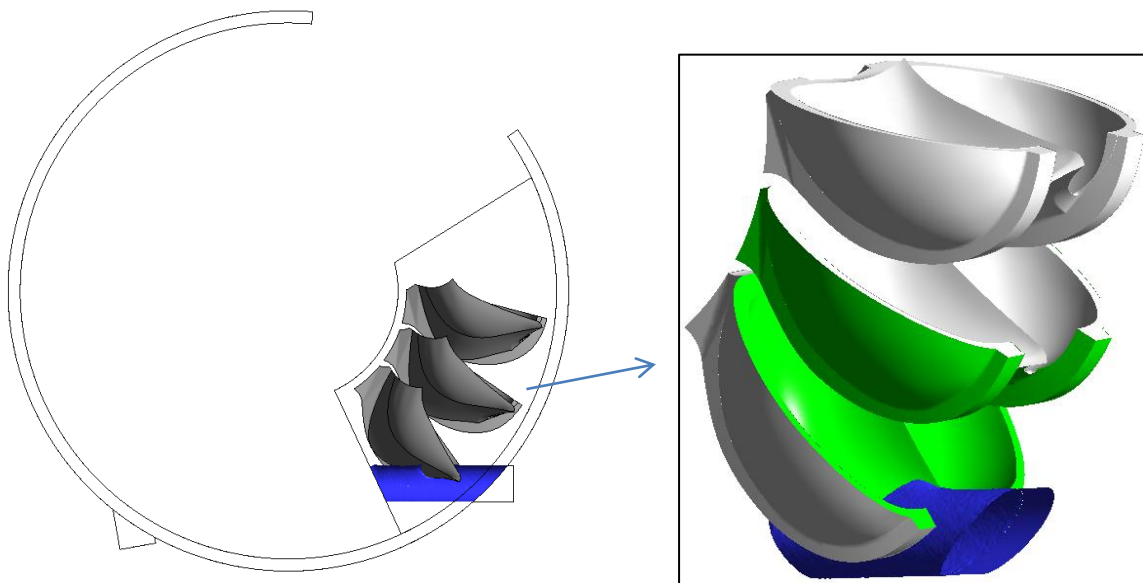


Fig. 6.12. Stationary and rotating domains of the simulation with 2 jets and 3 buckets of the Original runner. Surfaces contributing to the torque measurement are highlighted in green on the right hand side.

Efficiency improvement predicted by the single jet and the two jet simulations was consistent for the Optimised runner with 18 buckets. However, the predicted efficiency improvement for the Optimised runner with 15 buckets was noticeably lower in the two jet simulation as can be seen from Fig. 6.13. This corresponds well with the assumption that there was an interference between the jets and suggests that the runner with 15 buckets would benefit from a larger angle between the jets and could provide higher efficiency when operating with both jets.

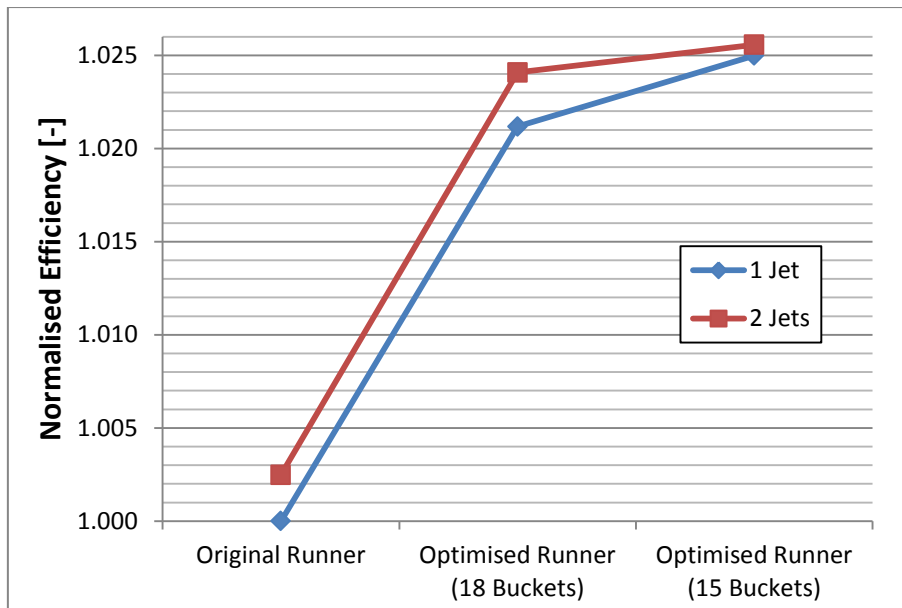


Fig. 6.13. CFD predicted efficiency improvement from 1 jet and 2 jet simulations.

It was also observed in Fig. 6.13 that for all the three runners the simulated efficiency using two jets was higher than using the single jet. This result was unexpected. By analysing the torque curves it was found that using only few buckets to represent the whole runner operating at stable periodic conditions has some effect on the results. The limitations are mostly due to the wall boundary treatment and the fact that the domain is initially 100% dry (air volume fraction = 1). More detailed analysis is provided in the following section.

6.3. Limitations of the CFD Model

Fig. 6.14 and Fig. 6.15 present the torque curves of runners with 18 buckets from the two jet simulations overlaid on the single jet simulation results that were copied and shifted by 80°. In both the Original and the Optimised runners, the torque created by the first jet is consistent. However, the torque curves created by the second jet are different in the simulations with two jets. The torque curves show unexpected increase in the energy created by the second jet on the inside of the bucket and reduction on the outside. In the Optimised runner with 15 buckets (Fig. 6.16) this phenomenon is even more pronounced. This indicates that the second jet is pulling the bucket at the outside surface for shorter time before it gets detached and has more remaining energy to be utilised on the inside surface of the adjacent bucket.

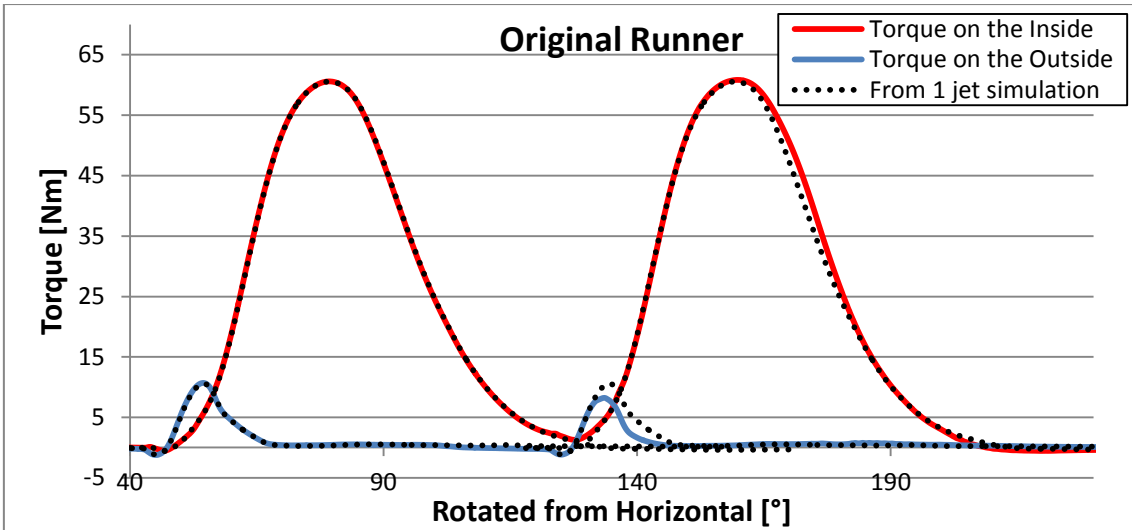


Fig. 6.14. Two torque peaks. Original runner.

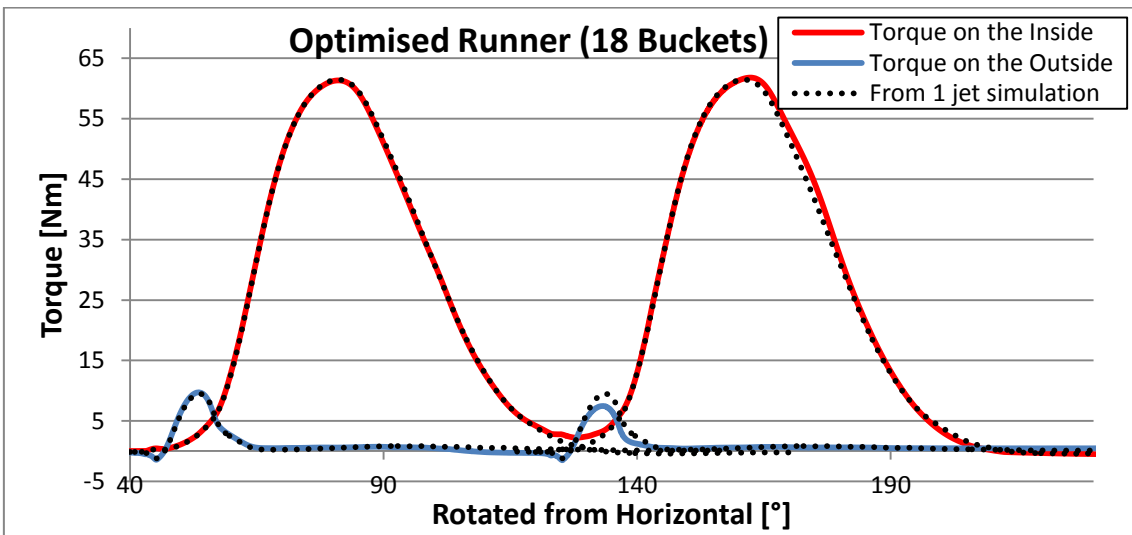


Fig. 6.15. Two torque peaks. Optimised runner with 18 buckets.

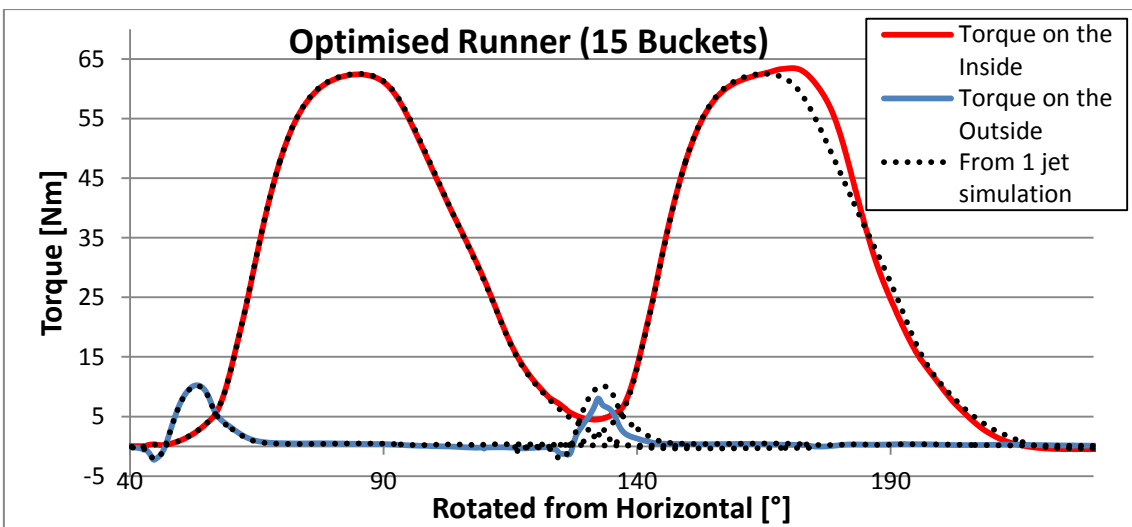


Fig. 6.16. Two torque peaks. Optimised runner with 15 buckets.

The reason why the first jet is acting differently to the second jet as they are at the suction part of the duty cycle is because the bucket is completely dry when the first jet comes and there is some remaining water on the surface when the second jet comes. The amount of the remaining water is minute. Taking the interface between water and air as volume fraction of 0.5 for each phase it seems as there is no remaining water. However, looking at much lower volume fractions of water (water volume fraction = 0.05) it can be seen that some amount of water is attached to the outside surface of the bucket when the second jet comes into contact as presented in Fig. 6.17.

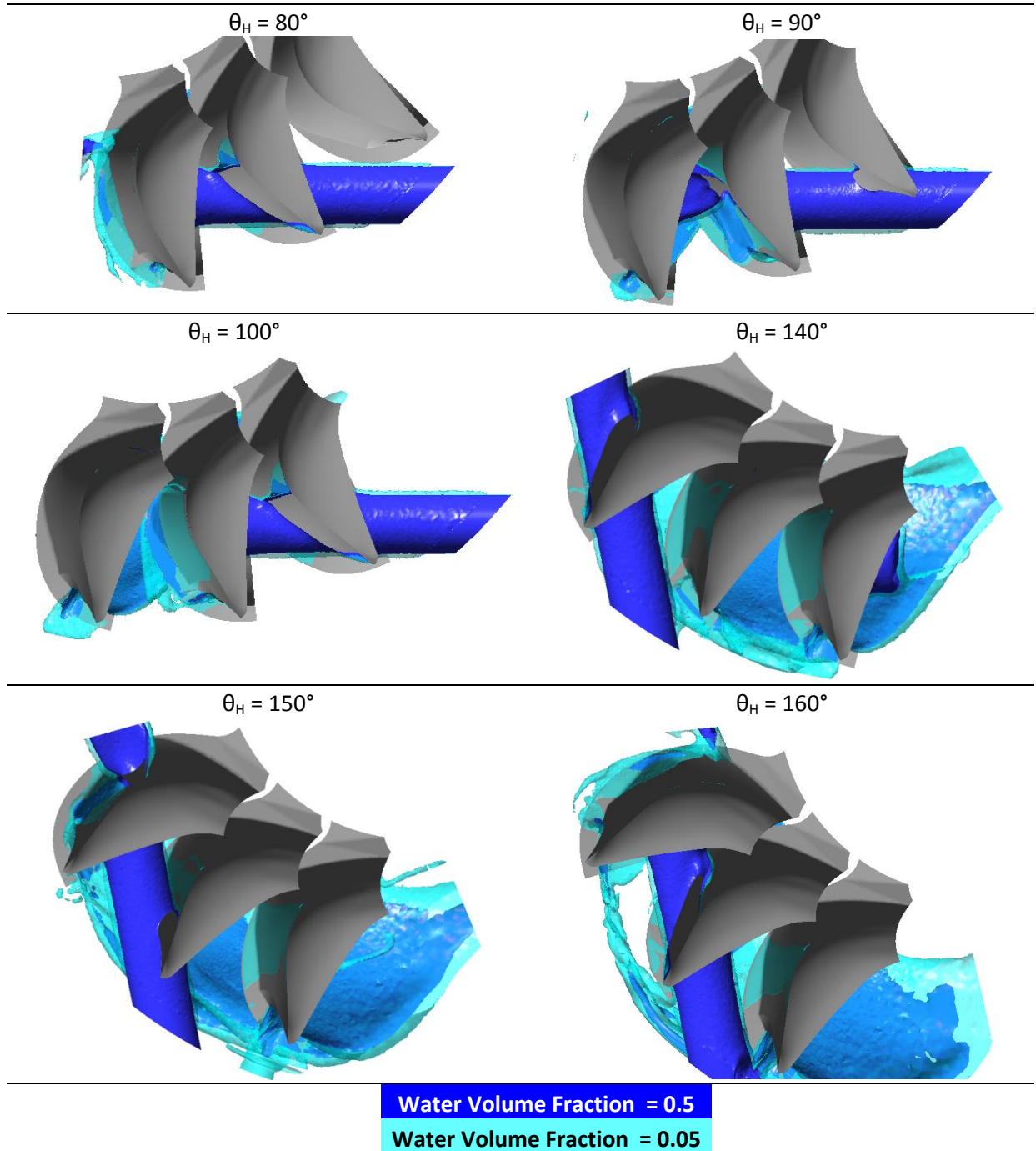


Fig. 6.17. Water-air interface iso-surfaces at two different volume fractions during various moments of the two jet simulation.

Even though the amount of water and its volume fraction is minute it changes the way how the jet detaches from the outside surface of the bucket as shown in Fig. 6.18. To verify that this effect is caused by the remaining water on the outside surface of the bucket a standard single jet simulation was performed by specifying some amount of water on the surface as the initial conditions (Fig. 6.19). The resultant torque curve in comparison to the single jet dry initial conditions and two jet simulations is provided in Fig. 6.20.

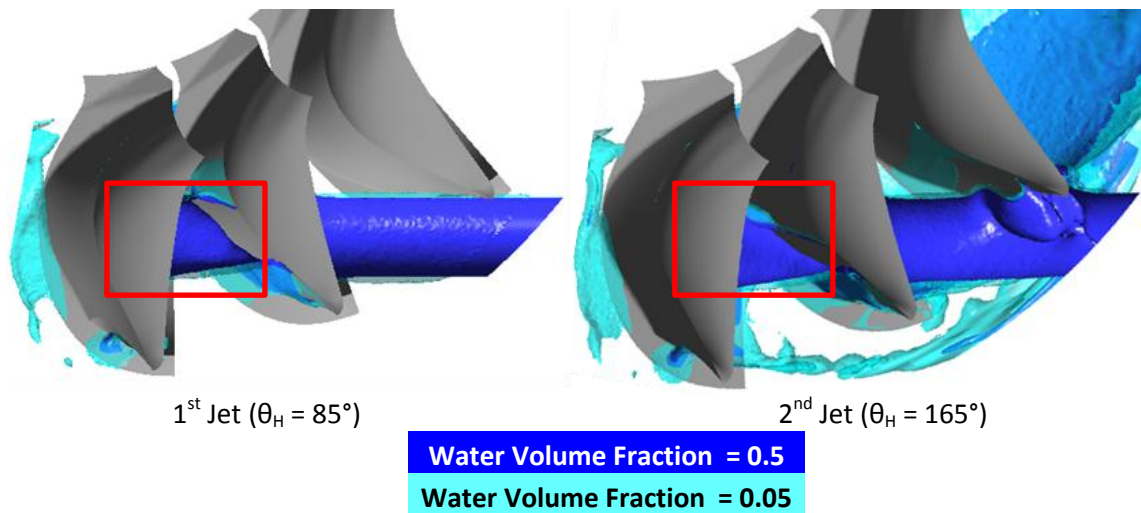


Fig. 6.18. 1st and 2nd jet detaching in a different way.

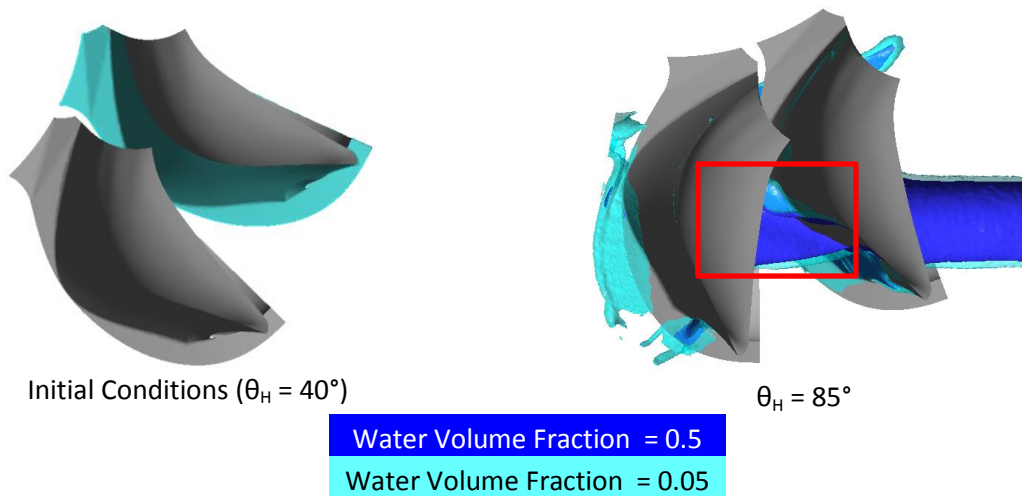


Fig. 6.19. Simulation with wet surface initial conditions.

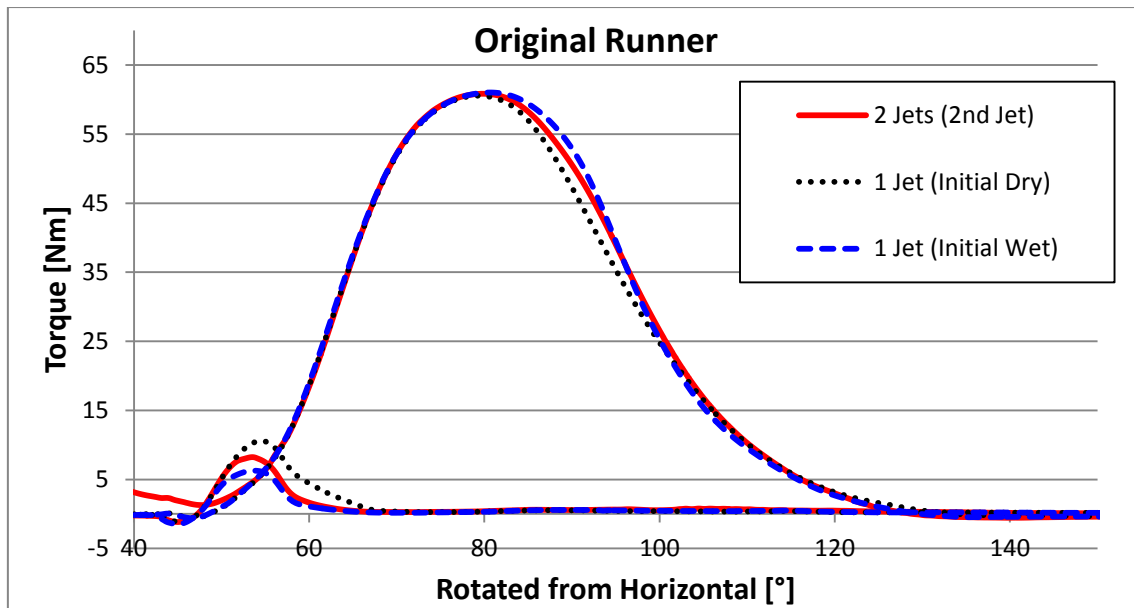


Fig. 6.20. Comparison of results from simulations with different initial conditions.

Clearly a simulation with one jet having a layer of water volume fraction = 0.05 on the surface when the simulation starts has a similar effect to having similar layer created by the water left from the first jet in the two jet simulation. I.e. the jet separates quicker (Fig. 6.19) causing the reduction in the torque produced on the outside of the bucket and the increase in the torque produced on the inside of the adjacent bucket (Fig. 6.20). Two main things can be concluded from this observation:

- 1) The current setup of the simplified simulation where only few buckets are used does not entirely represent the performance that would be modelled using a much more computationally expensive simulation where a full runner is modelled and enough revolutions are made to reach stable periodic conditions.
- 2) Wall boundary treatment factors such as surface tension or adhesion are not only important to improve the absolute CFD accuracy of Pelton simulations as suggested by Perrig (2007) but also very important for comparative studies used for optimisation. Numerical error created by the absence of surface tension and adhesion cannot be simply assumed as constant offset for parameters where the jet separation from the backside of the bucket has a major role. Examples of such parameters are the backside shape of the bucket, the inclination angle or the angle between the buckets (i.e. the number of buckets).

Even though it was possible to successfully improve the efficiency of a modern industrial runner, this limitation might be the main reason why the measured amount in improved efficiency is different from the numerically predicted. Moreover, it raises a question if 15 buckets is the optimum amount for this runner. The optimised runner with 15 buckets is more efficient than with 18 as shown by experimental results; however, it might be that the optimum number is in between, i.e. a runner with 16 or 17 buckets or even more extreme, e.g. 14.

Chapter 7. Conclusions and Recommendations

This is the final chapter that summarises the outcomes of the research and reflects on the goals set and success in meeting them. Recommendations for the future work are also provided in this chapter.

7.1. Summary

The main objective of this thesis was to create a methodology that applies Computational Fluid Dynamics in development of Pelton turbines. To achieve this objective an accurate CFD model that can simulate performance and efficiency of a turbine within a reasonable timescale was required. Such model was created based on suggestions of the most recent studies that were available in the literature and applying a number of assumptions that reduce the timescale. These assumptions were verified against computationally more demanding simulations where available while the whole methodology was validated experimentally. The whole thesis was concentrating on the most complex and key part of the turbine which is the runner. Modelling of a free surface jet interacting with a rotating runner includes such problems as multiphase free surface flow, multi fluid interaction, rotating frame of reference and unsteady time dependent flow. Because of these complex phenomena there was a lack of publications showing CFD being used for impulse turbine optimisation purposes even though CFD was successfully used in the development of reaction turbines.

To create a feasible CFD model that is reliable but also relatively fast in addition to the physical and engineering assumptions a meshing technique was created that was based on the results of the mesh refinement study. Two different mesh sizing options were used: fine mesh and coarse mesh. Mesh independent sizing was used for the fine mesh simulations creating meshes containing approximately 3 million mesh elements and taking 4 to 5 days to model a single data point on a quad core Intel Xeon, 3.4GHz with 16GB memory RAM desktop PC. These simulations were used to verify the key design changes created during the optimisation process. Coarse mesh simulations were using mesh sizing that was not entirely mesh independent and tended to underpredict the peak torque on the bucket generated by the jet. These simulations were taking 20 hours to solve and therefore were used for parametric optimisation assuming that the underpredicted torque is nearly systematic.

After the CFD model was verified to be reliable and the timescale was reduced to the acceptable level, optimisation of the runner design was performed. 12 design parameters were identified and modified either using the design of experiments approach, analytically or as a result of other modifications. The baseline design referred as the Original design in this thesis was a modern commercial runner design provided by Gilbert Gilkes and Gordon Ltd. As an output of this parametric study two optimised runner designs were created. Optimised runner 1 contained all the bucket shape design modifications

but the number of buckets remained unchanged. It was predicted by CFD simulation results that the efficiency improvement of this runner will be 2.2 % of the Original runner efficiency. Optimised runner 2 used identical bucket shape design as Optimised runner 1 but the number of buckets was reduced by 3 to have 15 buckets on the runner. The CFD predicted efficiency for this runner was 2.5 % of the original efficiency.

These predictions were checked experimentally. All the three runners: Original, Optimised 1 and Optimised 2 were manufactured and tested. Tests were made for operation with single jet and with both jets. Each test consisted of approximately 60 data points. The experimental results showed that the efficiency improvement of the Optimised Runner 1 was 1.0 % of the original efficiency for the single jet operation and 1.4 % when both jets were operating. Optimised Runner 2 showed 2.0 % and 1.8 % respectively. It was identified that when both jets were in operation the peak efficiency of the Optimised Runner 2 was affected by the angle between the jets. As the number of buckets is reduced the minimum angle between the jets ensuring no interaction needs to be increased.

Finally, comparing the experimental results to the numerically predicted and analysing the interference between the jets the main limitation of this simplified CFD model was identified. This limitation was caused by the wall treatment and the way how the jet was separating from the backside surface of the bucket. Therefore, when optimising the parameters that are related to the backside shape or position of the bucket, it is very important to have this limitation in mind.

7.2. Contribution and Novelty of the Present Work

7.2.1. Parametric Optimisation of Pelton Runner Design

Despite the vast amount of publications on modelling of Pelton turbines suggesting that CFD has reached a stage where it can be used for design optimisation there is a lack of publications on successful Pelton runner design improvements validated experimentally. This makes the current work presented in this thesis where CFD based parametric optimisation of the runner design was performed and validated by experimental testing unique and valuable for the academic community. 12 runner design parameters were identified and analysed numerically discussing their importance. The contribution of this research is the described parametric study confirmed by experimental testing that can be used to optimise any Pelton turbine runner.

7.2.2. Drastically Reduced Number of Buckets

There are plenty of design guidelines for Pelton runner design. However, no consistent guidance based on numerical or experimental research is publically available to determine the optimum number of buckets which is an important parameter when optimising any Pelton turbine runner. In this thesis a reduction of the number of buckets from the original number of 18 to a number beyond any available guidance was suggested based on the CFD results. Experimental testing showed that indeed a runner with 15 buckets was more efficient than a runner with 18 buckets. In addition to this slight increase the main achievement is that the runner design was simplified meaning that the manufacturing cost or timescale can be reduced providing a direct economic effect for the turbine manufacturers.

In general, a question can be raised on the reliability of available guidelines to determine the optimum number of buckets. Perhaps, more Pelton runner designs can benefit from the reduced number of buckets: if not from increased efficiency point of view then at least by maintaining the same efficiency but reducing the complexity of their design. This would further increase the usage of Pelton turbines and therefore expand the hydropower and the renewable energy usage in general. However, more work is required to establish more general, experimentally validated guidelines.

7.2.3. Economic Effect

The economic effect achieved by optimising the runner presented in this thesis is combined of two factors. Firstly, the increase in the efficiency by almost 2 % (1.9 % of the original efficiency) means that the optimised runner can generate 2 % higher income over its lifetime which can easily be more than 20 years. Secondly, reducing the number of buckets reduces the capital expenditure of the hydropower project where a runner is one of the most expensive components. Traditionally Pelton runners are cast as a single piece; therefore, using fewer buckets reduces the amount of material required per runner. In this particular case, the mass of the runner or in other words the amount of material required is reduced by 4 %. Moreover, casting is usually followed by processes such as grinding and cleaning which include long timescales and high labour costs. Having fewer buckets means that after the casting process less work is required. Furthermore, the increased spacing between the buckets allows improved access for tools and may open the ways for alternative manufacturing processes. CNC machining could be used to improve the delivery times and reduce the labour cost either after the casting process or possibly replace the whole manufacturing process.

7.3. Recommendations for Future Work

7.3.1. Coanda Effect

As described in Chapter 6, Section 6.3 *Limitations of the CFD Model*, the current CFD model has some limitations that are of key importance when comparing different Pelton designs. The model used for optimisation was shown to experience problems in providing a reliable prediction of the suction torque at the backside of the bucket and the location of separation. This limitation comes from the absence of surface tension and wall adhesion models as well as not reaching the periodic conditions by allowing the runner to do more than one revolution. Therefore further work is required to address this limitation. However, finer meshes might be required for accurate modelling when surface tension and wall adhesion factors are included. Moreover, numerical verification of periodic behaviour is required as the water that remains on the surface might be affecting the results.

7.3.2. Optimum Number of Buckets

Current classical guidelines on the optimum number of buckets are based on the theoretical assumptions that inevitably include simplifications of complex flow behaviour in the runner. There is a lack of guidelines that were based on experimental or CFD studies. Even though it was experimentally shown in this thesis that the runner with 15 buckets was more efficient than the runner with 18 buckets, a question remains unanswered if 15 was the optimum number as predicted by CFD. As described in the previous section, further work is required to improve the CFD modelling of Pelton turbines in order to perform a detailed and reliable numerical study on the optimum number of buckets. However, the optimum number of buckets can also be analysed experimentally since the bucket design is constant in such a study. When identifying the optimum number of buckets, it is very important to be adjusting the inclination angle and the radial distance for each number of buckets analysed.

7.3.3. High Capacity Computing

Rapidly increasing computational resources open new opportunities for further CFD application on the development of Pelton turbines. Using faster machines or parallel computing on the high capacity computing clusters allow more complex simulations to be solved or more simulations of the same complexity to be solved within the same timescale.

If the current CFD model presented in this thesis was solved faster or more parallel simulations were solved during the same amount of time, larger sets of related parameters using the design of

experiments technique could be investigated and higher chances to create an optimum design would be provided.

On the other hand, having more computational resources, a more elaborate CFD model can be created. At the moment, an ideal jet interacting with only two buckets of the runner not enclosed by the casing was modelled. These simplifications create plenty of limitations and therefore unknowns. A highly complex but complete turbine model would include the injector or even a branchpipe, the complete runner and the casing. In the near future it is not expected to use such a complex model for optimisation purposes and analysis of each design point however such model could be used for design validation.

7.3.4. Injector Design

Injector geometry design is also very important. The design can be optimised in standalone to simply reduce the losses in the injector. However, in addition to reducing the losses in the injector, improving the jet quality is also very important. Secondary flows and the velocity profiles of the real jet (as opposed to the ideal jet with uniform velocity) also have an impact on the overall performance. The aforementioned CFD model of a complete turbine would allow verification of injector design improvements on the overall efficiency of a turbine.

7.3.5. Multi Jet Operation

The optimisation study performed in this thesis was using only the single jet operation for efficiency assessment. However, adding more jets create new challenges. It was shown that in the two jet operation, an angle between the jets becomes an important factor as there is a limit below which the flow interference begins. For a horizontal axis machine with two jets, this angle can be easily adjusted to avoid this interference. However, in vertical axis arrangements Pelton turbines can have as many as 6 jets meaning that the limit on the maximum angle between the jets can be as low as 60° . Therefore, for a vertical axis multi-jet arrangement, the runner has to be designed with regards to this limitation.

7.3.6. Turbine Casing Design

Turbine casing design is very important for Pelton turbines in both horizontal and vertical axis arrangement. Modelling of the flow interference with the casing parts or any back splashing effects require large spaces to be discretized using fine meshes through the whole domain; hence, increasing the computational cost. However, the computational resources are constantly increasing; therefore, more complex simulations become possible with time.

7.3.7. Turgo Impulse Turbine Runner Development

Successful optimisation of the Pelton runner shows how CFD can be used to optimise the performance of impulse turbines that include such numerical problems as multiphase modelling, free surface jets, rotating frame of reference and transient flows. Operating principals of another impulse turbine, the Turgo, include all these complex features (Židonis, Benzon et al. 2015). It is suggested that a very similar optimisation approach to the one used for Pelton runner optimisation and described in this thesis can be used to optimise the Turgo runner.

References

1. Aggidis, G. A., 2010. *Hydro Resource Evaluation Tool*. [online] Available at: <<http://www.engineering.lancs.ac.uk/lureg/nwhrm/engineering/>> [Accessed 14 April 2015].
2. Aggidis, G. A., E. Luchinskaya, R. Rothschild and D. Howard, 2010. The costs of small-scale hydro power production: Impact on the development of existing potential. *Renewable Energy* 35(12), pp. 2632-2638.
3. Aggidis, G. A. and A. Židonis, 2014. Hydro turbine prototype testing and generation of performance curves: Fully automated approach. *Renewable Energy* 71, pp. 433-441.
4. Anagnostopoulos, J. S., P. K. Koukouvinis, F. G. Stamatelos and D. E. Papantonis, 2012. Optimal design and experimental validation of a Turgo model Hydro turbine. In: *ASME 2012, 11th Biennial Conference on Engineering Systems Design and Analysis*, Nantes International Convention Centre, 2-4 July 2012.
5. Anagnostopoulos, J. S. and D. E. Papantonis, 2006. A numerical methodology for design optimization of Pelton turbine runners. In: *HYDRO 2006 International Conference*, Porto Carras, 2006, pp. 25-27.
6. Anagnostopoulos, J. S. and D. E. Papantonis, 2007. Flow modeling and runner design optimization in Turgo water turbines. *World Academy of Science, Engineering and Technology* 28, pp. 206-211.
7. Anagnostopoulos, J. S. and D. E. Papantonis, 2012. A fast Lagrangian simulation method for flow analysis and runner design in Pelton turbines. *Journal of Hydrodynamics, Ser. B* 24(6), pp. 930-941.
8. ANSYS Inc., 2013a. *ANSYS CFX Solver Modeling Guide, Release 15*. Canonsburg, USA: ANSYS, Inc.
9. ANSYS Inc., 2013b. *ANSYS CFX Solver Theory Guide, Release 15*. Canonsburg, USA: ANSYS, Inc.
10. ANSYS Inc., 2013c. *ANSYS Fluent Theory Guide, Release 15*. Canonsburg, USA: ANSYS, Inc.
11. Atthanayake, I. U., 2009. Analytical study on flow through a Pelton turbine bucket using boundary layer theory. *International Journal of Engineering and Technology* 9(9), pp. 241-245.
12. Avellan, F., P. Dupont, S. Kvicinsky, L. Chapuis, E. Parkinson and G. Vuillioud, 1998. Flow Calculations in Pelton Turbines,-Part 2: Free Surface Flows. In: *IAHR Proceedings of the 19th IAHR Symposium*, Singapore, Republic of Singapore, 1998, Vol. 1. No. LMH-CONF-1998-002.
13. Barstad, L. F., 2012. *CFD Analysis of a Pelton Turbine*. Master. Norwegian University of Science and Technology.
14. Batchelor, G. K., 1973. *An introduction to fluid Dynamics*. Cambridge: Cambridge University Press.
15. Benzon, D., A. Židonis, A. Panagiotopoulos, G. A. Aggidis, J. S. Anagnostopoulos and D. E. Papantonis, 2015a. Impulse turbine injector design improvement using Computational Fluid Dynamics. *Journal of Fluids Engineering* 137(4), p. 041106.
16. Benzon, D., A. Židonis, A. Panagiotopoulos, G. A. Aggidis, J. S. Anagnostopoulos and D. E. Papantonis, 2015b. Numerical investigation of the spear valve configuration on the performance of Pelton and Turgo turbine injectors and runners. *Journal of Fluids Engineering* 137(11), p. 111201.

17. Brekke, H., 1984. *A general study on the design of vertical Pelton turbines*. Ljubljana, Slovenia: Turboinstitut.
18. Brekke, H., 2010. Performance and safety of hydraulic turbines. In: IOP Conference Series, *Earth and Environmental Science*, IOP Publishing, 2010. p. 012061.
19. British Hydropower Association., 2010. *Hydropower: Opportunities, challenges & sharing best practice - The British Hydropower Association perspective*. [pdf] London: Environment Agency – CIWEM. Available at: <http://www.ciwem.org/media/142437/The%20British%20Hydropower%20Association%20Perspective.pdf> [Accessed 14 April 2015]
20. Chongji, Z., X. Yexiang, Z. Wei, Y. Yangyang, C. Lei and W. Zhengwei, 2014. Pelton turbine Needle erosion prediction based on 3D three-phase flow simulation. In: IOP Conference Series, *Earth and Environmental Science*, IOP Publishing, 2014. p. 052019.
21. Davidson, S. C., 1900. *Impact-wheel or turbine*. U. S. Pat. 641,847.
22. Draper, N. R. and D. K. Lin, 1990. Small response-surface designs. *Technometrics* 32(2), pp. 187-194.
23. Ecopolis., 2010. *Pelton Turbine HHP - H*. [image online] Available at: <http://www.ecopolisla.com/en/hydro-power/products/turbines/detail-pelton-turbine-hhp---h-50/> [Accessed 14 April 2015].
24. Eisenring, M., 1991. *Micro pelton turbines*. St. Gallen, Switzerland: Swiss Center for Appropriate Technology.
25. European Commission, 2009. *Directive 2009/28/EC of the European Parliament and of the Council of 23 April 2009 on the promotion of the use of energy from renewable sources and amending and subsequently repealing Directives 2001/77/EC and 2003/30*. *Official Journal of the European Union Belgium*.
26. European Renewable Energy Council, 2010. *Renewable Energy in Europe: Markets, Trends, and Technologies*. London: Earthscan.
27. Favre, J., H. Garcin and E. Parkinson, 2005. Computational analysis in Pelton hydraulic turbines. In: 23rd CADFEM users meeting, *International Congress on FEM Technology with ANSYS CFX & ICEM CFD Conference*, International Congress Center Bundeshaus Bonn, Germany, 9-11 November 2005.
28. Ferreño, D., J. Álvarez, E. Ruiz, D. Méndez, L. Rodríguez and D. Hernández, 2011. Failure analysis of a Pelton turbine manufactured in soft martensitic stainless steel casting. *Engineering Failure Analysis* 18(1), pp. 256-270.
29. Fulton, A., 1937. Present Tendencies in Water Turbine Machinery. *Proceedings of the Institution of Mechanical Engineers* 135(1), pp. 387-444.
30. Furnes, K., 2013. *Flow in Pelton turbines*. Master. Norwegian University of Science and Technology.
31. Gupta, V. and V. Prasad, 2012. Numerical investigations for jet flow characteristics on pelton turbine bucket. *International Journal of Emerging Technology and Advanced Engineering* 2(7), pp. 364-370.
32. Gupta, V., V. Prasad and R. Khare, 2014. Effect of Jet Shape on Flow and Torque Characteristics of Pelton Turbine Runner. *International Journal of Engineering Research and Application* 4(1), pp. 318-323.
33. Hana, M., 1999. *Numerical analysis of non-stationary free surface flow in a Pelton bucket*. Ph. D. Norwegian University of Science and Technology.

34. International Electrotechnical Commission, 1999. *IEC 60193 Hydraulic Turbines, Storage Pumps and Pump-Turbines—Model Acceptance Tests*. Geneva, Switzerland: IEC.
35. Janetzky, B., E. Göde, A. Ruprecht, H. Keck and C. Schäfer, 1998. Numerical simulation of the flow in a Pelton bucket. In: IAHR, *Proceedings of 19th IAHR Symposium on Hydraulic Machinery and Cavitation*, pp. 276-283. Singapore, 9-11 September 1998.
36. Jošt, D., A. Lipej and P. Mežnar, 2008. Numerical Prediction of Efficiency, Cavitation and Unsteady Phenomena in Water Turbines. In: ASME 2008, *9th Biennial Conference on Engineering Systems Design and Analysis*, pp. 157-166. Haifa, Israel, 7-9 July 2008.
37. Jošt, D., P. Mežnar and A. Lipej, 2010. Numerical prediction of Pelton turbine efficiency. In: IAHR, *25th IAHR Symposium on Hydraulic Machinery and Systems, IOP Conf. Series: Earth and Environmental Science*, 012080. Timisoara, Romania, 20-24 September 2010.
38. Keck, H. and M. Sick, 2008. Thirty years of numerical flow simulation in hydraulic turbomachines. *Acta mechanica* 201(1-4), pp. 211-229.
39. Klemensten, L. A., 2010. *An experimental and numerical study of the free surface Pelton bucket flow*. Master. Norwegian University of Science and Technology.
40. Koukouvinis, P. K., J. S. Anagnostopoulos and D. E. Papantonis, 2010. Flow Analysis Inside a Pelton Turbine Bucket Using Smoothed Particle Hydrodynamics. In: *HYDRO 2010 International Conference*. Lisbon, Portugal, 2010.
41. Koukouvinis, P. K., J. S. Anagnostopoulos and D. E. Papantonis, 2011. SPH Method used for Flow Predictions at a Turgo Impulse Turbine: Comparison with Fluent. *World Academy of Science, Engineering and Technology*, 79(55), pp. 659-666.
42. Krause, E., 2014. The Millennium-Problem of Fluid Mechanics—The Solution of the Navier-Stokes Equations. *The History of Theoretical, Material and Computational Mechanics—Mathematics Meets Mechanics and Engineering*, Springer: pp. 317-341.
43. Kvicinsky, S., J.-L. Kueny, F. o. Avellan and E. Parkinson, 2002. Experimental and numerical analysis of free surface flows in a rotating bucket. In: IAHR, *The proceeding of the 21st IAHR Symposium on hydraulic machinery and systems*, Lausanne, Switzerland, 9-12 September 2002.
44. Ladyzhenskaya, O. A., 2003. Sixth problem of the millennium: Navier-Stokes equations, existence and smoothness. *Russian Mathematical Surveys* 58(2), p. 251.
45. Lamb, H., 1994. *Hydrodynamics*. Cambridge: Cambridge University Press.
46. Marongiu, J. C., F. Leboeuf, J. E. Caro and E. Parkinson, 2010. Free surface flows simulations in Pelton turbines using an hybrid SPH-ALE method. *Journal of Hydraulic Research* 48(S1), pp. 40-49.
47. Marongiu, J. C., P. Maruzewski and E. Parkinson, 2005. Modelling the flow in a Pelton turbine. *SPHERIC newsletter*, 1st issue Dec. pp. 8-9.
48. Matthias, H. B. and O. Promper, 2004. Numerical simulation of the free surface flow in Pelton turbines. In: *The 6th International Conference on Hydraulic Machinery and Hydrodynamics*. Timișoara, Romania, 21-22 October 2004.
49. MESA Associates and Inc. and Oak Ridge National Laboratory, 2012. *Compilation of Best Practice Catalog: Hydropower Advancement Project*. [pdf] Available at: http://hydropower.ornl.gov/docs/HAP/CompilationBestPracticeCatalog%28BPC%29Rev2_1.pdf [Accessed 14 April 2015].
50. Mosonyi, E., 1987. *Water Power Development: Low-Head Power Plants*. Budapest, Hungary: Akademiai Kiado.

51. Mosonyi, E., 1991. *Water Power Development: High-head power plants*. Budapest, Hungary: Akademiai Kiado.
52. Muggli, F., Z. Zhang, C. Schärer and L. Geppert, 2000. Numerical and experimental analysis of Pelton turbine flow. Part 2: the free surface jet flow. In: IAHR, *The proceeding of the 20th IAHR Symposium on hydraulic machinery and cavitation*, Charlotte (NC), USA, 6-9 August 2000.
53. Munson, B. R., D. F. Young and T. H. Okiishi, 2005. *Fundamentals of Fluid Mechanics*, 5th ed. USA: John Willey & Sons, Inc.
54. Nakanishi, Y., T. Fujii and S. Kawaguchi, 2009. Numerical and experimental investigations of the flow in a stationary Pelton bucket. *Journal of Fluid Science and Technology* 4(3), pp. 490-499.
55. Nasir, B. A., 2013. Design of High Efficiency Pelton Turbine for Micro-Hydropower Plant. *International Journal of Electrical Engineering & Technology* 4(1), pp. 171-183.
56. National Grid., 2014. *Data explorer*. [online] Available at: <<http://www2.nationalgrid.com/uk/Industry-information/Electricity-transmission-operational-data/Data-Explorer/>> [Accessed 1 December 2014].
57. Nechleba, M., 1957. *Hydraulic turbines: Their design and equipment*. Prague, Czechoslovakia: Artia.
58. OpenFOAM Foundation., 2012. *OpenFOAM User Guide, Version 2.1.1*. [online] Available at: <<http://www.openfoam.org/version2.1.1>> [Accessed 14 April 2015].
59. Padhy, M. and R. Saini, 2011. Study of silt erosion on performance of a Pelton turbine. *Energy* 36(1), pp. 141-147.
60. Panthee, A., H. P. Neopane and B. Thapa, 2014. CFD Analysis of Pelton Runner. *International Journal of Scientific and Research Publications* 4(8), pp. 1-6.
61. Parkinson, E., H. Garcin, G. Vulliod, F. Muggli, Z. Zhang and E. Casartelli, 2002. Experimental and numerical investigations of the free jet flow at a model nozzle of a Pelton turbine. In: IAHR, *The proceeding of the 21st IAHR Symposium on hydraulic machinery and systems*, Lausanne, Switzerland, 9-12 September 2002.
62. Parkinson, E., C. Neury, H. Garcin, G. Vulliod and T. Weiss, 2006. Unsteady analysis of a Pelton runner with flow and mechanical simulations. *International Journal on Hydropower & Dams* 13(2), pp. 101-105.
63. Parkinson, E., G. Vulliod, L. Geppert and H. Keck, 2002. Analysis of Pelton turbine flow patterns for improved runner-component interaction. *International Journal on Hydropower & Dams* 9(5), pp. 100-103.
64. Patel, K., B. Patel, M. Yadav and T. Foggia, 2010. Development of Pelton turbine using numerical simulation. In: IAHR, *25th IAHR Symposium on Hydraulic Machinery and Systems, IOP Conf. Series: Earth and Environmental Science*, 012048. Timisoara, Romania, 20-24 September 2010.
65. Pelton, L. A., 1880. *Water wheel*. U.S. Pat. 233,692.
66. Pelton Water Wheel Company, 1898. *The Pelton Water Wheel. Embracing in Its Variations of Construction and Application the Pelton System of Power*. San Francisco, USA: Pelton Water Wheel Company.
67. Peron, M., E. Parkinson, L. Geppert and T. Staubli, 2008. Importance of jet quality on Pelton efficiency and cavitation. In: IGHEM, *The 7th IGHEM conference*, Milan, Italy, 3-6 September 2008.

68. Perrig, A., 2007. *Hydrodynamics of the free surface flow in Pelton turbine buckets*. Ph. D. École polytechnique fédérale de Lausanne.
69. Perrig, A., F. Avellan, J.-L. Kueny, M. Farhat and E. Parkinson, 2006. Flow in a Pelton turbine bucket: numerical and experimental investigations. *Journal of Fluids Engineering* 128(2), pp. 350-358.
70. Pidwirny, M., 2006. *The Hydrologic Cycle: Fundamentals of Physical Geography, 2nd Ed.* [e-book] PhysicalGeography.net. Available at: <<http://www.physicalgeography.net/>> [Accessed 14 April 2015].
71. Prasad, B., Hino, T. and Suzuki, K., 2015. Numerical simulation of free surface flows around shallowly submerged hydrofoil by OpenFOAM. *Ocean Engineering* 102, pp. 87-94.
72. Prášil, F., 1911. Results of Experiments with Francis Turbines and Tangential (Pelton) Turbines. *Proceedings of the Institution of Mechanical Engineers* 81(1), pp. 647-679.
73. Roache, P.J. 1994. Perspective: A Method for Uniform Reporting of Grid Refinement Studies. *ASME Journal of Fluids Engineering* 116, pp. 405-413.
74. Rygg, J. R., 2013. *CFD Analysis of a Pelton Turbine in OpenFOAM*. Master. Norwegian University of Science and Technology.
75. Santolin, A., G. Cavazzini, G. Ardizzon and G. Pavesi, 2009. Numerical investigation of the interaction between jet and bucket in a Pelton turbine. *Proceedings of the Institution of Mechanical Engineers, Part A: Journal of Power and Energy* 223(6), pp. 721-728.
76. Scardovelli, R. and Zaleski, S., 1999. Direct numerical simulation of free-surface and interfacial flow. *Annual review of fluid mechanics* 31(1), pp. 567-603.
77. Schroeder, S., Kim, S. E. and Jasak, H. 2009. Toward predicting performance of an axial flow waterjet including the effects of cavitation and thrust breakdown. In: *First International Symposium on Marine Propulsors*.
78. Sharma, A., A. Kothari and A. Agrawal, 2011. CFD Analysis for Energy Loss Computation in Half Opening Geometry of Pelton Turbine Nozzle. *International Journal on Emerging Technologies* 2(1), pp. 148-156.
79. Shen, Z. and Wan, D., 2014.. Computation of Steady Viscous Flows around Ship with Free Surface by Overset Grids Techniques in OpenFOAM. In: *The Twenty-fourth International Ocean and Polar Engineering Conference*. International Society of Offshore and Polar Engineers.
80. Sick, M., H. Keck, R. Grunder, E. Parkinson and M. Sallaberger, 2005. Recent Examples of Modern CFD - Methods and Their Application in Practical Turbine Designs. In: 23rd. CADFEM users meeting, *International Congress on FEM Technology with ANSYS CFX & ICEM CFD Conference*, International Congress Center Bundeshaus Bonn, Germany, 9-11 November 2005.
81. Sick, M., H. Keck, E. Parkinson and G. Vullioud, 2000. New challenges in pelton research. In: *HYDRO 2000 International Conference*. Bern, Switzerland, 2000.
82. Soares, C., Noriler, D., Wolf Maciel, M. R., Barros, A. A. C., and Meier, H. F., 2013. Verification and validation in CFD for a free-surface gas-liquid flow in channels. *Brazilian Journal of Chemical Engineering* 30(2), pp. 323-325.
83. Solemslie, B. and O. Dahlhaug, 2012. A reference Pelton turbine design. In: *IAHR, 26th IAHR Symposium on Hydraulic Machinery and Systems, IOP Conf. Series: Earth and Environmental Science*, 032005. Beijing, China: 19-23 August 2012.
84. Stat-Ease, Inc., 2014. *Design-Expert[®] Software Version 9*. [online] Available at: <<http://www.statease.com/>> [Accessed 14 April 2015].

85. Staubli, T., A. Abgottspon, P. Weibel, C. Bissel, E. Parkinson, J. Leduc and F. Leboeuf, 2009. Jet quality and Pelton efficiency. Proceedings of Hydro 2009 Progress-Potential-Plans. In: *HYDRO 2009 International Conference*. Lyon, France, 2009.
86. Staubli, T., P. Weibel, C. Bissel, A. Karakolcu and U. Bleiker, 2010. Efficiency increase by jet quality improvement and reduction of splashing water in the casing of Pelton turbines. In: *16th International Seminar on Hydropower Plants*. Vienna, Austria, 24-26 November 2010.
87. Taylor, M. J. H., 1980. *Jane's encyclopedia of aviation*. London: Grolier Educational Corp.
88. Thake, J., 2000. *The micro-hydro Pelton turbine manual: design, manufacture and installation for small-scale hydro-power*. London: ITDG publishing.
89. Tucker, P. 2014. Computational Methods for Unsteady Flows. *Unsteady Computational Fluid Dynamics in Aeronautics*, Springer: 33-92.
90. Turner, D. S., 1969. *Applied earth science*. Dubuque, Iowa, W.C., USA: Brown Co.
91. United Nations Framework Convention on Climate Change., 2011. *Fact sheet: The Kyoto Protocol*. [pdf] United Nations Framework Convention on Climate Change. Available at: http://unfccc.int/files/press/backgrounders/application/pdf/fact_sheet_the_kyoto_protocol.pdf [Accessed 14 April 2015].
92. Veselý, J. and M. Varner, 2001. A case study of upgrading 62.5 MW Pelton turbine. In: *Proceedings of International Conference: IAHR 2001*. Prague, Czech Republic, 2001.
93. Wang, B., X. L. Liu, C. X. Yue, J. Du, L. Xu and X. Chen, 2010. Study on NC Machining Technology for Integral Impeller of Pelton Turbine. *Advanced Materials Research* 102, pp. 861-865.
94. Wei, X., K. Yang, H. Wang, R. Gong and D. Li, 2015. Numerical investigation for one bad-behaved flow in a Pelton turbine. In: IOP Publishing, *IOP Conference Series: Materials Science and Engineering*. 72(4), p. 042033.
95. Xiao, Y., T. Cui, Z. Wang and Z. Yan, 2012. Numerical simulation of unsteady free surface flow and dynamic performance for a Pelton turbine. In: IOP Publishing, *IOP Conference Series: Earth and Environmental Science*. 15(5), p. 042033.
96. Xiao, Y., Z. Wang, J. Zhang, C. Zeng and Z. Yan, 2014. Numerical and experimental analysis of the hydraulic performance of a prototype Pelton turbine. *Proceedings of the Institution of Mechanical Engineers, Part A: Journal of Power and Energy* 228(1), pp. 46-55.
97. Zhang, Z. and M. Casey, 2007. Experimental studies of the jet of a Pelton turbine. *Proceedings of the Institution of Mechanical Engineers, Part A: Journal of Power and Energy* 221(8), pp. 1181-1192.
98. Židonis, A. and G. Aggidis, 2015a. Pelton Turbine: Identifying the Optimum Number of Buckets Using CFD. *Journal of Hydrodynamics, Ser. B* (in-press).
99. Židonis, A. and G. Aggidis, 2015b. State of the art in numerical modelling of Pelton turbines. *Renewable and Sustainable Energy Reviews* 45, pp. 135-144.
100. Židonis, A., D. S. Benzon and G. A. Aggidis, 2015. Development of Hydro Impulse Turbines and New Opportunities. *Renewable and Sustainable Energy Reviews* 51, pp 1624–1635
101. Židonis, A., A. Panagiotopoulos, G. A. Aggidis, J. S. Anagnostopoulos and D. E. Papantonis, 2015. Parametric Optimisation of Two Pelton Turbine Runner Designs Using CFD. *Journal of Hydrodynamics, Ser. B* 27(3), pp. 403-412.
102. Zoppé, B., C. Pellone, T. Maître and P. Leroy, 2006. Flow analysis inside a Pelton turbine bucket. *Journal of turbomachinery* 128(3), pp. 500-511.

Appendices

Appendix A Tables of Physical Properties

Physical properties data taken from the international testing standards (IEC 60193:1999).

Table A. 1. Acceleration due to gravity g [m/s^2]

Latitude ϕ °	Altitude above mean sea level z [m]				
	0	1000	2000	3000	4000
0	9.780	9.777	9.774	9.771	9.768
5	9.781	9.778	9.775	9.772	9.769
10	9.782	9.779	9.776	9.773	9.770
15	9.784	9.781	9.778	9.775	9.772
20	9.786	9.783	9.780	9.777	9.774
25	9.790	9.787	9.784	9.781	9.778
30	9.793	9.790	9.787	9.784	9.781
35	9.797	9.794	9.791	9.788	9.785
40	9.802	9.799	9.796	9.793	9.790
45	9.806	9.803	9.800	9.797	9.794
50	9.811	9.808	9.805	9.802	9.799
55	9.815	9.812	9.809	9.806	9.803
60	9.819	9.816	9.813	9.810	9.807
65	9.822	9.820	9.817	9.814	9.811
70	9.826	9.823	9.820	9.817	9.814

Table A. 2. Density of distilled water ρ_{wd} [kg/m³]

Temperature θ °C	Absolute pressure 10 ⁵ [Pa]							
	1	10	20	30	40	50	60	70
0	999.8	1000.3	1000.8	1001.3	1001.8	1002.3	1002.8	1003.3
1	999.9	1000.4	1000.9	1001.4	1001.9	1002.4	1002.9	1003.4
2	1000.0	1000.4	1000.9	1001.4	1001.9	1002.4	1002.9	1003.4
3	1000.0	1000.4	1000.9	1001.4	1001.9	1002.4	1002.9	1003.4
4	1000.0	1000.4	1000.9	1001.4	1001.9	1002.4	1002.9	1003.4
5	999.9	1000.4	1000.9	1001.4	1001.9	1002.4	1002.8	1003.3
6	999.9	1000.4	1000.9	1001.4	1001.8	1002.3	1002.8	1003.3
7	999.9	1000.3	1000.8	1001.3	1001.8	1002.3	1002.7	1003.2
8	999.9	1000.3	1000.8	1001.2	1001.7	1002.2	1002.7	1003.2
9	999.8	1000.2	1000.7	1001.2	1001.6	1002.1	1002.6	1003.1
10	999.7	1000.1	1000.6	1001.1	1001.6	1002.0	1002.5	1003.0
11	999.6	1000.0	1000.5	1001.0	1001.4	1001.9	1002.4	1002.9
12	999.5	999.9	1000.4	1000.9	1001.3	1001.8	1002.3	1002.7
13	999.4	999.8	1000.3	1000.7	1001.2	1001.7	1002.1	1002.6
14	999.2	999.7	1000.1	1000.6	1001.1	1001.5	1002.0	1002.4
15	999.1	999.5	1000.0	1000.4	1000.9	1001.4	1001.8	1002.3
16	998.9	999.4	999.8	1000.3	1000.7	1001.2	1001.7	1002.1
17	998.8	999.2	999.6	1000.1	1000.6	1001.0	1001.5	1001.9
18	998.6	999.0	999.5	999.9	1000.4	1000.8	1001.3	1001.7
19	998.4	998.8	999.3	999.7	1000.2	1000.6	1001.1	1001.5
20	998.2	998.6	999.1	999.5	1000.0	1000.4	1000.9	1001.3
21	998.0	998.4	998.9	999.3	999.8	1000.2	1000.7	1001.1
22	997.8	998.2	998.6	999.1	999.5	1000.0	1000.4	1000.9
23	997.5	997.9	998.4	998.8	999.3	999.7	1000.2	1000.6
24	997.3	997.7	998.1	998.6	999.0	999.5	999.9	1000.4
25	997.0	997.4	997.9	998.3	998.8	999.2	999.7	1000.1
26	996.8	997.2	997.6	998.1	998.5	999.0	999.4	999.9
27	996.5	996.9	997.4	997.8	998.3	998.7	999.1	999.6
28	996.2	996.6	997.1	997.5	998.0	998.4	998.9	999.3
29	995.9	996.3	996.8	997.2	997.7	998.1	998.6	999.0
30	995.7	996.1	996.5	996.9	997.4	997.8	998.3	998.7
31	995.3	995.7	996.2	996.6	997.1	997.5	997.9	998.4
32	995.0	995.4	995.9	996.3	996.8	997.2	997.6	998.1
33	994.7	995.1	995.5	996.0	996.4	996.9	997.3	997.7
34	994.4	994.8	995.2	995.7	996.1	996.5	997.0	997.4
35	994.0	994.4	994.9	995.3	995.8	996.2	996.6	997.1
36	993.7	994.1	994.5	995.0	995.4	995.8	996.3	996.7
37	993.3	993.7	994.2	994.6	995.0	995.5	995.9	996.3
38	993.0	993.4	993.8	994.2	994.7	995.1	995.5	996.0
39	992.6	993.0	993.4	993.9	994.3	994.7	995.2	995.6
40	992.2	992.6	993.1	993.5	993.9	994.4	994.3	995.2

Table A. 2 (continued)

Temperature Θ °C	Absolute pressure 10^5 [Pa]							
	80	90	100	110	120	130	140	150
0	1003.8	1004.3	1004.8	1005.3	1005.8	1006.3	1006.8	1007.3
1	1003.9	1004.3	1004.8	1005.3	1005.8	1006.3	1006.8	1007.3
2	1003.9	1004.4	1004.8	1005.3	1005.8	1006.3	1006.8	1007.3
3	1003.9	1004.4	1004.8	1005.3	1005.8	1006.3	1006.8	1007.3
4	1003.8	1003.4	1004.8	1005.3	1005.8	1006.3	1006.7	1007.2
5	1003.8	1004.3	1004.8	1005.3	1005.7	1006.2	1006.7	1007.2
6	1003.8	1004.2	1004.7	1005.2	1005.7	1006.2	1006.2	1007.1
7	1003.7	1004.2	1004.7	1005.1	1005.6	1006.1	1006.5	1007.0
8	1003.6	1004.1	1004.6	1005.0	1005.5	1006.0	1006.5	1006.9
9	1003.5	1004.0	1004.5	1005.0	1005.4	1005.9	1006.4	1006.8
10	1003.4	1003.9	1004.4	1004.8	1005.3	1005.8	1006.2	1006.7
11	1003.3	1003.8	1004.3	1004.7	1005.2	1005.6	1006.1	1006.6
12	1003.2	1003.7	1004.1	1004.6	1005.0	1005.5	1006.0	1006.4
13	1003.1	1003.5	1004.0	1004.4	1004.9	1005.4	1005.8	1006.3
14	1002.9	1003.4	1003.8	1004.3	1004.7	1005.2	1005.7	1006.1
15	1002.7	1003.2	1003.7	1004.1	1004.6	1005.0	1005.5	1005.9
16	1002.6	1003.0	1003.5	1003.9	1004.4	1004.8	1005.3	1005.8
17	1002.4	1002.8	1003.3	1003.8	1004.2	1004.7	1005.1	1005.6
18	1002.2	1002.7	1003.1	1003.6	1004.0	1004.5	1004.9	1005.4
19	1002.0	1002.4	1002.9	1003.3	1003.8	1004.2	1004.7	1005.1
20	1001.8	1002.2	1002.7	1003.1	1003.6	1004.0	1004.5	1004.9
21	1001.6	1002.0	1002.5	1002.9	1003.3	1003.8	1004.2	1004.7
22	1001.3	1001.8	1002.2	1002.7	1003.1	1003.5	1004.0	1004.4
23	1001.1	1001.5	1002.0	1002.4	1002.9	1003.3	1003.7	1004.2
24	1000.8	1001.3	1001.7	1002.2	1002.6	1003.0	1003.5	1003.9
25	1000.6	1001.0	1001.5	1001.9	1002.3	1002.8	1003.2	1003.7
26	1000.3	1000.7	1001.2	1001.6	1002.1	1002.5	1002.9	1003.4
27	1000.0	1000.5	1000.9	1001.3	1001.8	1002.2	1002.7	1003.1
28	999.7	1000.2	1000.6	1001.1	1001.5	1001.9	1002.4	1002.8
29	999.4	999.9	1000.3	1000.8	1001.2	1001.6	1002.1	1002.5
30	999.1	999.6	1000.0	1000.4	1000.9	1001.3	1001.7	1002.2
31	998.8	999.3	999.7	1000.1	1000.6	1001.0	1001.4	1001.9
32	998.5	998.9	999.4	999.8	1000.2	1000.7	1001.1	1001.5
33	998.2	998.6	999.0	999.5	999.9	1000.3	1000.8	1001.2
34	997.8	998.3	998.7	999.1	999.6	1000.0	1000.4	1000.9
35	997.5	997.9	998.4	998.8	999.2	999.7	1000.1	1000.5
36	997.1	997.6	998.0	998.4	998.9	999.3	999.7	1000.2
37	996.8	997.2	997.6	998.1	998.5	998.9	999.4	999.8
38	996.4	996.8	997.3	997.7	998.1	998.6	999.0	999.4
39	996.0	996.5	996.9	997.3	997.8	998.2	998.6	999.0
40	995.7	996.1	996.5	996.9	997.4	997.8	998.2	998.7

Appendix B CFX Command Language for the Run

```
LIBRARY:
CEL:
  EXPRESSIONS:
    FrozenTime = 0.005 [s]
    FrozenTimestep = FrozenTime/nFrozen
    JetR = (29.7/2) [mm]
    JetVel = VolumeFlow/ (0.5*pi*JetR^2)
    JetVelVar = \
      JetVel*((-1/50)*atstep+1050/50)*step(1050-atstep)*step(atstep-1000)+\
      step(1000-atstep)
    MassFlow = VolumeFlow*998.78 [kg/m^3]
    MassFlowIn = 2*(Water.massFlow()@SInlet)
    MassFlowOut = -2*(Water.massFlow()@SOpening+Water.massFlow()@ROpening)
    MeanVel = areaAve(Velocity)@SInlet
    Omega = 942.5 [rev/min]
    OmegaVar = -step((Time-FrozenTime-0.5*TimeStep)/1[s])*Omega
    PitchR = 316 [mm] /2
    TimeStep = dOmega/Omega
    TimeStepVar = \
      step((-Time+FrozenTime-0.5*TimeStep)/1[s])*FrozenTimestep+step((Time-\
      FrozenTime+0.5*TimeStep)/1[s])*TimeStep
    Torque1Cut = -2*torque_x()@NS_RBucket1Cut
    Torque1In = -2*torque_x()@NS_RBucket1In
    Torque1Out = -2*torque_x()@NS_RBucket1Out
    Torque2 = -2*torque_x()@RWall12
    Torque2Cut = -2*torque_x()@NS_RBucket2Cut
    Torque2In = -2*torque_x()@NS_RBucket2In
    Torque2Out = -2*torque_x()@NS_RBucket2Out
    VFAir = 1 - VFWater
    VFWater = step((x-0.1 [m])/1[mm]) * step((JetR - sqrt(z^2 + \
      (y+PitchR)^2))/1[mm])
    VFWaterVar = \
      ((-1/50)*atstep+1000/50)*step(1000-atstep)*step(atstep-950)+step(950-\
      atstep)
    VolumeFlow = 0.5*0.0231 [m^3/s]
    dOmega = 0.05 [degree]
    nFrozen = 200
  END
END
MATERIAL: Air at 15C
  Material Group = User
  Option = Pure Substance
  PROPERTIES:
    Option = General Material
    EQUATION OF STATE:
      Density = 1.2257 [kg m^-3]
      Molar Mass = 1.0 [kg kmol^-1]
      Option = Value
    END
    DYNAMIC VISCOSITY:
      Dynamic Viscosity = 1.7965E-5 [Pa s]
      Option = Value
    END
    THERMAL EXPANSIVITY:
      Option = Value
      Thermal Expansivity = 3.4704E-3 [K^-1]
    END
  END
END
MATERIAL: Water at 15C
```

```

Material Group = User
Option = Pure Substance
PROPERTIES:
  Option = General Material
  EQUATION OF STATE:
    Density = 9.9878E+2 [kg m^-3]
    Molar Mass = 1.0 [kg kmol^-1]
    Option = Value
  END
  DYNAMIC VISCOSITY:
    Dynamic Viscosity = 1.1080E-3 [Pa s]
    Option = Value
  END
  THERMAL EXPANSIVITY:
    Option = Value
    Thermal Expansivity = 3.4704E-3 [K^-1]
  END
END
END
FLOW: Flow Analysis 1
SOLUTION UNITS:
  Angle Units = [rad]
  Length Units = [m]
  Mass Units = [kg]
  Solid Angle Units = [sr]
  Temperature Units = [K]
  Time Units = [s]
END
ANALYSIS TYPE:
  Option = Transient
EXTERNAL SOLVER COUPLING:
  Option = None
END
INITIAL TIME:
  Option = Automatic with Value
  Time = 0 [s]
END
TIME DURATION:
  Number of Timesteps per Run = 3000
  Option = Number of Timesteps per Run
END
TIME STEPS:
  Option = Timesteps
  Timesteps = TimeStepVar
END
END
DOMAIN: R
  Coord Frame = Coord 0
  Domain Type = Fluid
  Location = Assembly 2
BOUNDARY: Domain Interface 1 Side 1
  Boundary Type = INTERFACE
  Location = NS_RInterface
BOUNDARY CONDITIONS:
  MASS AND MOMENTUM:
    Option = Conservative Interface Flux
  END
  TURBULENCE:
    Option = Conservative Interface Flux
  END
END
NONOVERLAP CONDITIONS:
  Boundary Type = WALL

```

```

BOUNDARY CONDITIONS:
  MASS AND MOMENTUM:
    Option = Free Slip Wall
  END
END
END
BOUNDARY: ROpening
Boundary Type = OPENING
Frame Type = Rotating
Location = NS_ROpening
BOUNDARY CONDITIONS:
  FLOW REGIME:
    Option = Subsonic
  END
  MASS AND MOMENTUM:
    Option = Entrainment
    Relative Pressure = 0 [Pa]
  END
  TURBULENCE:
    Option = Zero Gradient
  END
END
FLUID: Air
BOUNDARY CONDITIONS:
  VOLUME FRACTION:
    Option = Value
    Volume Fraction = 1
  END
END
FLUID: Water
BOUNDARY CONDITIONS:
  VOLUME FRACTION:
    Option = Value
    Volume Fraction = 0
  END
END
END
BOUNDARY: RSymmetry
Boundary Type = SYMMETRY
Location = NS_RSymmetry
END
BOUNDARY: RWall1
Boundary Type = WALL
Frame Type = Rotating
Location = NS_RBucket1In,NS_RBucket1Cut,NS_RBucket1Out
BOUNDARY CONDITIONS:
  MASS AND MOMENTUM:
    Option = No Slip Wall
  END
  WALL ROUGHNESS:
    Option = Smooth Wall
  END
END
END
BOUNDARY: RWall2
Boundary Type = WALL
Frame Type = Rotating
Location = NS_RBucket2Cut,NS_RBucket2In,NS_RBucket2Out
BOUNDARY CONDITIONS:
  MASS AND MOMENTUM:
    Option = No Slip Wall

```

```

    END
    WALL ROUGHNESS:
        Option = Smooth Wall
    END
END
DOMAIN MODELS:
    BUOYANCY MODEL:
        Option = Non Buoyant
    END
    DOMAIN MOTION:
        Angular Velocity = OmegaVar
        Option = Rotating
    AXIS DEFINITION:
        Option = Coordinate Axis
        Rotation Axis = Coord 0.1
    END
    END
    MESH DEFORMATION:
        Option = None
    END
    REFERENCE PRESSURE:
        Reference Pressure = 1 [atm]
    END
END
FLUID DEFINITION: Air
    Material = Air at 15C
    Option = Material Library
    MORPHOLOGY:
        Option = Continuous Fluid
    END
END
FLUID DEFINITION: Water
    Material = Water at 15C
    Option = Material Library
    MORPHOLOGY:
        Option = Continuous Fluid
    END
END
FLUID MODELS:
    COMBUSTION MODEL:
        Option = None
    END
    HEAT TRANSFER MODEL:
        Homogeneous Model = On
        Option = None
    END
    THERMAL RADIATION MODEL:
        Option = None
    END
    TURBULENCE MODEL:
        Option = SST
    END
    TURBULENT WALL FUNCTIONS:
        Option = Automatic
    END
END
FLUID PAIR: Air | Water
    INTERPHASE TRANSFER MODEL:
        Option = Free Surface
    END
    MASS TRANSFER:
        Option = None
    END
END

```

```

SURFACE TENSION MODEL:
  Option = None
END
END
MULTIPHASE MODELS:
  Homogeneous Model = On
  FREE SURFACE MODEL:
    Option = Standard
  END
END
END
DOMAIN: S
  Coord Frame = Coord 0
  Domain Type = Fluid
  Location = B137,B136,B135,B134
  BOUNDARY: Domain Interface 1 Side 2 1
    Boundary Type = INTERFACE
    Location = NS_SInterface
    BOUNDARY CONDITIONS:
      MASS AND MOMENTUM:
        Option = Conservative Interface Flux
      END
      TURBULENCE:
        Option = Conservative Interface Flux
      END
    END
  NONOVERLAP CONDITIONS:
    Boundary Type = WALL
    BOUNDARY CONDITIONS:
      MASS AND MOMENTUM:
        Option = Free Slip Wall
      END
    END
  END
  BOUNDARY: SInlet
    Boundary Type = INLET
    Location = NS_SInlet
    BOUNDARY CONDITIONS:
      FLOW REGIME:
        Option = Subsonic
      END
      MASS AND MOMENTUM:
        Normal Speed = JetVelVar
        Option = Normal Speed
      END
      TURBULENCE:
        Option = Medium Intensity and Eddy Viscosity Ratio
      END
    END
  FLUID: Air
    BOUNDARY CONDITIONS:
      VOLUME FRACTION:
        Option = Value
        Volume Fraction = 1-VFWaterVar
      END
    END
  FLUID: Water
    BOUNDARY CONDITIONS:
      VOLUME FRACTION:
        Option = Value
        Volume Fraction = VFWaterVar
      END

```

```

    END
  END
END
BOUNDARY: SOpening
  Boundary Type = OPENING
  Location = NS_SOpening
  BOUNDARY CONDITIONS:
    FLOW REGIME:
      Option = Subsonic
    END
    MASS AND MOMENTUM:
      Option = Entrainment
      Relative Pressure = 0 [Pa]
    END
    TURBULENCE:
      Option = Zero Gradient
    END
  END
FLUID: Air
  BOUNDARY CONDITIONS:
    VOLUME FRACTION:
      Option = Value
      Volume Fraction = 1
    END
  END
FLUID: Water
  BOUNDARY CONDITIONS:
    VOLUME FRACTION:
      Option = Value
      Volume Fraction = 0
    END
  END
END
BOUNDARY: SSymmetry
  Boundary Type = SYMMETRY
  Location = NS_SSymmetry
END
BOUNDARY: SWall
  Boundary Type = WALL
  Location = NS_SWall
  BOUNDARY CONDITIONS:
    MASS AND MOMENTUM:
      Option = Free Slip Wall
    END
  END
END
DOMAIN MODELS:
  BUOYANCY MODEL:
    Option = Non Buoyant
  END
  DOMAIN MOTION:
    Option = Stationary
  END
  MESH DEFORMATION:
    Option = None
  END
  REFERENCE PRESSURE:
    Reference Pressure = 1 [atm]
  END
END
FLUID DEFINITION: Air
  Material = Air at 15C

```

```

Option = Material Library
MORPHOLOGY:
  Option = Continuous Fluid
END
END
FLUID DEFINITION: Water
Material = Water at 15C
Option = Material Library
MORPHOLOGY:
  Option = Continuous Fluid
END
END
FLUID MODELS:
COMBUSTION MODEL:
  Option = None
END
HEAT TRANSFER MODEL:
  Homogeneous Model = On
  Option = None
END
THERMAL RADIATION MODEL:
  Option = None
END
TURBULENCE MODEL:
  Option = SST
END
TURBULENT WALL FUNCTIONS:
  Option = Automatic
END
END
FLUID PAIR: Air | Water
INTERPHASE TRANSFER MODEL:
  Option = Free Surface
END
MASS TRANSFER:
  Option = None
END
SURFACE TENSION MODEL:
  Option = None
END
END
MULTIPHASE MODELS:
  Homogeneous Model = On
FREE SURFACE MODEL:
  Option = Standard
END
END
DOMAIN INTERFACE: Domain Interface 1
Boundary List1 = Domain Interface 1 Side 1
Boundary List2 = Domain Interface 1 Side 2 1
Interface Type = Fluid Fluid
INTERFACE MODELS:
  Option = General Connection
FRAME CHANGE:
  Option = Transient Rotor Stator
END
MASS AND MOMENTUM:
  Option = Conservative Interface Flux
MOMENTUM INTERFACE MODEL:
  Option = None
END
END
PITCH CHANGE:

```

```

        Option = Specified Pitch Angles
        Pitch Angle Side1 = 360 [degree]
        Pitch Angle Side2 = 360 [degree]
    END
END
MESH CONNECTION:
    Option = GGI
END
INITIALISATION:
    Frame Type = Stationary
    Option = Automatic
    FLUID: Air
        INITIAL CONDITIONS:
            VOLUME FRACTION:
                Option = Automatic with Value
                Volume Fraction = 1
            END
        END
    END
    FLUID: Water
        INITIAL CONDITIONS:
            VOLUME FRACTION:
                Option = Automatic with Value
                Volume Fraction = 0
            END
        END
    END
    INITIAL CONDITIONS:
        Velocity Type = Cartesian
        CARTESIAN VELOCITY COMPONENTS:
            Option = Automatic with Value
            U = 0 [m s^-1]
            V = 0 [m s^-1]
            W = 0 [m s^-1]
        END
        STATIC PRESSURE:
            Option = Automatic with Value
            Relative Pressure = 0 [Pa]
        END
        TURBULENCE INITIAL CONDITIONS:
            Option = Medium Intensity and Eddy Viscosity Ratio
        END
    END
END
OUTPUT CONTROL:
    MONITOR OBJECTS:
        MONITOR BALANCES:
            Option = Full
        END
        MONITOR FORCES:
            Option = Full
        END
        MONITOR PARTICLES:
            Option = Full
        END
        MONITOR POINT: InFlow
            Coord Frame = Coord 0
            Expression Value = MassFlowIn
            Option = Expression
        END
        MONITOR POINT: Inlet Velocity
            Coord Frame = Coord 0
            Expression Value = JetVelVar
    
```

```

    Option = Expression
END
MONITOR POINT: Max YPlus 1
    Coord Frame = Coord 0
    Expression Value = MaxYPlus1
    Option = Expression
END
MONITOR POINT: Max YPlus 2
    Coord Frame = Coord 0
    Expression Value = MaxYPlus2
    Option = Expression
END
MONITOR POINT: Mean Velocity
    Coord Frame = Coord 0
    Expression Value = MeanVel
    Option = Expression
END
MONITOR POINT: OutFlow
    Coord Frame = Coord 0
    Expression Value = MassFlowOut
    Option = Expression
END
MONITOR POINT: Torque 1
    Coord Frame = Coord 0
    Expression Value = Torque1
    Option = Expression
END
MONITOR POINT: Torque 1 Cut
    Coord Frame = Coord 0
    Expression Value = Torque1Cut
    Option = Expression
END
MONITOR POINT: Torque 1 Inside
    Coord Frame = Coord 0
    Expression Value = Torque1In
    Option = Expression
END
MONITOR POINT: Torque 1 Outside
    Coord Frame = Coord 0
    Expression Value = Torque1Out
    Option = Expression
END
MONITOR POINT: Torque 2 Cut
    Coord Frame = Coord 0
    Expression Value = Torque2Cut
    Option = Expression
END
MONITOR POINT: Torque 2 Inside
    Coord Frame = Coord 0
    Expression Value = Torque2In
    Option = Expression
END
MONITOR POINT: Torque 2 Outside
    Coord Frame = Coord 0
    Expression Value = Torque2Out
    Option = Expression
END
MONITOR RESIDUALS:
    Option = Full
END
MONITOR TOTALS:
    Option = Full
END
END

```

```

RESULTS:
  File Compression Level = Default
  Option = Standard
END
TRANSIENT RESULTS: Transient Results 1
  File Compression Level = Default
  Option = Standard
  Output Equation Residuals = All
  OUTPUT FREQUENCY:
    Option = Timestep Interval
    Timestep Interval = 5
  END
END
TRANSIENT RESULTS: Transient Results 2
  File Compression Level = Default
  Include Mesh = No
  Option = Selected Variables
  Output Equation Residuals = None
  Output Variables List = Water.Volume Fraction
  OUTPUT FREQUENCY:
    Option = Timestep Interval
    Timestep Interval = 2
  END
END
SOLVER CONTROL:
  Turbulence Numerics = First Order
  ADVECTION SCHEME:
    Option = High Resolution
  END
CONVERGENCE CONTROL:
  Maximum Number of Coefficient Loops = 10
  Minimum Number of Coefficient Loops = 3
  Timescale Control = Coefficient Loops
  END
CONVERGENCE CRITERIA:
  Residual Target = 0.0001
  Residual Type = RMS
  END
TRANSIENT SCHEME:
  Option = Second Order Backward Euler
  TIMESTEP INITIALISATION:
    Option = Automatic
  END
  END
  END
  END
COMMAND FILE:
  Version = 14.5
  Results Version = 14.5
  END
SIMULATION CONTROL:
  EXECUTION CONTROL:
    EXECUTABLE SELECTION:
      Double Precision = Off
    END
  INTERPOLATOR STEP CONTROL:
    Runtime Priority = Standard
  MEMORY CONTROL:
    Memory Allocation Factor = 1.0
  END
  END
PARALLEL HOST LIBRARY:
  HOST DEFINITION: egc042000008

```

```

    Host Architecture String = winnt-amd64
    Installation Root = C:\Program Files\ANSYS Inc\v%v\CFX
  END
END
PARTITIONER STEP CONTROL:
  Multidomain Option = Independent Partitioning
  Runtime Priority = Standard
EXECUTABLE SELECTION:
  Use Large Problem Partitioner = Off
END
MEMORY CONTROL:
  Memory Allocation Factor = 1.0
END
PARTITIONING TYPE:
  MeTiS Type = k-way
  Option = MeTiS
  Partition Size Rule = Automatic
  Partition Weight Factors = 0.25000, 0.25000, 0.25000, 0.25000
END
END
RUN DEFINITION:
  Run Mode = Full
  Solver Input File = CFX.def
END
SOLVER STEP CONTROL:
  Runtime Priority = Standard
MEMORY CONTROL:
  Memory Allocation Factor = 1.0
END
PARALLEL ENVIRONMENT:
  Number of Processes = 4
  Start Method = Platform MPI Local Parallel
  Parallel Host List = egc042000008*4
END
END
END
END

```

Appendix C

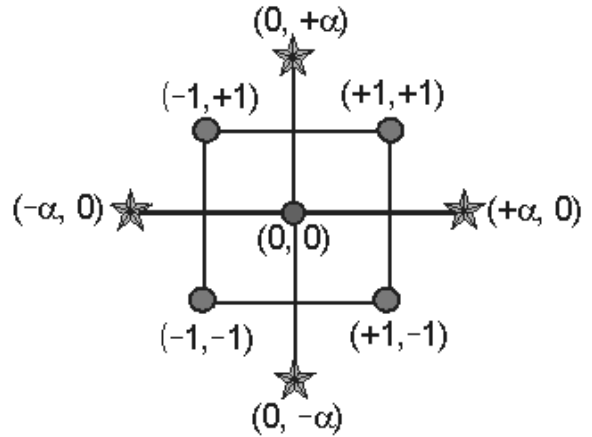
Excerpt from the documentation of the Design Expert 9 software.

Design of Experiments - Response Surface Method

Central Composite Design

The most popular response surface method (RSM) design is the central composite design (CCD). A CCD has three groups of design points:

- (a) two-level factorial or fractional factorial design points
- (b) axial points (sometimes called "star" points)
- (c) center points



CCD's are designed to estimate the coefficients of a quadratic model. All point descriptions will be in terms of coded values of the factors.

Factorial Points

The two-level factorial part of the design consists of all possible combinations of the +1 and -1 levels of the factors. For the two factor case there are four design points:

$(-1, -1)$ $(+1, -1)$ $(-1, +1)$ $(+1, +1)$

Star or Axial Points

The star points have all of the factors set to 0, the midpoint, except one factor, which has the value +/- Alpha. For a two-factor problem, the star points are:

$(-\text{Alpha}, 0)$ $(+\text{Alpha}, 0)$ $(0, -\text{Alpha})$ $(0, +\text{Alpha})$

The value for Alpha is calculated in each design for both rotatability and orthogonality of blocks. The experimenter can choose between these values or enter a different one. The default value is set to the rotatable value.

Another position for the star points is at the face of the cube portion on the design. This is commonly referred to as a face-centered central composite design. You can create this by setting the alpha

distance to one, or choosing the Face Centered option. This design only requires three levels for each factor.

Center Points

Center points, as implied by the name, are points with all levels set to coded level 0 - the midpoint of each factor range: (0, 0)

Center points are usually repeated 4-6 times to get a good estimate of experimental error (pure error). For example, with two factors the design will be created with five center points by default. These runs can be identified in the design layout by doing a right mouse click on the **Block column** and choosing **Point Type**.

To summarize, central composite designs require 5 levels of each factor: -Alpha, -1, 0, 1, and +Alpha. One of the commendable attributes of the central composite design is that its structure lends itself to sequential experimentation. Central composite designs can be carried out in blocks.

Categorical Factors

You may also add categorical factors to this design. This will cause the number of runs generated to be multiplied by the number of combinations of the categorical factor levels.

Small Central Composite Design

Small central composite designs are available when the number of factors is 3 or more. You can choose a small CCD by selecting the central composite design and then clicking on the pull-down menu labeled "Type" and selecting "Small". These designs are the minimal-point designs needed to estimate the terms in a second order model. See the table below for a comparison of the full and fractional CCD's versus the small CCD for the 1 block case. The numbers include center points.

Factors	CCD Full	CCD Frac	Small CCD
3	20	---	15
4	30	---	21
5	50	32	26
6	86	52	33
7	152	88	41
8	278	154, 90	51
9	536	284, 156	61
10	1050*	542, 158	71

* - not available in Design-Expert.

CAUTION:

Small central composite designs are unbalanced minimal-point designs. They are not rotatable and are extremely sensitive to outliers. The choice of the alpha value to ensure orthogonal blocking for 3, 4 and 6 factors is calculated in the usual manner for a CCD. For 5, 7, 8, 9 and 10 factors there is no alpha that ensures orthogonal blocking. These designs have runs deleted, making the cube part of the design non-orthogonal, violating one of the requirements for orthogonal blocks. For these designs the alpha for blocks is chosen to minimize the average squared correlation of the block effect with all second order model coefficients, ignoring the constant.

For further reference on Small Central Composite Designs, please see the article "Small Response-Surface Designs" in *Technometrics*, May 1990, Vol. 32, No. 2, pp. 187-194.